Testbeds for Advancement of Powder Bed Additive Manufacturing with Application to Reactive Binder Jetting of Ceramics

by

Daniel Oropeza Gomez

B.S., The University of Texas at Austin (2012)
M.S., Stanford University (2014)

Submitted to the Department of Mechanical Engineering
in partial fulfillment of the requirements for the degree of

Doctor of Philosophy of Mechanical Engineering

at the

MASSACHUSETTS INSTITUTE OF TECHNOLOGY

September 2021

Author……
Daniel Oropeza Gomez
Department of Mechanical Engineering
July 26, 2021

Certified by……
A. John Hart
Professor of Mechanical Engineering
Thesis Supervisor

Accepted by……...
Nicolas. G. Hadjiconstantinou
Chairman, Department Committee on Graduate Theses

Testbeds for Advancement of Powder Bed Additive Manufacturing with Application to Reactive Binder Jetting of Ceramics

by

Daniel Oropeza Gomez

Submitted to the Department of Mechanical Engineering
on July 26, 2021, in partial fulfillment of the
requirements for the degree of
Doctor of Philosophy of Mechanical Engineering

Abstract
Binder jet additive manufacturing (BJAM) offers design flexibility and compatibility with a variety of materials due to material processing in the solid state. The formation of the powder bed is a critical step to ensuring quality parts are produced via binder jetting, but low powder bed densities and a lack of understanding of the effect of recoating parameters have limited the applicability of binder jet components. Furthermore, polymer-based binders are most commonly used despite the need for a debinding step and challenges with part warping during sintering. Adaptations to the binder jet AM process, such as the use of powder spreading optimization and reactive binders, could facilitate the development of high-density ceramics from dry powder feedstock. To attain this, an understanding of powder spreading, binder-powder interactions, and reactive metal salt decomposition and interparticle-bridge evolution is required.

This thesis: (1) describes the design and fabrication of testbeds for powder spreading, ink jetting, and binder jetting processes, (2) explores the effects of powder feedstock and spreading parameters on powder bed density and uniformity of alumina ceramics for application in binder jet additive manufacturing, (3) establishes a process for novel binder ink development and applies it to the production of reactive metal salt binders for preceramic binder jetting, and (4) fabricates alumina ceramic components through BJAM and compares the efficacy of polymer and reactive binders in microstructural and dimensional control during post-process sintering. The powder spreading and BJAM testbeds are validated using representative experiments to characterize powder layer and green component fabrication. By coupling the powder spreading tested with an x-ray-based powder layer density measurement methodology, the influence of powder size and shape distribution, as well as spreading and dispensing methodologies is interrogated. A process including characterization of ink rheology, jetting properties, decomposition, and green strength is applied to the development of novel reactive binders with sustained strength during sintering. Finally, the BJAM testbed is utilized to fabricate ceramic components using polymer and reactive binders, showcasing the capability for microstructural and dimensional control of ceramics through the use of reactive binders.

Thesis Supervisor: A. John Hart
Title: Professor of Mechanical Engineering

Acknowledgements

I want to thank and praise God for the many blessings in my life. During the hardships you are my strength and during the victories you share my joy. Despite my many flaws and errors, you let me know that I am known, I am valued, I am loved.

"For what shall it profit a man, if he shall gain the whole world, and lose his own soul?"
- Mark 8:36 (KJV)

I want to thank my wife, Connor, for her unwavering love and support throughout this program. I cannot imagine this experience without you and am so excited to cross into the next phase of life together.

I want to thank my amazing family: thank you for your love and guidance, thank you for your beautiful example, thank you for your encouragement.

I want to thank my thesis committee - Prof. A. John Hart, Prof. Gareth McKinley, and Prof. Jennifer Rupp - for their time and advice during the PhD process. Thanks for your interest in my work, your assistance with getting the necessary resources, and your guidance during the research process.

I've been blessed to make many friends within the Mechanosynthesis Group, whom I thank for their advice, collaboration, and friendship. Thanks in particular to Ryan Penny, Adam Stevens, Nick Dee, Michael Arnold, Nigamaa Nayakanti, Reimar Weissbach, Jon Gibbs, Bethany Lettiere, Christine Jacob, Ricardo Roberts. I'd also like to thank MIT FC for giving me the opportunity to meet an amazing group of folks from many walks of life all brought together in our love for futbol – thanks for giving me to opportunity to play, coach, and lead – ¡VAMOS EQUIPO! Throughout my time at MIT, I have felt incredible support from the MIT UCEM program – I want to thank Prof. Leslie Kolodziejski, Cindy Higgins, Zoe Lemon, Dr. Ashley Carpenter, and Gloria Anglon for creating an inviting and supporting culture for UCEM at MIT. It was an honor to serve as part of the Mechanical Engineering DEI Task Force – I thank Prof. Asegun Henry, Katey Stewart, Dr. Dawn Wendell, Fiona Grant, Vishnu Jayaprakash, Prof. Cullen Buie, Yadira Rivera, Bryan

Nance, Jonathan Tagoe, Stacey Godfreey-Igwe, and Daniel Diaz for their dedication to making MIT MechE a welcoming environment for all and for giving me the opportunity to learn from them. Additionally, I want to thank the MechE Graduate Office, particularly Leslie Reagan and Saana McDaniel, for their support.

Throughout the program, I've had the privilege to interact with some incredible people. I want to thank Dr. Ned Allen and Dr. Luke Uribarri for their belief, support, and friendship. From the NASA family: I want to thank Mike Halbig from Glenn Research Center (GRC) for being an amazing resource at throughout my fellowship, as well as Dr. Jay Singh at GRC for being embracing mentors during my time at GRC and the opportunity to present our work at ICAAC; I want to thank Dr. Doug Hofmann and Dr. Tent Bordeenithikasem from NASA Jet Propulsion Lab (JPL) for welcoming me in during my time at JPL and for their mentorship throughout the publication process; I want to thank Imelda Terrazas-Salinas and Enrique Carballo from NASA Ames Research Center for their time and collaboration; thanks as well to John Vickers from Marshall Space Flight Center for his time, support, and mentorship. Additionally, I want to thank Prof. Fred Higgs from Rice University, David Niño from MIT, and Prof. Dava Newman from MIT for their advice, mentorship, and helping in developing my career path and professional network.

I want to acknowledge support from Lockheed Martin, the Ain A. Sonin Fellowship, the Zakhartchenko Fellowship, the NASA Space Technology Research Fellowship, and the Alfred. P Sloan Foundation's Minority PhD program for making my time at MIT possible.

Contents

List of Figures

List of Tables

Chapter 1

Introduction

1.1 Binder jet additive manufacturing

Additive manufacturing (AM), a set of processes that fabricates components in a layer-by-layer fashion, is of high interest due to the capability to fabricate complex geometries, possible reduction in lead time for part production, and batch-to-batch flexibility in manufacturing [1]. In particular, binder jet additive manufacturing (BJAM) is compatible with a variety of materials (i.e., metals, polymers, ceramics) as the shaping and densification steps are separate steps of the fabrication process for BJAM [1–3]. Additionally, BJAM is capable of fabricating at a high build rate compared to other AM methods, capable of high resolution (<100μm), and scalability to very large build volumes (e.g., 100s mm length) [1,2].

Binder jet additive manufacturing consists of two primary steps to shape a component: powder spreading and inkjet deposition of a binder. In the powder spreading step, a thin layer (20-100μm) of powder is created using a spreading mechanism (e.g., roller) into a uniform and homogenous layer [1–4]. In the binder deposition step, inkjet nozzles deposit a polymer binder (10s of μm diameter droplets) on the powder bed to

consolidate the layer into a desired geometry and adhere to the prior layer [1–4]. Figure 1.1 shows the powder spreading and binder ink deposition steps of the BJAM process.

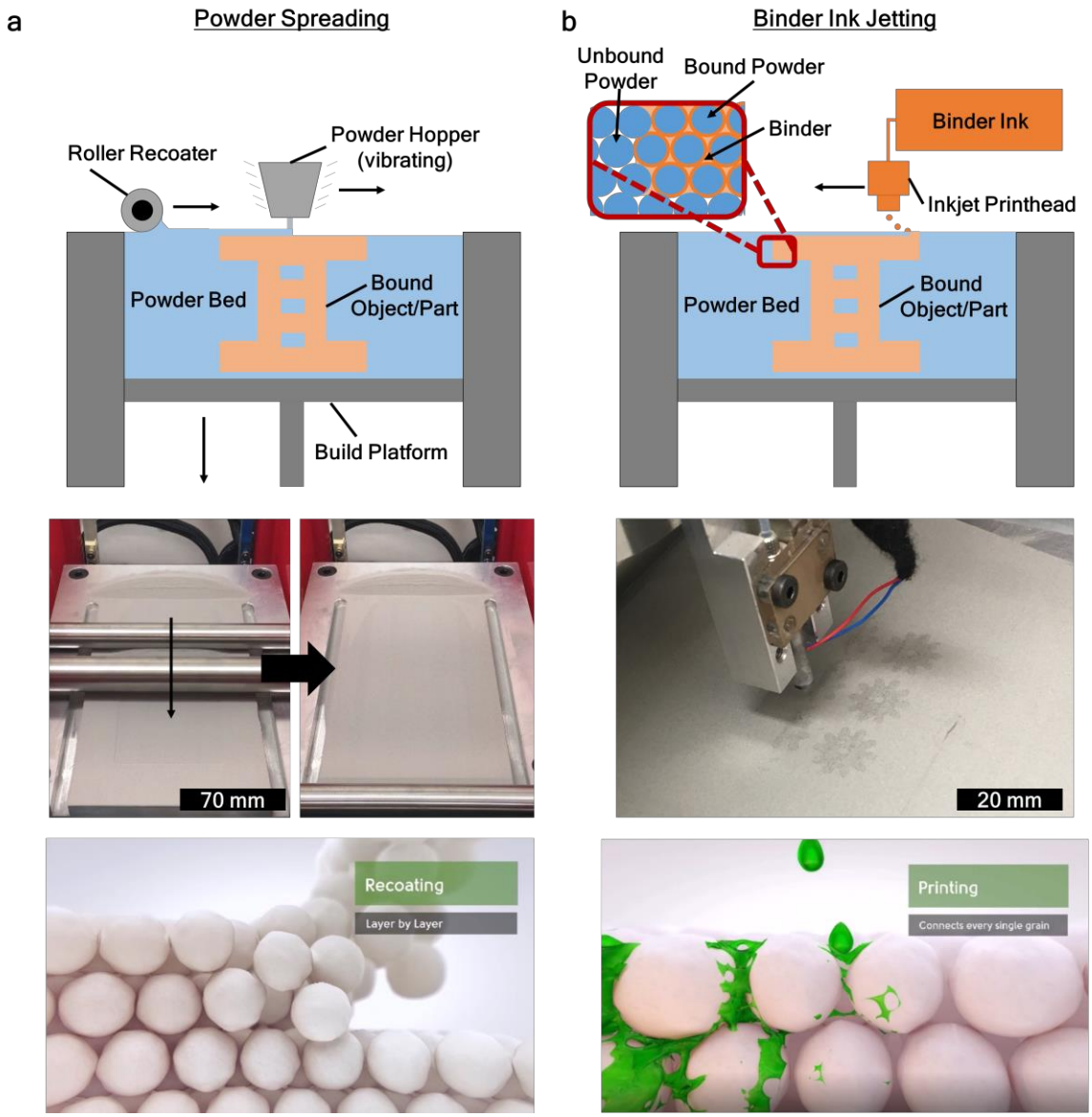

Figure 1.1: (a) Powder spreading step for binder jet additive manufacturing with conceptual image (top), exemplary machine showing powder spreading step (center), and idealization of powder spreading process (bottom, image taken from ExOne video [5]) and (b) binder ink deposition step with conceptual image (top), exemplary machine showing binder deposition process (center), and idealization of inkjet deposition process (bottom, image taken from ExOne video [5]).

After shaping of the desired layers, the printed (or green) component can be removed from the build platform, possibly requiring a thermal curing step for the binder prior to part removal. To improve material properties (e.g., mechanical) post-processing consolidation through thermal sintering is commonly performed for BJAM materials [1,4]. Figure 1.2 highlights the consolidation process for the powder feedstock utilized in BJAM – a process very similar to that followed in powder metallurgy and conventional ceramic processing [1,6–9]. The loose powder is bound into a green shape during the BJAM process through the selective deposition of binder ink. The polymer binder is burnt-off during a debinding step to ensure no undesired residue remains on the powder that could negatively influence the component's microstructure. Finally, through high-temperature sintering, the part is consolidated, followed by additional post-processing (e.g., infiltration, hot isostatic pressing) to further improve densification if necessary [1,4,7,10].

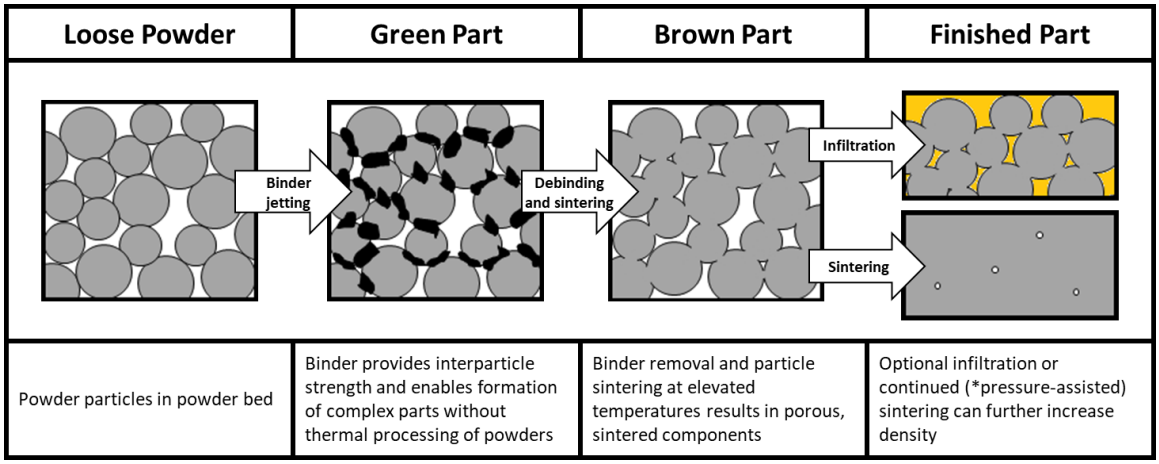

Figure 1.2: Consolidation process for BJAM, beginning from powder feedstock, followed by formation into green shape using a binder, and post-shaping densification through a thermal sintering step.

Due to its inherent separation of shaping and densification steps and thus similarity to conventional ceramic processing, BJAM is well-suited to the fabrication of complex geometries for ceramic materials [1,11–13]. Prior work in BJAM of ceramics has resulted in processing for bioceramics (e.g., hydroxyapatite, tricalcium phosphate), structural ceramics (e.g., aluminum oxide, zirconium oxide, silicon carbide), and functional ceramics (e.g., barium titanate, silicon nitride), with exemplary aluminum oxide BJAM samples

shown in [11,12,14,15]. Ceramics with high temperature resistance, corrosion resistance, oxidation resistance, and high hardness are well-suited for applications in aerospace, metals processing, and energy generation, with certain functional ceramics exhibiting excellent electrical and magnetic properties [8,9,12,16,17].

Figure 1.3: Sample geometries of parts fabricated using binder jet additive manufacturing and aluminum oxide powder for use in catalysis (image from Johnson Matthey [15]).

Challenges in BJAM of ceramics stem from the competing requirements for powder spreading and sintering densification: with coarse powders (>25μm) exhibiting better powder blowability and less cohesion than fine powders (<25μm), but fine powders preferable for sintering as the sintering densification rate is inversely proportional to particle size [4,10–12]. The spreading of dry fine powders, thus, results in low powder layer (and green part) densities which ultimately result in part inhomogeneities and low sintered density [4,11,12,18–21]. Additionally, due to the high temperatures required for sintering of ceramics, warping and part distortion results due to loss of strength after polymer binder decomposition without appropriate sintering support – thus restricting the possible geometry complexity of parts fabricated by BJAM [4,9,11,12,22].

In order to address issues of low green density, sintering densification, and dimensional control, it is imperative to understand the fundamentals of powder spreading, ink jet deposition, and sintering processes. By utilizing custom-developed testbeds and a process for the development of novel binders, it is possible to probe the fundamentals of

binder jet additive manufacturing in an effort to influence decision-making for manufacturing conditions with improved control.

To that end, this thesis describes the fabrication of precision testbeds for powder spreading and binder jet additive manufacturing, a development process for binder ink characterization, and printing of ceramic components utilizing polymer and reactive binders with post-process sintering and warping studies. By coupling the powder spreading testbed system with an x-ray-based measurement methodology, the influence of feedstock and process parameter on layer density is explored. The binder development process is implemented to synthesize polymer and reactive binders to compare their efficacy for the BJAM process and post-process sintering. BJAM of ceramic components is performed using a custom testbed and synthesized polymer and reactive binders, with post-process sintering and characterization detailing the influence of binder composition on densification and warping.

1.2 Thesis outline

The remainder of the thesis is organized as follows:

Chapter 2: Design, fabrication, and validation of a powder spreading testbed.

The design, fabrication, and validation of a testbed for modular, mechanized, multi-layer powder spreading is presented. The testbed is designed to replicate the operating conditions of commercial AM equipment, yet features full control over motion parameters including the translation and rotation of a roller spreading tool, and precision motion of a feed piston and the build platform. The powder spreading mechanism is interchangeable and therefore can be customized, including the capability for dispensing of fine, cohesive powders using a vibrating hopper. Validation of the resolution and accuracy of the machine and its subsystems, as well as the spreading of exemplary layers from a range of powder sizes typical of BJAM and PBF processes, are described. The precision engineered testbed can therefore enable the optimization of powder spreading parameters for AM and correlation

to build process parameters in future work, as well as exploration of spreading of specialized powders for AM and other techniques.

This content in this chapter was published in:

D. Oropeza, R. Roberts, A.J. Hart, A modular testbed for mechanized spreading of powder layers for additive manufacturing, Rev. Sci. Instrum. 92 (2021) 015114. https://doi.org/10/ghszgr.

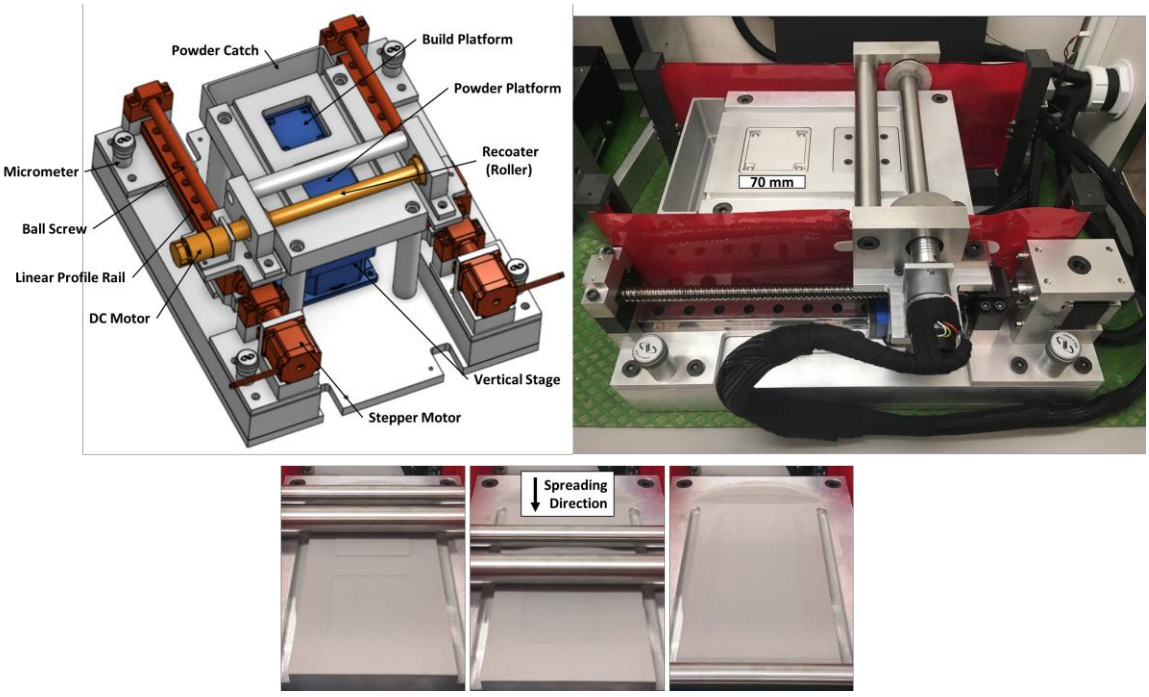

Figure 1.4: Graphical summary of Chapter 2, highlighting design, fabrication, and validation experiments for powder spreading testbed.

Chapter 3: Design, fabrication, and validation of a binder jet additive manufacturing testbed.

The design, fabrication, and qualification of a testbed for modular, mechanized, BJAM testbed is presented. The testbed seeks to replicate the operating conditions of commercial AM equipment and features fully programmable motion control including

powder spreading using a precision roller mechanism, powder supply via a vibrating hopper, and gantry positioning of an inkjet printhead. The inkjet deposition system allows for the use of variable nozzle diameters, the exploration of novel binder compositions, and full control of jetting parameters. Validation of the accuracy and repeatability of the machine and its subsystems, as well as the fabrication of exemplary stainless steel components, are described. The precision engineered testbed can therefore enable the study of the BJAM process, exploration of novel binder compositions, and processing of custom powders to further scientific research and industrial applicability of BJAM.

The content in this chapter was published in:

D. Oropeza, A.J. Hart, A laboratory-scale binder jet additive manufacturing testbed for process exploration and material development, Int. J. Adv. Manuf. Technol. 114 (2021) 3459–3473. https://doi.org/10/gkhbcm.

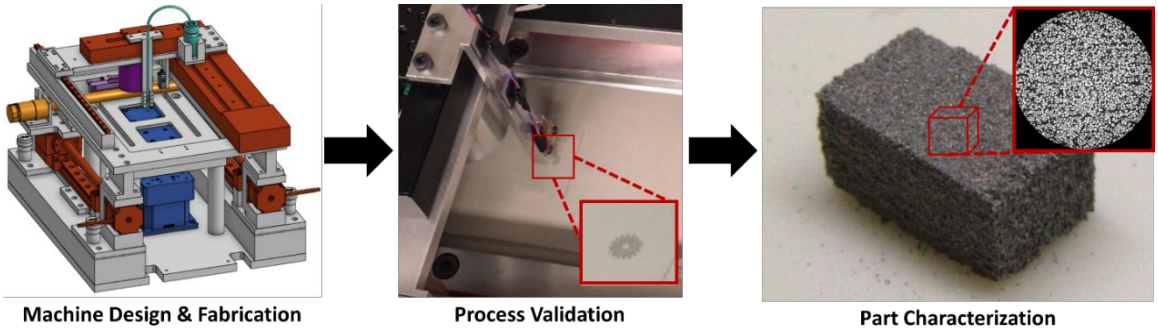

Figure 1.5: Graphical summary of Chapter 3, highlighting the design, fabrication, and validation experiments for a binder jet additive manufacturing testbed

Chapter 4: Binder development process and application to reactive metal salt binders.

A process for the development of custom binder inks for use in binder jet additive manufacturing is presented, including the characterization of ink rheology, ink jetting, wetting and infiltration, binder decomposition, and green strength characterization. Custom polymer and reactive (metal salt) binders are synthesized and characterized, highlighting

the compatibility of reactive binders for use in binder jet additive manufacturing for continuous green strength throughout sintering process. An indentation-based method for characterizing the green strength of simulated binder jet components is presented and the green strength of polymer and reactive (metal salt) are compared.

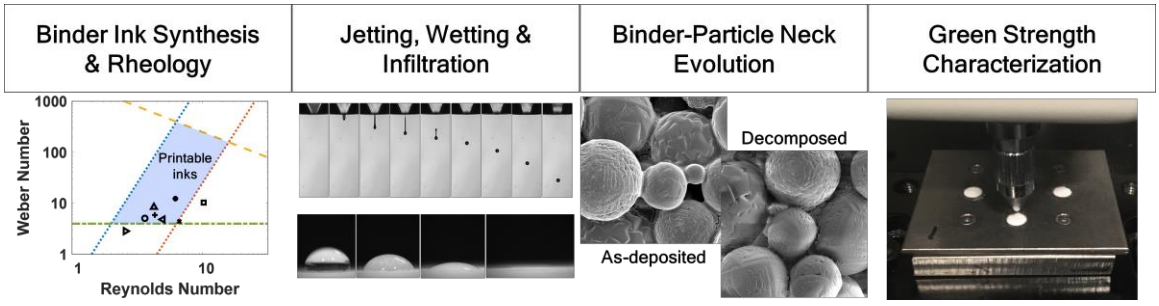

Figure 1.6: Graphical summary of Chapter 4, highlighting the binder development process utilized to develop polymer and reactive metal binder inks.

Chapter 5: Powder spreading and layer density characterization of ceramics.

Coupling of the powder spreading testbed with non-contact transmission x-ray imaging system is presented for localized, in-situ powder layer density measurements of ceramic materials. The influence of powder size and shape distribution, spreading parameters, and dispensing mechanisms is explored. Particle shape are shown to greatly influences layer density, with spherical powders resulting in higher layer density than irregular powders. For fine (20 μm) spherical and irregular powders, the use of roller counter-rotation increased layer density and increased traverse speed decreased powder layer density and uniformity, however the use of roller counter-rotation for coarse (40 μm) spherical and (35 μm) irregular powder decreased layer density. Spreading tool geometry influenced powder layer density, with density increasing for roller geometry without rotation compared to blade spreading for coarse (40 μm) spherical powders. Vibrating hopper dispensing resulted in increase to powder layer density over piston-fed powder spreading for fine (20 μm) spherical powders.

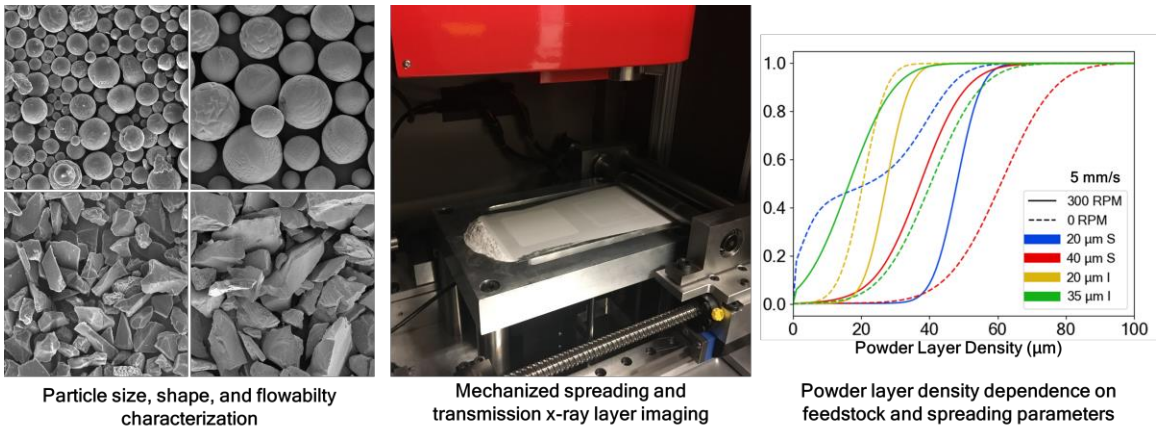

Figure 1.7: Graphical summary of Chapter 5, highlighting powder feedstock properties, mechanized powder spreading rig and x-ray-based layer density measurement, and influence of feedstock and spreading parameters on layer density.

Chapter 6: Reactive binder jet additive manufacturing of ceramics for microstructural control.

The binder jet additive manufacturing testbed is utilized to fabricate components using polymer and reactive metal salt binders. Green density and sintered density measurements through geometric and µCT are performed, highlighting that the use of sintering aid precursors as reactive binders results in improved densification, while the use of self-similar reactive binders reduces part shrinkage. The use of reactive metal salt binders improves part strength during densification, resulting in less part warping and fracture as compared to polymer binders.

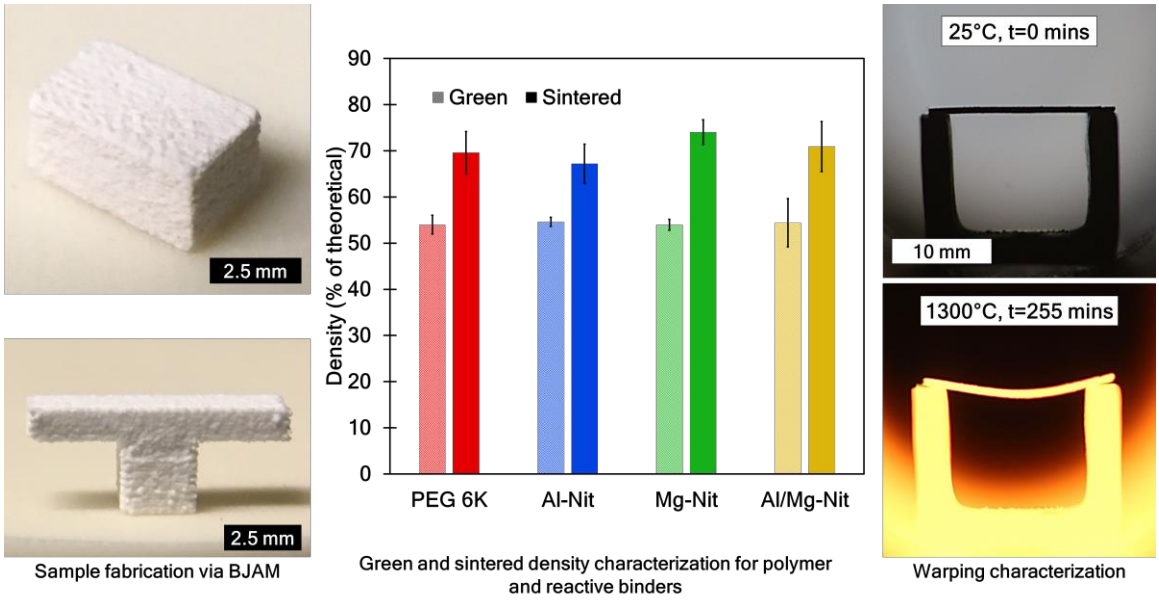

Figure 1.8: Graphical summary of Chapter 6, highlighting sample fabrication via BJAM, influence of polymer and reactive binders on densification, and in-situ warping experiments for printed samples.

Chapter 7: Conclusion and outlook.

A summary of the work performed as part of the thesis is provided, along with a discussion of future work beyond the scope of this work. Additionally, the contributions and outlook of the work performed in this thesis are summarized.

Chapter 2

Design, fabrication, and validation of a powder spreading testbed

This content in this chapter was published in:

D. Oropeza, R. Roberts, A.J. Hart, A modular testbed for mechanized spreading of powder layers for additive manufacturing, Rev. Sci. Instrum. 92 (2021) 015114. https://doi.org/10/ghszgr.

Powder bed additive manufacturing (AM) processes, including binder jetting (BJAM) and powder bed fusion (PBF), can manufacture complex three-dimensional components from a variety of materials. A fundamental understanding of the spreading of thin powder layers is essential to develop robust process parameters for powder bed AM, and to assess the influence of powder feedstock characteristics on the subsequent process outcomes. Toward meeting these needs, this work presents the design, fabrication, and qualification of a testbed for modular, mechanized, multi-layer powder spreading. The testbed is designed to replicate the operating conditions of commercial AM equipment, yet

features full control over motion parameters including the translation and rotation of a roller spreading tool, and precision motion of a feed piston and the build platform. The powder spreading mechanism is interchangeable and therefore can be customized, including the capability for dispensing of fine, cohesive powders using a vibrating hopper. Validation of the resolution and accuracy of the machine and its subsystems, as well as the spreading of exemplary layers from a range of powder sizes typical of BJAM and PBF processes, are described. The precision engineered testbed can therefore enable the optimization of powder spreading parameters for AM and correlation to build process parameters in future work, as well as exploration of spreading of specialized powders for AM and other techniques.

2.1 Introduction

Additive manufacturing (AM), referring broadly to techniques that build three-dimensional parts through digitally controlled layer-by-layer processing, offers the possibility of geometric part complexity, batch-to-batch flexibility, reduced time for prototyping and iteration, and reduced material waste. As such, AM has applications in aerospace, automotive, healthcare, consumer goods, construction, and other industries [1,23–28]. Powder bed-based additive manufacturing process, including binder jetting (BJAM) and powder bed fusion (PBF), are of particular interest and can build intricate components from polymers, metals and ceramics, using powder feedstocks [1,3,18,27,29–32].

BJAM uses inkjet printing technology to selectively bind powders in each layer of the build [1]. For BJAM, spreading of a thin layer of powder (on the order of 10s μm in thickness) is commonly performed using a roller [3]. The choice of a roller and tailoring of its surface characteristics (e.g., material, roughness) is particularly important when smaller powder sizes (e.g., 5-25 μm diameter for steel alloys) are used, as the spreading mechanism must overcome interparticle forces that overwhelm gravitational forces [3]. After the formation of the powder layer in BJAM, an inkjet printhead is rastered over the build area and a binding agent is selectively deposited; the binder adheres the powders locally and to

the previous layer [1]. After all the layers have been deposited and bound, the object is extracted and post-processed to produce the final part, often including final curing of the binder. For metal and ceramic BJAM, additional post-processing includes debinding, sintering and/or infiltration with a secondary material to increase part density [1,3,18].

In PBF processes, which typically use powders in the 15-45 μm diameter range, commercial equipment typically uses a blade mechanism rather than a roller [1,33]. This is because larger powders experience less significant cohesive forces, and the compliance and localized forces exerted by the blade accommodate surface deviations in the component (e.g., due to thermal stresses) [34,35]. After the formation of the powder bed layer in PBF, an energy source (i.e., laser or electron beam) is used to locally melt the powder particles into the desired geometry – fusing the powder particles within the layer and to the previous layer [1]. Heat treatments for metal PBF components are common to relieve internal stresses induced by the thermal gradients imposed by the process but may not be required for plastic components fabricated via PBF [1,36,37].

Therefore, spreading of a thin layer of powder (Figure 2.1) is a critical step which must be optimized to ensure fabrication of quality components through BJAM and PBF. For BJAM, particularly of metals and ceramics, the green part must undergo sintering to produce the final component, analogous to conventional sintering practices in powder metallurgy, powder injection molding, and ceramic processing [1,10]. Thus, homogeneous density of the powder bed and green part are necessary for uniform shrinkage and densification [7,10,38–40]. Additionally for BJAM, a highly-packed powder bed can reduce the adverse effect of powder ejection that results from ballistic impact of the binder droplet with the powder surface, which can otherwise cause defects in the powder bed [41–43]. For PBF, the formation of a dense and uniform powder bed is critical to the fabrication of dense and homogenous final parts, since low packing density and variations in the powder bed will result in melt pool instabilities that create voids and undesired surface roughness [44]. Ultimately for both BJAM and PBF, part density will influence the material properties (e.g., mechanical, electrical, thermal, magnetic) [45–51]. Thus, careful understanding of the underlying processes that can produce porosity and control homogeneity must be explored to ensure the process, part, and property optimization.

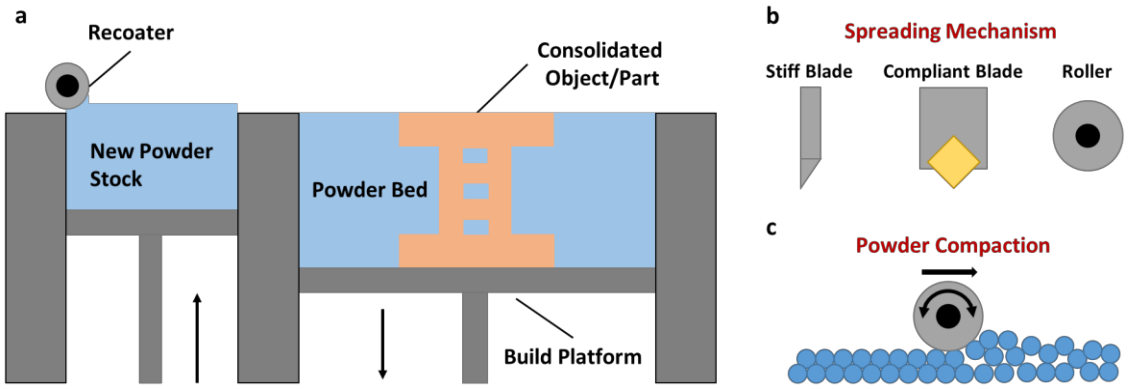

Figure 2.1: Conceptual image of (a) powder spreading process for powder-based additive manufacturing, (b) powder spreading mechanisms, and (c) powder compaction during spreading process.

Prior studies of powder spreading for AM have utilized both commercial and custom equipment [2,4,34,35,52–78]. Escano et al. utilized a custom single-layer blade recoating testbed coupled with in-situ high-energy x-ray imaging to explore the effect of particle size on spreading dynamics (e.g., dynamic repose angle, slope surface speed, slope surface roughness) [34]. Yee utilized a multi-layer powder spreading testbed with a blade mechanism to explore the variation of surface quality and particle size distribution due to spreading speed and amount of excess powder [66]. Snow et al. developed a single-layer blade spreading mechanism to correlate powder rheology experiments (e.g., angle of repose, flow funnel, apparent/tapped density) with avalanche angle (i.e., dynamic repose angle) [68]. Using a commercial BJAM machine (ExOne R2), Bai et al. studied the effects of particle size distribution on powder bed green density [72]. Ali et al. adapted a commercial PBF AM machine (EOS M290) with a blade spreading mechanism) to explore the variation of powder bed density and surface roughness across the build volume [77]. Tan Phuc et al. used a contact image sensor along with a custom-built mechanism to detect powder bed defects during powder spreading with a blade [78]. And, Myers et al. employed a commercial BJAM machine (ExOne Innovent+), having a roller spreading mechanism, to study the influences of layer height and spreading speed on powder bed density and surface roughness [61]. These studies have provided insights on the role of powder size, size distribution, and spreading mechanism motion on layer quality, density, and

roughness. Powder spreadability and thus packing density are typically best for particle sizes (>10 μm) and those with spherical shape [2,52,60,62,66,67,72].

However, the advancement of powder bed AM and its industrialization requires transferrable knowledge, which in turn requires precision instrumentation to facilitate parametric studies of each process step. In the case of powder spreading, such instrumentation must achieve representative AM spreading parameters (e.g., spreading traverse speed, layer height, roller rotation), include characterization of the precision of machine motion, enable exploration of different spreading and dispensing mechanisms (e.g., blade vs. roller, piston fed vs. hopper), and attain multi-layer powder spreading in a repeatable manner. In roller-based spreading, reported roller translation speeds range from 5-130 mm/s, and reported rotation speeds are 250-350 RPM [4,52,54–61,72,73,79]. When a blade is used for spreading, blade speeds of up to 150 mm/s are typically reported [68–71]. Thus, any custom research equipment must be capable of replicating similar conditions, in order to be relevant to commercial applications of BJAM and PBF. Additionally, few studies consider compaction of the powder using a roller [65,67], yet theory suggests that small amounts of compaction force can significantly increase packing density of the powder bed [39,82,83]. Further, powder bed density measurement techniques often require movement of the sample to a measurement device thus potentially affecting the accuracy and repeatability of the density measurement [52,62,66,67,77,84].

Here, we present the design and fabrication of a precision powder spreading testbed suited to investigation of fundamentals and process variables that influence powder spreading in BJAM and PBF techniques. Our testbed is modular and enables multi-layer spreading experimentation, and therefore can facilitate correlation among powder flowability experiments (e.g., angle of repose, flow funnel), AM process parameters (e.g., spreading speed, layer height, spreading mechanism), and powder bed properties. Compared to commercial AM equipment, the testbed allows for experimentation with smaller quantities of powder and fully programmed control of the spreading device, feed piston, and build platform. The testbed's functionality is demonstrated via spreading of exemplary layers of powder having size distributions typically used in BJAM and PBF.

2.2 Design and construction of powder spreading testbed

2.2.1 Overview of system and specifications

The powder spreading testbed fits on a tabletop (500 mm x 500 mm x 250 mm) and was designed according to the target specifications listed in Table 2.1. The testbed is suited for spreading of polymer, metal, or ceramic powders depending on the tool and experiment parameters chosen. Figure 2.2 shows the corresponding CAD model and fabricated powder spreading testbed. Exemplary images from a powder spreading experiment are show in Figure 2.2d. The following are the major modules of the machine:

Powder supply platform: Powder is supplied using a vertical platform (travel distance of 20 mm), consisting of a motorized axis and a custom-machined pillar and piston.

Build platform: The build platform emulates the surface where the part would be built in an AM machine. The build platform of the spreading testbed has a removable build plate with integrated load cell. These are attached to a motorized (vertical) axis via a custom-machined pillar and piston. The build platform has a vertical travel distance of 20 mm, is capable of measuring loads up to 100 N, and the build (spreading) area is 60 mm x 60 mm.

Modular powder spreading mechanism: A custom-designed linear motion system is used to translate the powder spreading mechanism over the powder supply and build platforms. The spreading mechanism has mounting features that allow the interchange of different spreading tools (e.g., motorized roller, stiff blade, compliant blade) and the addition of a hopper dispensing system for fine powders.

Software: A custom LabView program controls all system operations and allows for specification of all process parameters.

Table 2.1: Summary of desired design specifications for powder spreading testbed.

Parameter	**Design Values**
Spreading Tool Traverse Speed	0-100 mm/s
Roller Rotation	0-300 RPM
Build Platform Minimum Incremental Motion	5 μm
Powder Spreading Mechanism and Machine Platform Offset	0-1000 μm
Spreader Type	Modular; roller or blade
Powder Dispensing Mechanism	Modular; piston or hopper
Build Volume	60 x 60 x 20 mm
Machine Volume	480 x 415 x 250 mm

2.2.2 Detailed description of powder spreading testbed

The powder spreading testbed consists of a modular spreading mechanism mounted on a linear motion system to provide translational motion for powder spreading and two vertical stages to serve as the powder supply and platform, shown in Figure 2.2. During operation, the powder is supplied by raising the supply platform and the spreading mechanism (e.g., roller, blade) is advanced to transfer and spread the powder over the second vertical stage (build platform). The build platform thus dictates the layer thickness, as well as moderates the level of compaction performed by the roller. For the powder spreading and build platform, control over the spreader geometry, spreading mechanism translation speed and rotation, compaction, and layer height are possible in our custom system.

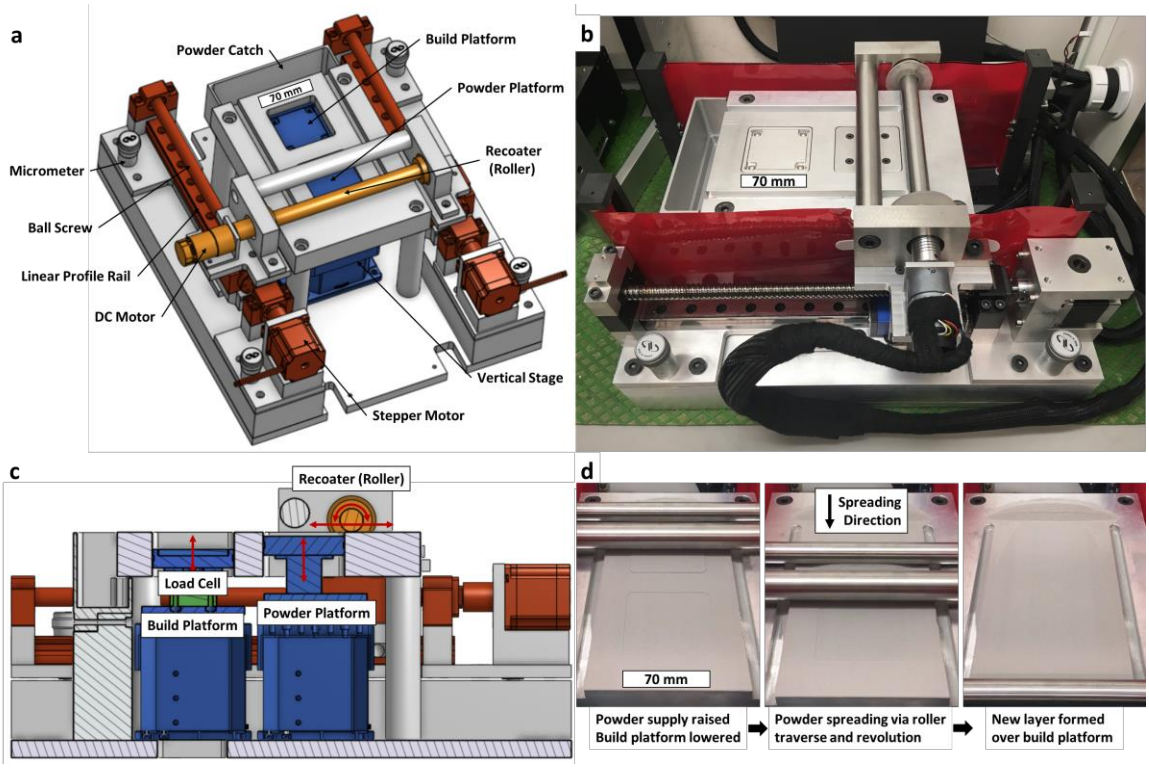

Figure 2.2: Powder spreading testbed: (a) computer model showcasing major components with roller as powder spreading mechanism; (b) fabricated powder spreading testbed; (c) sectional side-view of testbed highlighting moving components and motion trajectories; (d) images from powder spreading experiment using stainless steel 316L 15-45 µm powder and 250 µm layer height.

2.2.2.1 Powder and build platforms

Each of the power and build platforms is driven by a vertical stage (Standa 8MVT100-25-1) which is capable of reported 5 µm resolution in full-step, a travel range of 25 mm, and a maximum load of 8 kg. The vertical stages are controlled via a stepper motor controller (Standa 8SMC5-USB-B9-2). A custom machined piston attaches to each stage, and to a powder plate and removable build plate, respectively. The piston plate and build plate holder have a recessed portion where a piece of felt is attached to seal the gap between the pistons and machine wells to prevent powder from falling through the powder wells. A load cell (MeasureX MLD66, 100 N capacity, 0.1 N resolution) can be mounted underneath the build platform to record the load experienced by the build platform during powder

spreading and compaction. The load range of 0-100 N was selected to monitor forces during forward-rotating powder compaction which can optionally be used to densify the powder layer after spreading [82,83]. The load cell data is recorded using a data acquisition system (National Instruments NI-9237).

2.2.2.2 Linear motion system

Each side of the linear motion system consists of a stepper motor (Anaheim Automation 13Y104S-LW8), a ballscrew for linear actuation (Thomson Linear RM1610Z2), a flexible shaft coupling (uxcell L30xD25mm 6.35x10mm), and a linear profile rail with roller bearing block (Thomson Linear 522P25A and 512P25A1) – the linear motion system is mounted in a parallel configuration. The two stepper motors are synchronously controlled using a motion controller (Synthetos tinyG). To enable adjustment of parallelism and vertical offset between the spreading mechanism, the machine platform and the build plate, the linear motion system is mounted to the testbed baseplate using micrometers (Newport BM30.10, 10.0 mm travel range, 409 N individual load capacity) and bolts fed through stacked Belleville disc springs (McMaster Carr 96445K503). The parallelism between the spreading mechanism and build plate is set using bubble levels and the vertical offset is set using a shim of known thickness (e.g., 100 μm).

2.2.2.3 Modular powder spreading system

The carriage for the linear motion system contains mounting features enabling the attachment of a spreading mechanism suited to be chosen for powder and experiment. As examples, CAD models of three mechanism designs – motorized roller, stiff blade, and compliant blade – are shown in Figure 2.3. The roller mechanism has been fabricated here using a 20 mm high-speed steel shaft. To hold the roller, the 20 mm shaft is mounted on tapered roller bearings (SKF 32004 X/Q, static load capacity of 27 kN) and attached to a DC motor (Pololu 37D Gearmotor with Encoder) using a flexible shaft coupling (uxcell L30xD25mm 6x12mm). The DC motor is controlled via a motor controller (Pololu Jrk G2 18v19 USB) and the optical encoder integrated to the DC motor is read using a microcontroller (Arduino Nano).

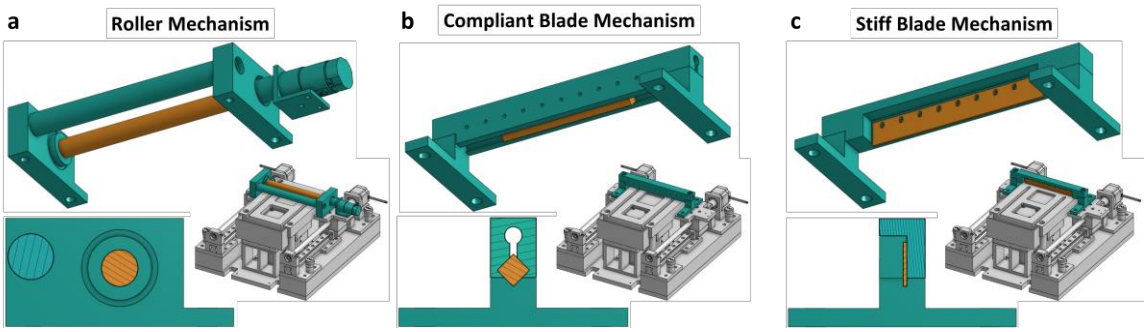

Figure 2.3: Designs of various powder spreading mechanism configurations for testbed shown in assembled machine configuration, mechanism close-up, and side-view: (a) motorized roller, (b) compliant blade, (c) stiff blade.

2.2.2.4 Powder hopper dispenser

To facilitate mechanized metering of powder onto the build platform ahead of the spreading mechanism, a vibratory powder dispenser was developed. Direct, metered dispensing is desirable when spreading fine, cohesive powders, and as such the mechanism is integrated with the roller apparatus in the testbed. A CAD model of the dispensing system and picture of integration into the testbed are shown in Figure 2.4. The hopper consists of a custom machined aluminum funnel and sieve cover located at the base of the funnel, stainless steel wire cloth with 100 x 100 mesh size (McMaster Carr 85385T101), a turbine vibrator (McMaster Carr 3987K69), damping bolt attachments (McMaster Carr 93945K31), and a pressure regulator for the turbine vibrator. The vibration frequency and force of the turbine vibrator is set by the backpressure supplied through the pressure regulator and cycled on/off using a microcontroller (Arduino Nano), a power relay, and an electric solenoid valve. The powder hopper system can be utilized in replacement of the piston feed system for supplying powder to the spreading mechanism, or in conjunction with the piston feed system to supply a secondary powder (i.e., material, size, shape) for additional exploration.

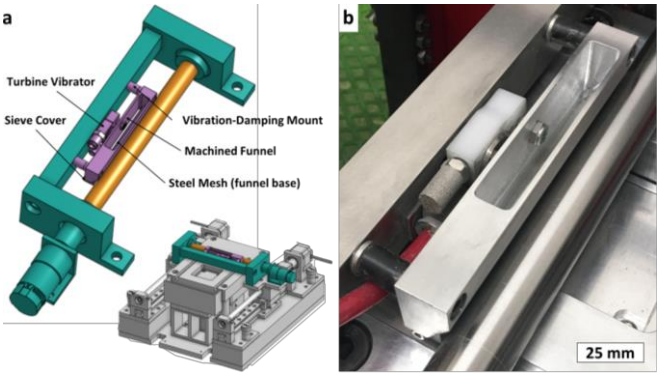

Figure 2.4: Powder hopper dispensing system: (a) CAD design showing major components of hopper system and integration into testbed and (b) picture of hopper system mounted onto powder spreading testbed.

2.2.2.5 Powder containment system

A powder catch has been fabricated from machined aluminum, polymer via stereolithography, and compressive felt to fit at the end of the testbed's top plate to capture excess powder during the powder spreading process – shown in Figure 2.2a and Figure 2.2b. To prevent powder contamination of the linear motion system, a thin plastic curtain (visible in Figure 2.2b) attached to retracting spring loaded tubes mounted to the machine baseplate separates the linear motion system from powder zone (i.e., powder supply, build platform, excess powder catch), thus preventing fouling of guides and ballscrews.

2.2.2.6 Control and software architecture

A custom LabView program was developed to enable integrated control of the testbed, and to allow automated repetition of layer spreading. Figure 2.5 schematically shows the electrical wiring and communications within the system. To provide inputs to the LabView program, a MATLAB script was developed to convert user inputs (e.g., desired layer height, spreader traverse speed, roller RPM, etc.) to a text file which contains LabView-compatible machine commands. The text file is then used as an input to the LabView code which uses the control commands to drive the machine.

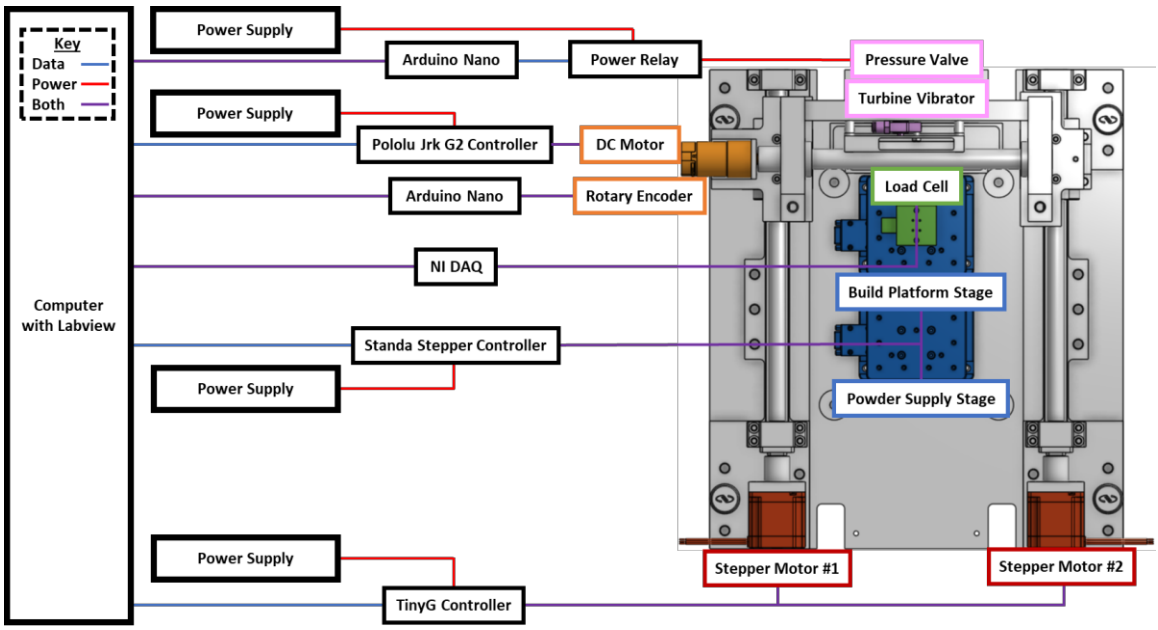

Figure 2.5: Electronic connection diagram for powder spreading testbed.

2.3 Validation and analysis of the powder spreading testbed

2.3.1 Powder spreading testbed validation

To validate the motion system for the powder spreading testbed, the spreading traverse speed, vertical stage resolution, vertical stage stiffness, roller revolution, and roller runout were measured.

2.3.1.1 Linear motion system: traverse speed

The traverse speed of the linear motion system was measured using an optical encoder (US Digital EM-2) and linear encoder strip with 2000 LPI resolution (US Digital LIN 2000 LPI). The system was given commands to traverse forward and backward at speeds between 1.67 mm/s and 100 mm/s, with two measurements performed for each condition

(i.e., speed and direction). Linear correlation was demonstrated within ±0.5 mm/s for the range of 0-100 mm/s for set and measured speeds using the encoder, as shown in Figure 2.6.

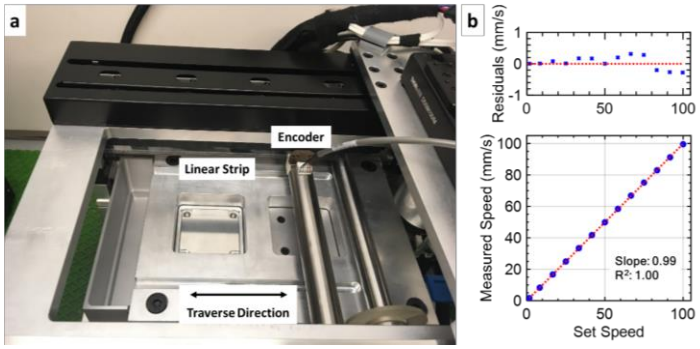

Figure 2.6: (a) Validation test setup for spreading traverse speed and (b) plot of set versus measured speed with residuals to linear fit.

2.3.1.2 Build platform: vertical stage resolution and stiffness

The motion resolution of the build platform's vertical stage was measured using a dial indicator (Mitutoyo 543-791B Absolute Digimatic Indicator, resolution 0.001 mm, accuracy of 0.006 mm). The vertical stage was given commands to traverse up and down at increments ranging between 25 and 400 µm, with three measurements performed for each condition (i.e., position and direction). Linear correlation was demonstrated within ±2 µm for the range of -400 to 400 µm for set and measured vertical positions using the dial indicator, as shown in Figure 2.7a and Figure 2.7b.

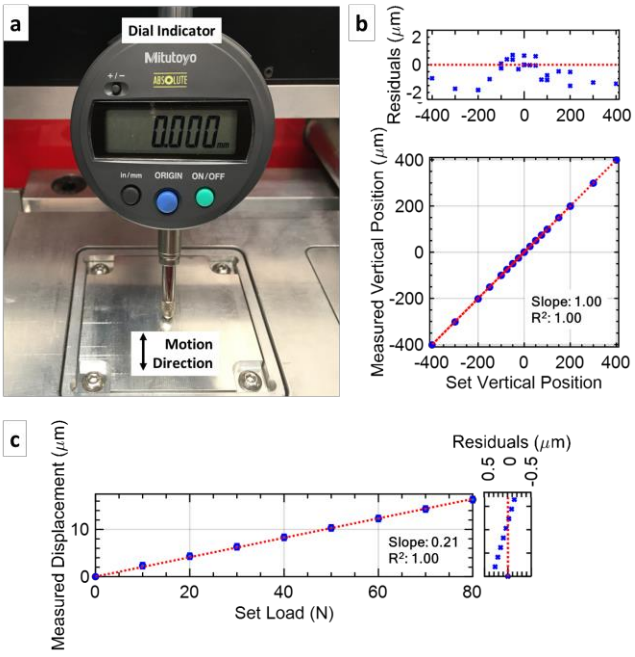

Figure 2.7: (a) Validation test setup for vertical stage motion resolution, (b) plot of set versus measured position with residuals to linear fit, and (c) plot of set load versus measured displacement for build platform stiffness calculation with residuals to linear fit.

The stiffness of the vertical stage was measured using a dial indicator and a force gauge (Nextech DFS100, maximum 100 N, resolution 0.01 N). The measurements were performed by applying a force and measuring the deflection of the dial indicator. The stiffness was calculated from a linear fit of the force vs. displacement data, shown in Figure 2.7c, indicating a stiffness of 4.76 N/μm for the vertical stage. For estimated vertical forces during powder spreading of <100 mN [85], the expected deflection of the vertical stage due to powder spreading would be <0.1 μm.

Additionally, the load cell mounted under the build platform was calibrated using a set of precision weights and the native LabView Load Cell Calibration wizard. The calibration was performed with felt material placed within the powder well, reflecting the configuration intended for use during powder spreading experiments.

2.3.1.3 Roller powder spreading mechanism: roller revolution and runout

The rotational speed of the roller was measured using a non-contact tachometer (Checkline CDT-1000HD), with the DC motor at a gear ratio of 30:1 (Pololu 37D Metal Gear Motor with Encoder). RPM measurements were taken while providing the DC motor with speeds -330 to 330 RPM, with three measurements performed for each condition (i.e., RPM setting and direction). Linear correlation was demonstrated within ±1 RPM for the range of -330 to 330 RPM for set and measured rotational speeds using the tachometer, as shown in Figure 2.8.

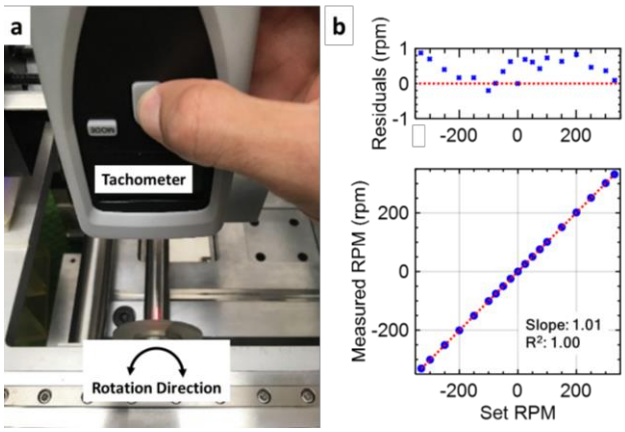

Figure 2.8: (a) Validation test setup for roller RPM and (b) plot of set versus measured RPM with residuals to linear fit.

The roller runout was characterized using a high-speed 2D laser profiler (Keyence LJ-V7060) by taking linear scans of a 40 mm section of the roller (parallel to its rotation axis) as the roller was rotated, thus providing a three-dimensional rendering of the roller shape. The runout measured over the 40 mm section was 30 µm, and for the central 10 mm region of the roller, the runout was 15 µm, as shown in Figure 2.9. The total runout is comparable to the average particle sizes typical for BJAM and PBF, yet importantly less than the typical thickness of a powder layer which is, to give uniform spreading, recommended as 3-5 times the mean particle diameter [86]. Also, additional energy is transferred to the powder particles from frictional shear between the powder and the roller,

enhancing local layer uniformity. As such, it is important for the rotational speed to create a contact velocity between the roller and particle that is greater than the lateral traverse speed of the spreading mechanism. As an example, for a roller of 20 mm diameter, rotation at 250 RPM results in a surface speed of 262 mm/s which is greater than the common range of 1-20 mm/s for roller spreading mechanisms [4].

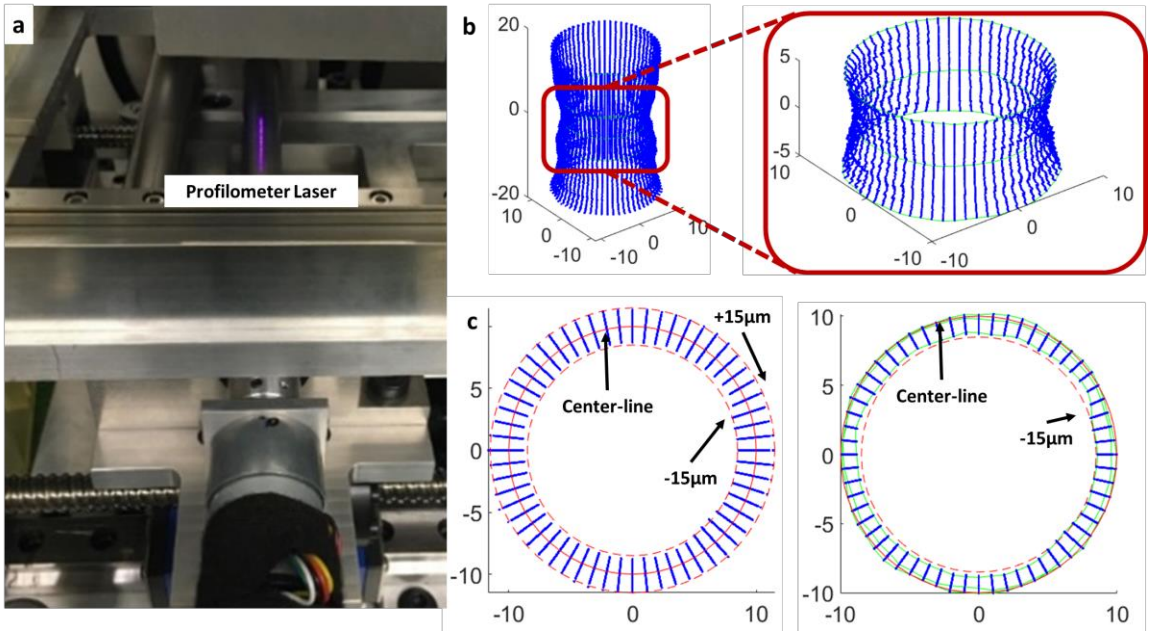

Figure 2.9: (a) Validation test setup for roller runout and plots of runout versus position, (b) runout of roller for 40 mm measured section and 10 mm central section with runout values 100X for visualization, (c) runout plot for 40 mm measured section and 10 mm central section showing runout of 30 µm and 15 µm respectively. All axis units for runout figures (b, c) show position in mm.

2.3.1.4 Hopper powder dispensing system: powder flow rate

The amount of powder dispensed from the hopper depends on the supplied pressure to the turbine vibrator and the length of time the hopper is vibrated. To develop an estimate of the powder flow rate from the hopper, the hopper was activated for pressures ranging from 20-60 psi and hold times between 0.5 and 20 seconds. Fine stainless steel 17-4 PH powder (<22 µm, Carpenter) was dispensed into on a weighing boat and weighed using a laboratory scale (Ohaus Corporation DV215CD, 0.01 mg resolution) after each experimental

condition. Tests were completed three times for each condition and were performed at 55.5% humidity (AcuRite 01080M), in an ambient lab environment. Figure 2.10a shows the correlation between pressure, time, and deposited mass – with deposited mass increasing with deposition time and backpressure. Figure 2.10b shows the dispensing rate for each pressure condition estimated from a linear fit of each dataset. This data can be used to estimate the parameters required for powder deposition via the hopper: for the given 17-PH powder (bulk density of 7.81 g/cm^3), an approximated powder bed packing density of 50%, and a build area of 60 mm x 60 mm, the required mass of powder for a 50 µm and 100 µm layer are 703 mg and 1406 mg, respectively. Additionally, for a spreading traverse speed of 5 mm/s and 10 mm/s, the traverse time will be 12 seconds and 6 seconds, respectively. Thus, for a 100 µm layer and 10 mm/s traverse speed, a setpoint of approximately 22 psi should provide sufficient powder for recoating of the layer. However, since the build piston area (70 mm x 70 mm) is larger than then build area (60 mm x 60 mm), the width (75.6 mm, perpendicular to motion direction) of the dispensing slot in the hopper is larger than the width of the build piston, and the build platform has recessed mounting features (11 mm x 11 mm x 3.5 mm) at its corners the dispensed powder will not all be deposited on the build platform and thus these calculations should only be utilized as first-order estimates.

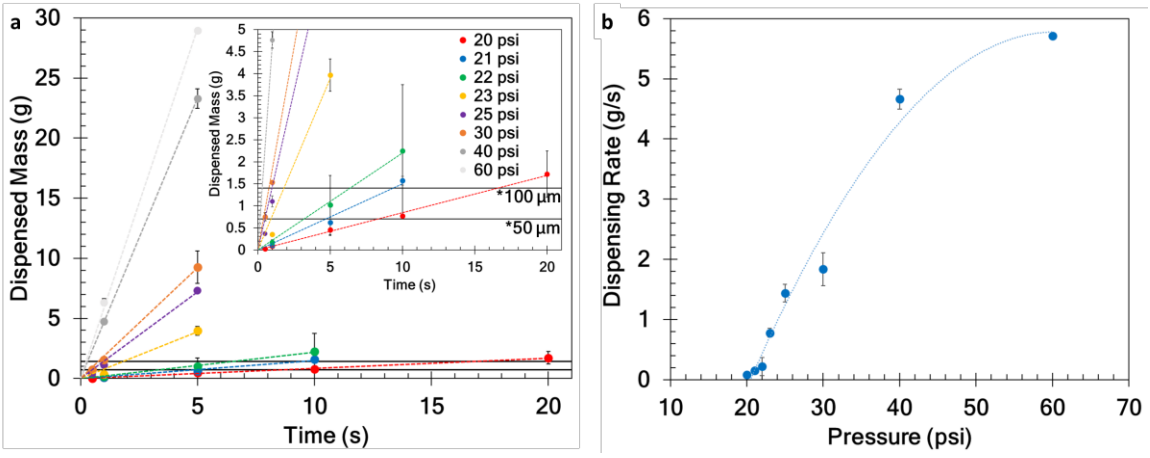

Figure 2.10: Validation data from powder hopper dispensing experiment showcasing: (a) the relationship between backpressure to turbine vibrator, dispensing duration, and dispensed mass; and (b) the calculated dispensing rate at each pressure with quadratic fit.

In summary, these validation experiments demonstrate that the powder spreading testbed will be capable of attaining spreader traverse speed of 0-100 ±0.5 mm/s, roller RPM of 0-330 ±1 RPM, and micron-scale vertical piston motion for layer height control.

2.3.2 Powder spreading experiments

To validate the utility of the testbed, exemplary spreading experiments are now presented. The purpose of the following experiments is to showcase the operational capabilities of the powder spreading testbed (i.e., achieve AM-process relevant powder spreading) and is not intended as a full description of possible characterization methods for powder spreading experiments (e.g., powder bed density, powder surface roughness) to be performed by the testbed in future work.

2.3.2.1 Effect of layer height on layer uniformity

To showcase the influence of layer height on powder layer formation, stainless steel 316L powder (15-45 μm, John Galt Steel) was spread at set layer heights of 50 and 100 μm. To assess the influence of layer height on uniformity, an imaging setup (Thorlabs CMOS Camera DCC3240M, Thorlabs Coaxial Zoom Lens MVL6X3Z, Extension Tube MVL05A, C-Mount Adapter MVLCMC) was placed over the build platform using a coaxial lighting setup, as shown in Figure 2.11c. Powder was spread at a traverse speed of 50 mm/s without roller rotation at 47.7% humidity (AcuRite 01080M), in an ambient lab environment. For the 50 μm layer height (Figure 2.11a), we see regions of brightness which are the result of light reflection from the build plate, the result of sparse powder spreading due to inadequate layer height for the given powder size. For the 100 μm layer height (Figure 2.11b), we do not see high brightness regions, but instead a uniform powder distribution over the imaged area. A close-up and enhanced brightness image of the 100 μm layer, Figure 2.11d, reveals the packing of individual powder particles that make up the layer.

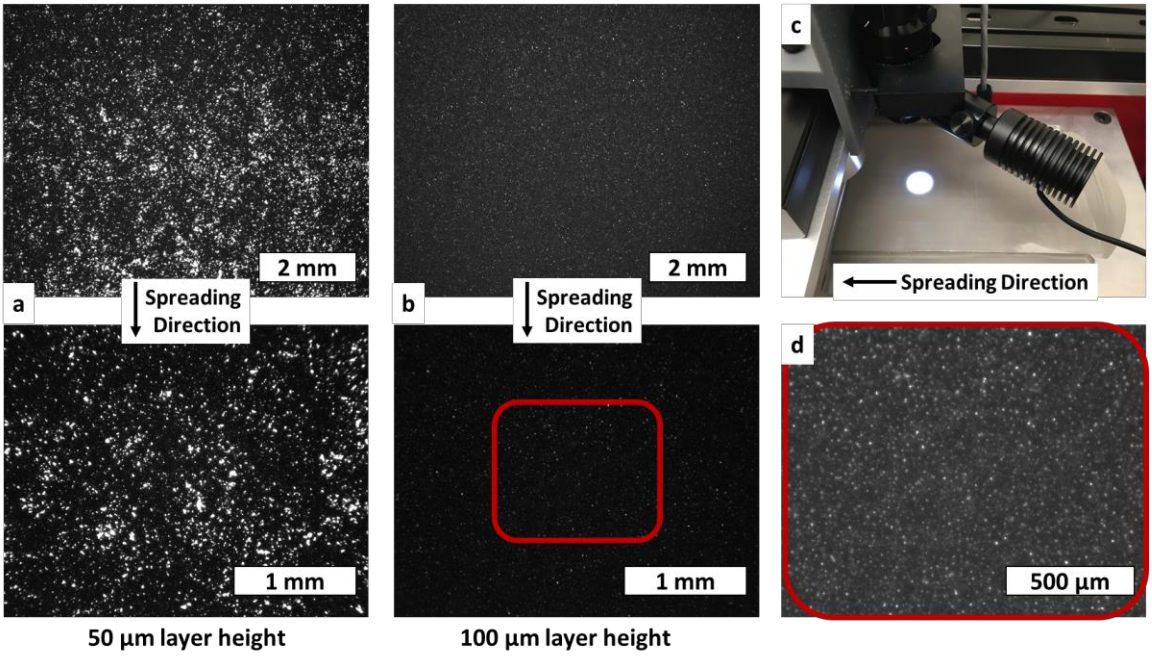

Figure 2.11: Overhead images of powder layers of stainless steel 316L 15-45 µm powder at (a) 50 µm layer height and (b) 100 µm layer height showcasing difference in powder uniformity. Brightness in (a) is a result of light reflection from the baseplate and suggests an improperly spread powder layer. (c) Picture of testing condition and coaxial light setup. (d) Close-up and brightness enhanced image of 100 µm layer showing individual powder particles in layer.

2.3.2.2 Effect of simulated defect on powder layer

To showcase the capability of the system to capture anomalies that may occur during AM, a simulated defect was placed on the roller by attaching Kapton tape with thickness of 55 µm and width of 6.00 mm (measured using a Mitutoyo Digital Micrometer Series 293), see Figure 2.12c. Stainless steel powder (15-45 µm, John Galt Steel) was spread with a layer height of 100 µm, on top of a previously spread powder layer of 250 µm. Powder was spread at a traverse speed of 50 mm/s without roller rotation at 47.7% humidity (AcuRite 01080M), in an ambient lab environment. To assist in imaging the defect, two imaging conditions were used – coaxial light and lateral light directed at the zone of interest, shown in Figure 2.12. For a control spreading experiment performed without a simulated defect (Figure 2.12a) we see a uniform powder layer with no noticeable difference between the

coaxial and lateral lighting conditions; a close-up image of the lateral lighting condition reveals individual particles. For the spreading experiment performed with the simulated defect (Figure 2.12b), a defect is visible in the lateral light condition but not in the coaxial condition. The width of the defect (measured using ImageJ) is 6.02 mm which agrees with the 6.00 mm width of the Kapton tape used as the simulated defect.

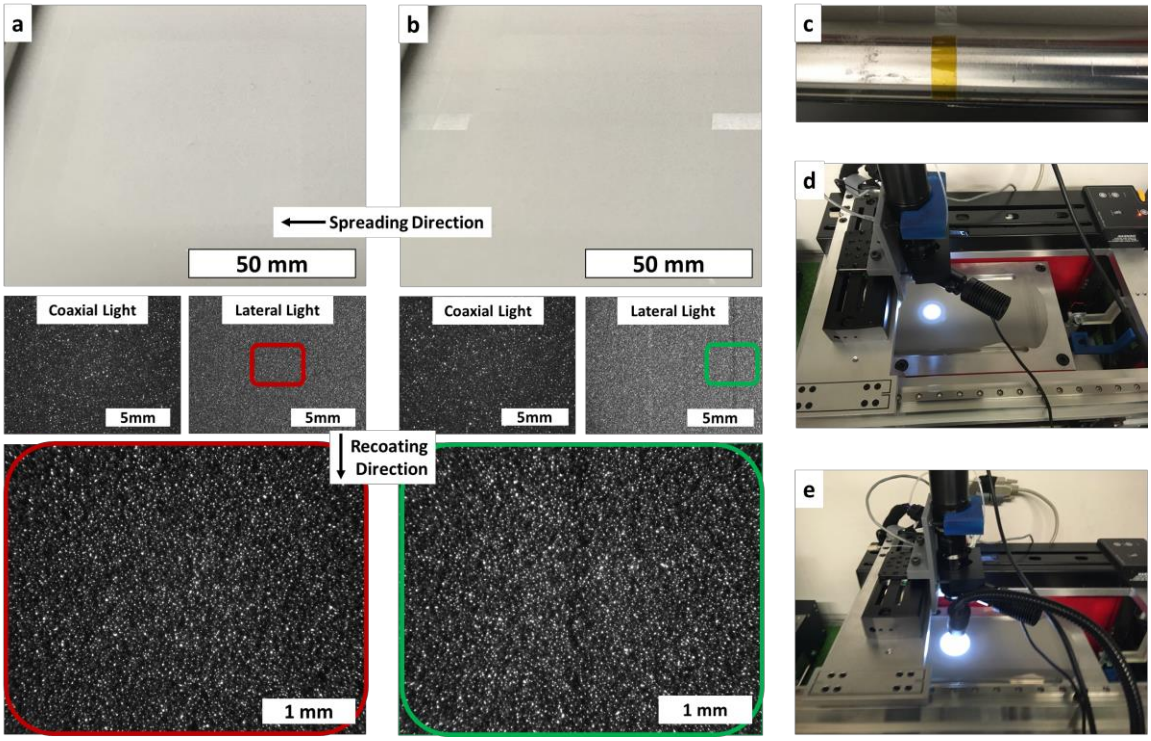

Figure 2.12: Overhead images of powder layers of stainless steel 316L 15-45 µm powder using (a) no simulated defect and (b) simulated defect on the spreading mechanism. The lateral light imaging condition reveals the defect in (b). (c) Picture of simulated defect created by placing Kapton tape on the roller. (d) Picture of testing condition for coaxial lighting setup. (e) Picture of testing condition for lateral lighting setup.

2.3.2.3 Spreading of fine powders

Finally, the spreading of small powder—as suited to BJAM—can be challenging due to interparticle friction and cohesion. To showcase the possibility of using the testbed to explore spreading methodologies for fine powders used AM, fine stainless steel 17-4 PH powder (<22 µm, Carpenter) was spread using the testbed in various configurations. First,

spreading was attempted using the roller with a machine-set layer height of 100 µm and traverse speed of 5 mm/s: (1) without rotation; (2) with rotation of 250 RPM; and (3) with rotation of 250 RPM and simulated texture using Kapton tape strips at 90-degree intervals, shown in Figure 2.13c. Powder experiments were performed at 47.7% humidity (AcuRite 01080M), in an ambient lab environment. Optical images of the spread layers were taken under identical camera settings and coaxial lighting conditions, as seen in Figure 2.13. For the roller without rotation, Figure 2.13a, non-uniform powder spreading occurs over the build platform, with regions of peaks and valleys, as well as vacant regions. For the roller with rotation, Figure 2.13b, non-uniform powder spreading occurs again, with vacant regions and fewer perceptible peaks and valleys on for the formed layer. For the roller with rotation and the textured surface, Figure 2.13c, powder is spread over the whole build area without vacancies, but peaks and valleys are still visible after spreading.

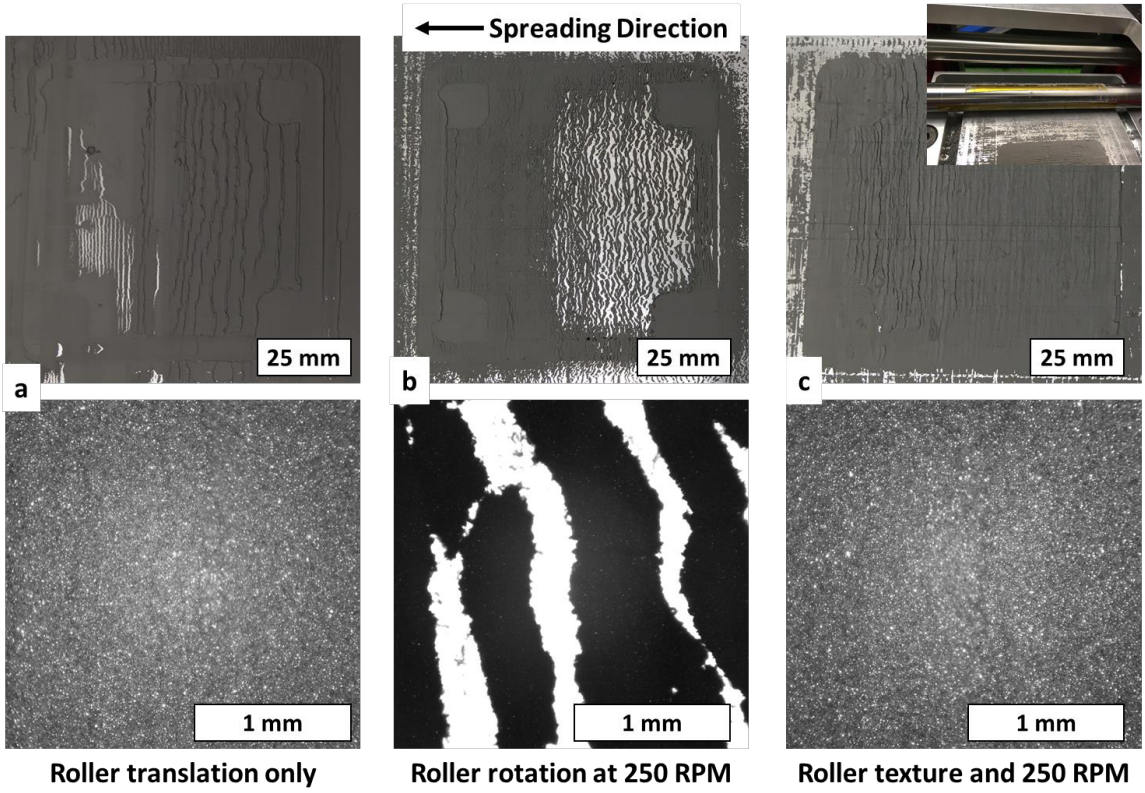

Figure 2.13: Overhead images of powder layers of stainless steel 17-4 PH <22 µm powder using (a) no roller rotation, (b) roller rotation of 250 RPM and (c) roller rotation of 250 RPM and a simulated textured surface.

To further improve the results, the fine powder was deposited using the vibratory hopper and subsequently spread using the roller with traverse speed of 10 mm/s and roller rotation of 250 RPM. The powder was deposited and spread with a layer height of 100 μm, on top of a previously deposited and spread powder layer of 1000 μm at 55.5% humidity (AcuRite 01080M) in an ambient lab environment; the spreading sequence is shown in Figure 2.14a (Multimedia View). To ensure sufficient powder was supplied by the hopper, the hopper dispensing parameters were 25 psi pressure for the 1000 μm layer and 23 psi pressure for the 100 μm layer, with a dispensing time of 10 seconds. Optical images of the final layer were taken under identical camera settings as the previous fine powder spreading experiments and coaxial lighting conditions. The fine powder spread after deposition from the hopper results in uniform powder spreading, as seen in Figure 2.14b. In this case, powder is spread uniformly over the build area, with exception at the corners where powder dispensing does not fill the gaps for the build platform bolts), with limited peaks and valleys visible. Together, these results validate the testbed's capabilities for a variety of powder sizes, and show that combination of spreading parameters (e.g., spreading mechanism texture, roller RPM, traverse speed, powder dispensing mechanism) are critical for optimization of spreading of fine, cohesive powders.

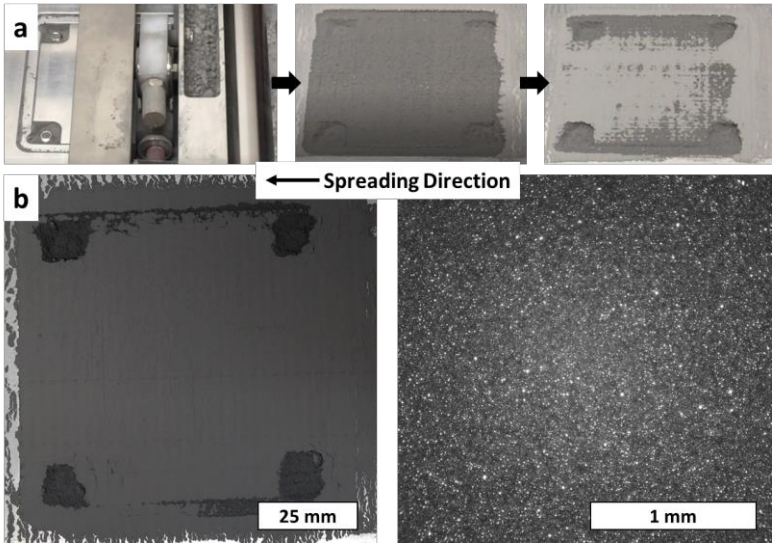

Figure 2.14: Spreading of stainless steel 17-4 PH <22 μm powders using hopper dispensing and counter-rotating roller mechanism at 250 RPM: (a) showcasing deposition and spreading sequence of fine powders for base layer via hopper dispensing followed by roller spreading and (b) overhead images of final 50 μm thickness powder layer.

2.4 Conclusions

This chapter has presented the design, fabrication, and validation of a modular powder spreading testbed suited to study process fundamentals and novel adaptations of powder-based AM processes. Testbed subsystems were validated using relevant measurement techniques and exemplary powder spreading experiments were performed to showcase full testbed functionality. The modular design of the testbed allows for interchangeability of spreading tools, and the adaptation of spreading conditions to address differing powder sizes, materials, and particle shapes. By coupling this testbed with appropriate powder bed density and surface roughness measurement techniques, future work utilizing this testbed will study in detail the influence of powder parameters (e.g., powder shape, powder size distribution, material) and spreading parameters (e.g., spreading method, layer height, traverse speed, roller RPM, compaction methodologies) on powder bed formation, enabling correlation with relevant build parameters for BJAM and PBF AM.

Chapter 3

Design, fabrication, and validation of a binder jet additive manufacturing testbed

The content in this chapter was published in:

D. Oropeza, A.J. Hart, A laboratory-scale binder jet additive manufacturing testbed for process exploration and material development, Int. J. Adv. Manuf. Technol. 114 (2021) 3459–3473. https://doi.org/10/gkhbcm.

Binder jet additive manufacturing (BJAM) is capable of fabricating complex three-dimensional components from a variety of material classes. Understanding the fundamentals of BJAM, including spreading of thin layers of powder, powder-binder interactions, and post-processing is critical to develop robust process parameters for BJAM. Toward meeting these needs, this work presents the design, fabrication, and qualification of a testbed for modular, mechanized, BJAM. The testbed seeks replicate the operating conditions of commercial AM equipment and features fully programmable motion control including powder spreading using a precision roller mechanism, powder

supply via a vibrating hopper, and gantry positioning of an inkjet printhead. The inkjet deposition system allows for the use of variable nozzle diameters, the exploration of novel binder compositions, and full control of jetting parameters. Validation of the accuracy and repeatability of the machine and its subsystems, as well as the fabrication of exemplary stainless steel components, are described. The precision engineered testbed can therefore enable the study of the BJAM process, exploration of novel binder compositions, and processing of custom powders to further scientific research and industrial applicability of BJAM.

3.1 Introduction

Binder jet additive manufacturing (BJAM), initially named Three Dimensional Printing (3DP) upon its inception at MIT by Sachs, Cima et al. [1,42,87,88] operates by layer-wise inkjet deposition of a binder onto a powder bed, followed by optional consolidation to a dense component. BJAM is a highly attractive additive manufacturing (AM) process due to its compatibility with virtually any powder material, high build rate compared to other AM methods, capability for high resolution, and scalability to very large build volumes (e.g., 100s mm length) [1,2]. A further attribute of BJAM is that the materials remain in the solid state throughout the process, and the geometrical shaping of the part is decoupled from the thermal densification step. This enables some degree of microstructural control during sintering, but presents challenges in maintaining shape accuracy due to shrinkage and warping [1,2].

More specifically, BJAM follows four steps to produce finished parts: (1) powder layer deposition and spreading, (2) binder delivery via inkjet deposition, with steps (1) and (2) repeated until the desired 3D geometry is completed, (3) removal of the green (i.e., binder-bound or printed) part from powder bed with optional binder curing prior to part removal, (4) post-processing of the green part (e.g., debinding, sintering, infiltration), followed by optional post-processing (e.g., sand blasting, polishing, coating). Thus, the two mechanisms for material delivery in BJAM are powder spreading and inkjet deposition,

and these mechanisms are responsible for the part geometry and green density that ultimately affect final part properties. Figure 3.1 shows a conceptual image of the binder jetting process with possible variations of spreading tool geometries (i.e., stiff or compliant blade, roller) and compaction strategies for powder spreading, as well as the powder-binder interactions that occur through the inkjet binder deposition process.

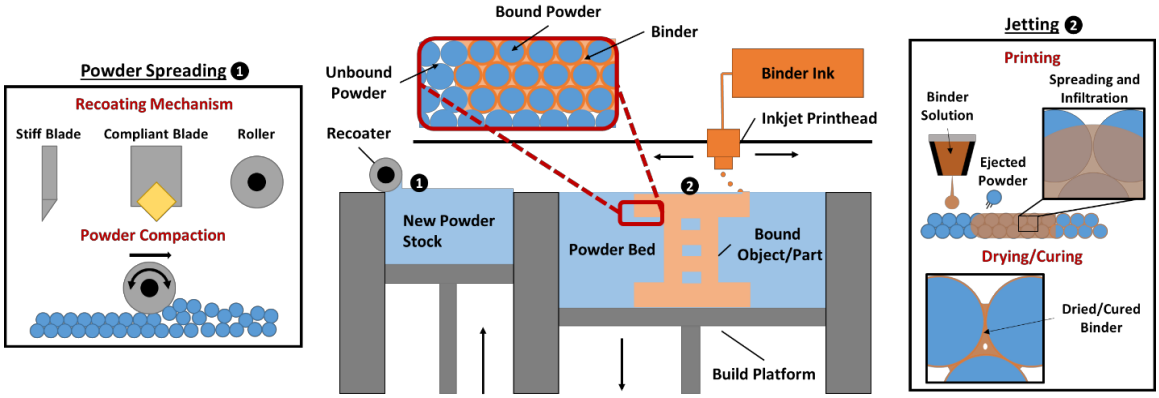

Figure 3.1: Conceptual image of binder jet additive manufacturing highlighting (1) powder spreading variations and (2) powder-binder interactions during jetting.

For extensive reviews on prior work for BJAM, the reader is directed to review articles by Mostafei et al. [4], Ziaee and Crane [2], and Mirzababei and Pasebani [3]. Briefly, BJAM is compatible with stainless steels [3,54], titanium alloys [79], Inconel [52,60,89], tungsten alloys [90], copper [91], sand [92,93], alumina ceramics [14,94], carbide ceramics [57,58,95], magnetic alloys [59], and many other materials. Commonly, BJAM produces components with green (as-printed) density between 40-60% [2–4]. Challenges for BJAM process development stem from the need to form uniform, high-density powder layers and the deposition of appropriate binder to provide green strength and enable post-processing (e.g., infiltration, sintering) to attain the desired geometry, microstructure and properties [1,2,4,10]. Defects introduced during BJAM are exacerbated during post-processing (e.g., sintering) and result in strength-limiting flaws and geometric distortion [2,4,10]. The favorable inverse relationship between sintering rate and powder size [10], and the diversity of materials compatible with BJAM, suggests that the ability to optimize powder spreading, binder development, powder-binder interactions, and post-process densification can result in impactful advances for the BJAM process.

Exploration of processing parameters for powder spreading and inkjet deposition for BJAM has led to key insights on the use of multi-modal and fine powders as feedstocks [52,60,72,96], the use of roller mechanisms and vibration in the recoating process [61,62,65,67,84], and the influence of powder-binder interactions on print quality [41–43,94,97]. Although the use of finer powder sizes results in increased sintering rates during BJAM post-processing, powders with average size <20 μm tend to result in agglomeration during spreading due to strong cohesive forces [10,39,86,98]. Using non-spherical particle shapes compromises powder spreadability and packing density, but reduces particle ejection during ballistic impact from inkjet droplets due to higher interparticle friction [39,43]. Therefore, when fine or irregular powder particles are used in BJAM, and in powder bed AM overall, a shear force must be applied (usually via a counter-rotating roller) to break powder agglomerates and improve spreadability and packing density. The use of powders with a tailored multi-modal size distribution has been proven to increase the green density of a powder compact, however the multi-modal distribution can result in non-homogenous sintering conditions and limited gain in densification if powder size distributions are not optimized for sintering [10,39,72,98]. Optimization of powder spreading, via spreading mechanism design and roller motion is key to forming a dense powder bed [52,62,67,84]. Additionally, vibration of the spreading mechanism or powder bed can result in increased powder bed densities, but can have the adverse effect of disturbing the printed part [67,99].

Jetting parameters such as droplet velocity, droplet spacing, droplet frequency, and binder saturation must be characterized and optimized for any chosen binder system to produce high density green parts [41,43,57,97]. Additionally, the interactions which govern powder-binder wetting and infiltration, binder primitive formation, and powder particle ejection are unique to each powder-binder combination [41–43,97,100–104]. Polymer binders are commonly used in BJAM as they bind most materials and can decompose to leave little organic residue [20,105,106]. However, the polymer is not an active participant in the densification of the printed component, requiring a debinding step that can result in part warping and deformation [22,40,107,108]. To prevent part warping

and improve densification, nanoparticle additives have been used either as a post-process addition or for a limited range of materials [14,22,107,109–115].

Although commercial BJAM equipment has been available for >20 years, recent interest in industrialization of BJAM has resulted in increased research and commercial activity [1,2,4]. Other AM methods (e.g., extrusion-based, powder bed fusion) have benefited not only from the development of commercial equipment, but also precision testbeds capable of exploring AM process fundamentals [26,116–122]. For powder bed fusion (PBF), testbeds to explore powder spreading, laser-powder interactions, and in-process metrology and control [34,68,116,117] have advanced fundamental understanding of the process and accelerated the development of process standards. For BJAM, further understanding of powder spreading and powder-binder interactions, exploration of low-cost fine powders (e.g., based on metal injection molding feedstock), and development of new binding agents, will further industrialization.

No standard equipment exists for characterization of powder spreading or inkjet deposition for BJAM, although various studies have utilized ExOne or similar commercial printers [22,52,54,57–61,72,79,84,89,91,94–96,107,111,123,124]. For reference, the ExOne Innovent+ printer is capable of a build volume of 160 mm x 65 mm x 65 mm, layer thicknesses between 30-200 μm, and nozzle diameters available between ~10 and ~30 μm (10-80 pL volumes) for a minimum voxel size of 30 μm [125]. Further, reported recoating (spreading) lateral speeds are 10-130 mm/s, and when a roller is used the rotation rate is typically 250-350 RPM [4,52,54,57–60,60,72,73,79,94]. Although some open-source hobby/maker designs exist for BJAM (e.g., Oasis 3DP, Plan B), the precision of these printers has not been qualified and the use of a thermal printhead places limitations on the fluids that can be dispensed and results in heat-induced kogation (i.e., deposition of residue from ink decomposition). Therefore, the majority of industrial BJAM printers use piezoelectric inkjet printheads [126–128]. Moreover, exploration of novel powder feedstock materials produced at small quantities (<100 g) and novel binders at small volumes (<10 mL) provide great benefit through rapid and cost-effective parameter development and component prototyping via BJAM. Yet, the exploration of novel binders is limited by issues such as printhead loading, clogging, and cleaning, as well as

maintaining solvent compatibility for printhead ink and cleaning solutions; early stage process development is thus difficult using commercial equipment with industrial inkjet printheads [109,110,123,124].

Here, we present the design and fabrication of a precision BJAM testbed suited to the investigation of process fundamentals, parameter development, and novel materials in small quantities. Our testbed is modular and enables fabrication of multi-layer components, and therefore can facilitate correlation among powder and binder characteristics, process parameters (e.g., spreading parameters, layer height, jetting parameters), and green part properties. Compared to commercial AM equipment, the testbed allows for experimentation with smaller quantities of powders and binders, as well as fully programmed control of the spreading device, powder supply mechanism, and build platform. The testbed's functionality is demonstrated via printing and characterization of exemplary green parts using stainless steel powder and a polymer binder.

3.2 Design and construction of the binder jetting testbed

3.2.1 Overview of system and capabilities

The BJAM testbed fits on a tabletop (500 mm x 500 mm x 400 mm) and is the combination of a powder spreading testbed (previously fabricated and described by in Chapter 2 [129]) and an inkjet printing testbed, which are mechanically and electrically integrated to enable programmed 3D printing. Figure 3.2 shows the CAD model and fabricated apparatus, as well as images taken during a binder jetting experiment. During operation of the BJAM testbed, powder is supplied to the spreading mechanism (e.g., roller, blade) via the powder supply piston or a powder hopper, the powder is spread over the build platform (which controls layer thickness), inkjet deposition occurs over the build platform, and then binder drying and/or curing is performed with the integrated heat lamp (Online Resource 1). For spreading, the user can choose the spreading tool geometry, spreading translation speed and rotation, layer height, and optional post-print compaction. Control over the inkjet

nozzle diameter, inkjet droplet frequency, inkjet droplet velocity, printhead traverse velocity, jetting position, and heating time, as well as control over the spreader mechanism, spreading translation speed and rotation, layer height, and compaction are all possible with the custom testbed.

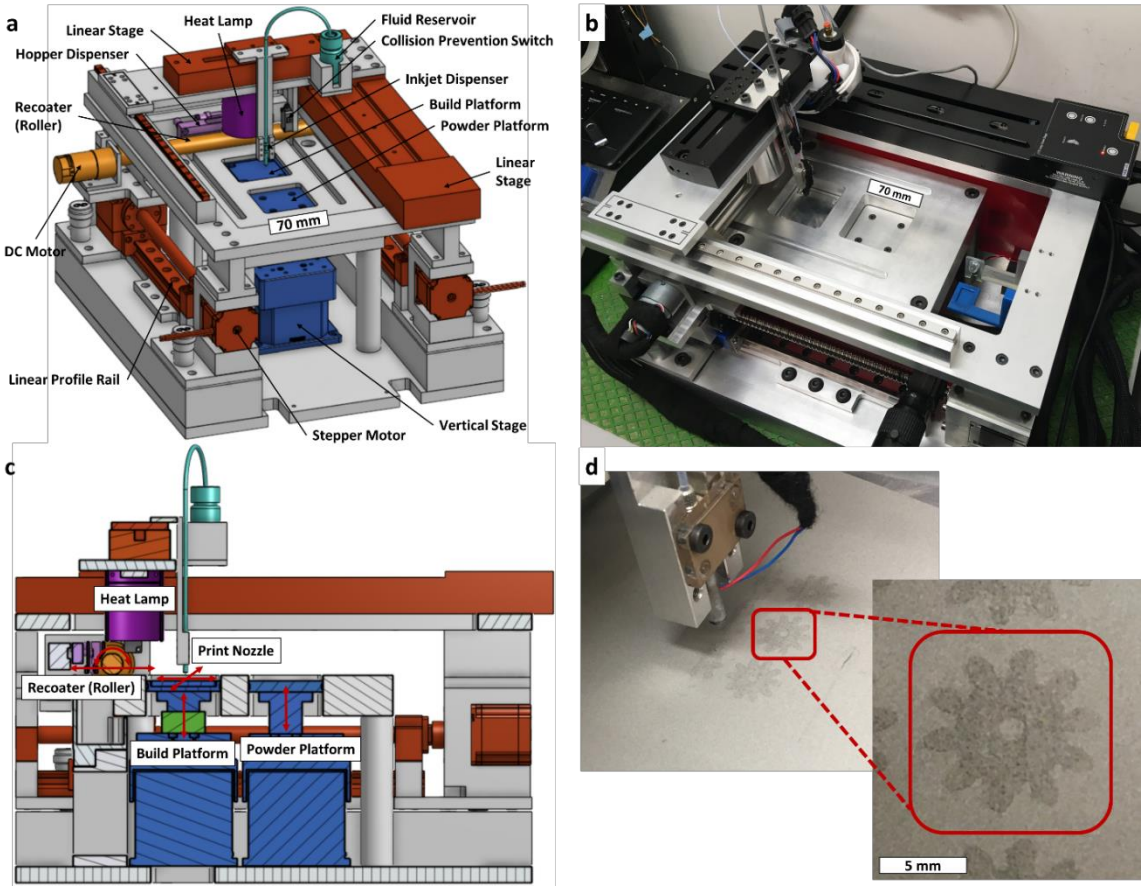

Figure 3.2: Binder jetting testbed: (a) CAD model showcasing major components with roller installed as the powder spreading tool; (b) fabricated binder jetting testbed; (c) sectional side-view highlighting moving components and trajectories; (d) images from binder jetting experiment using stainless steel 316L 15-45 µm powder and polymer binder, printing an array of gear geometries on the build platform.

The testbed was designed according to the target specifications listed in Table 3.1, and is suited for processing custom powder feedstocks (e.g., polymer, metal and ceramic powders) and binder compositions (e.g., polymer, nanoparticle suspensions, metal salt solutions). The following are the major modules of the machine, including a summary of

the modules for powder spreading testbed (denoted by * below) described in Chapter 2 [129]:

Powder supply platform*: Powder is supplied using a vertical platform (travel distance of 20 mm), consisting of a motorized axis and a custom-machined pillar and piston.

Modular powder spreading mechanism*: A custom-designed linear motion system is used to translate the powder spreading mechanism. The spreading mechanism has mounting features that allow the interchange of different spreading tools (e.g., motorized roller, stiff blade, compliant blade). For the BJAM experiments described here, a precision roller is used to spread powder from the powder supply platform and onto the build platform. A hopper dispensing system may alternatively be used for direct deposition of powder on the build platform, followed by spreading using the motorized tool.

Build platform*: The build platform presents the surface onto which the part is built. The build platform has a removable build plate and an integrated load cell, which can be used to measure powder compaction forces. These components are attached to a motorized (vertical) axis via a custom-machined pillar and piston. The build platform has a vertical travel distance of 20 mm, is capable of measuring loads up to 100 N, and the build (spreading) area is 60 mm x 60 mm.

Inkjet deposition system: An X-Y gantry motion system coupled with a piezoelectric inkjet dispensing system enable precise deposition of <100 μm droplets over the build area. Additionally, a heat lamp mounted on the inkjet motion system assists drying and curing of the binder after deposition.

Vision system: A video camera is focused at the inkjet nozzle home location and along with a controllable strobe LED, assist in setting and validating ink jetting parameters.

Control software: A custom LabView program controls all system operations and allows for specification of all process parameters.

Table 3.1: Summary of desired design specifications for binder jetting testbed, including specifications for powder spreading testbed.

Parameter	Design Values
Spreader Type	Interchangeable; roller or blade
Powder Dispensing Mechanism	Piston and/or hopper
Spreading Tool Traverse Speed	0-100 mm/s
Roller Rotation	0-300 rpm
Build Platform Minimum Incremental Motion	5 μm (vertical)
Dispenser Nozzle Diameter	Modular; 20-80 μm*
Jetting Frequency	< 1 kHz*
Binder Viscosity	< 20 cPs*
Binder Surface Tension	20-70 dynes/cm*
Minimum Binder Reservoir Volume	10 mL
Build Volume	60 x 60 x 20 mm (LxWxH)
Machine Volume	450 x 500 x 400 mm (LxWxH)
*Specifications of MicroFab Dispensing System	

3.2.2 Detailed description of testbed modules

Here we detail the inkjet module which consists of an inkjet dispenser mounted on single-axis linear motion systems stacked in an X-Y configuration. The module is kinematically mounted on top of the powder spreading testbed; the modules and validation of the powder spreading apparatus have been previously presented in detail [129], and therefore are not described further in this chapter.

3.2.2.1 Linear motion system: long-direction (Y-axis) and short-direction (X-axis)

The long-direction of motion (Y-axis) controls the position of the inkjet dispenser in the non-jetting direction, ultimately setting the line spacing during BJAM. The linear stage for the Y-axis (Thorlabs LTS300/M) provides a maximum travel velocity of 50 mm/s with listed repeatability of 2 μm and accuracy of 5 μm. The Y-axis motion system includes an integrated controller to drive the stepper motor. The short-direction of motion (X-axis) controls the position and velocity of the inkjet dispenser in the jetting direction. The linear

stage for the X-axis of motion, or jetting direction, (Thorlabs DDSM100/M) provide a maximum 500 mm/s printhead traverse velocity with manufacturer-listed repeatability of 1.5 μm and accuracy of 5 μm. The X-axis linear stage is controlled using a brushless DC servo driver (Thorlabs KBD 101).

3.2.2.2 Inkjet droplet generation system

The jetting system consists of a piezoelectric drive controller (Microfab JetDrive V, CT-M5-01), a 20 mL fluid reservoir, gas and fluid tubing (LeeCo MINSTAC tubing), a single piezoelectric dispensing nozzle (Microfab MJ-AT-01-xxx, where xxx dictates the nozzle diameter), and a digital pressure controller (APEX Vacuum LLC). The diameter of the droplet can be varied by utilizing dispensing nozzles (available from 20-80 μm orifice diameter), the frequency of droplet ejection can be controlled up to 1 kHz, and the waveform sent to the piezoelectric dispenser can deliver up to 70V with dwell times up to 100s of μs. The pressure controller regulates the backpressure in the fluid reservoir and thus provides the appropriate static pressure at the nozzle tip for droplet ejection. The use of a single dispensing nozzle simplifies interchange of the binder system and reduces the time required to purge nozzle clogs which can occur when utilizing novel binders. Furthermore, the testbed was designed to be compatible with multi-nozzle inkjet printheads (e.g., Xaar 1201) that offer higher throughput for binder deposition.

3.2.2.3 Vision system

A custom optical setup allows imaging of droplets to determine suitable jetting parameters and ensure continuous jetting during binder jetting experiments. The setup comprises a USB CCD camera (Thorlabs High-Sensitivity USB 3.0 CMOS Camera), optics (Thorlabs 6.5X Zoom Lens with 3 mm Fine Focus, 0.50X Extension Tube, C-Mount Adapter, and 0.75X Magnifying Lens Attachments, with 6.28 μm resolving limit at high magnification), and a strobe LED (Microfab Technologies, Inc.). The strobe LED can be controlled to pulse at the same frequency as the piezoelectric actuator, with an additional pulse delay to capture droplets at different stages of jetting.

3.2.2.4 Heat lamp

As an optional drying and/or curing mechanism for the binder jetting process, a custom heat lamp system was constructed utilizing a halogen bulb (Sunlite ENH 250W Bulb, MR16 400W Socket), fully encapsulated and protected using a UV filter lens (WAC Lighting LENS-16-UVF) and a custom-machined aluminum casing. The power to the heat lamp is controlled using a microcontroller (Arudino Nano) and power relay (Digital Loggers IoT Relay). Use of the lamp to heat the powder bed can, for instance, assist in evaporation of binder solvent, or initiate polymerization or cross-linking of certain binders.

3.2.2.5 Collision prevention switch

To prevent potential damage to the inkjet system from errant contact with the recoating system, a switch which cuts power to machine was incorporated. The switch is mounted to the inkjet motion gantry and is triggered upon contact with the powder spreading system. The miniature push-button limit switch (McMaster Carr 7779K61) is connected to a microcontroller (Arudino Nano) and power relay (Digital Loggers IoT Relay) which controls the power to the testbed.

3.2.2.6 Software for binder jet testbed

Figure 3.3 schematically shows the electrical wiring and communications within the system. A custom LabView program was developed for control of all machine components, including concurrent control of the powder spreading testbed. For binder deposition onto the powder bed, synchronization of nozzle dispenser motion with triggering of the piezoelectric jetting system is critical. Therefore, the software controls the steps of each layer-wise cycle of BJAM which involves powder spreading, and controls the binder deposition process. A MATLAB script was written to convert user inputs (e.g., from a text file with part geometry generated via Autodesk Netfabb, jetting line spacing, nozzle diameter, etc.) to a text file which contains LabView-compatible machine commands. The text file is then used as an input to the LabView code which uses the control commands to drive the machine.

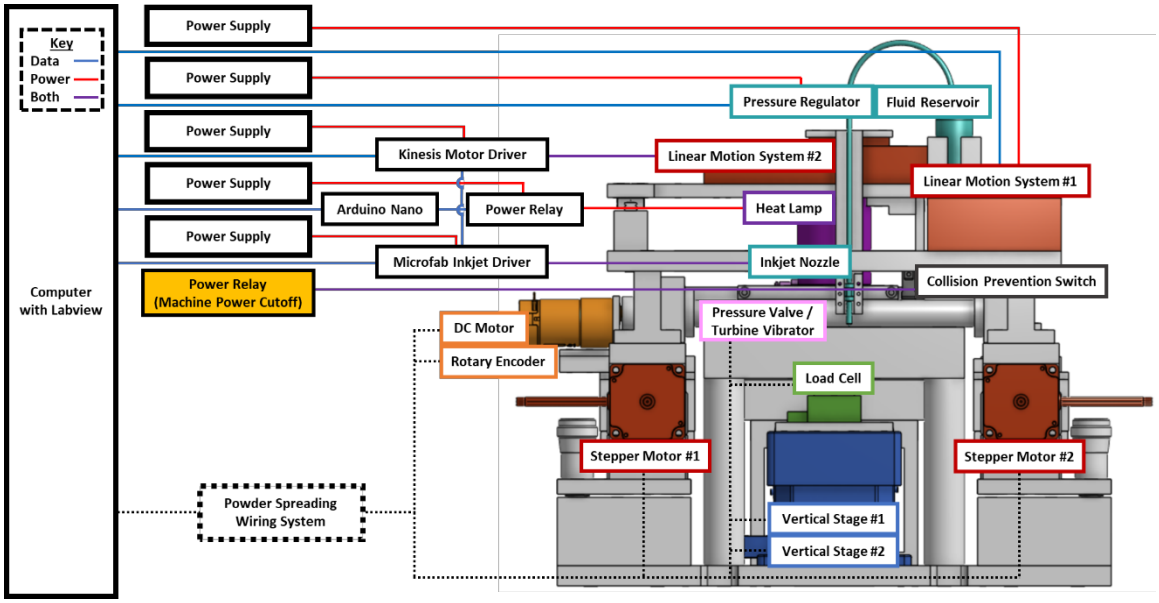

Figure 3.3: Electronic connection diagram for binder jetting testbed, including abbreviated connections for powder spreading system.

3.3 Validation and experimentation

3.3.1 Binder jetting testbed validation

3.3.1.1 Linear motion system: traverse position

The resolution of the traverse motion of the inkjet nozzle in both the Y and X axes was measured using a laser point scanner (Keyence LK-G152, reported accuracy 0.5 µm). Measurements were performed by sending motion commands to a single axis with intervals ranging from 25 µm to 5 mm across the total range of -20 mm to +20 mm, with each condition being measured three times. As shown in Figure 3.4a, linear correlation for the Y-axis was demonstrated within ±50 µm, with repeatability within 30 µm (Figure 3.5a). Similarly, for the X-axis, linear correlation was demonstrated within ±30 µm as shown in Figure 3.4b, with repeatability within 5 µm (Figure 3.5b).

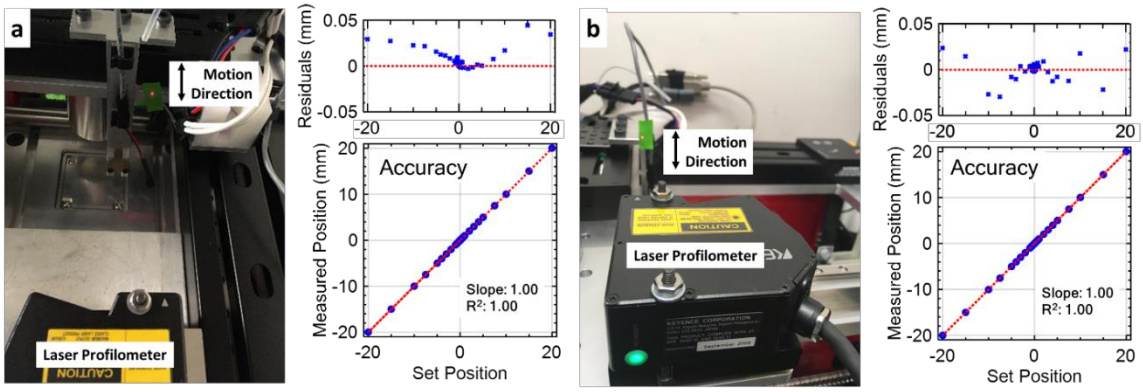

Figure 3.4: Validation test setup, motion position accuracy and residuals to linear fit for (a) Y-axis and (b) X-axis (jetting direction).

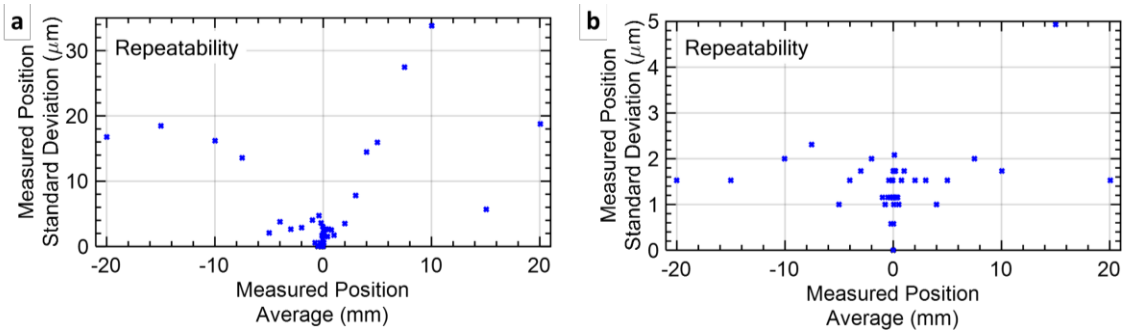

Figure 3.5: Position repeatability for (a) Y-axis and (b) X-axis (jetting direction).

3.3.1.2 Heat lamp: build area temperature profile

To estimate the energy deposition from the heat lamp over the build platform, the temperature above the build platform was measured using a thermometer (PerfectPrime TC2100) connected to a K-type thermocouple (McMaster Carr 6441T942). The measurement provides an estimate of the heating capabilities of the heat lamp and was performed by placing the thermocouple above the build platform (Figure 3.6a) and providing power to the heat bulb for a set amount of time. To estimate the heating profile at the center of the build platform, the heat lamp was turned on for 50 seconds, showcasing that the center of the build area reaches 100°C in 8 seconds and reaches 200°C in 48 seconds (Figure 3.6b) Furthermore, by varying the position of the thermocouple to nine

positions over the build platform, we can estimate a heat profile for the build area after 30 seconds of energy deposition from the heat lamp over the build plate (Figure 3.6c).

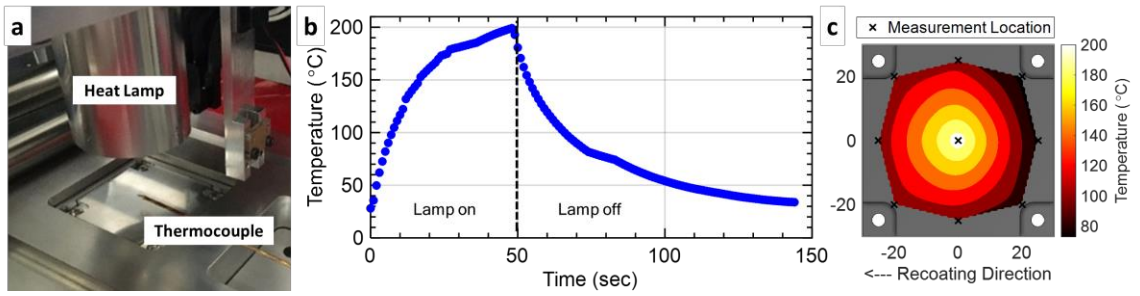

Figure 3.6: (a) Validation test setup for temperature profile above build platform using thermocouple after energy deposition from heat lamp, (b) temperature versus time profile over the center of the build area and (c) estimated heat map over build platform after 30 seconds of heating.

To analyze the thermal conditions of a powder bed during an exemplary heating cycle, an infrared thermal camera (HTI HT-A2) was used to image the surface temperature of a 500 µm stainless steel powder layer (SS 316L, 15-45 µm, John Galt Steel). Powder was spread at a traverse speed of 50 mm/s without roller rotation at 55.5% humidity (AcuRite 01080M), in an ambient lab environment. Images were taken after 10 seconds, 30 seconds, and 60 seconds of heating. As shown in Figure 3.7, the central region (~40mm diameter) of the powder bed surface exceeds 80°C after 10 seconds and the region exceeds 100°C after 30 seconds of heating. This bed temperature of 100°C is sufficient to assist in drying of common binder solvents (e.g., deionized water, 2-methoxyenthanol, ethanol), as well as being greater than the glass transition temperature for various polymers (e.g., polyethylene glycol, polyvinyl alcohol, polymethyl methacrylate), therefore showing the heating capability can assist in formation of a uniform binder film over powder particles [130]. The time-temperature dynamics attained by the powder bed will depend on the powder material (e.g., absorptivity), bed properties (e.g., packing density), and heat lamp parameters (e.g., bulb wattage, heating time), and should be calibrated for each experimental condition.

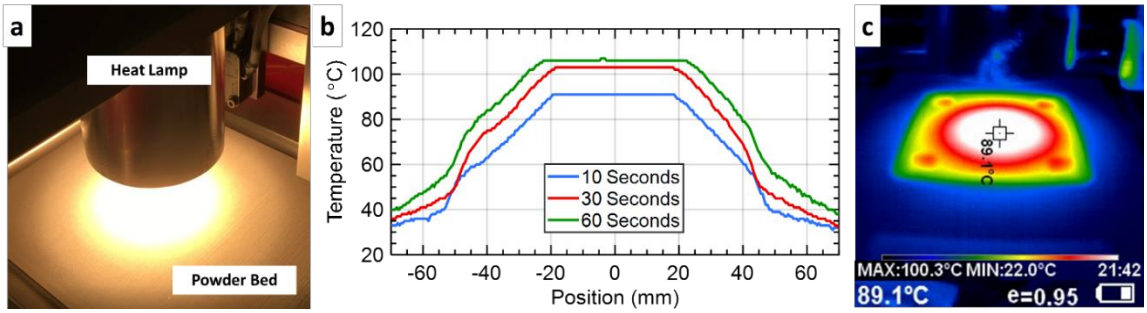

Figure 3.7: (a) Validation test setup for thermal profile of powder bed after heating, (b) thermal profile over central region of build platform and (c) representative infrared image from experiments.

3.3.1.3 Vision system: droplet generation and imaging

To establish a stable jetting condition, the back pressure is set to the maximum value to purge the nozzle, then reduced until the meniscus is flush with the nozzle orifice. Once the pressure condition is set, the voltage and jetting time are adjusted until a droplet is generated by the system. To showcase the capabilities of the vision system, images of the inkjet dispensing nozzle and ejected droplets were taken using the custom optics system, shown in Figure 3.8. The outer diameter of the nozzle tip was determined to be 600.5 µm using a digital microscope (Zeiss Smartzoom 5). This value is used to set the scale for images taken using the vision system, and in turn to estimate the diameter and velocity of the ejected droplets. To estimate the diameter of ink droplets ejected from the 80 µm dispensing nozzle, a polyethylene glycol (PEG) binder (10% m/m PEG 6000 in DI water/ethanol, 20% mole ratio ethanol) was dispensed from the tip with a jetting voltage of 65 V and dwell time of 20 µs at 120 Hz jetting frequency. Ten different droplet images were captured at a 500 µs strobe delay and analyzed in Fiji/ImageJ to compute the droplet diameter from the droplet area estimated using the oval measurement tool, resulting in a droplet size of 81.0 ±1.4 µm. To estimate the droplet velocity, the same binder and jetting conditions were utilized, but sequential droplet images were taken at increasing strobe delays, resulting in capturing of the jetting sequence and droplet, shown in Figure 3.8b. The velocity was estimated using Fiji/ImageJ by dividing the change in droplet position by

the change in strobe delay for the 350-750 µs images and averaged over five separate jetting sequences, resulting in a speed of 2.0 ±0.1 m/s.

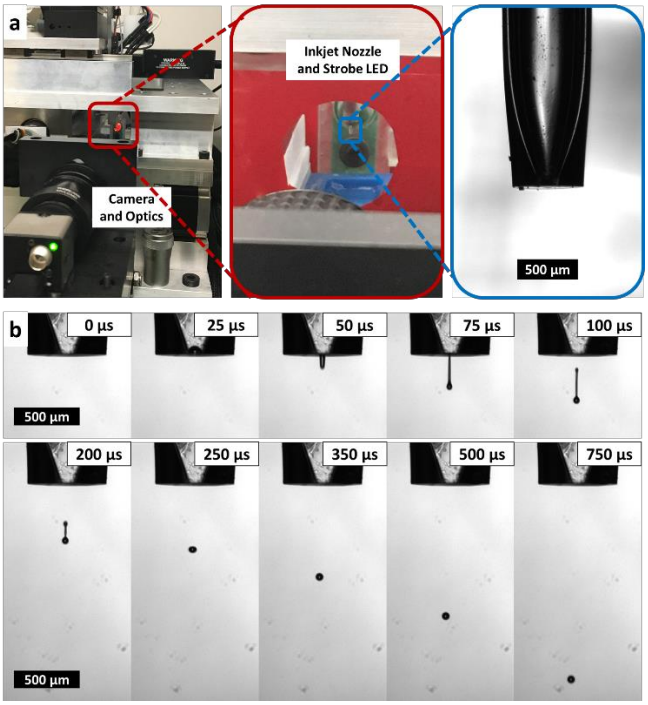

Figure 3.8: (a) Vision system setup and (b) inkjet sequence of binder droplets using transparent (undyed) PEG binder.

3.3.1.4 Inkjet system: positional accuracy and drop spacing control for line formation

To showcase functionality and test the positional accuracy of the full inkjet module, a rectangle pattern of droplets (19 Y-axis x 21 X-axis) was deposited with a drop spacing and line spacing of 250 µm. To assist in imaging the droplets after deposition, the PEG binder was modified by adding 1% m/m black dye (Sigma Aldrich 211842) and the droplets were deposited on white copy paper (Xerox Business 4200) at a jetting traverse velocity of 25 mm/s, jetting voltage of 65 V, and jetting dwell time of 20 µs. A comparison between the MATLAB-generated droplet map and printed map is shown in Figure 3.9a. The deviation of each droplet position from its intended position was estimated using Fiji/ImageJ via the multi-point tool, showing a mean signed error of 4.9 ±20.5 µm and a

mean absolute error of 17.3 ±12.1 μm for the droplet position in the X-axis (jetting direction) and a mean signed error of 15.5 ±10.8 μm and a mean absolute error of 5.5 ±18.1 μm for the droplet position in the Y-axis (non-jetting direction). These deviations are the result of compounding effects from the motion system, jetting anomalies at the nozzle tip during jetting, and wetting characteristics of the binder and substrate. Additionally, the size of the printed droplet was estimated using the particle analysis tool in Fiji/ImageJ as 187.9 ±5.5 μm or approximately 2.4X the droplet diameter. Thus, the droplet position deviation is an order of magnitude smaller than the critical dimension (i.e., diameter) of the droplet.

Additional patterns printed using the same dyed PEG binder and paper substrate, were used to evaluate the capability of the inkjet system to control droplet spacing and form continuous print lines, which is ultimately necessary to control binder saturation (i.e., the ratio of deposited binder volume to powder bed pore volume) and thereby ensure homogenous green strength and feature quality in the powder bed during BJAM. Droplet spacing ranging from 40 μm (i.e., 0.5X droplet diameter) to 250 μm was controlled by varying the jetting frequency from 625 Hz to 100 Hz (i.e., jetting traverse velocity was held constant at 25 mm/s), shown in Figure 3.9b. It was found that decreasing the droplet spacing below 120 μm (i.e., 1.5X droplet diameter) results in stable line formation throughout the print line for this setup. Fiji/ImageJ was used to estimate the line width, with an approximate line width of 368 μm for a 40 μm droplet spacing, 331 μm for 80 μm droplet spacing, and 295 μm for 120 μm droplet spacing. These line widths are only representative of the chosen binder and the paper test substrate, however, the formation of a stable line at nominal spacing of ≤0.5X droplet diameter is consistent with prior work on selection of droplet spacing for BJAM [14,97] and therefore this condition was utilized for binder jetting experiments that follow. Despite the obvious difference between the substrate-binder interactions (e.g., binder permeability and infiltration, particle displacement and ejection, substrate surface properties) of printing on paper versus a powder bed, the use of a monolithic porous substrate can serve as an initial screening tool. In the future, experiments could be performed to enable direct correlation of drop spreading on a model porous substrate to the behavior on the powder bed.

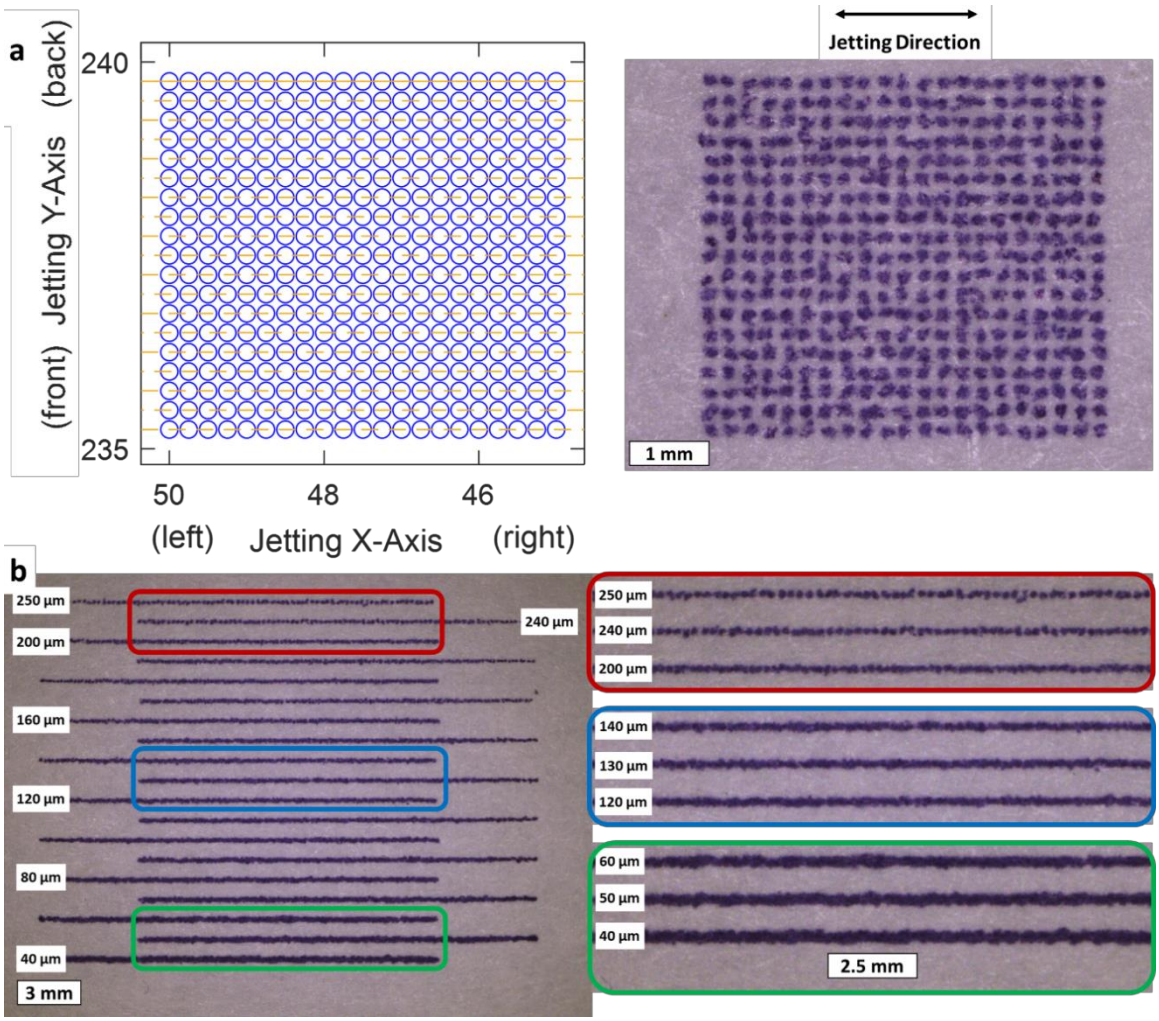

Figure 3.9: (a) Droplet jetting map as created by MATLAB script and as-printed using dyed PEG binder on white paper; (b) Line formation by inkjet droplets at varying droplet spacing, with close-up of select lines, printed using dyed PEG binder on white paper.

3.4 Binder jetting experiments

To validate the utility of the full testbed, exemplary binder jetting experiments are now presented. The purpose of the following experiments is to showcase the operational capabilities of the testbed and is not intended as a full description of possible process parameter variations, nor is post-processing explored. For this validation study, a 3 mm x 5 mm x 2.5 mm rectangular prism was selected as the print geometry. Stainless steel 316L

powder (15-45 μm, John Galt Steel) was spread to 100 μm layer heights using the roller mechanism at a traverse speed of 5 mm/s and a roller counter-rotation of 250 RPM. A PEG 6000 binder with 10% m/m concentration in a DI water / ethanol (20% mole fraction ethanol) solvent was deposited on the powder bed using the 80 μm nozzle dispenser, with a droplet spacing of 40 μm (0.5X droplet diameter), and a jetting traverse speed of 25 mm/s – thus controlling the binder saturation through the line spacing dimension. A base layer of 250 μm thickness was spread prior to beginning the printing process to facilitate part removal after printing. Printing was performed at 58.0 % humidity (AcuRite 01080M) in an ambient lab environment. After each layer, drying of the binder was performed by setting the heat lamp over the build area and providing power to the heat lamp for 20 seconds. After completion of the full print (i.e., printing of all 25 layers), the build platform along with the printed component and excess surrounding powder were removed. These were heated to 60°C for 30 minutes in a furnace (Pentron Laboratory Technologies, LLC JP 1200 Porcelain Furnace) to cure the binder. After binder curing, excess powder was removed from the build platform using a brush, followed by careful removal of excess powder around the part using pressurized air, and finally removal of the printed component using soft-tipped tweezers.

3.4.1 Effect of binder saturation on print quality

To study the effect of binder saturation on print quality, parts were printed with 150% and 200% estimated binder saturation. Estimated binder saturation, a process parameter for our testbed, is calculated by using the jetting parameters of droplet diameter (d), droplet spacing (D_s), line spacing (L_s) and an estimated powder bed packing fraction ($P_{f,est}$), as follows

$$S_{est} = \frac{\pi}{6} \frac{d^3}{\left(1 - P_{f,est}\right) * D_s * L_s} \tag{3.1}$$

An estimated powder bed packing ratio ($P_{f,est}$ = 0.5) is used in the calculation of the estimated binder saturation, since the powder bed density (equivalently, the packing fraction) is difficult to measure in-situ without disturbing the powder bed and is further locally affected by powder feedstock, spreading parameters, and environmental conditions. This value can be verified by measurement of green density after printing, and therefore can be fed back into the process parameter calculation as development proceeds. The component printed with 150% estimated binder saturation (90 μm line spacing) resulted in shifting of printed layers, shown in Figure 3.10. Although individual layers approach the desired area dimensions (5.02 mm x 3.05 mm), insufficient adhesion occurs between printed lines, resulting in visible individual print lines on the part. Also, the shifted layers suggest insufficient adhesion between layers also occurs, resulting in sub-optimal inter-layer strength that does not withstand the forces of spreading the next layer. The inter-line and inter-layer defects suggest the selected line spacing (and thus binder saturation) is suboptimal for this selected binder and powder combination.

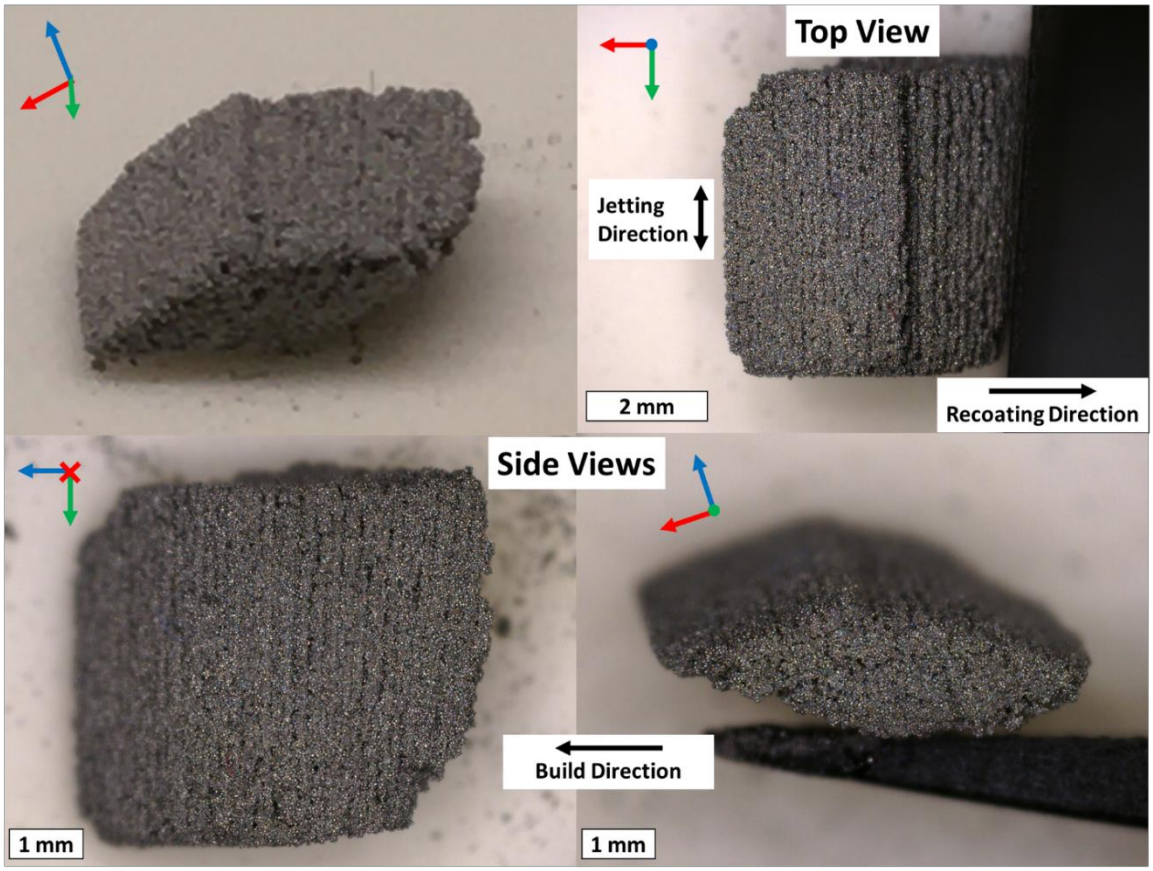

Figure 3.10: Images of binder jet part (intended to be 3 mm x 5 mm x 2.5 mm right rectangular prism) printed with stainless steel 316L 15-45 µm powder with PEG binder at 150% estimated binder saturation. The result is an oblique rectangular prism due to shifted layers resultant from insufficient inter-layer binder penetration and layer shifting during powder spreading.

Alternatively, 200% estimated binder saturation (67 µm line spacing) resulted in a regular rectangular prism with dimensions of 3.09 ±0.03 mm x 5.17 ±0.02 mm x 2.51 ±0.03 mm, shown in Figure 3.11. For this component, individual lines are no longer visible for the top layer and no shifting occurs between layers during the print. Some defects can be seen in the side views of the component, possibly due to printing error or green part deformation through handling after printing. Additionally, the component is slightly oversized when compared to the design file, a result of excessive binder saturation at the shell regions of the print. Despite the small defects, the successful printing of the prism shows the capability of the binder jet testbed to produce relevant BJAM components

utilizing custom-developed binders. Optimization of binders, printing parameters, and post-processing procedures will lead to improvements in dimensional accuracy and part strength.

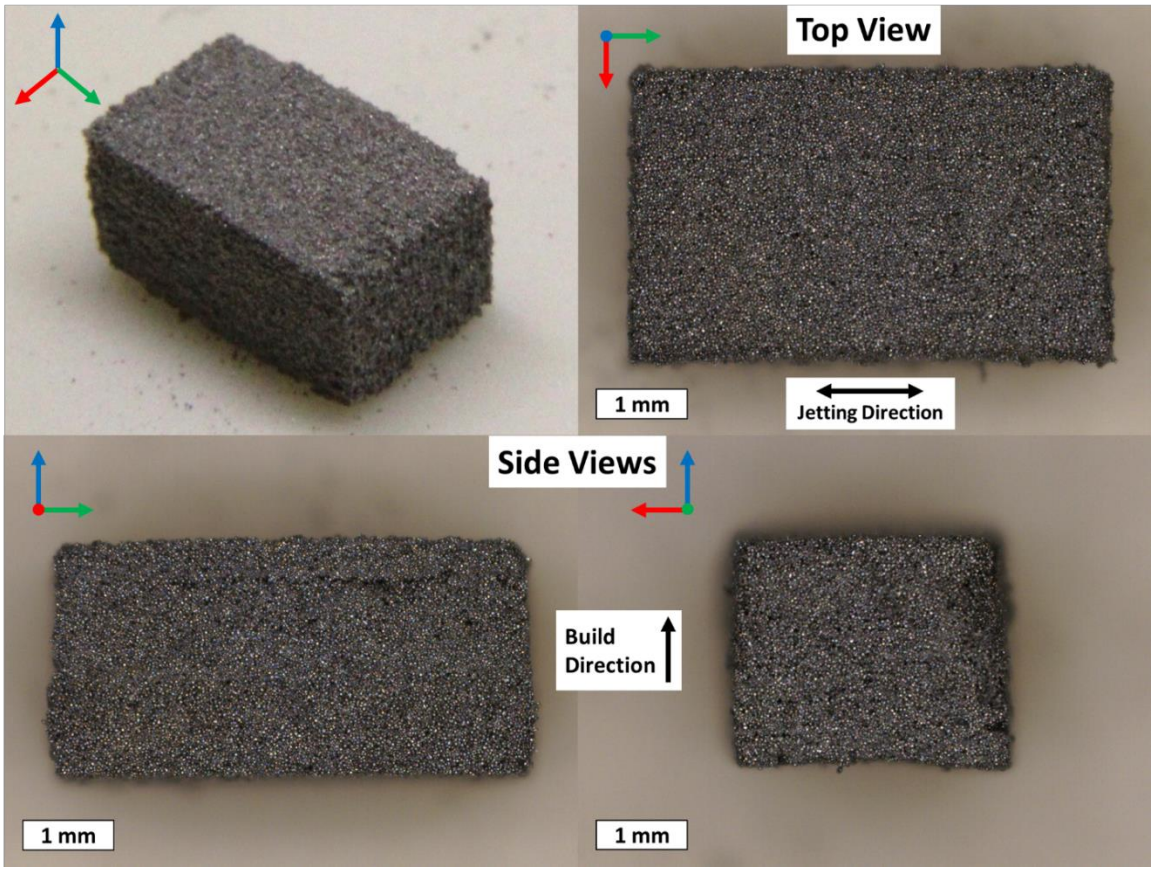

Figure 3.11: Images of binder jet part (intended to be 3 mm x 5 mm x 2.5 mm right rectangular prism) printed with stainless steel 316L 15-45 µm powder with PEG binder at 200% estimated binder saturation. The result is a right rectangular prism with dimensions of 3.09 ±0.03 mm x 5.17 ±0.02 mm x 2.51 ±0.03 mm.

3.4.2 Density and µCT analysis of printed component

To further quantify the quality of the printed rectangular prism component, green density measurements were determined via micro-computed tomography (µCT), according to the parameters in Table 3.2. Reconstruction was performed automatically using the control and

acquisition software (Zeiss Scout-and-Scan). Fiji/ImageJ was used for image processing of the μCT 16-bit tomograms by converting to 8-bit, enhancing brightness/contrast (ImageJ auto), sharpening (ImageJ default), and thresholding (ImageJ default, IJ_IsoData) to segment the data into solid material and pores, demonstrated in Figure 3.12b. The processed tomograms were uploaded to Dragonfly (Object Research Systems, Inc.), which was used to estimate the density of the central region of the CT scan (1.40 mm x 1.40 mm x 1.90 mm), shown in Figure 3.12d. The central region was selected to avoid usage of the CT scan mask in the density calculation. The calculated green density for the component is 54.6%, in good agreement with green densities fabricated via BJAM [2–4]. Using the measured green density for the component (P_f = 0.546) instead of the estimated powder bed packing ratio ($P_{f,est}$ = 0.5), along with Equation (1), the measured binder saturation for the printed component is 220% for the selected print parameters.

Table 3.2: μCT scan parameters.

Parameter	**Value**
Equipment	Zeiss Xradia 520 Versa
Source-to-detector distance (mm)	49.1
Field of view (μm x μm)	2054.9 x 2054.9
Pixel size (μm)	2.0245
Voltage (kV)	160
Power (W)	10
Source filter	HE2
Exposure time (s)	1.7
Objective	4X
Field mode	Normal
Binning	2
Number of projections	3201
Cone angle (deg)	3.98
Fan angle (deg)	3.98

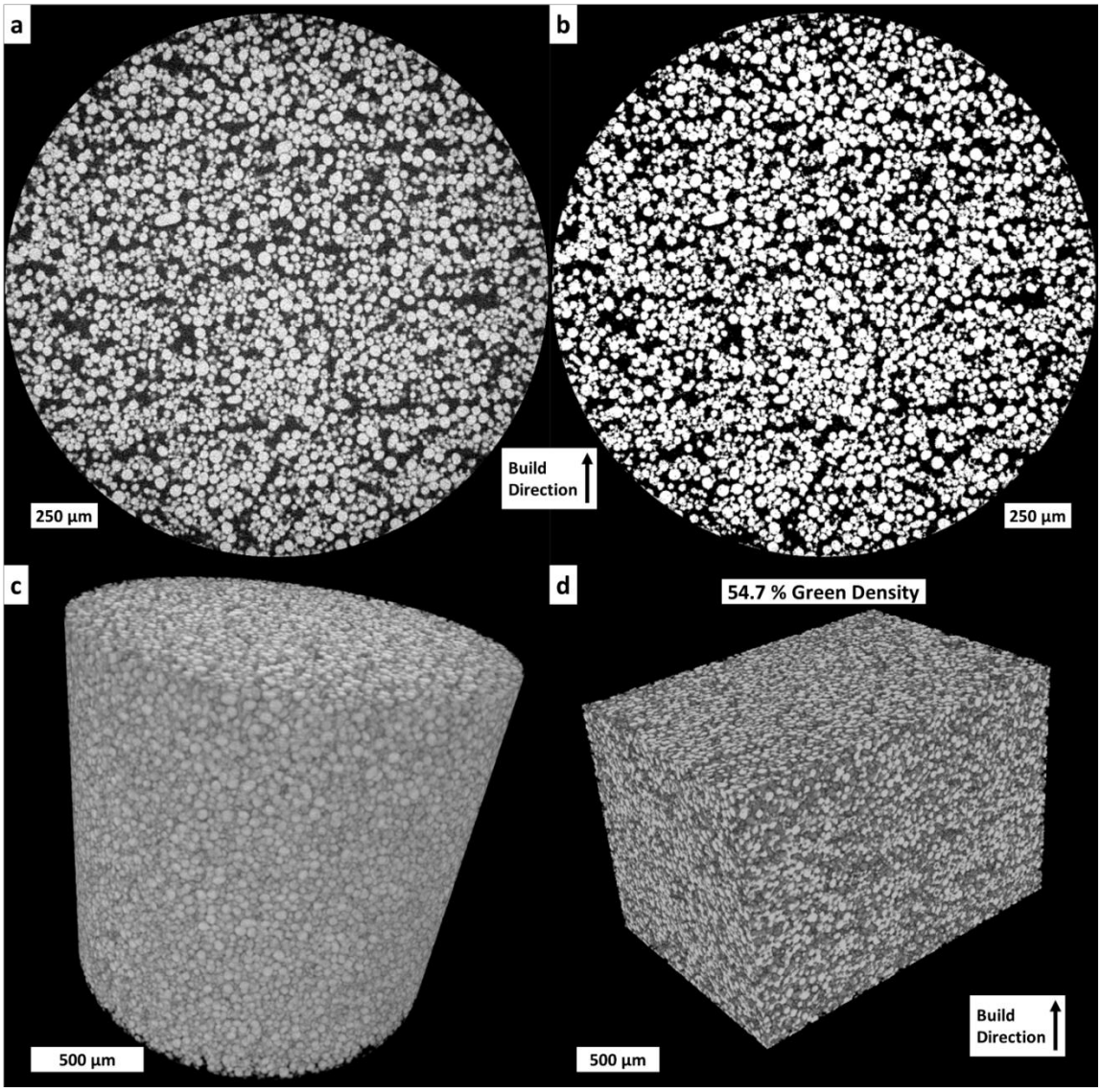

Figure 3.12: µCT scan of printed part with 200% binder saturation showing: (a) exemplary tomogram from µCT scan; (b) same tomogram after contrast, sharpness, and threshold adjustment performed for density analysis; (c) 3D rendering of full µCT scan; (d) 3D rendering of µCT scan section utilized for density analysis with a calculated density of 54.6% for the green part.

3.5 Conclusions

This work has highlighted the design, fabrication, and validation of a modular binder jetting (BJAM) testbed. Testbed modules were validated using relevant measurement techniques and exemplary fluid jetting and binder jetting experiments were performed to showcase the system's functionality, with comparable performance to commercial testbeds (i.e., powder size on the order of 10 μm, layer height of 100 μm, inkjet droplet diameter on the order of 10 μm, printed primitive lines on the order of 100 μm and green density of 40-60%). The modular design allows full authority over process parameters, as well as adaptation of spreading conditions to address powder characteristics. In particular, a single-nozzle piezoelectric inkjet dispenser, coupled with a vision system, allows identification of stable jetting parameters for arbitrary binders, and screening of jetting patterns and binder saturation levels to enable more efficient process development toward net-shape three-dimensional components. Powder spreading parameters, and incorporation of additional implements such as a dispensing hopper, could further be tailored for BJAM of fine, cohesive powders, and powders with non-spherical particle shapes. By coupling this testbed with additional characterization techniques for the powder bed, powder spreading, and powder-binder interactions, as well as post-processing capabilities (e.g., debinding and sintering), future work will explore custom binders to improve part strength and density, and study in detail the relationship between process conditions at each stage of BJAM. Research and process development using this testbed could also be translated to commercial BJAM equipment.

Chapter 4

Binder development process and application to reactive metal salt binders

Binder jet additive manufacturing (BJAM) enables processing of metals, ceramics, polymers and composites through the deposition of a binding agent onto a powder bed in a layer-by-layer sequence. Most commonly, a polymer binder is utilized to provide temporary strength to the printed component enabling part removal and handling from the printer; however, it is challenging to manage distortion and shrinkage during sintering. Reactive binders, which create solid interparticle bridges upon decomposition, provide additional benefit beyond temporary green strength and can lead to enhanced densification kinetics, control of warping and shrinkage, and tailoring of local composition. This chapter presents a process for the development of custom binder inks which includes exploration of binder ink rheology, wetting and infiltration interactions between the binder ink and powder, ink jetting and the effect of drop spacing on line formation, thermal decomposition of the binder, and evaluation of green strength using indentation. The binder ink development process is applied to the synthesis of custom polymer and reactive (metal salt) binder inks, showcasing the capability to control jetting behavior through rheological modifications and the favorable comparability of wetting, infiltration, and green strength

of the reactive binders to the studied polymer binders. The viscosity and surface tension of the binder inks vary by 10 cP and 35 mN/m, respectively, with successful jetting and powder binding achieved by polymer and metal salt binder inks, with green strengths measured between 2-18 MPa. Through our presented process, rapid sampling of binders can be performed and through the implementation of reactive binders into BJAM in the future, a powerful tool for control of densification and warping is identified.

4.1 Introduction

Additive manufacturing (AM) offers design flexibility, small-batch product customization, as well as product development and lead-time reduction when compared to traditional manufacturing methods [131]. Binder jet additive manufacturing (BJAM), in particular, offers compatibility with powder materials [132,133], a high build rate [133], good resolution, scalability to large build areas (e.g., 100s mm) [131], and separation of geometrical shaping of the part from the thermal densification phase enabling microstructural control during sintering and application to a variety of materials [133,134]. To build a green, or binder-bound, part the binder jetting process consists of deposition and spreading of a powder layer (<100 μm) and delivery of a binder via inkjet deposition, with repetition of these two steps performed until the desired 3D geometry is fabricated, conceptually shown in Figure 4.1a. To assist in removal of the green part from the build platform, binder curing is performed and after liberation, the green part undergoes post-processing (e.g., debinding, sintering, infiltration) for part consolidation and optional post-processing (e.g., sand blasting, polishing, coating) as required by the intended application. The evolution of the binder ink and binder-particle interactions during BJAM and post-processing is conceptually shown in Figure 4.1b.

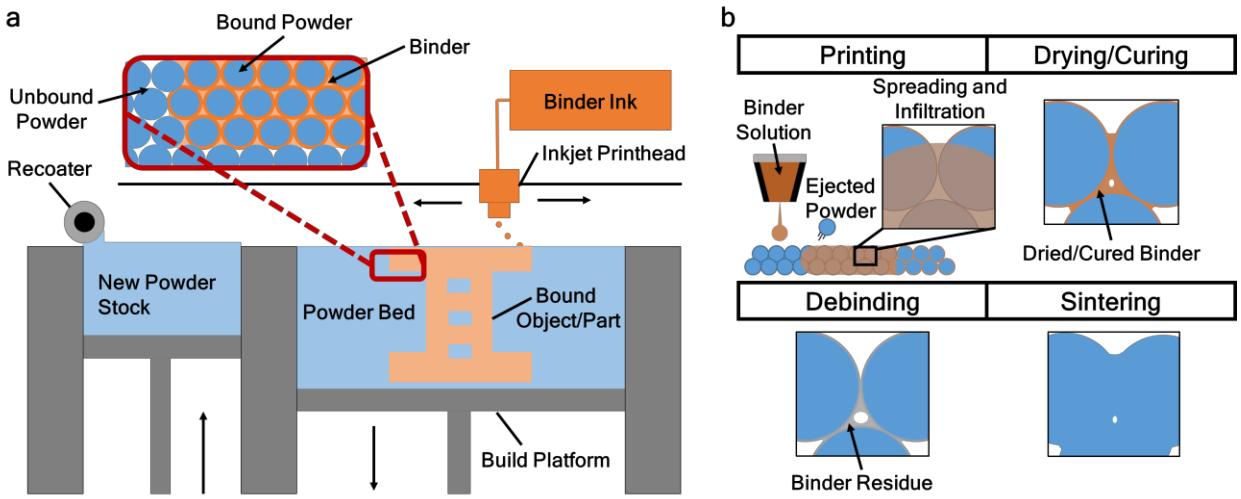

Figure 4.1: Conceptual images of (a) binder jetting process showcasing powder spreading from a piston-fed system and deposition of a binding agent through an inkjet printhead, subsequently creating a 3-dimensional component within the build platform; and (b) binder-powder interactions during inkjet deposition onto a powder bed and subsequent evolution of binder and powders through thermal post-processing.

Binder development for BJAM requires understanding of various complex interactions, including appropriate binder ink rheology for jetting, adequate binder-powder interaction for binder infiltration, knowledge of binder decomposition, and sufficient strength of the binder for removal. Utela et al. summarized a process for the formulation and characterization of new binders for use in BJAM, including suggestions on optimizing viscosity, surface tension, and particulate loading for ink jetting [135].

The generation of binder ink droplets is governed by fluid mechanics and requires the careful matching of rheological properties (i.e., viscosity, surface tension, density) with printing conditions (e.g., nozzle diameter, ejection velocity) [126]. The behavior of the ink droplets is commonly characterized by dimensionless numbers, in particular the Reynolds (Re), Weber (We), and Ohnesorge (Oh) numbers [136]. The Reynolds number relates inertial and viscous forces:

$$Re = \frac{\rho u d}{\eta} \tag{4.1}$$

where ρ is the density of the fluid, u is the fluid flow speed, d is a characteristic linear dimension (usually the droplet diameter for inkjet), and η is the dynamic viscosity of the fluid. The Weber number relates inertial and surface tension forces:

$$We = \frac{\rho u^2 d}{\gamma} \tag{4.2}$$

where γ is the surface tension of the fluid. The Ohnesorge number, and it's inverse (called the Z parameter), relate viscous, inertial, and surface tension forces:

$$Oh = \frac{\sqrt{We}}{Re} = \frac{\eta}{\sqrt{\rho \gamma d}} = \frac{1}{Z} \tag{4.3}$$

and provide an estimated range for printable inks of $2 < Z < 20$, with additional conditions for minimum energy for droplet formation ($We > 4$) and excessive energy such that splashing results upon impact with the substrate ($We^{1/2} Re^{1/4} > f(R) \approx 50$ for flat, smooth surfaces) [126,137]. For a summary of inkjet mechanics, the reader is directed to the articles by Derby, and Liu and Derby [126,137].

Bredt explored the fundamentals of feature formation via inkjet deposition onto powder beds for BJAM, including jet impacts, line coalescence, capillary migration, and powder bed infiltration – highlighting that the formation of features is dominated by line formation of consecutively printed droplets and developing a timeline for feature formation in BJAM [102]. Bai et al. explored binder-droplet interactions using granule formation from sessile drop goniometry as an estimate for the binder jet process, highlighting the influence of binder composition on wetting and infiltration, in this case showcasing that high copper nanoparticle solid loading in the ink decreases wettability, reduces penetration depth, and increases binder penetration time [101]. Colton and Crane explored the influence of droplet spacing and inter-arrival time on the formation of stable printed lines, showcasing that decreased droplet spacing and decreased printhead velocity increase line saturation [97]. Recently, Barui et al. used in-situ x-ray imaging to capture the wetting and infiltration of an inkjet ethylene glycol water solution into an alumina powder bed, showing the interrelation between spreading and infiltration and general consistency of the observed infiltration kinetics with a modified version of the Washburn equation [100]. The

Washburn equation is derived from the penetration of a liquid from a unlimited liquid reservoir into a cylindrical capillary pore in the absence of gravity:

$$L = \sqrt{\frac{\gamma r t cos(\phi)}{2\eta}} \tag{4.4}$$

where L is the penetration length/depth, r is the capillary pore radius, t is the penetration time, and ϕ is the contact angle between the solid capillary and penetrating liquid – Figure 4.2: depicts a graphical representation of the parameters for the Washburn equation [138]. The Washburn equation is commonly used to estimate capillary pore infiltration dynamics, including that of powder beds, with adaptations of the Washburn equation for capillaries modeled as a packed bed or powder surfaces requiring an additional constant to capture the effects of the different capillary geometry [138–144]. Rearranging the Washburn equation to determine the penetration/infiltration time:

$$t = \frac{2L^2\eta}{\gamma r cos(\phi)} \tag{4.5}$$

suggests a proportional relationship for infiltration time with viscosity and an inverse relationship with surface tension.

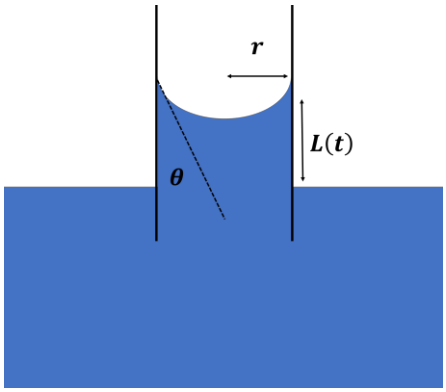

Figure 4.2: Schematic of variables for Washburn equation for the infiltration of capillary.

In addition to understanding binder-powder interactions, determining that a binder imparts sufficient green strength for removal and handling is critical for use in BJAM. Characterization of binder strength has been performed using compression tests [145], 3-point bending of printed or molded samples [123,146,147], and qualitatively estimated by

the ability to remove a fabricated sample from the build platform [80]. Compression testing, 3-point bending, and instrumented indentation have been used to explore the mechanical properties of partly sintered BJAM components [148]. Outside the field of AM, indentation experiments have been used to quantify the strength of binders for asphalt [149] and pharmaceutical compacts [150,151], thus suggesting the possible use of indentation to compare the green strength of binder-bound components and powder compacts.

In this work, a process for rapid binder exploration is introduced, summarized in Figure 4.3, that utilizes both established and custom yet straightforward lab-scale experiments to determine binder ink rheology, binder-powder interactions, and green strength. The process employs established rheological and thermal characterization methods, as well as AM-relevant jetting experiments to enable rapid exploration of different binder compositions and correlation of the influence of binder ink composition on ink utility for BJAM. Specifically for green strength, the use of indentation as a means to compare binder strength for polymer and metal salt binder ink systems is explored. This process is applied to the production of custom polymer and reactive metal salt binder inks, with jetting of <100 μm droplets, infiltration into metal and ceramic powder beds, and sufficient green strength for sample removal from surrounding excess powder.

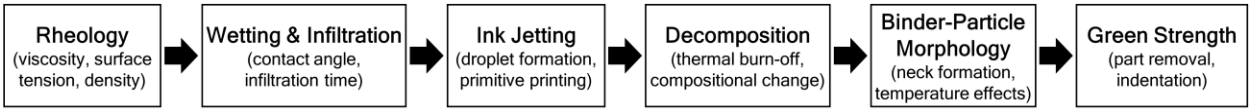

Figure 4.3: Development process for custom binders for BJAM.

4.2 Method

4.2.1 Ink formulation and synthesis

Eight different binder inks were synthesized for this study, two methacrylate-based (i.e., Acrysol) binder inks, three polyethylene glycol (PEG) based binder inks, and three

aluminum nitrate (metal salt) based binder inks. The compositions of each binder ink, with respective solvent and solid contents, are listed in

Table 4.1. The starting materials for the binder inks included deionized (DI) water, 200 proof ethanol (Sigma-Aldrich 459836), aluminum nitrate nonahydrate ≥98% (Sigma-Aldrich 237973), polyethylene glycol 1000 (Sigma-Aldrich 8.07488), polyethylene glycol 6000 (Alfa Aesar A1754130), polyethylene glycol 10000 (Sigma-Aldrich 8.21881), Triton-X 100 (Sigma-Aldrich X100), and Acrysol WS-24 (Dow Chemical Co.). PEG was selected as ethylene glycol monomers are commonly reported in binder jet literature [3,152,153]. Acrysol was selected as a binder because it was used in early research of BJAM, showcasing sufficient green strength for sample removal [14,154]. Finally, aluminum nitrate was selected as the reactive metal salt binder as it decomposes into aluminum oxide and has been previously used in simulated binder jet experiments [19]. To create each formulation, the solvent mixture was produced, then binder (i.e., PEG or aluminum nitrate) was added to the solvent mixture and dissolved using a vortex mixer (Four E's Scientific Digital Vortex Mixer) at 3000 rpm for 5 minutes.

Table 4.1: Composition of custom developed polymer and reactive binders.

Binder	**Solvent**	**Solids Content**
Acrysol 10%	DI water and ethanol (20% molar fraction ethanol)	10% mass fraction of Acrysol-WS 24
Acrysol 18%	DI water and ethanol (20% molar fraction ethanol)	18% mass fraction of Acrysol-WS 24
PEG 1K 10%	DI water and ethanol (20% molar fraction ethanol)	10% mass fraction of PEG 1000 (1K) to solvent
PEG 6K 10%	DI water and ethanol (20% molar fraction ethanol)	10% mass fraction of PEG 6000 (6K) to solvent
PEG 10K 10%	DI water and ethanol (20% molar fraction ethanol)	10% mass fraction of PEG 10000 (10K) to solvent
Al-Nit 1.5M W	DI water	1.5 molar concentration of aluminum nitrate
Al-Nit 1.5M WE	DI water and ethanol (50% volume fraction ethanol)	1.5 molar concentration of aluminum nitrate
Al-Nit 1.5M WX	DI water and Triton-X 100 (0.25% mass fraction Triton-X 100)	1.5 molar concentration of aluminum nitrate

4.2.2 Ink rheology

The viscosity of each binder ink was measured using a viscometer (Rheosense m-VROC) at shear rates of 5,000, 10,000, 25,000 and 50,000 1/s with temperature controlled between 26-27°C by a recirculating chiller (Solid State Cooling Systems ThermoCube). Surface tension measurements were performed using a tensiometer (DataPhysics DCAT 11) with Wilhelmy plate (DataPhysics PT 11, platinum-iridium, 10 mm length, 19.9 mm width, 0.2 mm thickness) using DCAT software for data collection, with ambient temperature between 22-23°C. Density measurements were performed using a 50 mL graduated cylinder (Karter Scientific, 1 mL graduations, +/-0.5 mL) and digital scale (Ohaus Corporation DV215CD, 0.01 mg resolution) at an ambient temperature of 20.6°C.

4.2.3 Wetting angle and powder infiltration of binder inks

Wetting angle and powder infiltration measurements were performed for all binder inks, following a similar procedure as Bai et al. [101], using a custom goniometer setup (Figure 4.4) consisting of an adjustable lab jack, a vertical mount, a micrometer dispenser (Gilmont GS-1200-A), and imaged using a USB CCD camera (Thorlabs High-Sensitivity USB 3.0 CMOS Camera) and optics (Thorlabs 6.5X Zoom Lens with 3 mm Fine Focus, 0.50X Extension Tube, C-Mount Adapter, and 2.0X Magnifying Lens Attachments, with 2.34 μm resolving limit at high magnification). The height of the droplet dispenser was set such that droplets were deposited on the substrates with minimal impact on the substrate during dispensing, the dispensing tip was between 4-5 mm from the surface. For solid substrates, an alumina disk (AdValue Technology, Al-D-42-2) and a polished stainless steel disk (McMaster Carr 9260K11) were used, wiped clean using isopropyl alcohol and DI water and dried after each droplet deposition. The surface roughness of the alumina disk and stainless steel disk were measured using a confocal microscope (Keyence VK-X1050), giving values of 2.43 μm Sa and 1.00 μm Sa respectively. To simulate a powder bed as would be found in BJAM, powder was spread manually into an aluminum plate substrate (McMaster Carr 8975K649, Al 6061), with two parallel sidewalls (a “track”) created using

adhesive tape (3.175 mm thick). Spreading was performed using a ¼-inch stainless steel rod (McMaster Carr 1327K65) in a single smooth motion. The powders used for this study were stainless steel (John Galt Steel, SS 316L, 15-45 µm) and alumina (Inframat Advanced Materials, 40 µm, 26R-8S40) and powder spreading was performed at ambient humidity of 25.2% and temperature of 21.3°C. These powder sizes were selected due to the simplicity of manual spreading using this powder size range. The wetting angle and infiltration measurements were captured by taking a video of the deposition and infiltration (for porous substrates) recorded at 15 fps, with each condition (binder ink and substrate) being repeated three times.

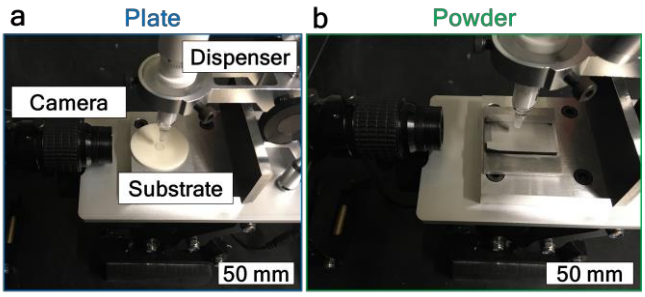

Figure 4.4: Wetting and infiltration experimental setup shown for: (a) solid substrate using the alumina disk; and (b) simulated powder layer using stainless steel powder.

The contact angle for all substrates was determined using Fiji/ImageJ with the Contact Angle plugin, after image sharpening (Sharpen, default) and edge finding (Find Edges, default). The Manual Points Procedure was used with five points used to define the droplet curvature, with the ellipse fit used for the contact angle. The contact angle for the solid substrates was measured at 30 frames after deposition of the droplet (2 seconds) to allow the contact angle to reach equilibrium. The contact angle on the porous substrates was taken one frame (67 ms) after droplet deposition on the powder bed (i.e., the second frame where the droplet is only in contact with the substrate), and the infiltration time was estimated to by the difference between frames where the droplet is formed on the substrate (i.e., liquid is no longer in contact with dispenser but only in contact with substrate) and where no perceivable fluid/motion is seen for the powder substrate.

To explore the infiltration depth and width of the binder inks, the spread powder layer samples with deposited binder-powder granules (i.e., the binder-bound powder aggregate fabricated via deposition of the binder via micrometer dispensing) were heated in air in a porcelain furnace (Pentron Laboratory Technologies, LLC JP 1200 Porcelain Furnace) for 30 minutes at 60 °C with a ramp rate of 5 °C /min to cure the binder. The granules were removed from the simulated layer after binder curing using plastic tweezers. Three granules were produced for each experimental condition and the dimensions of the granules were taken using a digital microscope (Zeiss Smartzoom 5).

Because the binder ink rheology affects the volume of the droplet dispensed from the micrometer dispenser for the wetting and infiltration studies, the volume of an individual droplet was estimated by measuring the mass of an individual droplet using the digital scale, with the mass measurement repeated five times for each binder ink. The individual droplet mass and binder ink density measurements were then used to calculate the dispensed volume for each binder ink. This volume was then used to normalize the infiltration time, granule dimensions, and binder strength as reported later. Furthermore, estimating the droplet as a sphere, the diameter can be determined – this diameter was used to normalize the diameter and thickness of the cured granule.

4.2.4 Thermal decomposition of binders

Thermal decomposition of the binders was performed using combined thermogravimetric analysis and differential scanning calorimetry (Mettler Toledo TGA/DSC1) in an alumina pan with vented cover (AdValue Technology, AL-6028 and AL-6504). Samples were run for PEG 1K, PEG 6K, PEG 10K, Acrysol solid, and aluminum nitrate nonahydrate with a ramp rate of 5 °C/min from 30 °C to 1100 °C in air. Additionally, x-ray diffraction (PANalytical X'Pert PRO XPRD) of aluminum nitrate samples was performed using as-received aluminum nitrate nonahydrate powder, aluminum nitrate nonahydrate heated up to 600 °C with a 1 hour hold and ramp rates of 5 °C/min in a tube furnace (Lindberg/Blue M STF55433C Tube Furnace) in air, and aluminum nitrate nonahydrate heated up to 1100

°C with a 1 hour hold and with ramp rates of 5 °C/min in the tube furnace in air. The reference XRD peak values were taken from the database from HighScorePlus software (Malvern Panalytical).

4.2.5 Inkjet printing of binder inks

Exploration of inkjetting was performed for all binder inks using a custom inkjet testbed (Figure 4.5) comprised of two linear translation stages with 50 mm travel distance (Thorlabs DDSM50/M) stacked in an X-Y configuration, a manual vertical stage with 13 mm travel distance (Thorlabs MVS005/M) for controlling nozzle-substrate distance, and an inkjet dispensing system consisting of a piezoelectric drive controller (Microfab JetDrive V, CT-M5-01), a 20 mL fluid reservoir, gas and fluid tubing (LeeCo MINSTAC tubing), a single piezoelectric dispensing nozzle (Microfab MJ-AT-01-xxx, where xxx dictates the nozzle diameter), and a digital pressure controller (APEX Vacuum LLC). The diameter of the droplet was set by the diameter of the dispensing nozzle (available from 20-80 μm orifice diameter; 80 μm was used in this study); the frequency of droplet ejection can be controlled up to 1 kHz; and the waveform sent to the piezoelectric dispenser can deliver up to 70V with dwell times up to 100s of μs. A vision system including a USB camera (Sentech STC-MB33USB), optics (Navitar 1.0X Adapter 1-61445, Navitar Precise Eye Body tube 1-61449, resolving limit of 4.76 μm), and a strobe LED (Microfab Technologies, Inc.) was used for droplet imaging. The strobe LED can be controlled to pulse at the same frequency as the piezoelectric actuator, with an additional pulse delay feature to capture droplets at different stages of jetting. A custom LabView program was used to control the ink jet testbed, with full authority over jetting position, nozzle traverse speed, jetting waveform parameters (e.g., voltage, frequency), and back pressure.

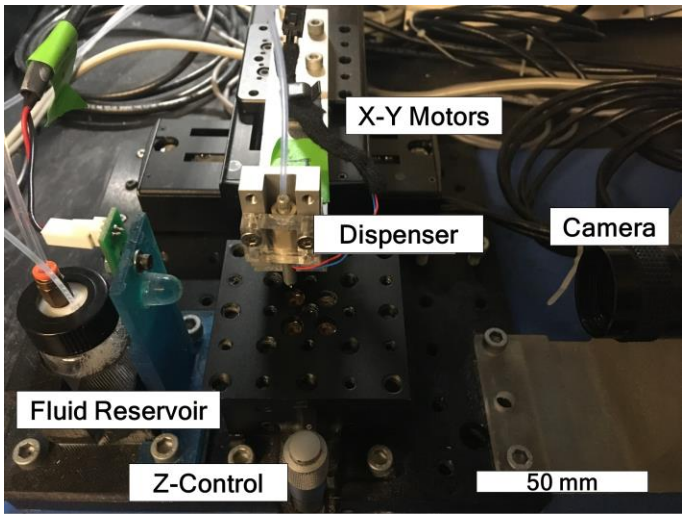

Figure 4.5: Image of custom inkjet testbed showing major components.

To determine jettability of the binder inks, jetting was attempted for each binder ink by setting the back pressure to establish a minimal meniscus at the nozzle tip and increasing jetting waveform dwell time and dwell voltage (rise/fall time held at 3µs) until jetting was achieved or the maximum 70V limit was reached for the dispenser. During this process, the nozzle tip was observed in real time through the vision system. For droplet diameter, five separate images at a 500 µs strobe delay were taken, where 0 µs corresponds to the initiation of the piezoelectric jetting pulse. To determine the droplet velocity, droplets were captured at 300, 400, and 500 µs, using the strobe delay feature, and the velocity was calculated as the distance traveled by the sequential droplets. Fiji/ImageJ was used to estimate both the droplet diameter and droplet velocity, with the image scaling based from the outer diameter of the nozzle, measured to be 600 µm using the digital microscope. For droplet diameter, the images were sharpened (Sharpen, auto), threshold (Auto), and the Particle Analysis tool was used to determine the droplet area, which provides an estimate of the diameter for an assumed spherical droplet. The position used for the velocity measurement for each strobe position was found using the centroid feature after particle analysis. For cases when satellite droplet formation occurred during jetting, an area averaged velocity calculation was performed to estimate the jetting velocity and for the case when jetting was not possible due to insufficient energy, the velocity was estimated

as by the farthest position of the forming droplet and the elapsed time (i.e., 100 μs for PEG 10K 10% binder).

Clogging of nozzles can be an issue for inkjet deposition, particularly when testing new binder ink formulations. To assess the propensity for clogging, after jetting was established for a given binder ink, jetting was paused for a given time interval (i.e., 10, 20, 30, 60 seconds). After the time interval, the same jetting waveform was sent to the dispenser and the vision system was used to visually determine if jetting re-occurred. If jetting did not occur, the nozzle was purged (increasing back-pressure to 30 psi) and returned to the backpressure of the previous jetting condition. The binder ink was determined to cause clogging if jetting did not occur after each set delay, and a note was made as to whether jetting was possible, with/without purge assistance.

4.2.6 Line formation and square sample fabrication

Using the inkjet setup, linear test patterns were printed with Acrysol 18%, PEG 6K 10%, Al-Nit 1.5M WE, and Al-Nit 1.5M WX inks. Lines were formed by varying the droplet spacing through controlling the droplet frequency, with the nozzle traverse speed held constant at 10 mm/s. Droplet spacing for the initial experiments included 10 μm, 20 μm, 40 μm, 60 μm, 80 μm, 100 μm, 120 μm, 140 μm, and 160 μm. Lines were printed on alumina powder layers with thickness 80 μm, 100 μm, and 160 μm, which were spread onto alumina disc plates (AdValue Technology, Al-D-42-2). The powder layer thickness was set by building 'rails' of kapton tape on the disc, and manual spreading of the powder performed using a stainless steel rod in a single smooth motion. The thickness of the powder layers was measured using a 2D laser profiler (Keyence LJ-V7060) before and after manual spreading of the powder, with average layer thickness of 82.2 ± 11.3 μm for the 80 μm layer, 106.3 ± 8.0 μm for the 100 μm layer, and 150.9 ± 26.5 μm for the 160 μm layer.

Inkjet deposition of binder inks onto the powder layers on alumina substrates therefore serves as a rapid experimentation tool for binder-powder interaction and feature

definition. After deposition of the binder ink, the powder-coated alumina substrates with the printed lines were cured in the porcelain furnace for 30 minutes at 60°C in air. Removal of excess power was performed by turning the printed sample upside down and lightly tapping the alumina disc with the stainless steel rod - qualitatively, this procedure removed excess powder and removed printed lines that did not exhibit sufficient adhesion strength to the substrate and would thus possibly not adhere to layer below in a 3D binder jetting process. Visual analysis of printed lines showed which droplet spacing created partial or full lines, and these droplet spacing conditions (i.e., 10 μm, 20 μm, 40 μm or 10 μm, 20 μm depending on the binder) were used to print three lines for each droplet spacing on an alumina disc with a 100 μm powder layer height. Binder curing and excess powder removal was performed following the same procedure as the previous line printing experiments, with imaging of the printed lines performed using the digital microscope to determine the printed line width.

To investigate formation of raster patterns into layers and examine the evolution of binder-particle morphology with temperature, 5 mm X 5 mm square designs were printed using Acrysol 18%, PEG 6K 10%, Al-Nit 1.5M WE, and Al-Nit 1.5M WX binder inks for a manually spread 100 μm layer height of alumina powder, with 10 μm droplet spacing, 240 μm line spacing, and 10 mm/s translation speed. All printed samples underwent the same curing and powder removal process as the line samples described above. Additionally, to explore the effect of thermal decomposition on the binders and powders of the printed squares, samples were heated to 600 °C for 1 hour in air with a 5 °C/min ramp rate, and separate samples additionally heated to 1100 °C for 1 hour in air in the porcelain furnace. For SEM imaging, printed square samples that had undergone different thermal treatments were coated with gold (~8 nanometers thickness, Quorum Technologies SC7640 Sputter Coater, 60 second coating time), then imaged via SEM (JEOL JSM-6010LA) at 10kV.

4.2.7 Indentation experiments for relative binder strength

Mechanical indentation of binder-infiltrated powder volumes was used as a proxy for green strength. To fabricate the binder-infiltrated powder volumes, cylindrical well molds for manual indentation of green parts were fabricated from 2.5mm thickness tight tolerance stainless steel (McMaster Carr 2953N116) with five 5 mm diameter thru-holes (drilled, then reamed using a 5mm cobalt steel round-shank reamer, McMaster Carr 2735A18) and bolted to a stainless steel substrate (McMaster Carr 2953N127). The individual cylindrical well dimensions (5.0mm diameter X 2.5mm thickness, 49.1 mm^3) were selected to be slightly smaller than the average granule size for the alumina samples fabricated through micrometer dispensing on the simulated powder layer (5.3 ± 0.6 mm diameter X 2.6 ± 0.4 mm thickness, ~56.4 mm^3) to ensure full infiltration of the binder ink into the powder well samples. The dimensions of the wells were confirmed using a digital caliper (Mitutoyo CD-8''-CS), with average dimensions of 4.98 ± 0.02 mm diameter X 2.50 ± 0.01 mm thickness. Alumina powder was deposited into the each well by manually spreading using a razor blade (Personna GEM 62-0178); excess powder around the well was removed using a brush. To estimate the powder bed density of the filled wells, the mass of the five-well sample holder was taken before and after filling with powder, assuming equivalent powder bed density for all wells, with an average mass per well of 107.21 ± 0.36 mg. Using the average mass per well, average well dimensions, and the supplier value for the alumina powder theoretical density (3.97 g/cm^3), the packing density within each well was estimated to be ~55%, thus within the range of BJAM experiments.

After powder deposition, the binder inks (Acrysol 10%, Acrysol 18%, PEG 1K 10%, PEG 6K 10%, PEG 10K 10%, Al-Nit 1.5M WE, Al-Nit 1.5M WX) were deposited into each well using the micrometer dispenser. To ensure adequate evaporation of the solvent, the samples were allowed to dry overnight between 21°C at 10.0% humidity in a controlled lab environment. The binder was then cured in air at 60°C for 30 minutes by placing the plate into the porcelain furnace. Additionally, for the Acrysol 18%, PEG 6K 10%, Al-Nit 1.5M WE, and Al-Nit 1.5M WX binder inks, separate samples were heated to 600°C for 1 hour with a ramp rate of 5°C/min to explore the strength after binder decomposition. Further, to make an equivalent strength measurement for binders with the

same solids content, an additional aluminum nitrate nonahydrate binder ink with 10% solid loadings in content by weight with DI water and ethanol (50% volume fraction ethanol) as the solvent was made for testing.

Figure 4.6 shows the fabricated well substrates and the subsequent process of powder spreading, binder deposition, and indentation testing. A force gauge (Nextech DFS100 with 100N capability and 0.2% accuracy, Nextech DFS500 with 500N capability and 0.2% accuracy) with a conical frustum tip geometry (contact diameter of 1514 μm and 60° cone angle, measured using digital microscope) was manually lowered onto the bound powder wells using a manual force test stand with digital displacement scale (Boshi Electronic Instruments). Indentation was performed to a depth of 1 mm, with an indentation velocity of approximately 0.1 mm/s. The indentation strength of the powder and green components was taken as the maximum force experienced by the force gauge. Additionally, samples from the as-deposited and 600°C indentation samples were prepared for SEM and imaged via the procedure noted above.

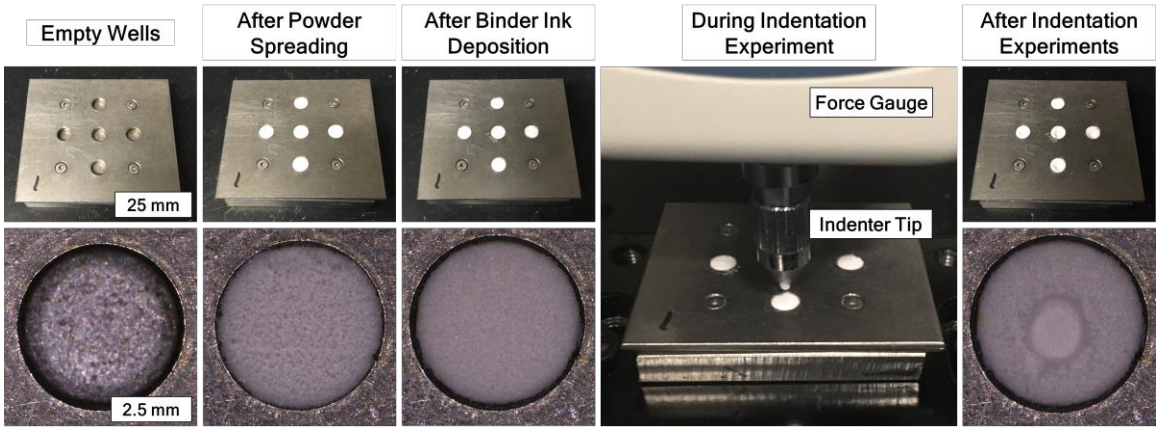

Figure 4.6: Green strength indentation sample wells and experimental sequence shown for alumina powder and PEG 6K 10% binder ink.

4.3 Results and discussion

4.3.1 Rheology and jetting

First, measurements of viscosity and surface tension of candidate binder inks were used to assess their suitability for inkjet printing according to the guidance of Derby et al [126,137]. The measured rheology, including viscosity (shear rate of 25,000 1/s used as a close approximation of the shear rate experienced for our inkjet conditions with an 80 μm nozzle and jetting speeds of ~2m/s), surface tension, density, jetting droplet diameter and jetting droplet velocity are shown in Table 4.2. The calculated Reynolds, Weber, Ohnesorge numbers and Z parameter are shown in Table 4.3. The surface tension and viscosity of the binder inks, along with whether the inks resulted in good, bad, or no jetting, are plotted in Figure 4.7a. Using the calculated Weber and Reynolds number, along with the jetting regimes described by Derby, and Liu and Derby [126,137], the custom developed binder inks are plotted on a printability map shown in Figure 4.7b. The Acrysol 10%, Acrysol 18%, PEG 1K 10%, PEG 6K 10%, and Al-Nit 1.5M WE binder inks fall within the printability regime. The Al-Nit 1.5M WX binder ink lies on the boundary of printability, satellite droplet formation, and insufficient energy for droplet formation. The Al-Nit 1.5M W binder ink lies in the satellite droplet formation region and the PEG 10K 10% binder ink lies in the insufficient energy for droplet formation region.

Table 4.2: Summary of rheological data for custom developed binder inks.

Binder	**Surface Tension (mN/m)**	**Viscosity (cP) 25,000 1/s shear rate**	**Density (g/cm^3)**	**Droplet Diameter (µm)**	**Droplet Velocity (m/s)**
Acrysol 10%	32.61 ± 0.01	4.39 ± 0.03	1.15 ± 0.01	61.2 ± 0.7*	2.4 ± 0.6
Acrysol 18%	31.22 ± 0.02	7.20 ± 0.05	1.14 ± 0.01	49.0 ± 0.5	1.7 ± 0.3
PEG 1K 10%	31.63 ± 0.03	3.50 ± 0.19	0.94 ± 0.01	51.5 ± 0.5	1.5 ± 0.3
PEG 6K 10%	31.51 ± 0.03	6.82 ± 0.19	0.94 ± 0.01	60.0 ± 1.6	2.2 ± 0.0
PEG 10K 10%	31.58 ± 0.03	12.48 ± 0.10	0.95 ± 0.01	80**	1.1 ± 0.0**
Al-Nit 1.5MW	65.93 ± 0.01	2.28 ± 0.01	1.16 ± 0.01	71.1 ± 3.5*	2.9 ± 0.1
Al-Nit 1.5MWE	34.38 ± 0.02	6.48 ± 0.02	1.12 ± 0.01	64.0 ± 0.3	1.7 ± 0.1
Al-Nit 1.5MWX	33.96 ± 0.01	2.27 ± 0.06	1.17 ± 0.01	57.7 ± 0.3	1.5 ± 0.8
*Droplet diameter and velocity calculated using weighted areal average due to satellite droplet formation **Droplet diameter estimated at nozzle diameter and droplet velocity calculated using distance of partly formed droplet due to no droplet ejection					

Table 4.3: Summary of calculated rheological data and jetting waveforms for custom developed binder inks.

Binder	Reynolds Number	Weber Number	Ohnesorge Number	Z	Jetting Waveform	
					Voltage (V)	*Dwell Time (μs)*
Acrysol 10%	38.5	12.4	0.09	10.9	40	20
Acrysol 18%	13.2	5.2	0.17	5.8	40	20
PEG 1K 10%	20.7	3.4	0.09	11.2	40	20
PEG 6K 10%	18.2	8.7	0.16	6.2	65	20
PEG 10K 10%	6.7	2.9	0.25	3.9	70	20
Al-Nit 1.5M W	104.9	10.5	0.03	32.3	40	20
Al-Nit 1.5M WE	18.8	6.0	0.13	7.7	65	20
Al-Nit 1.5M WX	38.5	12.4	0.09	10.9	65	20

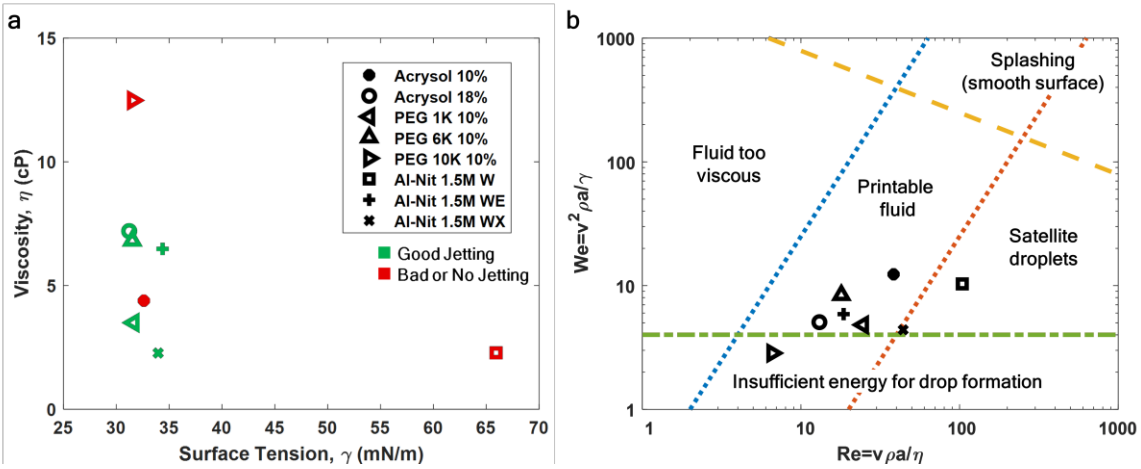

Figure 4.7: Summary of rheology for binder inks, showing (a) surface tension and viscosity for binder inks and observed jetting condition and (b) comparison of inkjet printability using non-dimensional (Reynolds and Weber) numbers for custom developed polymer and reactive binder inks.

The jetting conditions for each binder ink, as determined using the inkjet printing setup and vision system, and the results of the clogging study are shown in Table 4.4. Images of exemplary cases of good jetting ("printable fluid"), satellite droplet formation, and insufficient energy for drop formation are shown in Figure 4.8. Generally, there is good agreement between the printability map and the observed jetting conditions, as Acrysol 18%, PEG 1K 10%, PEG 6K 10%, Al-Nit 1.5M WE, and the Al-Nit 1.5M WX (borderline case) result in single droplet formation, as shown Figure 4.8. Additionally, the Al-Nit 1.5M W binder ink, due to high surface tension, results in satellite droplets similar to Figure 4.8, and the PEG 10K 10% binder, due to a high viscosity resulting in a low imparted velocity, cannot be ejected from the nozzle as seen in Figure 4.8. Interestingly, despite appearing in the printable region, the Acrysol 10% binder ink results in satellite droplet formation during jetting. This is possibly due to a difference in the equilibrium surface tension of the fluid (measured using the tensiometer) and the formation of surface tension gradients in the Acrysol 10% fluid during jetting due to the use of surfactants to form the Acrysol binder emulsion and the reduction of viscosity due to heavy dilution from the as-received condition (36% solids content) to the developed ink (10% solids content). Prior research has shown that kinetics of interfacial tension for surfactants can be slow and result in different surface tension values as the surfactant migrates to the newly created surface during fluid mixing and ejection [155,156].

Table 4.4: Jetting conditions and results of clogging experiments for custom binder inks.

Binder	**Jetting Condition**	**Clogging Time (Purge Clears)**
Acrysol 10%	Satellite droplets	N/A
Acrysol 18%	OK – single droplet	5 seconds, purge clears
PEG 1K 10%	OK – single droplet	30 seconds, purge clears
PEG 6K 10%	OK – single droplet	30 seconds, purge clears
PEG 10K 10%	No jetting	N/A
Al-Nit 1.5M W	Satellite droplets	N/A
Al-Nit 1.5M WE	OK	No clogging at 60 seconds
Al-Nit 1.5M WX	OK	No clogging at 60 seconds

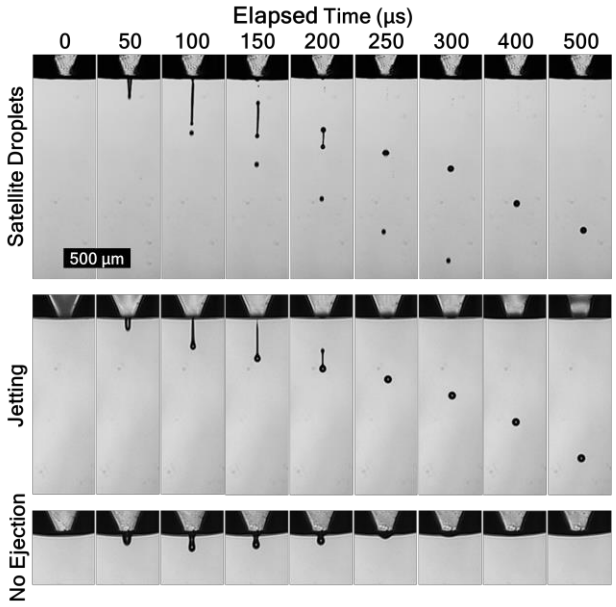

Figure 4.8: Exemplary images of ink jet sequences for: (top) formation of satellite droplets shown with Acrysol 10% binder ink; (center) good jetting through single droplet formation shown for PEG 6K 10% binder ink; and (bottom) insufficient energy for droplet formation shown for PEG 10K 10% binder ink.

Further, for the metal salt reactive binder inks, the use of a co-solvent (i.e., ethanol) or a surfactant (i.e., Triton-X 100) can reduce the surface tension of a fluid (i.e., DI water) to enable jetting of the ink. With the polymer PEG binders, increasing the molecular weight (MW) of the binder ultimately results in the viscosity being too high for jetting, specifically for the PEG 10K 10% binder ink. The longer polymer chains (higher molecular weight) entangle more in the solvent, increasing the viscosity and required energy for motion of the liquid and separation of the drop from the nozzle. Prior work has also shown that in addition to molecular weight, the solids concentration of the binder will directly influence viscosity [157,158], as is also the case for the Acrysol 10% and Acrysol 18% binders, so it is possible that a lower concentration of PEG 10K would exhibit good jetting behavior.

From the clogging study, shown in Table 4.4, the Acrysol 18% binder ink clogs after 5 seconds and requires a purge to re-establish jetting. This is likely due to solvent evaporation, and formation of an insoluble methacrylate film after breakdown of the Acrysol emulsion at the nozzle tip. PEG 1K 10% and PEG 6K 10% also require a purge to

re-establish jetting conditions after 30 seconds, similarly due to formation of a PEG film at the nozzle. Clogging did not occur for either aluminum nitrate ink after 60 seconds – with 60 seconds approximating the inactive period of an inkjet system used in BJAM during the powder spreading phase of the process [159].

4.3.2 Droplet wetting and infiltration (depth/width/time)

Exemplary results for the wetting angle on solid substrates (alumina disc) and infiltration into an alumina powder bed are shown in Figure 4.9 for two different binder inks (Al-Nit 1.5M W and Al-Nit 1.5M WE). Wetting angle and infiltration time into the powder bed are affected by the rheology of the ink composition, for instance shown by the high wetting angle of the Al-Nit 1.5M W binder ink on the alumna disc (74.3 ± 2.9°) and lack of infiltration into the alumina powder layer when compared to the Al-Nit 1.5M WE binder ink with increased viscosity and reduced surface tension resulting in a lower contact angle on the solid alumina substrate (37.3 ± 1.5°) and enabled infiltration into the alumina powder layer.

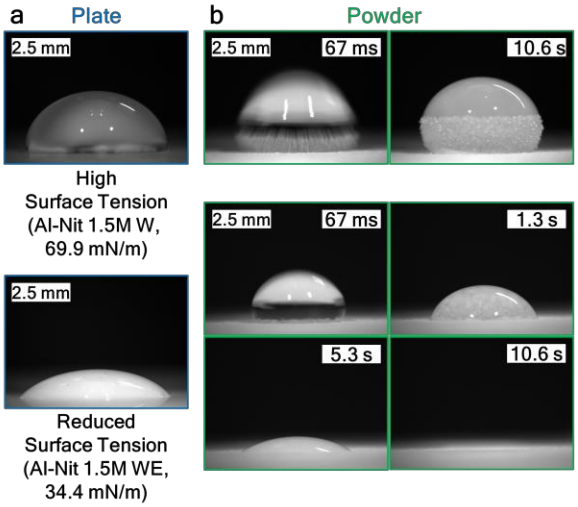

Figure 4.9: Exemplary images of high surface tension (Al-Nit 1.5M W) and reduced surface tension (Al-Nit 1.5M WE) binder inks: (a) wetting angle on a solid substrate (alumina disk); and (b) infiltration experiments on porous substrate (alumina powder).

The relationships between the normalized infiltration time (i.e., the infiltration time divided by the average droplet volume for a specific binder ink) and fluid properties of the binder inks deposited on alumina and stainless steel powders are shown in Figure 4.10a. As predicted by the Washburn equation, a decrease in normalized infiltration time occurs with increasing surface tension and decreasing viscosity. The Al-Nit 1.5M WX, which utilizes a surfactant as a rheological modifier to enable jetting and infiltration into the powder bed by reducing the surface tension of the parent fluid (i.e., DI water), results in higher-than-expected infiltration time, shown in Figure 4.10a. The infiltration time of the Al-Nit 1.5M WX is possibly affected by a change in the ink composition as infiltration occurs due to the kinetics of surfactant motion in the fluid and its interactions with the powder particles, that is - surfactant is used to enhance wetting at the start of infiltration and remains at the initial powder particles and thus less surfactant is available to assist with infiltration as the ink progresses deeper into the powder bed [141].

The normalized infiltration time is plotted against the contact angle of the solid substrates and the initial contact angle on the powder substrates in Figure 4.10b. The initial contact angle on the powder substrates gives strong indication of infiltration time, regardless of material, with increasing contact angle resulting in longer infiltration time, while the contact angle on solid substrates (i.e., disks) does not provide a clear indication of infiltration time. This is consistent with the mechanics of wetting and infiltration as a higher contact angle suggests poor spreading (wetting of external surface) between the ink and substrate (i.e., powder) such that a long time will be required for spreading of the ink, and additionally, the infiltration (wetting of internal surfaces) also requires a low contact angle, thus a high contact angle results in a long time for infiltration [141].

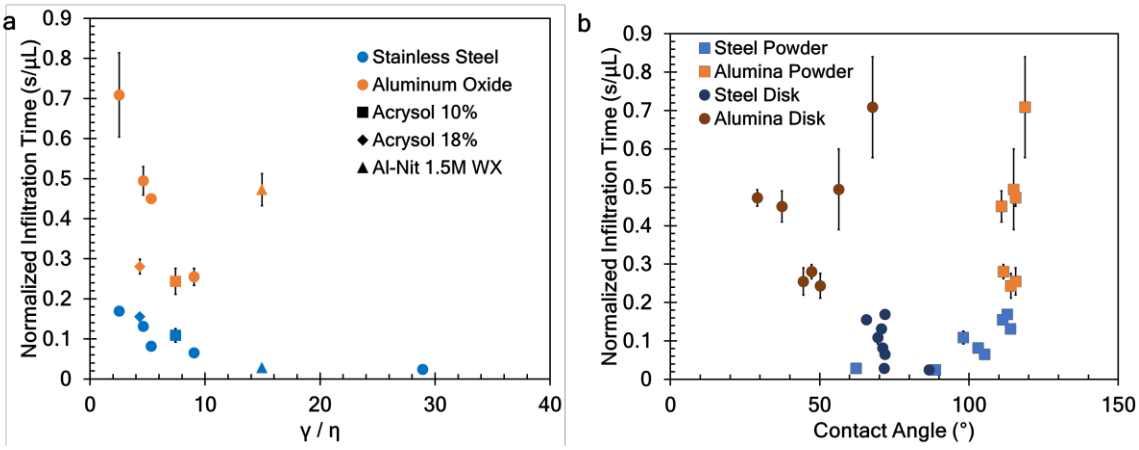

Figure 4.10: (a) Normalized infiltration time for micrometer dispensed binder inks on stainless steel and alumina porous substrates plotted against surface tension-to-viscosity ratio. (b) Normalized infiltration time for micrometer dispensed binder inks on stainless steel and alumina porous substrates plotted against contact angle of the inks on solid and porous substrates.

Next, the ability of the binder to form millimeter-scale powder aggregates was assessed using the micrometer dispenser deposition method for each powder, as shown in Figure 4.11. Table 4.5 summarizes whether successful removal of a contiguous granule was achieved, as well as the normalized granule diameter and thickness for the alumina powder granules. The PEG 1K 10% binder ink granules fractured during removable from the powder bed, suggesting that the PEG 1K binder does not supply enough green strength to the powders for BJAM applications. However, the other higher molecular weight PEG binders are removable, correlating with the increase in mechanical strength of polymers with increasing molecular weight [160]. Generally, an inverse correlation between normalized granule diameter and normalized thickness for different binder inks occurs, such that infiltration depth is sacrificed for larger spreading diameters, and higher loading concentration of polymer solids results in reduced infiltration depth (normalized thickness) due to increased binder ink viscosity. An interesting note is that all normalized thicknesses are <1, suggesting that for a single droplet, if inter-layer adhesion is desirable, then the layer height must be smaller than the ink droplet diameter – this was also found by Bai et al. for a polymer binder and copper powder in BJAM [101]. However, the micrometer

dispenser droplet method does not incorporate the inertial effects from the kinetic energy of the ejected droplet from a nozzle, nor the influence of multiple droplets stitched together, thus infiltration depth via inkjet is expected to be greater than the estimate provided by the granules.

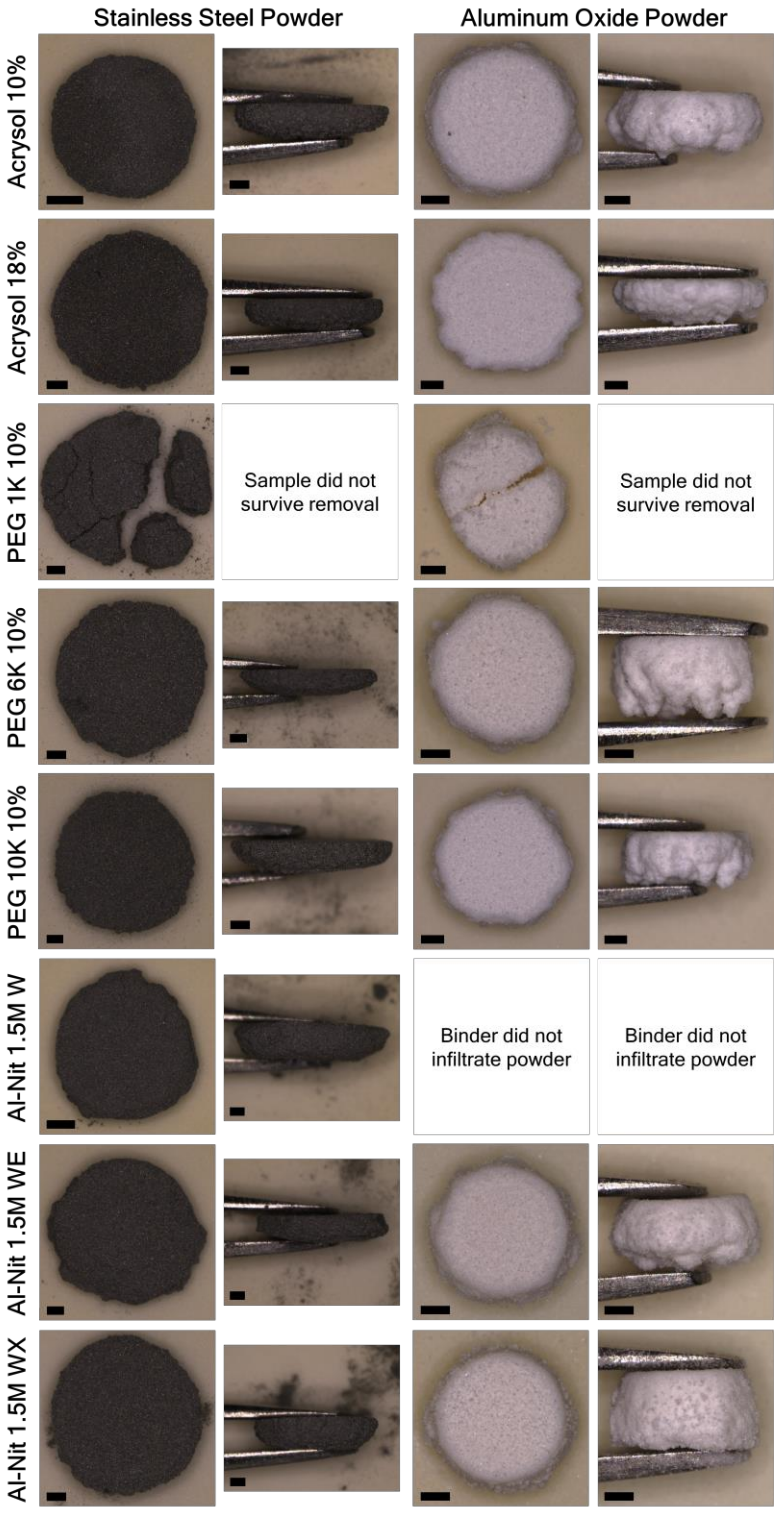

Figure 4.11: Images of stainless steel and alumina granules removed from simulated powder layers after deposition of binder inks via micrometer dispensing and curing (scale bars 1 mm).

Table 4.5: Summary of data for micrometer dispensed binder ink granules on alumina powder, highlighting removal from powder bed and normalized diameter and thickness of granules.

Binder	Removal (alumina)	Normalized Diameter (alumina)	Normalized Thickness (alumina)
Acrysol 10%	Yes	1.84 ± 0.14 mm	0.89 ± 0.07
Acrysol 18%	Yes	2.09 ± 0.16 mm	0.69 ± 0.05 mm
PEG 1K 10%	No	N/A	N/A
PEG 6K 10%	Yes	1.31 ± 0.08 mm	0.75 ± 0.04 mm
PEG 10K 10%	Yes	1.54 ± 0.06 mm	0.68 ± 0.05 mm
Al-Nit 1.5M W	No	N/A	N/A
Al-Nit 1.5M WE	Yes	1.40 ± 0.07 mm	0.83 ± 0.08 mm
Al-Nit 1.5M WX	Yes	1.53 ± 0.06 mm	0.86 ± 0.03 mm

4.3.3 Effect of jetting parameters

Although the dispensing of millimeter-scale ink droplets can provide some guidance on wetting, infiltration, and binder strength, the procedure is not fully representative of the powder-binder interactions that occur in ink jetting. Figure 4.12a shows the custom inkjet testbed during a printing experiment, along with printed line and square samples using the alumina powder at 100 μm layer thickness and the PEG 6K 10% binder ink. In Figure 4.12d, the trio of lines for each droplet spacing (10 μm, 20 μm, 40 μm) for the PEG 6K 10% binder ink show the printing of partial lines for larger spacings (40 μm), and full lines of increasing line width for the smaller droplet spacings (20 μm and 10 μm). The line widths for all full lines printed using the inkjet binder inks are listed in Table 4.6.

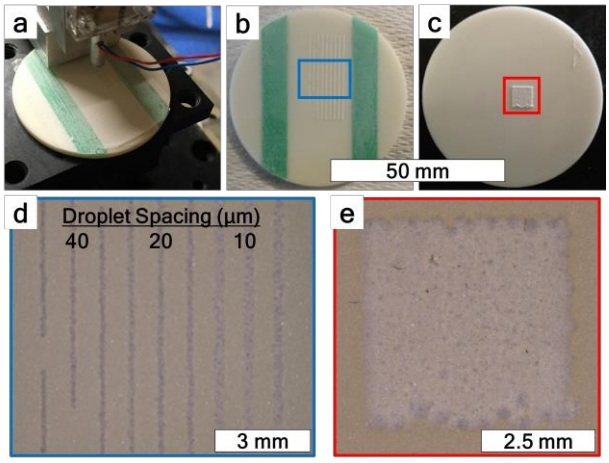

Figure 4.12: Exemplary images of single-layer binder jet experiments, showing: (a) custom inkjet setup during singe-layer binder jet experiments; (b) fabricated primitive lines for PEG 6K 10% binder ink and 100 µm layer height of alumina powder; (c) fabricated 5mm X 5mm square of PEG 6K 10% binder ink and 100 µm layer height of alumina; (d) magnified image of primitive lines showing increasing line width and adhesion to substrate with decreasing droplet spacing; and (e) magnified image of printed square sample highlighting printing defects at the boundaries of the print.

Table 4.6: Summary of line widths created for different inkjet droplet spacing for increasing layer heights.

Binder	**Droplet Spacing (µm)**	**Layer Height (µm)**		
		80	***100***	***160***
Acrysol 18%	*40*	Partial	None	None
	20	191 ± 3	Partial	None
	10	258 ± 4	246 ± 10	Partial
PEG 6K 10%	*40*	176 ± 2	Partial	None
	20	228 ± 2	226 ± 7	Partial
	10	295 ± 18	282 ± 5	250 ± 8
Al-Nit 1.5M WE	*40*	None	None	None
	20	223 ± 14	Partial	None
	10	313 ± 14	316 ± 2	None
Al-Nit 1.5M WX	*40*	None	None	None
	20	250 ± 14	243 ± 9	None
	10	328 ± 53	332 ± 8	None

Table 4.7 summarizes the droplet spacing that resulted in full or partial (P) lines for each binder at the different powder layer heights. Interestingly, the PEG 6K 10% results in the deepest penetration and most successful printed lines – attributed to the fastest droplet velocity (observed by the vision system) of the inkjet binder inks enabling deepest layer penetration. The Acrysol 18%, Al-Nit 1.5M WE and Al-Nit 1.5M WX binder inks result in full line prints for the 100 µm layer at 10 µm droplet spacing and partial lines at 20 µm droplet spacing. Despite the layer thickness being greater than the droplet diameter for all cases, there is successful printing of primitive lines for these binders, showcasing that the inertial effects of droplet velocity and the coalescence of adjacent droplets result in deeper relative penetration than predicted by the micrometer dispensing method.

Table 4.7: Summary of droplet spacing for binder inks that resulted in full or partial (P) printed primitive lines for increasing powder layer heights.

Binder	**80 µm layer height**	**100 µm layer height**	**160 µm layer height**
Acrysol 18%	10 µm, 20 µm, 40 µm (P)	10 µm, 20 µm (P)	10 µm (P)
PEG 6K 10%	10 µm, 20 µm, 40 µm, 60 µm (P)	10 µm, 20 µm, 40 µm (P)	10 µm, 20 µm (P)
Al-Nit 1.5M WE	10 µm, 20 µm (P)	10 µm, 20 µm (P)	None
Al-Nit 1.5M WX	10 µm, 20 µm	10 µm, 20 µm	None

Figure 4.12e shows an exemplary square print of PEG 6K 10% binder ink onto a 100 µm powder layer, with 10 µm droplet spacing, 240 µm line spacing, and 10 mm/s jetting translation speed. The jagged boundary at the top and bottom of the square suggest sub-optimal printing conditions for feature resolution, possibly resulting from excessive binder volume resulting in bulging (droplet spacing too small) or irregular nozzle conditions at the beginning of inkjet deposition that result in irregular binder droplets being ejected prior to normalization of the nozzle surface. Despite these shortcomings, the printed square samples showcase the ability of the selected binders to fabricate sample layers through stitching of primitive line prints.

4.3.4 Binder decomposition

Next, the thermal decomposition of the binder was assessed to determine the prospective ability to retain strength during early stages of sintering and the residue left behind after the decomposition process. The TGA data for the various binders used in this study is shown in Figure 4.13a. The polymers (i.e., PEG 6K, PEG 10K, and Acrysol) show loss of virtually all mass (0.0% PEG 6K, 0.2% PEG 10K, 0.5% Acrysol) by 600°C, although the majority of mass loss occurs between 360-400°C. This kind of polymer binder burnout is excellent if the goal is to prevent contamination of the powder during sintering, however it would provide little strength for materials with high sintering temperatures as is the case for refractory metals and ceramics, thus necessitating the use of support setting to prevent warping depending on part size and geometry. In contrast, although the aluminum nitrate

begins to decompose near 180 °C, 14.5% of the material mass remains at 600 °C and 13.1% of material mass remains at 1100 °C – this remaining material may provide continued strength during sintering of metals or ceramics to mitigate warping.

The evolution of the aluminum nitrate into aluminum oxide with temperature is shown by the XRD data in Figure 4.13b. The as-received aluminum nitrate nonahydrate shows the identifiable peaks for that material, however after heating to 600°C, no peaks in the XRD data occur suggesting the aluminum nitrate has decomposed into an amorphous aluminum oxide phase. Finally, after heating to 1100°C, the XRD peaks for alpha-phase aluminum oxide are visible. The thermal decomposition of aluminum nitrate into amorphous alumina and subsequently alpha alumina is congruent with other investigations that synthesize aluminum oxide from the nitrate precursor [161,162].

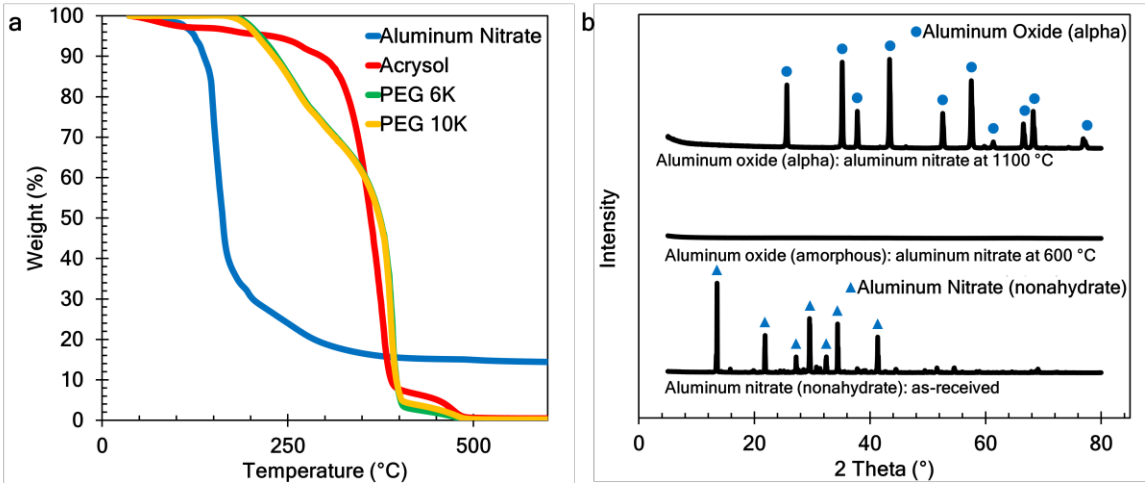

Figure 4.13: (a) Thermal decomposition of polymer (i.e., Acrysol and PEG) and aluminum nitrate binders up to 600 °C. (b) XRD data for aluminum nitrate nonahydrate powder in the as-received condition, after heating 600°C resulting in conversion to amorphous alumina, and after heating to 1100°C and conversion to alpha-phase alumina.

4.3.5 Binder neck formation on particles

Understanding of binder decomposition is complemented by visualization of the binder-powder neck formation by SEM, as shown in Figure 4.14. In the as-deposited condition inter-particle binder necks are observed in all cases, with more visible cracking for the aluminum nitrate binders, due to the brittle nature of the metal salts. After heat treatment at 600°C, binder necks are no longer identifiable for the polymer binders suggesting (in combination with TGA data above) minimal green strength, but necks are visible for the aluminum nitrate binders with additional cracking resulting from the metal salt decomposition. After heat treatment to 1100°C, the polymer binder samples did not survive preparation for the SEM, suggesting that all green strength had been lost. However, for the metal salt binders at 1100°C, material remains at the inter-particle necks, suggesting strength is retained at elevated temperatures.

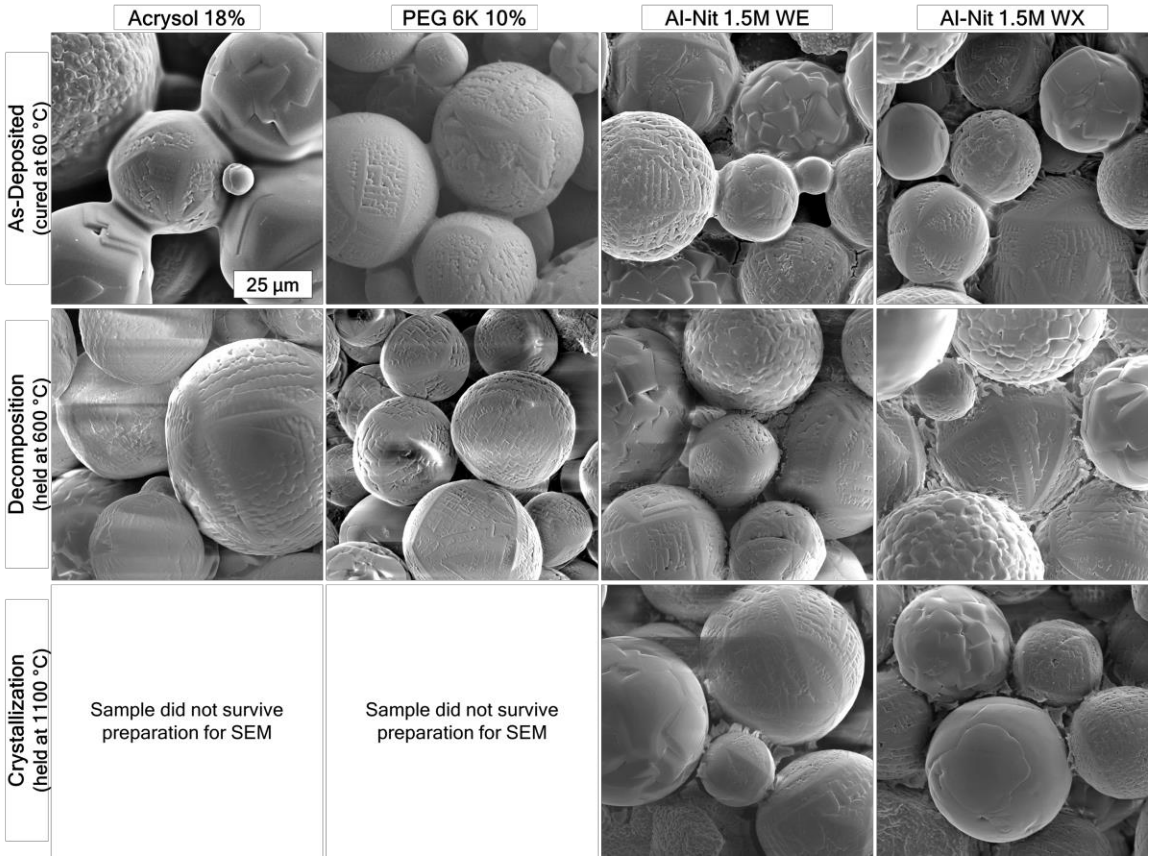

Figure 4.14: SEM showing progression binder-particle neck for inkjet deposited binders on alumina powder at different stages of thermal decomposition (i.e., as-deposited, after 600 °C, after 1100 °C) for: Acrysol 18%; PEG 6K 10%; Al-Nit 1.5M WE; and Al-Nit 1.5M WX.

4.3.6 Binder strength

Last, indentation experiments are performed on bound powders, constrained in millimeter-scale wells, as a further proxy for green strength in BJAM. The normalized indentation force for the samples is shown in Figure 4.15. The baseline case of powder without binder shows zero indentation force, with non-zero force for all cured binders. Acrysol 18% shows the greatest indentation force of all the binder inks – this is consistent with the higher strength of PMMA compared to PEG [130]. Additionally, an increase in indentation force

is measured with increasing polymer molecular weight for the PEG binder inks and increasing solid loading content for the Acrysol binder inks. The Al-Nit 1.5M WE and Al-Nit 1.5M WX have comparable strength to the Acrysol 10%. The aluminum nitrate binder ink with 10% solid loading content showcases superior strength to the PEG binders, but only 64% that of the Acrysol 10% binder. After heating to 600°C, no indentation force (0N) is found for the polymer binders (PEG and Acrysol) an indentation force remains for the aluminum nitrate binders (17% of as-deposited for Al-Nit 1.5M WE and Al-Nit 1.5M WX, respectively), confirming that strength is retained in the green component through elevated temperature treatment for the reactive binders. Further, using the dimensions of the indenter tip (1514 μm diameter), we estimate an indentation strength for the binders, summarized in Table 4.8, with an approximate green strength of 3.8 ± 0.3 MPa for PEG 6K, 12.7 ± 0.2 MPa for Al-Nit 1.5M WE, 2.2 ± 0.6 MPa for Al-Nit 1.5M WE after decomposition at 600°C, and 17.5 ± 0.1 MPa for Acrysol 18%.

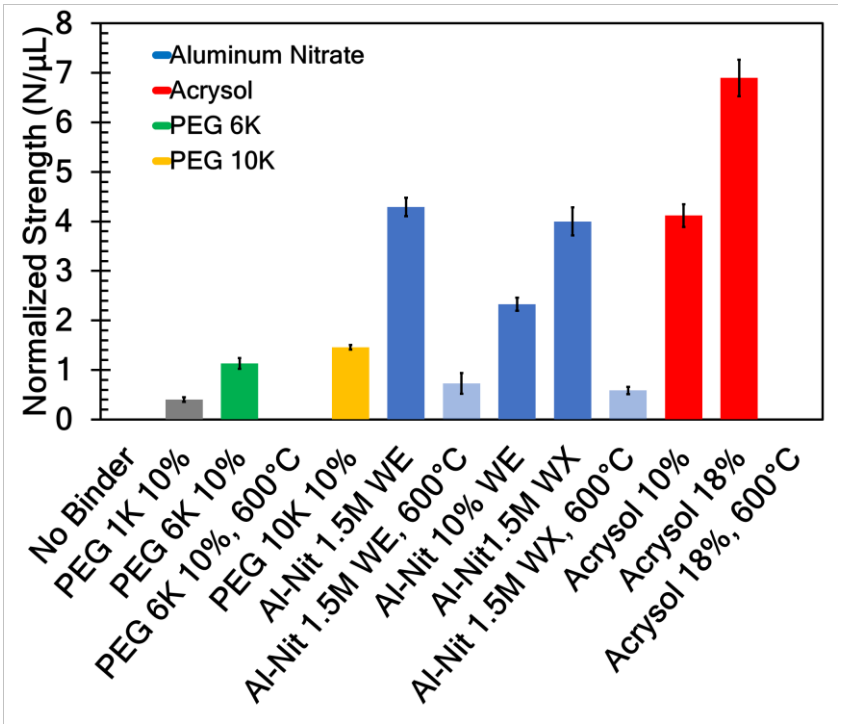

Figure 4.15: Normalized strength of binder inks deposited through micrometer dispensing into powder well samples in cured and decomposed conditions.

Table 4.8: Summary of indentation force and indentation strength different binder composition and thermal conditions.

Binder	Indentation Force (N)	Indentation Strength (MPa)
No binder	0.0	0.0
Acrysol 10%	80.0 ± 3.6	11.1 ± 0.5
Acrysol 18%	126.3 ± 0.7	17.5 ± 0.1
Acrysol 18%, 600°C	0.0	0.0
PEG 1K 10%	9.3 ± 0.9	1.3 ± 0.3
PEG 6K 10%	27.2 ± 2.2	3.8 ± 0.3
PEG 6K 10%, 600°C	0.0	0.0
PEG 10K 10%	35.3 ± 0.7	4.9 ± 0.1
Al-Nit 1.5M WE	91.3 ± 1.7	12.7 ± 0.2
Al-Nit 1.5M WE, 600°C	15.5 ± 4.4	2.2 ± 0.6
Al-Nit 1.5M 10% WE	51.8 ± 2.5	7.2 ± 0.3
Al-Nit 1.5M WX	79.6 ± 5.0	11.0 ± 0.7
Al-Nit 1.5M WX, 600°C	11.7 ± 1.4	1.6 ± 0.2

Visualization of the binder-powder neck formation at different stages of deposition and decomposition for the micrometer dispensed, indentation samples is shown in Figure 4.16. For the as-deposited samples, neck formation for all binders similar to the inkjet deposited case, with the addition of fractured binder neck surfaces visible for the indentation samples. After heat treatment at 600°C, the polymer binder samples did not survive removal from the indentation well samples suggesting minimal green strength. However, for the aluminum nitrate binders after 600°C treatment, interparticle necks remain – similar to the inkjet deposited samples. The similarity of the neck regions formed by the inkjet deposition method and the micrometer deposition method for indentation suggest the fabrication of green samples through micrometer deposition for green strength testing through indentation are representative of the green strength of BJAM samples.

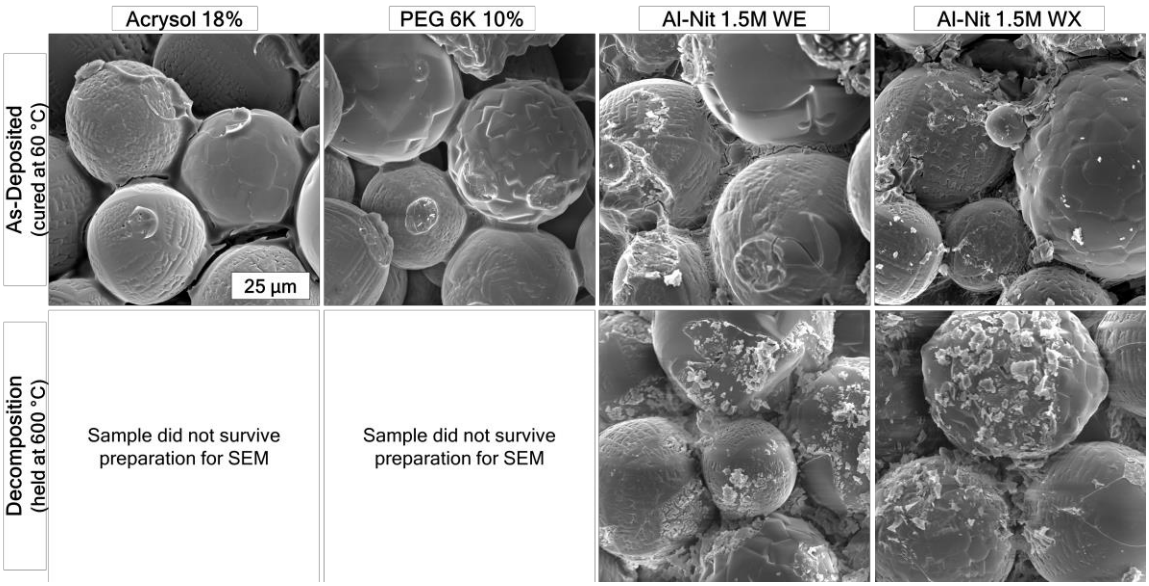

Figure 4.16: SEM showing progression binder-particle neck for micrometer dispenser deposited binders on alumina powder in wells after indentation at different stages of thermal decomposition (i.e., as-deposited, after 600 °C) for: Acrysol 18%; PEG 6K 10%; Al-Nit 1.5M WE; and Al-Nit 1.5M WX.

4.3.7 Binder development process summary and outlook

The binder development process described begins with characterization of basic rheological properties (e.g., surface tension, viscosity, density) for the binders. Rheological characterization was followed with relevant jetting and infiltration experiments to correlate the influence of rheology on jetting and infiltration of binder inks. Of note, high surface tension (represented by Al-Nit 1.5M W binder ink, surface tension of 65.93 ± 0.01 mN/m) resulted in formation of satellite droplets and high viscosity (represented by PEG 10K 10%, viscosity of 12.48 ± 0.10 cP) resulted in no jetting due to insufficient energy from the piezoelectric system – as predicted by ink jetting fundamentals. To overcome the high surface tension, a co-solvent (Al-Nit 1.5M WE) or surfactant (Al-Nit 1.5M WX) can be used to reduce the surface tension and create good jetting. To overcome high viscosity, the use of lower molecular weight polymers (PEG 1K 10% or PEG 6K 10%) reduces viscosity

to produce good jetting. Additionally, increasing the solids content of binder for polymers (demonstrated by Acrysol 10% versus Acrysol 18%) increases ink viscosity, and thus solids concentration can also be adapted to enable good jetting [163]. The use of millimeter-scale droplet dispensing onto a powder bed, as was previously done by Bai et al. [101], provided some comparison of for infiltration depth and time for the binder inks, generally highlighting good agreement for rheological influence on infiltration with the Washburn equation. The jetting and infiltration experiments also served to highlight binder inks (Acrysol 10%) that did not behave as expected, providing a screening tool for binder inks prior to use in BJAM to ensure desired print resolution via good jetting and adequate infiltration. Binder decomposition and single-layer jetting experiments showed the evolution of binder-particle morphology with temperature and highlighted the loss of interparticle bridges for polymer binders and evolution of interparticle bridges for reactive binders during decomposition. Finally, the indentation-based strength measurements provided a measure of green strength for samples, with strength above 3.8 ± 0.3 (PEG 6K 10%) correlating with removable granules for this study and suggesting sufficient strength for part removal in BJAM. Additionally, the strength experiments showcase that increasing polymer molecular weight, the use of polymers with higher strength (i.e., polymethyl methacrylate vs. polyethylene glycol [130]) and increasing polymer and metal salt binder concentration result in higher green strength. Finally, the indentation strength experiments highlighted that reactive metal salt binders retain strength after decomposition into metal oxides. The binder development and characterization process thus presents a methodology to correlate binder rheology with jetting, infiltration, and green strength to provide BJAM-relevant information for the creation of novel binders.

4.4 Conclusions

This chapter has presented the development and characterization of custom polymer and reactive metal salt binders through a process that involves the exploration of binder ink rheology, binder-powder interactions, binder decomposition, and component green strength. The influence of binder ink composition on the jetting and infiltration properties

of each custom binder was explored. The reactive metal salt binders showcase comparable green strength to polymer binders in the as-deposited condition and continuous green strength at elevated temperatures, concurrent with the continued existence of material at the powder inter-particle necks, further suggesting the possible use of reactive binders for shrinkage and warping control of BJAM parts. Future work will explore multi-layer processing with these reactive binders to determine the influence on sintering density and mechanical testing of multilayer components to compare the indentation strength results to traditional green strength methods like compression and 3-point bending tests, thereby correlating the measured presented in this chapter to macroscale mechanical properties of BJAM components. The development of custom binders and the establishment of a process for rapid binder scouting described in this chapter enables the implementation of binder systems to address BJAM challenges of densification and warping. This workflow will advance the BJAM community by enabling more rapid, data-driven development of binder inks to improve component properties including mechanical strength and dimensional accuracy and/or to achieve compositional control via BJAM.

Chapter 5

Powder spreading and layer density characterization of ceramics

The formation of dense and uniform powder layers through spreading is a critical requirement for powder bed additive manufacturing (AM) processes, with layer quality being influenced by powder feedstock selection and spreading parameters. Prior experimental work for powder spreading has required disruption of the powder layer for density measurement or has utilized spreading methodologies that do not adequately reflect the spreading process in AM. Thus, we present the exploration of powder spreading utilizing a precision, mechanized powder spreading testbed coupled with transmission x-ray imaging for non-contact powder layer density measurements. Specifically, we study the influence of powder size and shape for aluminum oxide powders, traverse speed, roller rotation, spreading implement selection (i.e., blade vs roller), and powder dispensing methodology (i.e., piston-fed vs hopper), on the density and uniformity of a powder layer. We find that the use of roller counter-rotation increases layer density for fine powders but decreases layer density for coarse powders. Additionally, we show that increasing traverse speed or the use of textured rollers results in reduced powder layer density for fine powders. For coarse powders, we find that the use of a roller geometry outperforms a blade geometry

for powder spreading, reaching the tapped density for the coarse spherical powder. Finally, we showcase that the use of vibrating hopper dispensing instead of piston-fed powder dispensing, coupled with a counter-rotating roller for powder spreading, results in high layer density for fine powders that attain the tapped density for the powder.

5.1 Introduction

The spreading of powder into a dense and homogenous layer is a critical step to the fabrication of components via powder bed additive manufacturing (AM) methods, including binder jet (BJAM) and powder bed fusion (PBF) [1]. For BJAM, high density and uniform layers are required as sintering is a common post-processing step and the path to part densification through thermal sintering is dependent on high green density (and thus powder bed density) [10,98,164]. Additionally, fine particle sizes (<20 μm) facilitate the densification process while inhomogeneities in the powder layer (and green part) can lead to part warping and loss of dimensional accuracy during the sintering process [10,98]. Specifically for high-temperature materials (i.e., ceramics, refractory metals), high temperatures required for sintering mean that spreading of fine powders to a high density is of utmost importance for formation of high density components via AM [4,10,98,164]. For PBF, like selective laser melting and electron beam melting, low powder bed density can result in melt pool instabilities which result in increased surface roughness and part defects [44,68,165]

Common methodologies for spreading powder in AM include roller systems (usually BJAM) and blades (usually PBF) [1,33]. For BJAM, fine powders (5-25 μm mean particle diameter) are preferable to facilitate densification [3]. However, fine powders tend to have higher cohesion and thus require assistance to increasing flowabilty and spreadability to form dense uniform layers, this is thus usually performed using a counter rotating roller and through metered deposition of the fine powders with an ultrasonic hopper [3,4,164,166] – shown in Figure 5.1a. For PBF, coarser powders (10-60 μm) are

with higher inherent flowability utilized and a blade style recoater is commonly employed, along with powder supply from a piston system [120] – shown in Figure 5.1b.

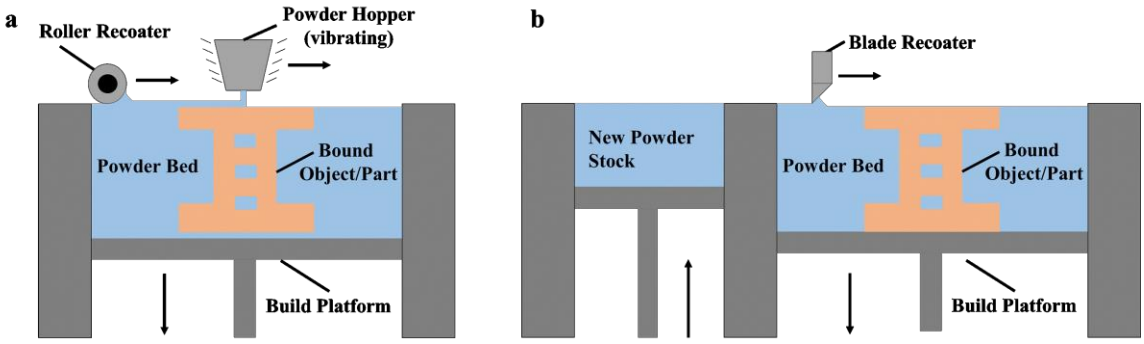

Figure 5.1: Conceptual images of common powder spreading methodologies using: (a) vibrating powder hopper for metered dispensing and roller recoater common in BJAM and (b) piston-fed powder dispensing and blade recoater common in PBF.

Characterization of powders for flowability and spreadabilty for use in AM tends to include particle size distribution (e.g., laser diffraction, static image analysis), powder density (e.g., apparent, tapped), static and dynamic angle of repose, and powder rheometry [6,8,120,167]. Static angle of repose (AOR) measurements are commonly used to group powders by flow properties, with an angle above 45° signifying a powder with poor flow properties that requires agitation to induce powder flow [6,168,169]. Additionally, the Hausner ratio and Carr index are used to scale the flowability of powders, defined as:

$$H_r = \rho_{tap}/\rho_b \tag{5.1}$$

$$CI = \frac{\rho_{tap} - \rho_b}{\rho_{tap}} = 1 - \frac{1}{H_r} \tag{5.2}$$

where H_r is the Hausner ratio, CI is the Carr index, ρ_b is the bulk or apparent density of the powder, and ρ_{tap} is the tapped density of the powder [170]. Generally, a Hausner ratio above 1.22 or Carr index above 0.18 indicates poor flowability, while a Hausner ratio below 1.18 or Carr index below 0.15 indicates good flowability [170].

Significant work has been performed, both experimentally and through simulations, to try to understand powder spreading for additive manufacturing - leading to insights on

the effect of powder feedstock properties and spreading parameters on the formation of powder layers. Lee explored the formation of layers using roller rotation for aluminum oxide (30 μm lamellar and 10 μm spherical) and stainless steel (15-30 μm spherical), showcasing that the use of vibration on the recoater increased layer density for both materials, with low traverse speed increasing density for the aluminum oxide powders, and stating a correlation between powder fluidity (angle of repose measurements) and dense layer packing [99]. Snow et al. developed a spreading test rig with a blade recoater to establish a correlation between powder characterization techniques (e.g., angle of repose, specific energy) and spreadability metrics (e.g., percent coverage of build plate) for Al-10Si-0.5Mg powder (volumetric D_{50} of 38.4 μm, 25.5 μm, and 27.1 μm), suggesting that the angle of repose can predict spreading performance for PBF (higher angle indicating poor spreadability), with a compliant silicone blade resulting in improved spreadabilty for cohesive powders and a rigid tool steel blade better for flowable powders, and recoating speed also influencing the spread quality [68]. Escano et al. utilized in-situ high speed x-ray imaging to explore the effects of particle size on spreading dynamics for 316L stainless steel (67 μm and 23 μm), with larger powder size resulting in higher dynamic angle of repose and average slope surface speed [34]. Mussatto et al. explored the influence of powder morphology, spreading velocity, and layer thickness on powder layer uniformity for 316L stainless (D_{v50} = 31.8 μm, D_{v50} = 36.7 μm, and D_{v50} = 28.0 μm) steel finding that particle sphericity (i.e., circularity) greatly influences spreading and segregation properties with higher circularity improving spreading properties, and low spreader velocity achieving higher uniformity [171]. Ali et al. explored the influence of build area location on the density and surface roughness of a powder bed through the ex-situ nano-computing tomography of Hastelloy X powder (D_{50} = 30 μm) bed samples bound by UV-curable polymer, highlighting that packing density and surface quality decreases along the recoating direction [77]. Tan-Phuc et al. developed a powder spreading testbed with a line-scanner and blade recoater to explore the powder layer uniformity and utilized the system to explore 316L stainless steel (29.86 μm mean diameter) powder spreading, highlighting that particle surface conditions, morphology, and moisture content influence particle cohesion and spreadability, with compliant blade recoaters creating higher layer thickness

and roughness uniformity while rigid blades created higher surface particle density uniformity, and high recoating speeds resulting in poor layer quality [78,172].

Ahmed et al. utilized a custom stencil for manual powder spreading of 316L stainless steel (15-55 μm) powder and a discrete element model (DEM), showcasing that poor spreading results with decreasing layer height [173]. Shaheen et al. used a discrete particle method (DPM) to simulate powder spreading using a blade and counter rotating roller, highlighting that the counter-rotating roller results in better layer quality over the blade, with increased spreading speed reducing layer quality [174]. Wang et al. utilized DEM to explore the effect of spreader geometry on layer density and uniformity, with a round blade resulting in least size segregation and large layer heights resulting in improved homogeneity [175]. Yee utilized a custom powder spreading testbed with a blade recoater for 316 stainless steel powder (10-60 μm diameter) and DEM to explore the influence of spreading parameters on powder layer surface roughness, finding that lower traverse speeds improve surface quality [66]. Parteli and Poschel utilized DEM to explore the spreading process for rotating rollers, showing that increasing traverse speed increases surface roughness and broader particle size distributions result in lower powder layer density [85]. Myers et al. explored the effect of traverse speed of a counter rotating roller for 316 L stainless steel powder (-22 μm), showcasing that increasing spread speeds decrease green density of binder jet parts, decreasing layer height increases green density, and surface roughness increasing for increasing spreading speeds [61]. Chen et al. performed experiments and DEM simulations to explore spreading for blade and rotating rollers, highlighting that packing quality decreases and surface roughness increases with increasing spreading speed [35,76]. Haeri et al performed DEM of powder spreading for polymer (PEK/PEEK), exploring particle shape and traverse speed, showing that increasing traverse speed increases surface roughness and decreases density, roller spreading creates higher quality layers than a blade recoater, and larger aspect ratio (less circular) powders decreasing layer density and increasing surface layer roughness [176]. Nan et al. utilized DEM to explore spreading using a rotating roller for varying powder size distributions, highlighting that for larger layer height and low rotational speed, particle

segregation in a layer can be reduced, with finer powders less sensitive to segregation and thus benefiting from the use of a rotating roller for spreading [177].

Despite the substantial investigations into powder spreading for AM and the importance of powder layer density to final part quality, powder layer density measurement techniques often require disruption of the powder layer, analyze the bulk (not local) layer density through powder removal from the build platform, perform measurements that do not analyze layer density (e.g., surface roughness/topography), or use spreading methodologies that do not fully resemble powder spreading for AM (i.e., manual spreading). Additionally, simulations require controlled, repeatable experiments for calibration – while simple experiments like AOR and manual spreading can provide initial guidance, representative powder spreading experiments for calibration of simulations will greatly improve the accuracy of simulations.

Chapter 2 described the development of a mechanized, modular, precision powder spreading testbed for the exploration of powder spreading for AM capable of spreading powder layers using blade and roller spreading implements [129]. Additionally, Penny et al. developed a non-contact methodology to interrogate the local powder layer density using a transmission x-ray system [178]. Accordingly, we present analysis of ceramic powder layers fabricated using the mechanized powder spreading testbed and analyzed using the transmission x-ray imaging technique. This novel combination permits exploration of the influence of the influence of powder size and shape, spreading parameters, spreading implement selection, and dispensing methodology on a statistical view of powder deposition, including direct assessment of powder layer density and uniformity. As illustrated through the following results, we find that these parameters are optimized by matching powder characteristics to spreading implement and dispensing methodology.

5.2 Material and methods

5.2.1 Powder characterization

Due to the availability of various powder size and shape distributions, aluminum oxide (alumina) ceramic was chosen as the material for this study. Four alpha-phase aluminum oxide ceramic powders (99.5+% purity) of different size and shape distributions were selected. Powders of 20 μm nominal diameter and spherical shape (Inframat Advanced Materials, 26R-8S20), 40 μm nominal diameter and spherical shape (Inframat Advanced Materials, 26R-8S40), 20 μm nominal diameter and irregular shape (Inframat Advanced Materials, 26R-0826AOFA), and 35 μm nominal diameter and irregular shape (Inframat Advanced Materials, 26R-0828AOFA) were procured. Particle size distribution measurements were conducted for all powders using both laser diffraction (Malvern Panalytical Masterisizer 2000) and static image analysis (Malvern Panalytical Morphologi G3S with a 10X objective, nominal size detection range of 3.5-210 μm) to compare the two techniques. Additionally, particle shape analysis (i.e., circularity) was performed using static image analysis. Finally, samples for all powders were gold coated with ~8 nanometers (Quorum Technologies SC7640 Sputter Coater, 60 second coating), in preparation for scanning electron microscopy (SEM) analysis, and imaged via SEM (JEOL JSM-6010LA).

Apparent and tapped density for the powders was measured by depositing powder into a graduated cylinder (Karter Scientific, 1 mL graduations, +/-0.5 mL) using a powder funnel (eisco, CH0459B) and measuring the mass using a digital scale (Ohaus Corporation DV215CD, 0.01 mg resolution), with tapping on the cylinder performed using a ¼-inch stainless steel rod (McMaster Carr 1327K65. The density measurements were repeated three times for each powder. For percent of theoretical density calculations, the theoretical density of 3.97 g/cm^3 (provided by Inframat Advanced Materials) was utilized.

5.2.2 Angle of repose

A custom angle of repose setup, comprising of a machined stainless steel powder funnel, an adjustable lab jack, a vertical mount, a USB CCD camera (Thorlabs High-Sensitivity USB 3.0 CMOS Camera) and optics (Thorlabs 6.5X Zoom Lens with 3 mm Fine Focus, 0.50X Extension Tube, C-Mount Adapter, and 0.5X Magnifying Lens Attachments, with 30.30 µm and 9.52 µm resolving limit at low and high magnification, respectively). The machined powder funnel was modeled after a Hall Flowmeter Funnel [179], with an opening of 50.0 mm, a cone half-angle of 30°, internal surface roughness of 0.4 µm, and an orifice with 2.50 mm diameter and 3.20 mm height. Powder was dispensed through funnel with an initial platform to funnel orifice distance of approximately 5 mm, then as the powder pile approached the orifice, the funnel was raised using the vertical mount to create a gap between pile and funnel so the pile could continue to grow until a static limit was reached and imaged using the camera. The powder was stirred in funnel using a brush to assist in dispensing out of the funnel. The AOR experiments were repeated three times for each powder and results analyzed using the angle tool in Fiji/ImageJ. An overview of the custom AOR system and the dimensions of the machined powder funnel are shown in Figure 5.2.

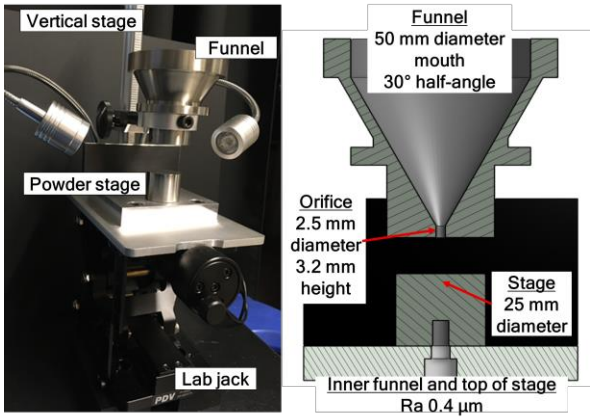

Figure 5.2: Test setup for angle of repose measurements with nominal dimensions for powder dispensing funnel.

5.2.3 Fabrication and characterization of spreading implements

To study the effect of the surface texture and roughness of the spreading roller, five custom rollers were fabricated: (1) smooth fabricated without additional machining of the spreading surface, (2) sandblasted with sandblasting performed using garnet abrasive (Barton ADIRONDACK 85 HPX) in a blast cabinet (Eastwood B40), (3) straight knurl with knurling performed on a manual lathe using a high-speed steel straight knurling tool (Accu Trak Tool Corp, MLS-0.4), (4) 30° knurl with knurling performed on a manual lathe using a high-speed steel 30° knurling tool (Accu Trak Tool Corp, MLL-0.4), and (5) diamond knurl with knurling performed on a manual lathe using a high-speed steel 30° diamond knurling tool (Accu Trak Tool Corp, MLF-0.4). All rollers were fabricated from tight-tolerance oil-hardening O1 tool steel (McMaster Carr 88625K81), with heat treatment at 810°C and oil-quenching performed after surface modification operations (i.e., sandblasting, knurling) to improve abrasion resistance. Additionally, to compare the effect of spreading with a rigid blade versus a roller, a rigid blade with a 45° blade angle was machined from 316L stainless steel (Zyci). The surface roughness of the rollers was characterized using a confocal microscope (Keyence VK-X1050) with a 10X objective lens, with four measurements of approximate area of 1mm X 7mm performed at distinct locations along the center of each roller. The hopper dispensing system, previously described in Chapter 2 as part of the custom powder spreading testbed, was installed with a 304 stainless steel 300X300 mesh (McMaster Carr 85385T713). The hopper dispensing flow rate was measured by activating the hopper for a pressure of 23 psi for 15 seconds and measuring the dispensed mass using a digital scale, repeating the measurement procedure three times. Hopper dispensing was performed at 27.9% humidity in a controlled lab atmosphere.

5.2.4 Powder spreading experiments

Powder spreading experiments were performed using a custom powder spreading testbed built and described in Chapter 2. [129] using a modified, x-ray compatible build platform.

The manual-controlled x-ray compatible build platform features a hollowed-out construction which allows for minimal x-ray absorption by the mechanical apparatus. A 2 mm thick aluminum 6061 T6 plate with known composition was used as the build platform, with a build area of 60 mm X 60 mm and measured thickness of 2.042 mm (measured using Mitutoyo Digital Micrometer Series 293) – knowledge of the plate composition is critical for the x-ray transmission calculations. The vertical height for the platform is set using two manual micrometers (Newport HR-6) with a 5 μm resolution and individual axial load capacity of 102 N and bolts fed through stacked Belleville disc springs (McMaster Carr 96445K25) enabling build plate travel of 5 mm. Figure 5.3 shows the x-ray compatible build platform and its integration into the powder spreading testbed. The layer height of 100 μm for all experiments was created by setting the gap between the spreading mechanism and the build platform using the manual micrometers and a precision gauge (Starrett 467M). To characterize the effective depth, and thus layer density, of the fabricated powder layers, the powder spreading testbed was installed in a custom x-ray imaging system (Figure 5.3). The x-ray imaging system and operational methodology to characterize the powder layer density was previously described in detail by Penny et al. [178]. Briefly, the x-ray imaging technique correlates observed transmission of x-rays through the powder layer to the effective powder layer height, measured in μm, using a radiation transport model. This model considers transmission spectra calculated for each item in the beam path (i.e., aluminum oxide powder layer and aluminum plate), as well as physics of x-ray generation and detection. As the layer height for the experiments was set to 100 μm, the effective powder layer height measured by the x-ray system and technique is numerically equivalent to the powder layer density expressed as a percentage. X-ray transmission measurements were performed by first imaging the blank plate (no powder) prior to each image of spread powder, clearing the platform using a brush and lint-free wipe (KimTech) prior to the blank plate measurement. To ensure no powder contamination between different experiments, the equipment was cleaned using a powder vacuum (Tiger-Vac) prior to changing out powder or spreading implement. X-ray source parameters were set to 50kV tube potential, 500 μA current, and medium focus mode (corresponding to a 20 μm emission spot size). Similarly, the detector was set to an integration time of 7500 ms. Finally, 130 individual frames are averaged to suppress shot noise and thereby ensure

2 μm uncertainty in layer thickness. Thermally-driven variation in dark current over the considerable length of these experiments is addressed by collecting a dark frame after every 5 image frames (26 in total), and using linear interpolation to determine the dark current during active measurements. The experimental matrix is shown in Table 5.1, with 5 measurements performed for the baseline study and 3 measurements performed for additional conditions. For experiments utilizing the piston powder supply system, a layer with 200 μm of powder was supplied by the powder supply platform. For experiments using the hopper supply system, a pressure of 23 psi was utilized for dispensing. Experiments were performed at humidity ranging from 10.0-39.4 % humidity with an average 24.4 % and temperature between 20-22°C (measured using an Extech Instruments Datalogger 42270).

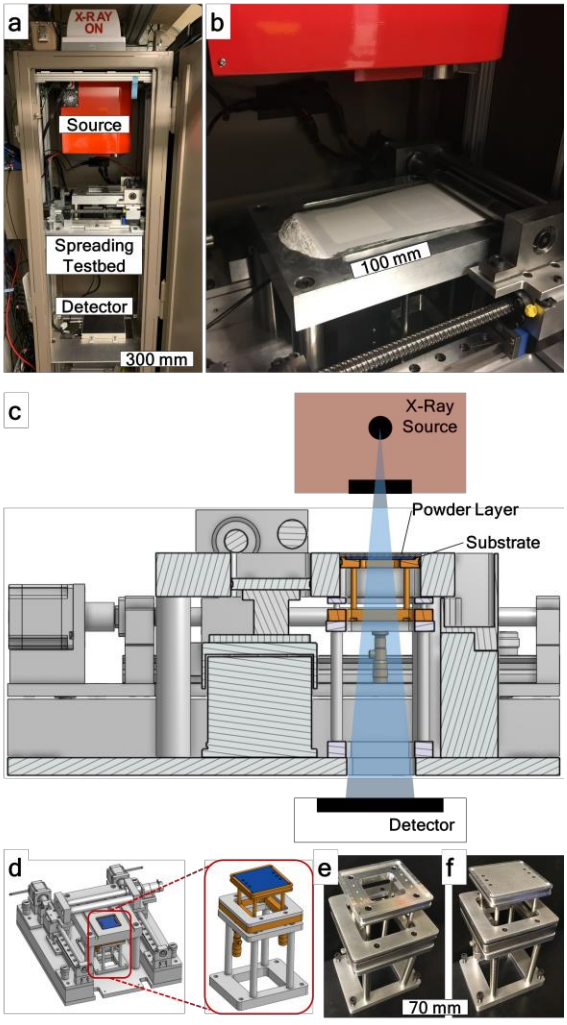

Figure 5.3: (a) Transmission x-ray measurement equipment with installed powder spreading testbed, (b) close-up of powder spreading testbed inside x-ray cabinet during powder spreading experiment, (c) concept of operations for x-ray powder layer density measurement for powder spreading testbed configuration (d) CAD image of powder spreading testbed highlighting x-ray compatible build platform, (e) x-ray compatible build platform without build plate, and (f) x-ray compatible build platform with build plate installed.

Table 5.1: Test matrix for powder spreading experiments

Spreading implement	Rotation	Traverse speed	Layer thickness	Powder size/shape	Powder supply method	Meas. performed
Smooth roller	300 RPM	5 mm/s	100 µm	20 µm spherical	Piston	5
Smooth roller	300 RPM	50 mm/s	100 µm	20 µm spherical	Piston	5
Smooth roller	0 RPM	5 mm/s	100 µm	20 µm spherical	Piston	5
Smooth roller	0 RPM	50 mm/s	100 µm	20 µm spherical	Piston	5
Smooth roller	300 RPM	5 mm/s	100 µm	40 µm spherical	Piston	3
Smooth roller	0 RPM	5 mm/s	100 µm	40 µm spherical	Piston	3
Smooth roller	300 RPM	5 mm/s	100 µm	35 µm irregular	Piston	3
Smooth roller	0 RPM	5 mm/s	100 µm	35 µm irregular	Piston	3
Smooth roller	300 RPM	5 mm/s	100 µm	20 µm irregular	Piston	3
Smooth roller	0 RPM	5 mm/s	100 µm	20 µm irregular	Piston	3
Straight knurl roller	300 RPM	5 mm/s	100 µm	20 µm spherical	Piston	3
30° knurl roller	300 RPM	5 mm/s	100 µm	20 µm spherical	Piston	3
Diamond knurl roller	300 RPM	5 mm/s	100 µm	20 µm spherical	Piston	3
Sandblasted roller	300 RPM	5 mm/s	100 µm	20 µm spherical	Piston	3
45° rigid blade	N/A	5 mm/s	100 µm	20 µm spherical	Piston	3
45° rigid blade	N/A	5 mm/s	100 µm	40 µm spherical	Piston	3
Smooth roller	300 RPM	5 mm/s	100 µm	20 µm spherical	Hopper	3

5.3 Results and discussion

5.3.1 Powder characterization

The volumetric powder size distribution for the 20 μm nominal diameter and spherical shape (20 S), 40 μm nominal diameter and spherical shape (40 S), 20 μm nominal diameter and irregular shape (20 I), and 35 μm nominal diameter and irregular shape (35 I), using two different measurement methodologies, laser diffraction (LD) and static image analysis (SIA), is shown in Figure 5.4a. Additionally, the D_{v10}, D_{v50}, and D_{v90} values for each powder and measurement technique is shown in Table 5.2. Generally, the static image analysis data presented a larger size distribution than that obtained through laser diffraction – this was due to selected objective and nominal measurement range which does not incorporate very fine (<1 μm diameter) particles and the smaller sample volume used for static image analysis compared to laser diffraction resulting in slightly skewed distributions. The difference for the volumetric average particle size between the two techniques was less than 6% for all powders. Additionally, the circularity for the powders (Figure 5.4b) extracted from static image analysis highlighted the high circularity of the spherical powders (D_{v50} = 0.995 for 20 S, D_{v50} = 0.992 for 40 S) and deviation from circular for the irregular powders (D_{v50} = 0.865 for 20 I, D_{v50} = 0.854 for 35 I). The SEM images of powders, Figure 5.4c, further highlight the highly spherical nature of spherical powders and shard-like nature of irregular powders.

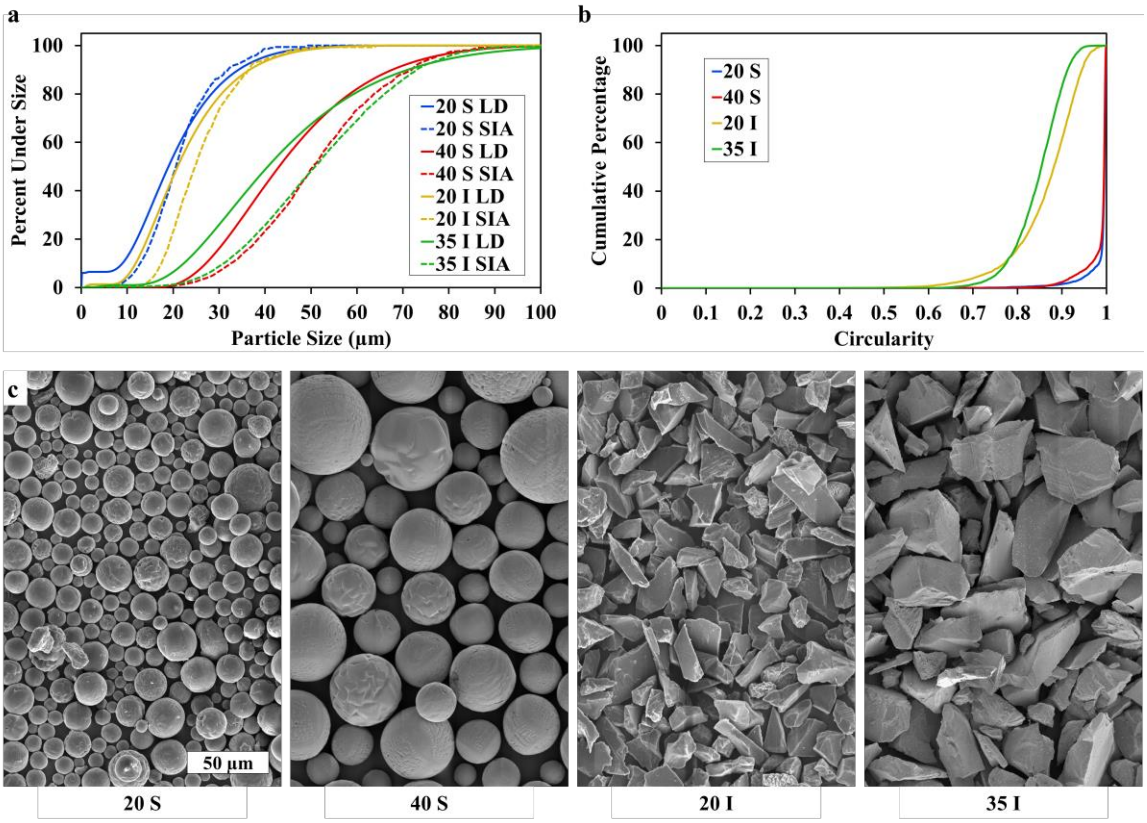

Figure 5.4: (a) Particle size distribution for fine (20 µm) and coarse (40 µm and 35 µm), spherical and irregular aluminum oxide powders, (b) circularity for powders, and (c) SEM images for powders.

Table 5.2: Powder size distribution (volumetric) for laser diffraction and static image analysis measurement techniques for fine (20 µm) and coarse (40 µm and 35 µm) spherical and irregular powders.

Powder	**Laser Diffraction**				**Static Image Analysis**			
	D_{10} (µm)	***D_{50} (µm)***	***D_{90} (µm)***	***Average (µm)***	***D_{10} (µm)***	***D_{50} (µm)***	***D_{90} (µm)***	***Average (µm)***
20 S	10.1	21.6	39.0	22.9	12.79	20.61	31.92	21.72
40 S	30.8	48.9	77.2	51.8	32.49	50.42	71.89	51.79
20 I	13.4	23.8	41.9	25.9	17.44	24.76	36.40	26.39
35 I	25.2	46.1	81.2	50.0	30.97	50.85	72.96	52.11

The powder density as a percentage of theoretical for apparent and tapped conditions, along with exemplary images for the angle of repose for all powders are shown in Figure 5.5. Additionally, the apparent and tapped density, as well as the calculated Hausner ratio and Carr index, and average angle of repose for all powders are summarized in Table 5.3. The apparent and tapped densities for both the 20 µm and 40 µm powders were higher than the values for the similarly sized irregular powders, which follows from particle packing fundamentals which states that non-spherical powders will result in lower random packing densities due to higher interparticle friction [39]. The tapped density for the spherical powders was 59% while the irregular powders had a tapped density of 46% for the 20 I and 48% for the 35 I powders. Using the Hausner ratio (H_r) and Carr index (CI) as measures of flowabilty, the 20 S, 40S, and possibly 35 I were categorized with "good flowability" (H_r < 1.18 or CI < 0.15) while the 20 I was categorized with "poor flowabiltiy" (H_r > 1.22 or CI > 0.18). Finally, the static angle of repose values categorized the 20 S as a cohesive powder with poor flowability, while 40 S, 20 I, and 35 I were categorized with fair-to-passable flowability.

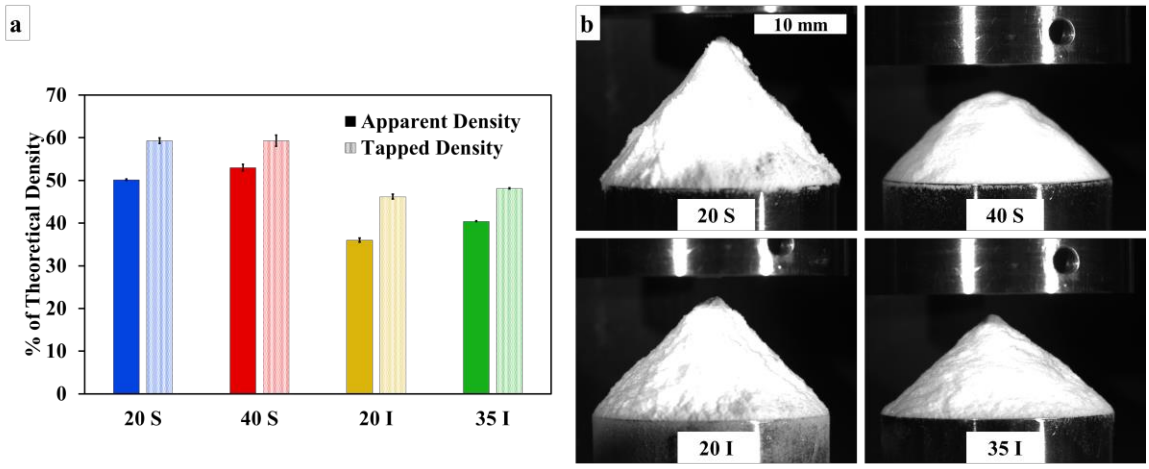

Figure 5.5: (a) Apparent and tapped densities as a percentage of theoretical for fine (20 µm) and coarse (40 µm and 35 µm), spherical and irregular aluminum oxide powders, (b) exemplary images for angle of repose measurements for powders.

Table 5.3: Results for apparent and tapped density for fine (20 μm) and coarse (40 μm and 35 μm), spherical and irregular aluminum oxide powders, along with calculations of Hausner ratio and Carr index, and average angle of repose.

	Apparent Density (g/cm^3)	**Tapped Density (g/cm^3)**	**Hausner Ratio**	**Carr Index**	**Angle of Repose (°)**
20 S	1.99 ± 0.01	2.35 ± 0.03	1.18	0.15	50.3 ± 0.6
40 S	2.10 ± 0.03	2.35 ± 0.05	1.12	0.11	42.5 ± 1.3
20 I	1.43 ± 0.02	1.83 ± 0.02	1.28	0.22	43.6 ± 1.8
35 I	1.61 ± 0.00	1.91 ± 0.00	1.19	0.16	41.2 ± 0.8

5.3.2 Influence of powder spreading traverse speed and rotation

To explore the influence of spreading traverse speed and roller rotation on powder layer density and uniformity, the 20 μm spherical powder was spread at 5 mm/s and 50 mm/s with (300 RPM) and without (0 RPM) roller rotation using the smooth roller, with powder supplied via the powder supply piston. Overhead images of exemplary powder layers for each condition, along with x-ray effective layer data shown for the central region of the powder layer (23.5 mm X 13 mm area), are shown in Figure 5.6. Powder deposition occurred over the full platform for both traverse speeds with roller rotation, however, incomplete deposition resulted for the spreading experiments without roller rotation (0 RPM) – as seen in both the camera and x-ray images. Furthermore, the condition with the slower traverse speed (5 mm/s) and roller rotation resulted in higher uniformity in the powder layer, with streaks resulting from sequential roller rotations as the spreading implement traverses across the build platform. For the higher traverse speed (50 mm/s) these streaks became larger as individual roller rotation required a longer traverse distance to complete due to the faster traverse speed.

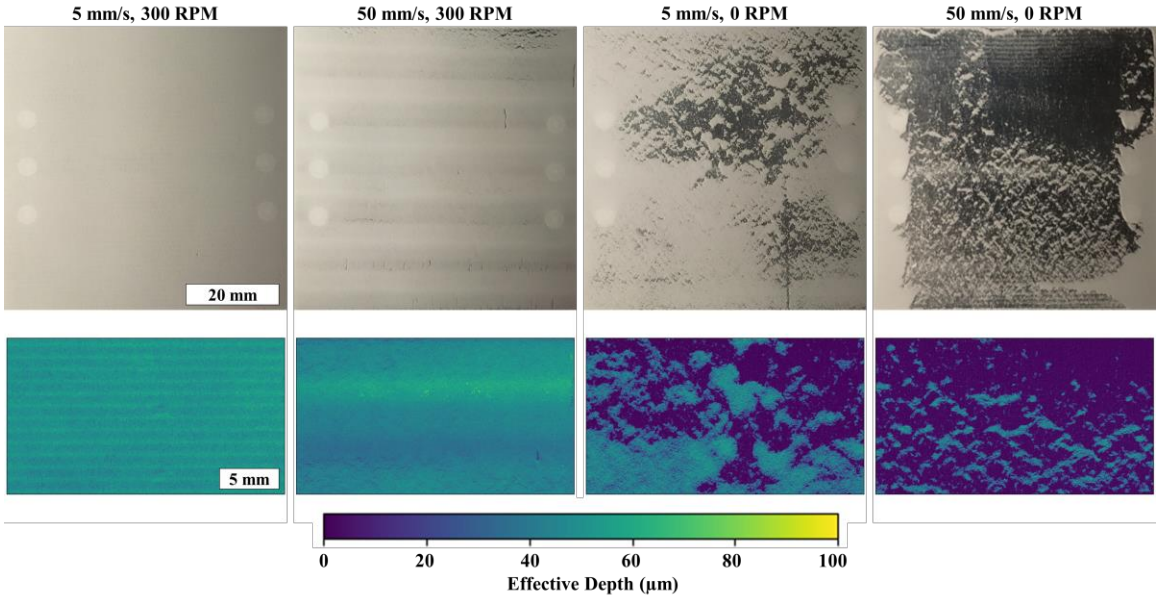

Figure 5.6: Images of fabriated powder layers of 20 µm spherical aluminum oxide powder for different spreading speeds and roller rotation parameters with x-ray transmission data showcasing effective depth of powder layer for central region of build plate (spreading direction is top to bottom).

The cumulative distribution of effective depth for each traverse and roller rotation condition (and the calculated average) is shown in Figure A.1, with a summary of the average powder layer density and cumulative distributions shown in Figure 5.7. A higher effective depth signifies a higher powder bed density and a steeper slope for the line signifies higher powder layer uniformity – recall that since the powder layer height was set at 100 µm, the effective depth is quantitatively equivalent to the powder layer density. Again, the use of roller rotation (300 RPM) resulted in higher average powder layer density (48.0 ± 1.6 for 5 mm/s and 46.2 ± 3.5 for 50 mm/s) compared to the no rotation condition (21.8 ± 14.7 for 5 mm/s and 10.0 ± 1.7 for 50 mm/s), with numerical values reported as the average and standard deviation of the multiple experiments for each condition. Additionally, in Figure 5.7b, from the higher slope for the 5 mm/s condition, a higher uniformity for the powder layer is inferred than for the 50 mm/s spreading condition. For the 20 µm spherical powder, the use of roller rotation was necessary to increase the

spreadability of the powder which is inherently low due to the high interparticle cohesion of the powder, with a low speed favorable in creating a more uniform powder layer.

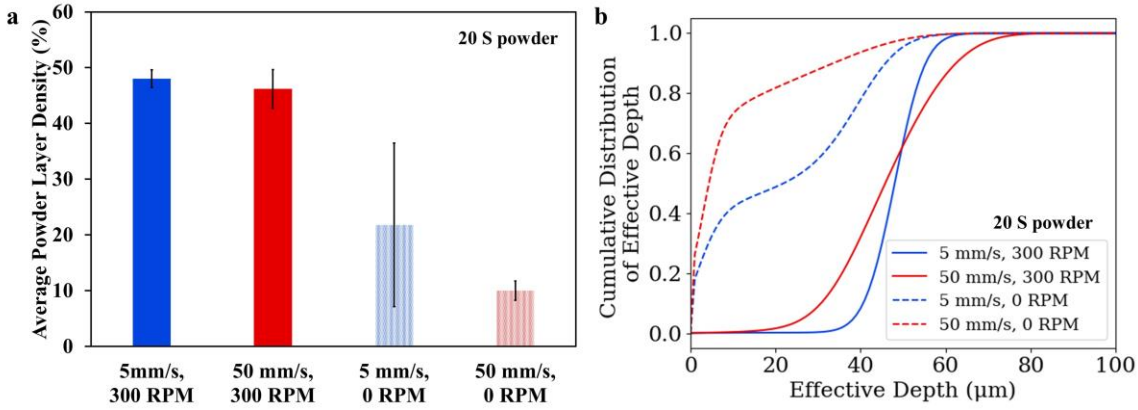

Figure 5.7: (a) Average powder layer density of 20 µm spherical aluminum oxide powder for different spreading speeds and roller rotation parameters and (b) average cumulative effective depth (powder layer density) versus effective depth for same conditions.

5.3.3 Effect of powder size and shape

To explore the influence of powder size and powder shape on powder layer density and uniformity, 20 µm irregular powder, 40 µm spherical powder, and 35 µm irregular powder were spread at a traverse speed of 5 mm/s with (300 RPM) and without (0 RPM) roller rotation using the smooth roller, with powder supplied via the powder supply piston. Overhead images of exemplary powder layers for each condition of the 20 I powder, along with x-ray effective layer data shown for the central region of the powder layer, are shown in Figure 5.8. Powder deposition occurred for both roller rotation conditions throughout the powder bed, however with lower layer density than for the 20 S powder for the case with roller rotation. For the case without roller rotation, the irregular powder (20 I) showcased more uniform spreading than the spherical powder (20 S) – this correlated with the AOR measurements in that the irregular powder showcased higher flowability than the spherical powder without the use of spreading assistance (e.g., roller rotation, vibration).

However, the irregular fine powder additionally benefited from the use of roller rotation to create a higher layer density.

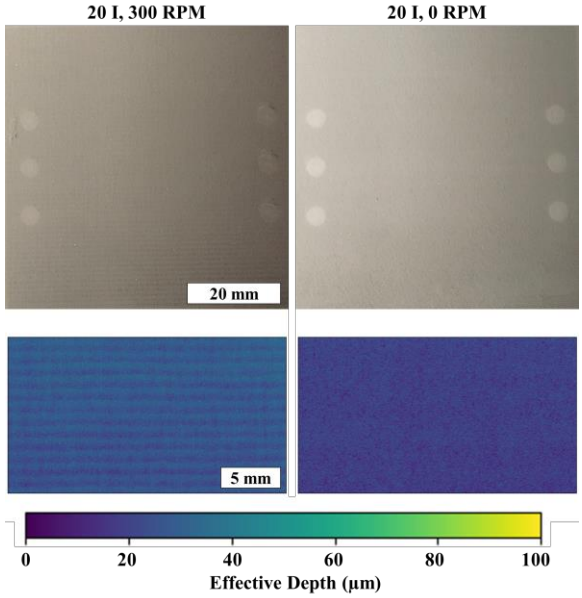

Figure 5.8: Images of fabriated powder layers of 20 µm irregular aluminum oxide powder for 5 mm/s spreading traverse speed and different roller rotation parameters with x-ray transmission data showcasing effective depth of powder layer for central region of build plate (spreading direction is top to bottom).

Overhead images of exemplary powder layers for each condition of the 40 S powder and 35 I powder, along with x-ray effective layer data shown for the central region of the powder layer, are shown in Figure 5.9. Higher layer density and uniformity occurred for the 40 S and 35 I powders for the case without roller rotation than with roller rotation, in contrast to the behavior of the 20 µm powders.

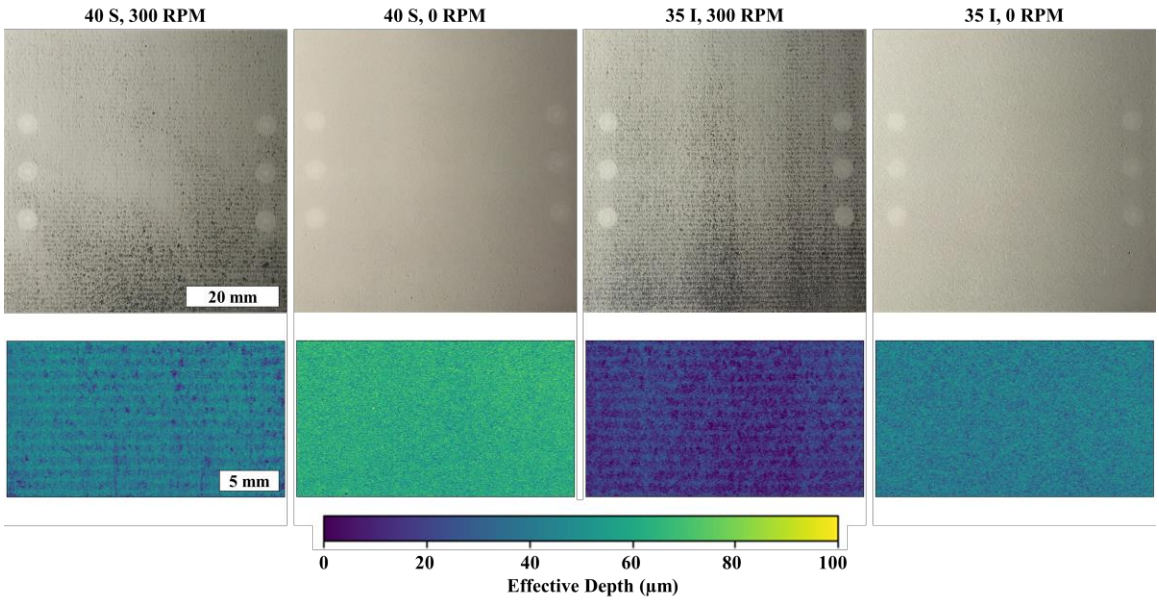

Figure 5.9: Images of fabriated powder layers of 40 µm spherical and 35 µm irregular aluminum oxide powder for 5 mm/s spreading traverse speed and different roller rotation parameters with x-ray transmission data showcasing effective depth of powder layer for central region of build plate (spreading direction is top to bottom).

The cumulative distribution of effective depth for the 20 I powder with and without roller rotation (and the calculated average) is shown in Figure A.2, the cumulative distribution of effective depth for the 40 S and 35 I powders with and without roller rotation (and the calculated average) is shown in Figure A.3, with a summary of the average powder layer density and cumulative distributions for 20 S, 40 S, 20 I, and 35 I at 5 mm/s traverse speed with (300 RPM) and without (0 RPM) roller rotation shown in Figure 5.10. For both the small (20 S and 20 I) and large (40 S and 35 I) powders, the spherical powders resulted in higher powder layer density for both roller conditions (20 S: 48.0 ± 1.6 at 300 RPM and 21.8 ± 14.7 at 0 RPM, 40 S: 37.2 ± 2.8 at 300 RPM and 60.8 ± 0.3 at 0 RPM) compared to the irregular powders (20 I: 27.5 ± 1.1 at 300 RPM and 20.4 ± 1.2 at 0 RPM, 35 I: 16.8 ± 0.5 at 300 RPM and 40.4 ± 1.6 at 0 RPM). This is due to inherent lower particle packing of non-spherical powders and correlated with the higher apparent and tapped density values for the spherical powders compared to the non-spherical powders. The powder layer density for the 40 µm spherical powder at 5 mm/s and 0 RPM slightly exceeded the tapped

density value for the powder, this suggests the tapped density value is a decent approximation for the upper limit on powder layer density without the application of additional powder compaction. Interestingly, for the coarse powders (40 S and 35 I), the use of roller rotation decreased the powder layer density whereas the use of roller rotation increased powder layer density for the fine powders (20 S and 20 I). This confirms the bifurcation in powder recoating strategies dependent on the powder size distribution, with fine, cohesive powders benefiting from the utilization of roller recoating to overcome interparticle friction while larger, flowable powders benefiting from the lack of rotation (and additional energy input to the powder) during powder spreading. Furthermore, the AOR provided some indication on the flowabilty of the powder – whether the powder could be spread uniformly without the use of rotation, but did not necessarily differentiate as to the impact on layer density of using roller rotation during spreading. However, Hausner ratio and Carr index did not correlate well, as the 20 S powder was expected to exhibit good flowability while the 20 I powder was expected to exhibit poor flowability.

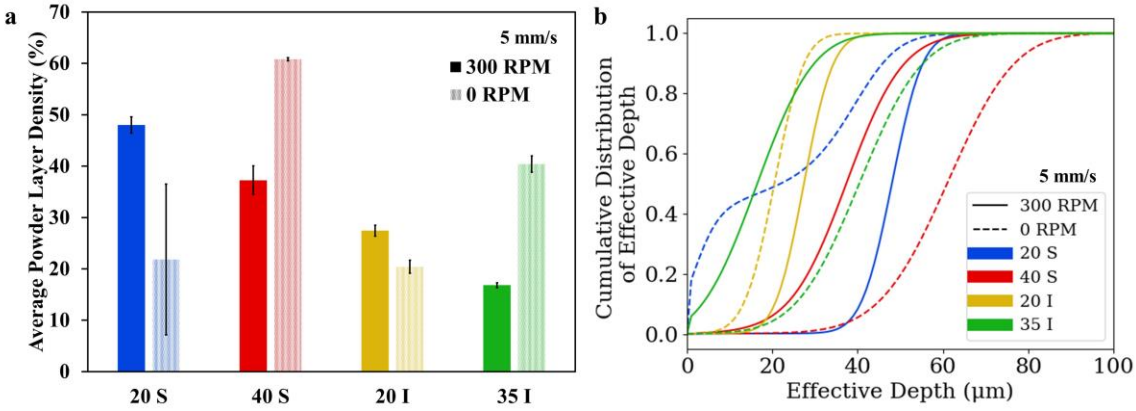

Figure 5.10: (a) Average powder layer density of fine (20 µm) and coarse (40 µm and 35 µm), spherical and irregular aluminum oxide powders for 5 mm/s traverse spreading speeds and different roller rotation parameters and (b) average cumulative effective depth (powder layer density) versus effective depth for same conditions.

5.3.4 Influence of spreader surface texture and spreader type

To explore the influence of surface texture and roughness on powder layer density and uniformity for spreading with roller rotation, the fabricated sandblasted and knurl rollers were utilized to spread the 20 μm spherical powder at 5 mm/s with roller rotation (300 RPM), with powder supplied via the powder supply piston. Figure 5.11 shows the various fabricated rollers, with showing the average surface roughness (Ra) and peak-to-valley surface roughness (Rz) values for each roller – in summary, the smooth roller had Ra = 1.2 ± 0.1 μm, the sandblasted roller had Ra = 2.4 ± 0.5 μm, the straight knurl roller had Ra 22.6 ± 2.4 μm, the 30° knurl roller had Ra = 47.1 ± 0.4 μm, and the diamond knurl roller had Ra = 17.9 ± 2.4 μm. Additional surface profile characterization of the rollers is shown in Appendix B. Overhead images of exemplary powder layers for each roller, along with x-ray effective layer data shown for the central region of the powder layer, are shown in Figure 5.12. No considerable increase in powder layer density was apparent from the use of knurled or sandblasted rollers, with the sandblasted roller (lowest surface roughness of the non-smooth rollers) exhibiting the highest density layer. Furthermore, defects introduced to the rollers during knurling operation were seen to reduce powder layer uniformity and density for the 30° knurl and diamond knurl rollers.

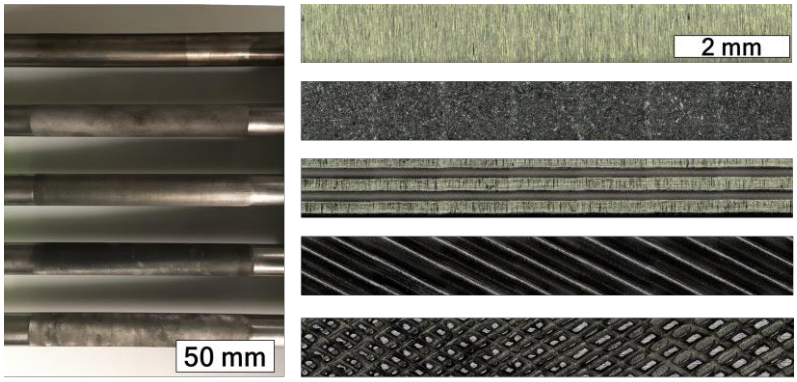

Figure 5.11: Image of smooth, sandblasted, straight knurl, 30° knurl, and diamond knurl rollers, with exemplary close-up microscope image of surface features and summary of average surface roughness (Ra) and peak-to-valley surface roughness (Rz).

Table 5.4: Average values for surface roughness (average and peak-to-valley) for fabricated rollers.

Roller	Ra (µm)	Rz (µm)
Smooth	1.2 ± 0.1	13.9 ± 1.5
Sandblasted	2.4 ± 0.5	25.2 ± 2.9
Straight Knurl	22.6 ± 2.4	126.5 ± 27.1
30° Knurl	47.1 ± 0.4	205.2 ± 11.2
Diamond Knurl	17.9 ± 2.4	114.0 ± 12.2

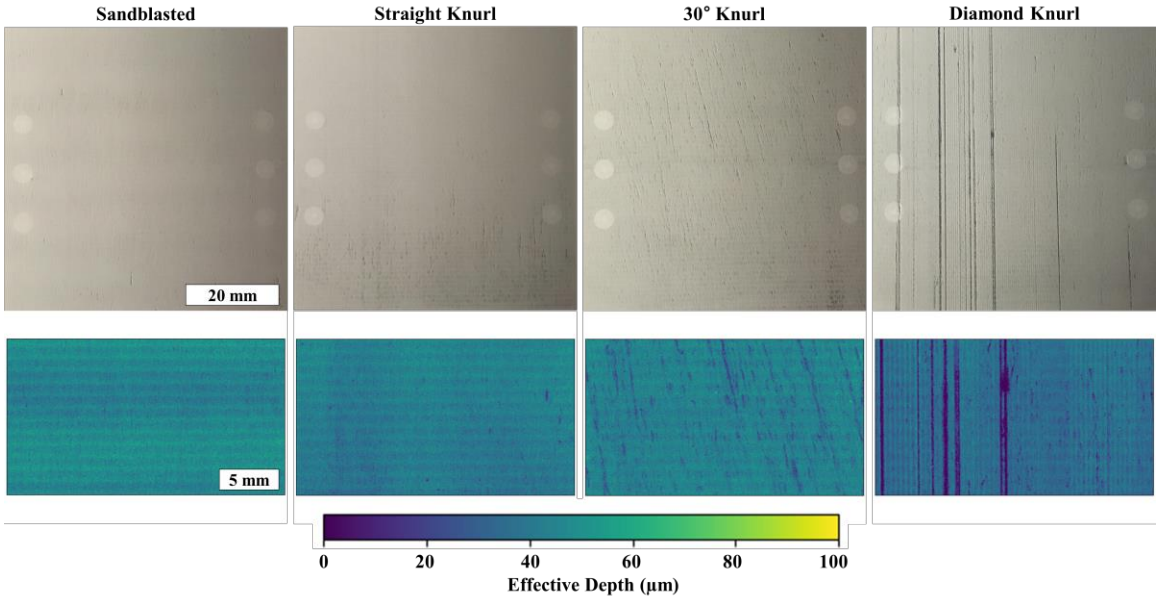

Figure 5.12: Images of fabriated powder layers of 20 µm spherical aluminum oxide powder for 5 mm/s traverse speed, 300 RPM roller rotation parameters, and different roller surface textures with x-ray transmission data showcasing effective depth of powder layer for central region of build plate (spreading direction is top to bottom).

The cumulative distribution of effective depth for each roller condition (and the calculated average) is shown in Figure A.4, with a summary of the average powder layer density and cumulative distributions shown in Figure 5.13. The powder layer density is decreased through the use of the knurled rollers (straight knurl: 42.0 ± 1.2, 30° knurl: 34.5 ± 7.3, diamond knurl: 34.4 ± 1.3), with the sandblasted roller (46.8 ± 1.2) resulting in a slight decrease from the smooth roller (48.0 ± 1.6). Generally, the powder bed density

decreased as the surface roughness (Ra and Rz) of the roller increased. For the fine, cohesive, spherical powder, the additional surface roughness thus increased the traction between the powder and roller which resulted in further disruption of the powder layer, thus reducing the layer density.

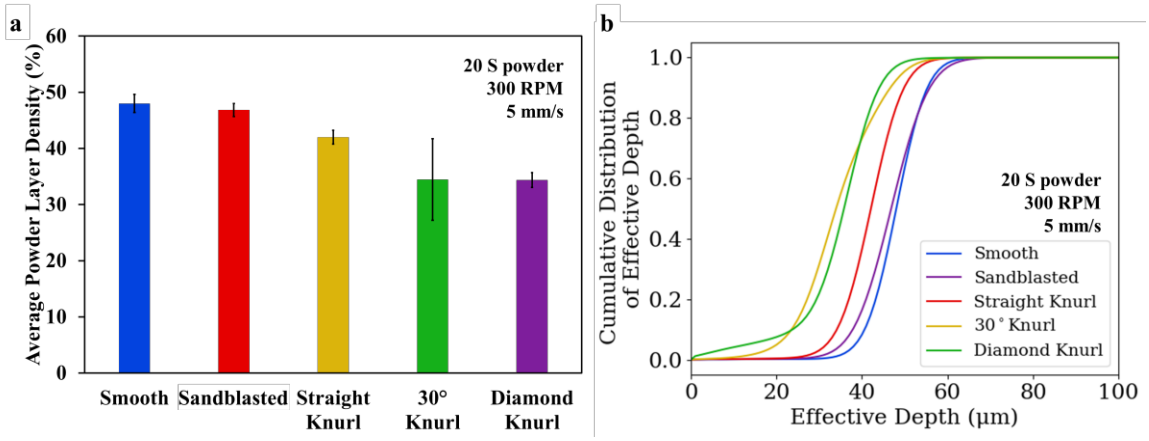

Figure 5.13: (a) Average powder layer density for 20 µm spherical aluminum oxide powder for 5 mm/s traverse speed, 300 RPM roller rotation parameters, and different roller surface textures and (b) average cumulative effective depth (powder layer density) versus effective depth for same conditions.

To compare the influence of powder spreading implement geometry on layer formation, 20 µm spherical and 40 µm spherical powders were spread at 5 mm/s with using a rigid blade with a 45° blade, with powder supplied via the powder supply piston. Overhead images of exemplary powder layers for each powder, along with x-ray effective layer data shown for the central region of the powder layer, are shown in Figure 5.14. Although powder spreading appeared to be fairly uniform over the build platform, the produced powder layer density using the blade was lower than that for the roller spreading implement.

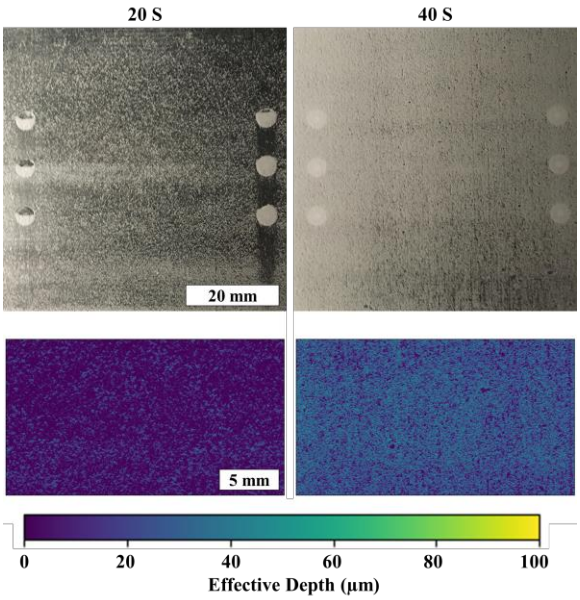

Figure 5.14: Images of fabriated powder layers of 20 µm spherical and 40 µm spherical aluminum oxide powder for 5 mm/s spreading traverse speed using blade recoater with x-ray transmission data showcasing effective depth of powder layer for central region of build plate (spreading direction is top to bottom).

The cumulative distribution of effective depth for each powder using the rigid blade (and the calculated average) is shown in Figure A.5, with a summary of the average powder layer density and cumulative distributions shown in Figure 5.15. The powder layer density decreased through the use of the rigid blade (20 S: 7.2 ± 1.2, 40 S: 25.3 ± 1.1) compared to the smooth roller with no rotation (20 S: 21.8 ± 14.7, 40 S: 60.8 ± 0.3). Thus the design of the surface geometry for powder spreading is of critical importance for the formation of a high density powder layer, with the smooth contour of the roller resulting in higher density layer formation than the sharp features from the rigid blade for the experiments.

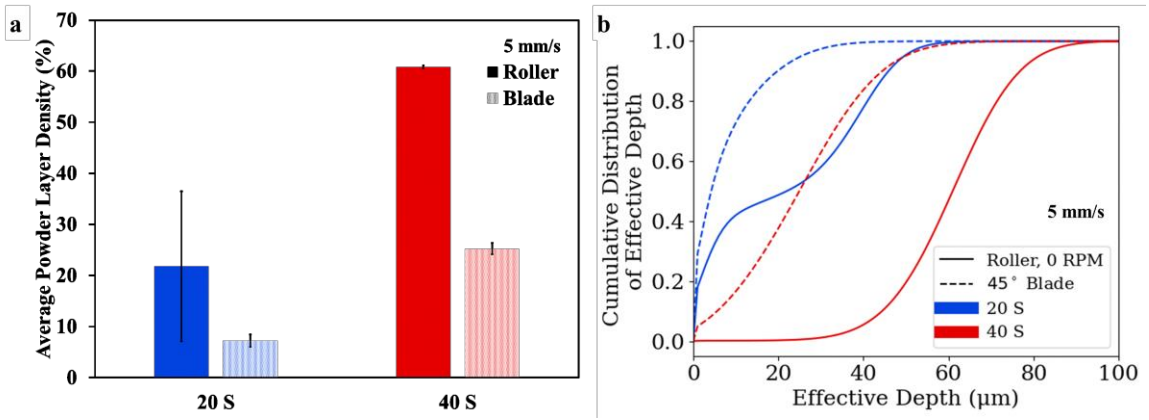

Figure 5.15: (a) Average powder layer density for 20 µm spherical and 40 µm spherical aluminum oxide powder for 5 mm/s traverse speed, and different spreading geometry (blade vs non-rotating smooth roller) and (b) average cumulative effective depth (powder layer density) versus effective depth for same conditions.

5.3.5 Influence of powder dispensing methodology

To explore the influence of the powder dispensing mechanism on powder layer formation, 20 µm spherical powder was spread at 5 mm/s and 300 RPM roller rotation with the smooth roller, with powder supplied via the vibrating hopper dispensing system. The mass flow rate dispensed by the hopper at 23 psi was 116 ± 19 mg/s, which for a traverse speed of 5 mm/s and a build area of with dimensions of 60 mm X 60 mm results in approximately 1500 mg deposited on the build area – comparatively, the mass of a 50% dense alumina powder layer for a build area of 60 mm X 60 mm and layer height of 100 µm is 715 mg. Overhead images of an exemplary powder layer for hopper dispensing and roller spreading, along with x-ray effective layer data shown for the central region of the powder layer, are shown in Figure 5.16. The layer showed high density and uniformity compared to the piston-fed powder supply methodology for the same spreading parameters.

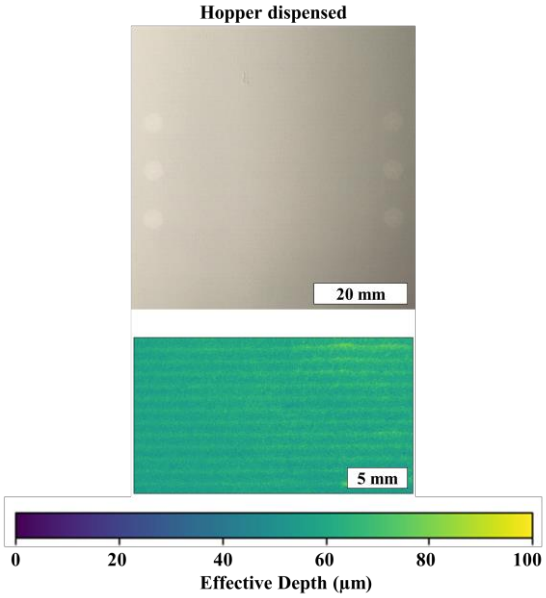

Figure 5.16: Images of fabriated powder layers of 20 µm spherical aluminum oxide powder for 5 mm/s traverse spreading speed, 300 RPM roller rotation, with vibrating hopper dispensing, with x-ray transmission data showcasing effective depth of powder layer for central region of build plate (spreading direction is top to bottom).

The cumulative distribution of effective depth for the hopper dispensing methodology (and the calculated average) is shown in Figure A.6, with a summary of the average powder layer density and cumulative distributions for piston-fed and hopper dispensing shown in Figure 5.17. The use of hopper dispensing for fine spherical powder (20 S) resulted in an increase in powder layer density (58.2 ± 2.3) when compared to the piston-fed system (48.0 ± 1.6). The layer density for the hopper dispensed 20 µm spherical powder at 5 mm/s with 300 RPM roller rotation using the smooth roller, approached the tapped density for the powder. This study suggests that hopper dispensing is a superior methodology for supplying powder for spreading of fine cohesive powders. This agreed with the AOR indication that high cohesion powders require agitation (i.e., hopper vibration) to increase flowabilty.

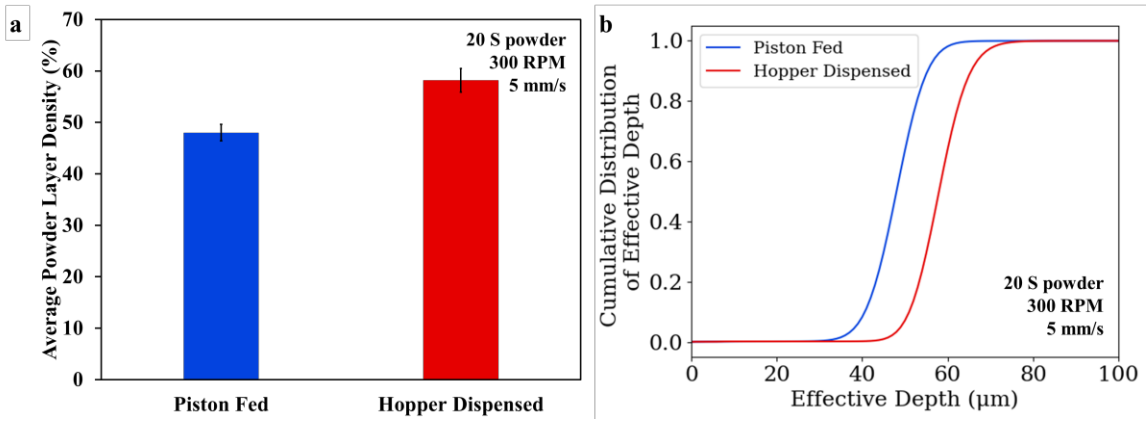

Figure 5.17: (a) Average powder layer density for 20 μm spherical aluminum oxide powder for 5 mm/s traverse spreading speed, 300 RPM roller rotation, with vibrating hopper dispensing and piston-fed dispensing and (b) average cumulative effective depth (powder layer density) versus effective depth for same conditions.

5.4 Conclusions

This chapter has presented the investigation of powder spreading of ceramic powders utilizing a custom precision powder spreading testbed coupled with a non-contact, localized powder layer density measurement technique using x-ray imaging – to our knowledge the first instance of in-situ layer density measurements for AM-relevant mechanized powder spreading. The effects of powder size, powder shape, traverse speed, roller rotation, roller surface texture and roughness, and powder dispensing mechanism were explored. Fine powders benefited from roller rotation with resultant higher layer density and uniformity, while the use of roller rotation reduced the powder layer density for coarse powders. For fine powders, lower traverse speeds resulted in higher powder layer density and uniformity. Powders with irregular shape resulted in lower powder bed densities than spherical powders due to increased interparticle friction and poorer particle packing. Surface roughness and texturing of roller did not improve layer density for fine powders. The surface geometry of the spreading implement greatly affected the spreading and powder layer density, with a roller geometry resulting in higher layer density for fine

powders (with rotation) and coarse powders (without rotation) when compared to a rigid blade. Finally, the dispensing mechanism of fine powders also influenced the powder layer density – such that the use of a dispensing hopper ahead of a roller spreading implement resulted in higher layer density than a roller spreading implement with a piston-fed powder system. Tapped density presented an approximate upper limit to powder layer density for fine and coarse spherical powders. Angle of repose experiments and categorization provided some indication to powder spreadabilty – with high angle of repose (low flowability) powders benefiting from the use of roller rotation and hopper dispensing to increase flowability and powder layer density.

The use of mechanized powder spreading for layer generation and non-contact powder layer density measurements via transmission x-ray imaging presented in this study enables direct correlation to powder spreading for powder bed AM. Further investigations will explore additional material classes (e.g., polymers, metals, composite powder), powder distributions (e.g., bimodal), and additional processing conditions (e.g., layer height, powder supply ratio) to further advance the knowledge of powder spreading for AM.

Chapter 6

Reactive binder jet additive manufacturing of ceramics for microstructural control

Binder jet additive manufacturing (BJAM) is particularly suited to processing brittle materials such as ceramics due as its process flow separates the steps of shaping and densification. Polymer binders are typically used in BJAM, including with ceramics. However, ceramics are especially prone to distortion or fracture during sintering, due to the low strength of polymer-bound parts after polymer decomposition. This paper presents the development and use of reactive metal salt binders for BJAM of ceramic components. Using aluminum oxide as the feedstock powder, we compare the performance of aluminum nitrate and magnesium nitrate metal salts as binders, and polyethylene glycol as a reference polymer binder. Test components are fabricated using a custom BJAM testbed, sintered, and characterized for density and deformation. The metal salt binders form solid interparticle bridges after decomposition, which provide continued strength to printed components during sintering. Additionally, increased densification results from the use of magnesium nitrate binders and reduced shrinkage results from use of aluminum nitrate

binders, showcasing the utility of reactive binders that convert into ceramic sintering aids upon decomposition and sustain part strength during sintering.

6.1 Introduction

Binder jet additive manufacturing (BJAM), due to its inherent separation of shaping and densification steps, is well-suited to the fabrication of complex geometries for high-temperature materials, including ceramics [1,11–13]. BJAM consists of two primary steps for the shaping of components: (1) spreading of thin powder layers and (2) inkjet deposition of a binder to adhere powders into the designed cross-sectional shape and to prior layers, as shown in Figure 6.1. After printing and binder curing, the printed (or green) ceramic samples are sintered to thermally consolidate the parts and improve material properties. BJAM commonly utilizes powders with particle size <20 μm to form layers 50-100 μm thick, with inkjet nozzles dispensing droplets of 10-50 μm diameter [1,4,133].

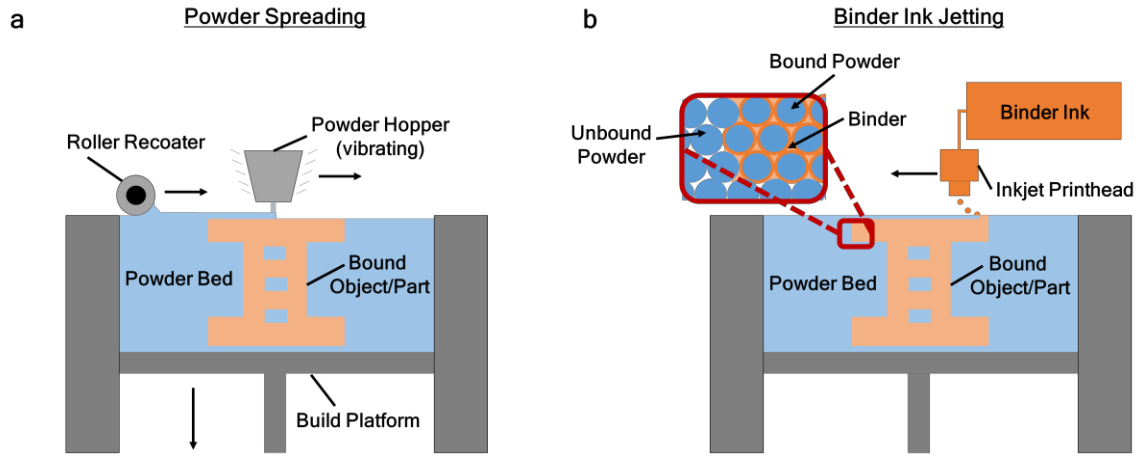

Figure 6.1: Schematic of binder jet additive manufacturing (BJAM) process including: (a) deposition of fine powders utilizing a vibrating powder hopper for dispensing and counter-rotation roller for powder spreading; and (b) layerwise inkjet printing of binder onto the powder layer create the desired 3D shape.

The purpose of the deposited binder in BJAM is to agglomerate powder particles to a desired geometry and to provide cohesive strength to retain the desired geometry during the powder removal stage and into the debinding/sintering phase of the manufacturing process [87,133]. The evolution of the binder ink and binder-particle interactions are shown in Figure 6.2. As the binder is deposited onto the powder bed, spreading and infiltration of the binder ink dictates part resolution and geometry, and after drying/curing of the binder ink the green part is provided strength through the consolidation of the binder at the interparticle necks. During debinding of polymer-bound parts, the majority of the binder is burnt off and the powder particles begin to consolidate, ultimately forming interparticle necks and improving in density through the sintering process.

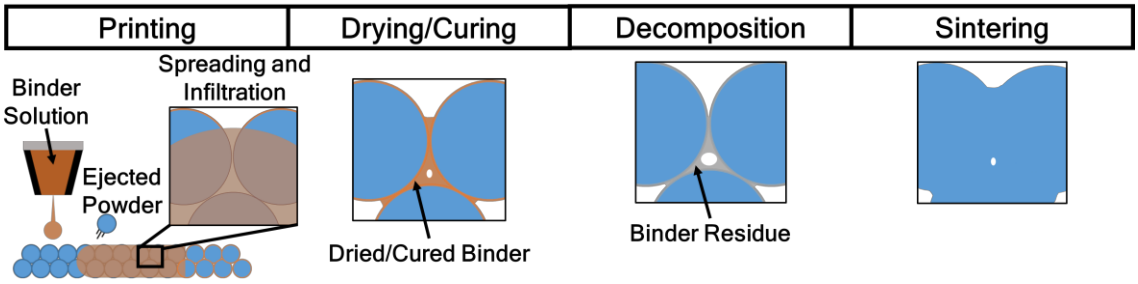

Figure 6.2: Particle-binder interactions that occur during BJAM and post-processing. Binder residue during decomposition is shown in exaggerated condition for polymer binders, but more representative of decomposition for reactive binders.

Although many binder formulations can be utilized in BJAM, polymers are commonly used as they bind most materials and can decompose to leave little organic residue [135,180,181]. Polymer-bound components typically exhibit green component strengths of 0.1-100 MPa depending on polymer composition and binder solid loading concentration. Values for low binder concentrations (<10%) may range from 1-25 MPa. A minimal desired green strength for handling is 10-20 MPa [130,182,183]. However, the polymer is not an active participant in the densification of the printed component, requiring a debinding step to remove the polymer to prevent material contamination. During debinding of the polymer, part warping and deformation can occur, as the part is extremely fragile prior to initiation of powder sintering [146,184], which occurs at a temperature above the decomposition temperature of the polymer.

Issues from injection molding and powder-based processes have carried over into BJAM, particularly warping and non-uniform shrinkage during sintering caused by a variety of sources including non-homogenous green density, differences in thermal gradients in the part and furnace, and inadequate support of cantilevered features during sintering [4,7]. The use of setter plates and sintering trays, along with design of green parts that accommodate for shrinkage such that the final part has the appropriate dimensional tolerances (which requires expertise and knowledge of the sintering/shrinkage process) is common practice for injection molding and ceramic processing [6,7,9]. Further, densification of both metal and ceramics can be challenging given the low green densities attained from powder spreading for BJAM (40-60%) compared to injection molding (IM) and powder pressing (solids content of 45-65% for IM; >60% to as high as 90% with sufficient compaction pressure for powder pressing), and the relatively larger powders (<20 μm) used compared to those used in IM and pressing (<10 μm powders for metals and commonly <1 μm powders for ceramics) [6,8,9,130,185,186]. Densification challenges stem from sintering mechanisms that are strongly dependent on the green density of the part and the initial particle size. Specifically, a higher green density provides more interparticle contacts, smaller initial pore sizes, and less required densification for full density. Smaller particles provide higher interface energy and more surface area which promote diffusion processes and ultimately lower the required thermal energy and/or time required for sintering [10,98].

To mitigate part warping and improve densification during sintering of BJAM parts, nanoparticle additives and metal salts (which form metal or ceramic nanoparticles upon decomposition) have been used either as a post-process infiltration step or as binder inks for a limited range of metallic materials [19,80,113,146,152,184,187–192]. Yoo first explored the use reactive binders—wherein the deposited binder material provides additional feature beyond solely green strength for part removal—via deposition of silver nitrate on stainless steel resulting in control of part shrinkage below 0.1% when fired and deposition of small particles of carbonyl iron/titanium carbide onto steel preventing major shrinkage (0.38% shrinkage) [113]. For the case of reactive metal salt binders, the reaction products from the binder after heating provide continued strength during sintering which

reduces shrinkage. Hadjiloucas deposited copper nitrate onto metal (molybdenum and silver) skeletons and slurries with fine particles of silver onto molybdenum powder with subsequent shrinkage limited to 0.15% [190]. Crane et al. used infiltration of iron nanoparticles into partially sintered stainless steel parts, reducing creep deflection by up to 95% and shrinkage by 60% [115,191]. More recently, Bai and Williams explored the use of inks with copper nanoparticles to print on copper powder [146]. Bai and Williams fabricated parts by BJAM using metal-organic-decomposition inks for copper, with successful part removal and showed higher density in central regions of printed parts [80]. Elliott et al. utilized post-print infiltration of stainless steel nanoparticles into partially sintered BJAM stainless steel discs, showing increased mass and density for the samples after nanoparticle deposition and secondary sintering [152]. Grant et al. utilized infiltration of a solution of titanium (IV) bis (ammonium lacto) dihydroxide into partially sintered titanium oxide parts, showing reduction in warping of cantilevered components during a secondary sintering step [184]. Kunchala and Kappagantula used infiltration of alumina nanoparticles into simulated binder jet alumina samples and showed an increase in part density and compressive strength with increasing nanoparticle loading [192]. For die pressed alumina powder components, Du et al. showed that a ceramic particle coating of amorphous alumina decomposed from aluminum nitrate increased sintered density [19]. Additionally, Khoshnevis et al. used inkjet deposition of a metal salt (aluminum sulfate) ink to create a mold boundary for metal sintering – a process they called selective inhibition sintering [187]. Towards development of novel polymer binders, Gilmer et al. developed a triethylene glycol dimethacrylate binder for in-situ cross-linking during BJAM for control of green strength and binder burnout [123]. For control of composition Godlinksi and Morvan used a binder ink containing carbon black nanoparticles to create carbon-graded steel parts [193]. Techapiesancharoenkij utilized ferrite and nickel oxide particle dispersions printed on iron-nickel powder to create parts with locally tailored composition [194].

Despite the prior work summarized above, a variety of opportunities remain for the use of reactive binders in BJAM to impart initial green strength, improve densification during sintering, and improve dimensional control by mitigating warping. Nominally, with

the intent to improve part densification without sacrificing dimensional stability, the decomposition products of a reactive binder should remain at high temperatures to provide continued strength without inhibiting sintering. A great variety of metals and oxides can be produced from metal salt precursors (e.g. oxides, metallic spinels, superconducting oxides, magnetic oxides), as shown by a thin film fabrication technique known as spray pyrolysis [195–197]. This range of ceramic and metal precursors suggests that should metal salts provide adequate green strength to a powder compact, a great variety of ceramic and metallic coatings could be deposited as binders during the jetting phase of the BJAM process. This would provide an avenue for BJAM of high-density ceramic parts with dimensional control, as well as multi-phase ceramics, or composite metal-ceramic materials fabricated from dry powder feedstock. The use of sintering aids (usually by adding a fraction of 1 wt. % of aid material) in traditional processing of ceramics can greatly improve densification and microstructure, with magnesium oxide (MgO) a common additive for the microstructural control of aluminum oxide (Al_2O_3) [10,198–201]. For magnesium oxide and alumina, the use of MgO above the solubility limit of 300 ppm stated by Peele resulted in reduced grain growth through the creation of second phase precipitates that favor densification mechanisms [10,200,201]. Thus, the development of binders to influence part microstructure through densification and dimensional control is an intriguing approach for BJAM of ceramics.

This chapter presents the development and application of reactive metal salt binders to BJAM, with improved part strength during sintering over polymer binders and microstructural control of part porosity, interparticle geometry, and shrinkage during sintering. Chapter 4 described a development process for inks for BJAM, showcasing the implementation of the process for a reactive metal salt ink incorporating aluminum nitrate [202]. Additionally, Chapter 3 described the development of a mechanized, modular, precision BJAM testbed for capable of processing custom powders and binders [203]. Accordingly, this chapter presents the development of inks utilizing aluminum nitrate and magnesium nitrate metal salts, and their implementation in BJAM of alumina components, to improve green strength and control microstructure during sintering. To our knowledge, this is the first implementation of a binder ink that converts to a sintering aid for a ceramic

component fabricated via BJAM. As shown by the findings in this work, the selection of reactive binders can influence the densification, shrinkage, and part strength of BJAM components, with improvements over polymer-based binders.

6.2 Method

6.2.1 Powder characterization

Aluminum oxide (alumina, Al_2O_3) powder of 99.5+% purity and alpha-phase composition with a 20 μm nominal particle size and spherical shape (Inframat Advanced Materials, 26R-8S20) was used for this study. Particle size distribution measurement was performed using laser diffraction (Malvern Panalytical Masterisizer 2000). For SEM imaging, powder was gold coated with ~8 nanometers (Quorum Technologies SC7640 Sputter Coater, 60 second coating). SEM imaging was performed using a JEOL JSM-6010LA. Particle size analysis and SEM imaging for the as-received powder, shown in Figure 6.3, highlighted the spherical nature of the powders and characterized the particle size distribution as D_{10} = 10.1 μm, D_{50} = 21.6 μm, and D_{90} = 39.0 μm.

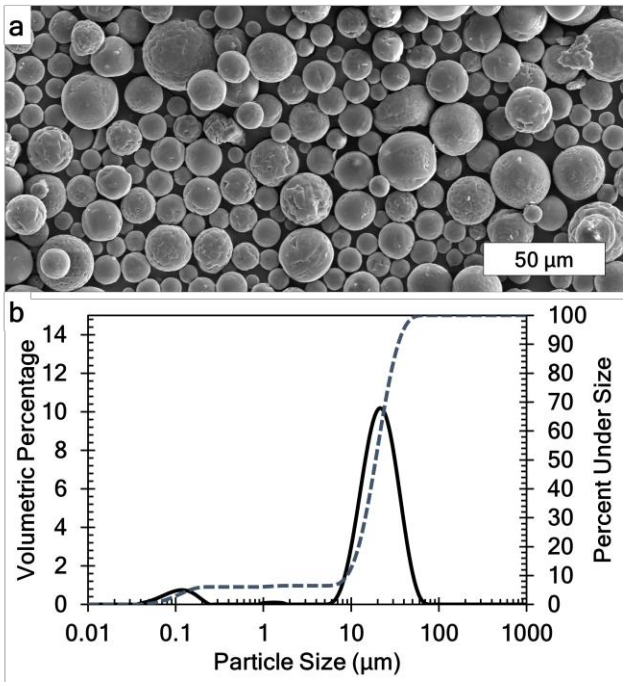

Figure 6.3: (a) SEM image of aluminum oxide powder and (b) particle size distribution of aluminum oxide powder characterized by laser diffraction.

6.2.2 Binder development and characterization

Four binder inks were synthesized for this study: one polymer-based (polyethylene glycol or PEG), and three metal salt (i.e., aluminum nitrate, magnesium nitrate) based binders. The compositions of each binder ink, with respective solvent and solid contents, and mass after decomposition estimated by stoichiometry are listed in Table 6.1. The starting materials for the binders included deionized (DI) water, 200 proof ethanol (Sigma-Aldrich 459836), aluminum nitrate nonahydrate ≥98% (Sigma-Aldrich 237973), magnesium nitrate hexahydrate 99% (Sigma-Aldrich 237175), and polyethylene glycol 6000 (Alfa Aesar A1754130). PEG was selected as the polymer binder as prior work by the authors showed its application to binder jet AM and use of ethylene glycol-based binders in literature[3,111,153,202]. Aluminum nitrate was selected as a reactive metal salt binder as it decomposes into aluminum oxide and has been previously used by the authors in jetting studies [202]. Magnesium nitrate was selected as a reactive metal salt binder as it

decomposes into magnesium oxide (magnesia, MgO), which is commonly used as a sintering aid for aluminum oxide (i.e., the selected powder). To create each binder ink, the solvent mixture was combined first (e.g., DI water/ethanol), then the solid binder (i.e., PEG or metal nitrate) was added to the solvent mixture and dissolved using a vortex mixer (Four E's Scientific Digital Vortex Mixer) at 3000 rpm for 5 minutes.

Table 6.1: Composition of custom developed polymer and reactive binders.

Binder	**Solvent**	**Solids Content**	**Estimated Remaining Mass**
PEG 6K	DI water and ethanol (20% molar fraction ethanol)	10% mass fraction of PEG 6000 (6K) to solvent	0% - full binder burn-off
Al-Nit	DI water and ethanol (50% volume fraction ethanol)	1.5 molar concentration of aluminum nitrate (39.1% salt mass fraction)	5.3% mass (1.9% volume) of aluminum oxide
Mg-Nit	DI water and ethanol (50% volume fraction ethanol)	1.5 molar concentration of magnesium nitrate (30.5% salt mass fraction)	4.8% mass (1.7% volume) of magnesium oxide
Al/Mg-Nit	DI water and ethanol (50% volume fraction ethanol)	0.16 molar concentration of magnesium nitrate, 1.33 molar concentration of aluminum nitrate (38.1% total salt mass fraction)	5.2% total mass (1.9% total volume), 0.5% mass (0.2% volume) of magnesium oxide*, 5.2% mass (1.7% volume) of aluminum oxide
*this binder composition results in ~1000 ppm mass (or 0.1% mass content) of MgO to Al_2O_3 (powder and decomposed nitrate) which is greater than the solubility limit of MgO to Al_2O_3 reported by Peele (300 ppm) [201].			

The viscosity of each binder ink was measured using a viscometer (Rheosense m-VROC) at a shear rate of 25,000 1/s, with temperature controlled between 26-27°C by a recirculating chiller (Solid State Cooling Systems ThermoCube). Surface tension measurements were performed using a tensiometer (DataPhysics DCAT 11) with Wilhelmy plate (DataPhysics PT 11, platinum-iridium, 10 mm length, 19.9 mm width, 0.2 mm thickness) using DCAT software for data collection, with the ambient temperature for measurements between 22-23°C. Density measurements were performed using a 50 mL

graduated cylinder (Karter Scientific, 1 mL graduations, +/-0.5 mL) and digital scale (Ohaus Corporation DV215CD, 0.01 mg resolution) at ambient temperature of 21.3°C. A summary of the rheological data is show in Table 6.2.

Table 6.2: Summary of rheological data for binders.

Binder	**Surface Tension (mN/m)**	**Viscosity (cP) 25,000 1/s shear rate**	**Density (g/cm^3)**	**Droplet Diameter (µm)**	**Droplet Velocity (m/s)**
PEG 6K	30.88 ± 0.02	6.95 ± 0.18	0.94 ± 0.01	67.9 ± 0.9	2.7 ± 0.2
Al-Nit	33.59 ± 0.02	6.46 ± 0.03	1.12 ± 0.01	65.3 ± 1.8	2.9 ± 0.3
Mg-Nit	32.33 ± 0.03	6.83 ± 0.06	1.06 ± 0.01	62.2 ± 3.1	1.7 ± 0.2
Al/Mg-Nit	33.14 ± 0.03	10.22 ± 0.22	1.11 ± 0.01	62.4 ± 0.9	1.0 ± 0.1

Thermal decomposition of the binders was performed using combined thermogravimetric analysis and differential scanning calorimetry (Mettler Toledo TGA/DSC1) in an alumina pan with vented cover (AdValue Technology, AL-6028 and AL-6504). Samples were run for as-received PEG 6K, aluminum nitrate nonahydrate, magnesium nitrate hexahydrate, and an aluminum nitrate nonahydrate and magnesium nitrate hexahydrate mixture (12.2 mass ratio of aluminum nitrate to magnesium nitrate, matches solid loading composition of Al/Mg-Nit binder) with a ramp rate of 5 °C/min from 30 °C to 1100 °C. X-ray diffraction (PANalytical X'Pert PRO XPRD) of metal salt samples was performed using as-received aluminum nitrate nonahydrate powder, as-received magnesium nitrate hexahydrate powder, mixed as-received aluminum nitrate nonahydrate and magnesium nitrate hexahydrate powder (12.2 mass ratio), magnesium nitrate nonahydrate heated up to 600 °C with a 1 hour hold and ramp rates of 5 °C/min in a tube furnace (Lindberg/Blue M STF55433C Tube Furnace) in air, mixed metal nitrates heated up to 600 °C with a 1 hour hold and ramp rates of 5 °C/min in the tube furnace in air, aluminum nitrate nonahydrate heated up to 1100 °C with a 1 hour hold and with ramp rates of 5 °C/min in the tube furnace in air, and mixed metal nitrates heated up to 1100 °C with a 1 hour hold and ramp rates of 5 °C/min in the tube furnace in air. The reference XRD peak values were taken from the database from HighScorePlus software (Malvern Panalytical).

For each binder, the jetting conditions were determined by taking images of the inkjet dispensing nozzle and ejected droplets using the custom optics system of the custom binder jetting testbed. The outer diameter of the nozzle tip was determined to be 600 μm using a digital microscope (Zeiss Smartzoom 5). This value was used to set the scale for images taken using the vision system, and in turn to estimate the diameter and velocity of the ejected droplets. To estimate the diameter of ink droplets ejected from the 80 μm dispensing nozzle, five different droplet images were captured at a 500 μs strobe delay and analyzed in Fiji/ImageJ to compute the droplet diameter from the droplet area estimated using the Oval Measurement tool. To estimate the droplet velocity, sequential droplet images at 250, 500, and 750 μs were taken at increasing strobe delays. The velocity was estimated using Fiji/ImageJ by dividing the change in droplet position by the change in strobe delay for the 250-750 μs images and averaged over three separate jetting sequences.

6.2.3 Binder jetting experiments

Binder jetting experiments were performed using the custom binder jetting testbed built and described by Oropeza et al [203]. A layer height of 100 μm, roller traverse speed of 5 mm/s, and roller counter-rotation of 300 RPM were used for spreading of powder layers. Powder dispensing was performed using the vibrating hopper system, with a backpressure of 10 psi. The powder hopper dispensing rate of 2.12 ± 0.38 g/s was quantifies by activating the hopper for a pressure of 10 psi for 15 seconds and measuring the dispensed mass using a digital scale, repeating the measurement procedure three times. Hopper dispensing was performed at 41.7% humidity.

Inkjet deposition of binders was performed using an 80 μm inner diameter dispensing nozzle (Microfab MJ-AT-01-080) with a 20 μm droplet spacing, 134 μm line spacing, and waveform voltage/hold time reflected in Table 6.3. To assist in drying the binder after printing each layer, the heat lamp used set to 60 second hold over build platform – the temperature of powder over the build platform reached 59.1 ± 4.2 °C maximum temperature (measured using Etekcity LaserGrip122 infrared thermometer,

emissivity setting of 0.95). After printing the desired geometry, the build platform was removed from the testbed and the printed component, along with excess powder on the build platform, were cured for 30 mins at 60°C in a porcelain furnace (Pentron Laboratory Technologies, LLC JP 1200 Porcelain Furnace). After curing, excess powder was carefully brushed away and the part was removed using soft-tipped tweezers (FEITA ESD-00). With each binder, samples in four geometries were fabricated for this study, with three shown in Figure 6.4: (a) a prism with nominal dimensions of 5 x 3 x 2.5 mm for sintering experiments, (b) a T-shape with nominal dimensions 8.5 x 1 x 2 mm top and 2.5 x 2.5 x 2mm base for binder strength experiments, and (c) a beam with nominal dimensions of 20 x 2.5 x 0.5 mm for warping experiments. Three identical samples were printed for each binder and sample geometry. Additionally, thin samples with nominal geometry of 3 x 3 x 0.5 mm were printed for imaging via SEM for each binder at different thermal stages. Binder jetting experiments were performed at ambient humidity ranging from 17-48% with an average of 34%, and temperature between 20-22°C (humidity and temperature measured by AcuRite 01080M).

Table 6.3: Jetting waveform conditions for binder jetting.

Binder	**Jetting Waveform**	
	Voltage (V)	***Dwell Time (µs)***
PEG 6K	65	20
Al-Nit	40	20
Mg-Nit	40	20
Al/Mg-Nit	40	20

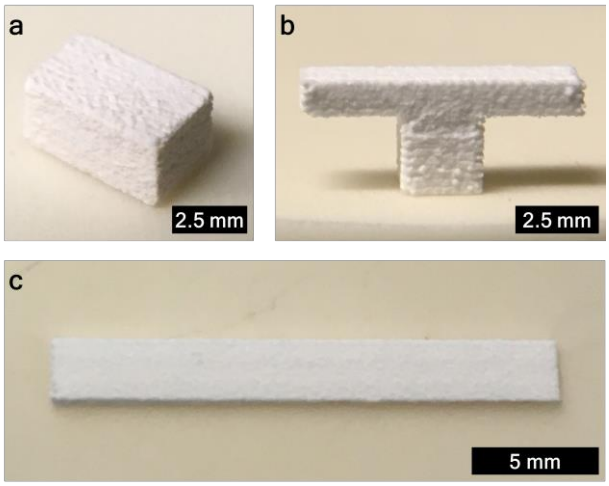

Figure 6.4: Images of exemplary alumina components fabricated by BJAM: (a) prism used for sintering experiments; (b) T-shape used for binder strength experiments; and (c) beam used for warping experiments.

6.2.4 Characterization of printed components

6.2.4.1 Green and sintered density of prism samples

Green density of all printed prism samples for sintering studies was measured using a digital microscope (Zeiss Smartzoom 5) for dimensions and the digital scale for mass. The geometric dimensions and mass were used to estimate the geometric green density of components, subtracting the estimated mass of the deposited binder solid after solvent evaporation to enable comparison of the printed density for the different binder systems with varying solid content compositions. This follows from the definition for green density utilized by Gregorski [65]. Binder solid mass was estimated from droplet diameter, droplet spacing, line spacing, and layer height. The theoretical density of 3.97 g/cm^3 of the alumina powder (provided by Inframat Advanced Materials) was used for percent of theoretical density calculations. For one prism component printed with each binder, green density was measured using micro-computed tomography (μCT), according to the parameters in Table 6.4.

After analysis in the green state, the printed samples were sintered using a box furnace (Across International GCF 1700 Atmosphere Furnace) with a 1700°C hold for 12 hours and ramp rates of 5°/min in air. An alumina separator powder sheet (C12 Advanced Technologies, SPS-AL-F) was used during sintering to facilitate sample part removal from the alumina setter disc (Advalue Technology, AL-D-42-2) after sintering. The dimensions and density after sintering were analyzed using the digital microscope and digital scale. Additionally, the sintered density of one sample printed with each binder was measured using μCT; these were the same samples previously used μCT in the green state. For all μCT measurements, reconstruction was performed automatically using the control and acquisition software (Zeiss Scout-and-Scan). Fiji/ImageJ was used for image processing of the μCT 16-bit tomograms by converting to 8-bit and thresholding (ImageJ default, IJ_IsoData) to segment the data into solid material and pores. The average content and standard deviation of solid material were calculated using the Area Fraction Measurement Tool for all tomograms. The processed tomograms were uploaded to Dragonfly (Object Research Systems, Inc.), which was used to create a reconstruction image of a central region of the CT scan (1.35 x 1.35 x 1.90 mm).

Table 6.4: Summary of parameters for μCT measurements.

Parameter	**Value**
Equipment	Zeiss Xradia 520 Versa
Source-to-detector distance (mm)	49.6
Field of view (μm x μm)	2038 x 2038
Pixel size (μm)	2.008
Voltage (kV)	80
Power (W)	7
Source filter	LE3
Exposure time (s)	1.0
Objective	4X
Field mode	Normal
Binning	2
Number of projections	3201
Cone angle (deg)	4.15
Fan angle (deg)	4.15

6.2.4.2 Evolution of T0shaped component strength during sintering

Green density for all printed T-shaped samples used for strength evolution experiments was measured using the digital microscope and digital scale, following the same procedure as for the prism samples. To assess sintering stability without additional applied load, T-shaped samples were placed base-down (Figure 6.5a) on a small alumina disc (MTI Corporation, EQ-CAL-25) and heated in air to 1300°C at a ramp rate of of 5°C/min in a tube furnace (Lindberg/Blue M STF55433C Tube Furnace). Images viewing into the furnace were taken using a DSLR camera (Canon EOS Rebel T6), a teleconverter lens (Tamron 2.0X Teleconverter TC-X20) a zoom lens (Canon EF 75-300 mm f/4-5.6 III Telephoto Zoom Lens), and a UV/IR cut filter (ICE IR/UV Cut MC 58) at 1 frame per minute. To assess compressive strength under additional load during sintering, as shown in Figure 6.5b, the T-shape component was placed top-side down on the alumina disc and another small alumina disc was placed on top of the component. The mass of the small alumina disc was 9.25g, measured using the digital scale. The assembly was heated in air and imaged using the same camera setup. The PEG binder samples were heated to 600°C and the metal salt binder samples were heated to 1300°C, with ramp rates of 5°C/min and an image acquisition rate of 1 frame per minute.

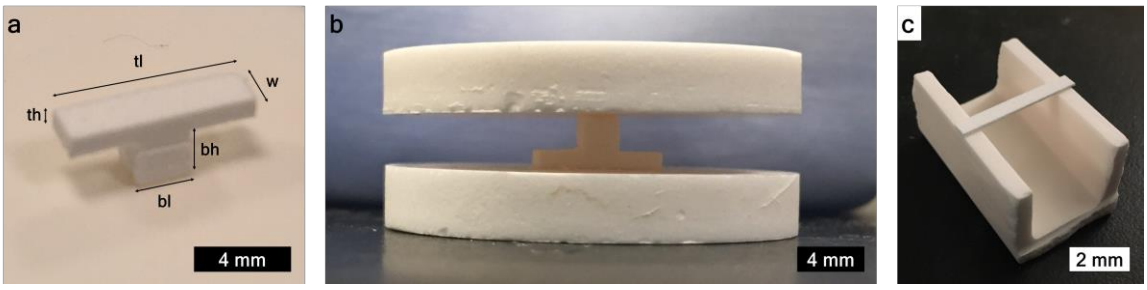

Figure 6.5: Images of configurations for dimensional stability experiments at temperature in (a) unloaded condition, (b) loaded condition, (c) beam warping experiments.

6.2.4.3 Warping of thin-beam samples

Green density for all printed beam samples used for warping experiments was measured using the digital microscope and digital scale, following the same procedure as the prism and T-shaped samples. Warping experiments were performed by placing the beam samples in a simply-supported configuration on a modified alumina combustion boat (AdValue Technology, Al-5020). The boat ends were removed to enable imaging during heating, giving the configuration shown in Figure 6.5c. Using the same furnace and imaging setup described above, the PEG binder samples were heated to 300°C, and the metal salt binder samples were heated to 1300°C, with ramp rates of 5°C/min. The image acquisition rate was 12 frames per minute for the PEG binder samples and 1 frame per minute for the metal salt binder samples. The beam deflection due to warping was calculated from the images using using Fiji/ImageJ, and was calibrated by the width of the opening of the boat (14.0 mm, measured using Mitutoyo CD-8’’-CS digital calipers).

6.2.4.4 SEM samples

Small samples for SEM were also fabricated for each binder with nominal dimensions of 3 x 3 x 0.5 mm. Samples were imaged via SEM in the as-deposited green condition, after heating for 1 hour at 600°C with ramp rates of 5°C/min in the porcelain furnace to induce binder burnout/decomposition, and after sintering for 12 hours at 1700°C with ramp rates of 5°C/min in the box furnace.

6.3 Results and discussion

6.3.1 Binder characterization

Development of reactive binders to meet the functional requirements of providing high green strength while enabling distortion-minimal consolidation requires understanding of the thermal decomposition kinetics of metal salts and evolution of binder-particle bridges with temperature. Thus, thermogravimetric analysis for the binders, shown in Figure 6.6a,

determined the peak decomposition regions and final binder mass for the different binders. PEG 6K decomposed between 180-500°C, with 0% remaining mass at 1100°C, aluminum nitrate decomposed between 100-400°C, with 13.1% remaining mass at 1100°C, and magnesium nitrate decomposed between 100-460°C, with 15.2% remaining mass at 1100°C. Additionally, the aluminum nitrate and magnesium nitrate mixture decomposed primarily between 100-400°C (as the aluminum nitrate did), with remaining mass of 16.6% at 400°C, and a secondary decomposition between 400-600°C with 13.9% remaining mass at 1100°C. The theoretical remaining mass for decomposition, calculated from stoichiometry, is 13.6% for aluminum nitrate nonahydrate to aluminum oxide, 15.7% for magnesium nitrate hexahydrate to magnesium oxide, and 13.7% for the aluminum and magnesium nitrate mixture.

XRD for the as-received and decomposed metal salts, shown in Figure 6.6b, showed the decomposition of aluminum nitrate to aluminum oxide by 1100°C and magnesium nitrate to magnesium oxide by 600°C. By combined TGA and DSC analysis, shown in Figure 6.7, the melting peaks for the binders occurred at 69°C for PEG 6K, 84°C for aluminum nitrate, 97°C for magnesium nitrate, and a primary peak at 85°C for the aluminum and magnesium nitrate mixture with decomposition peaks at 386°C for PEG 6K, 159°C for aluminum nitrate, 446°C for magnesium nitrate, and a primary peak at 166°C for the aluminum and magnesium nitrate mixture matching the regions of steepest mass loss in the TGA. The aluminum and magnesium nitrate mixture additionally appeared to have a secondary decomposition peak at 344°C, likely associated with the decoposition of the magnesium nitrate phase of the mixture.

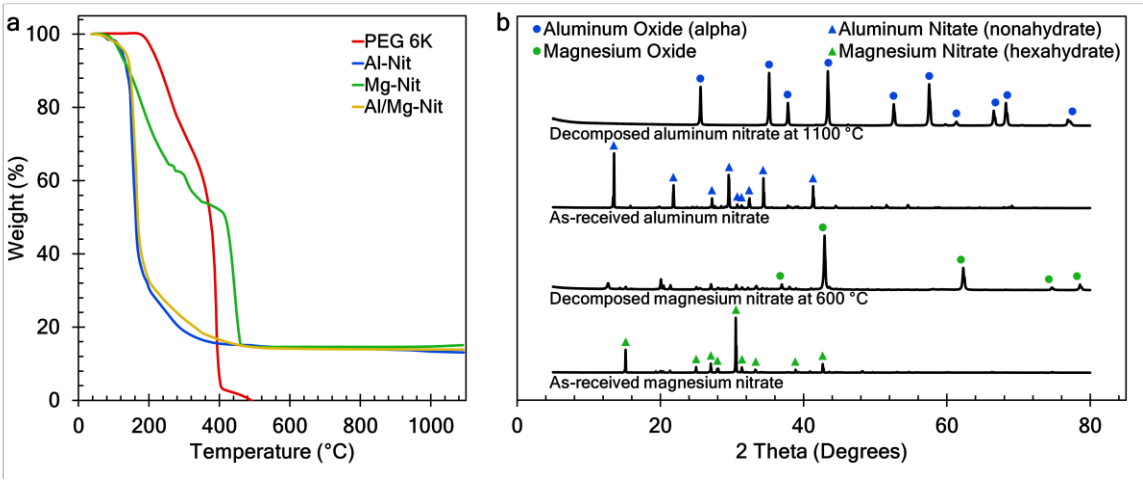

Figure 6.6: Decomposition data for binders: (a) thermogravimetric data for as-received polymer and metal salts and (b) x-ray diffraction of metal salts in as-received and decomposed conditions.

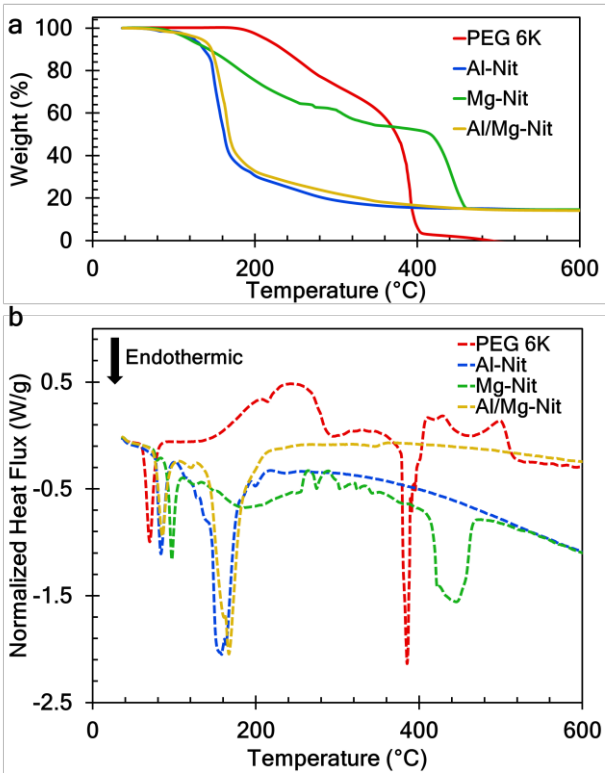

Figure 6.7: Thermal characterization of as-received binder solids: (a) TGA of binders highlighting mass loss during binder burnout and decomposition and (b) DSC highlighting melting and decomposition peaks for binders.

SEM images of the surface of exemplary (square) printed components after different thermal treatments are shown in Figure 6.8. In the as-printed state, all binders formed interparticle binder bridges – these interparticle binder bridges provide the green strength for sample removal and handling. After thermal treatment at 600°C, interparticle binder bridges were no longer visible for the PEG 6K binder, indicating full decomposition as predicted by TGA. However, for the reactive binders, interparticle bridges are visible but with a smaller contact area and more porous/fractured features than in the as-deposited state, again in agreement with remaining mass for the metal salts in TGA.

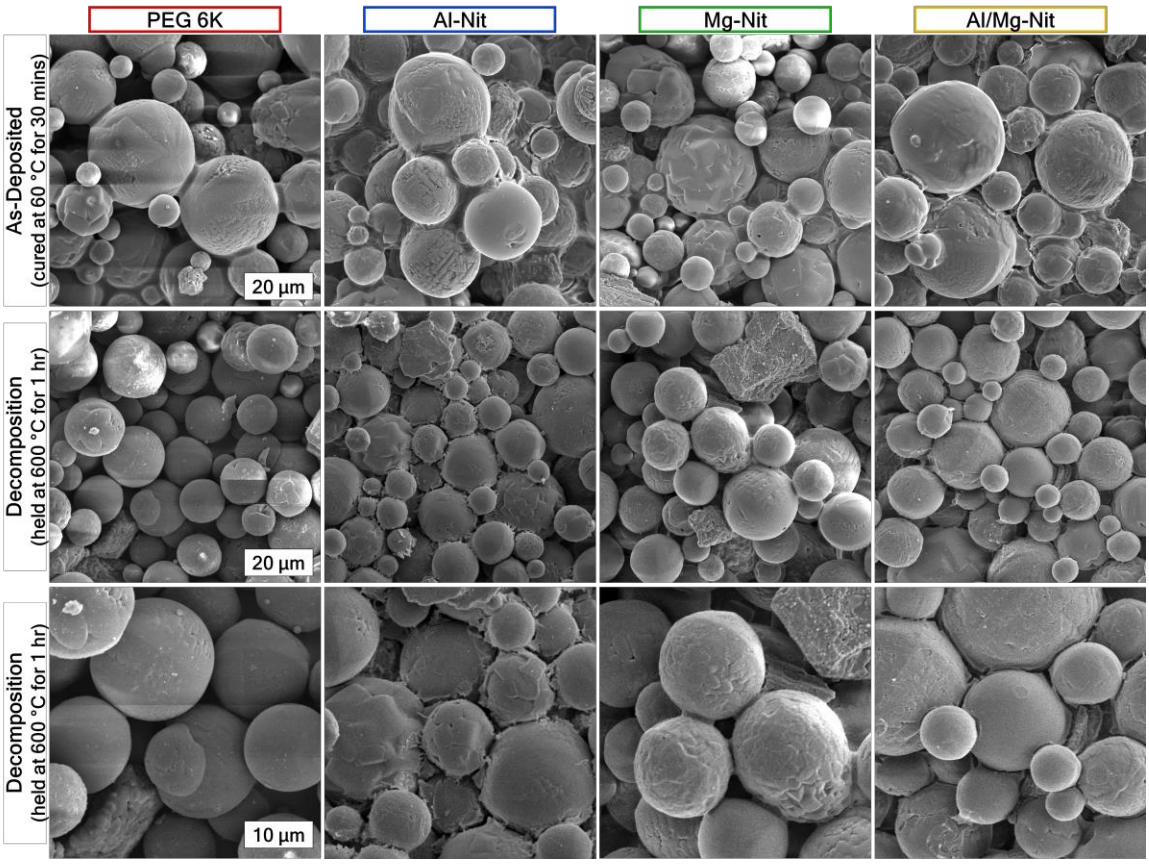

Figure 6.8: SEM images of printed samples highlighting evolution of binder interparticle bridges and sintering necks, for polymer and reactive binders in (top row) as-deposited and (middle row) decomposed states, along with close-up image of decomposed state (bottom row).

Finally, after sintering to 1700°C, signs of densification and sintering diffusion became visible for all samples (shown in Figure 6.9), with interparticle necks and particle coalescence seen for all samples. From the SEM images, it appeared that the PEG 6K, Mg-Nit, and Al/Mg-Nit binders had attained a higher degree of sintering than the Al-Nit binder, as particle consolidation was less pronounced with more interparticle necks visible for the Al-Nit binder.

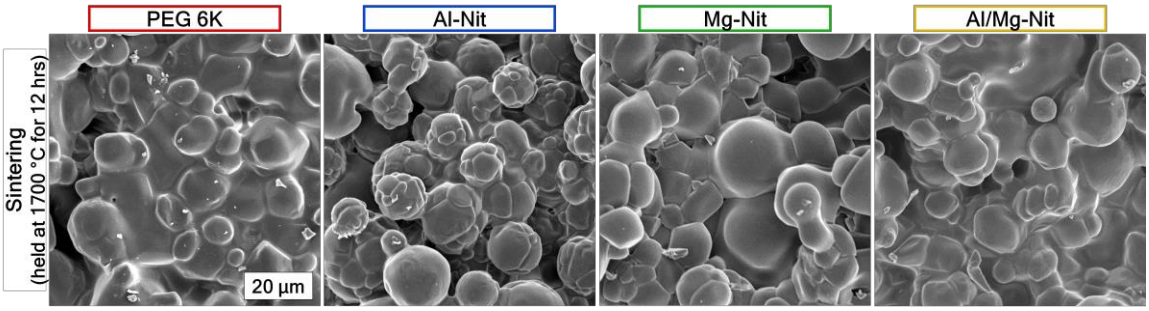

Figure 6.9: SEM images of printed samples after sintering for polymer and reactive binders.

6.3.2 Influence of reactive binders on densification during sintering

Exemplary images of the printed prism samples in the green state are shown in Figure 6.10, along with a representative tomogram from µCT characterization. The PEG 6K samples had average dimensions of 4.96 ± 0.04 x 2.97 ± 0.02 x 2.56 ± 0.02 mm in the green state, with a geometric density (i.e., using measured dimensions and mass) of 54 ± 2% of theoretical and a green density measured by µCT of 56.3 ± 0.4% of theoretical (µCT data represented as average density ± standard deviation of density between tomograms). The Al-Nit samples had average dimensions of 5.10 ± 0.04 x 3.09 ± 0.06 x 2.66 ± 0.10 mm in the green state, with a geometric density of 55 ± 1% of theoretical and a green density measured by µCT of 56.6 ± 0.7 % of theoretical. The Mg-Nit samples had average dimensions of 5.05 ± 0.02 x 2.98 ± 0.01 x 2.57 ± 0.03 mm in the green state, with a geometric density of 54 ± 1% of theoretical and a green density measured by µCT of 54.5 ± 0.7% of theoretical. The Al/Mg-Nit samples had average dimensions of 5.17 ± 0.12 x 3.09 ± 0.07 x 2.61 ± 0.01 mm in the green state, with a geometric density of 54 ± 5% of theoretical and a green density measured by µCT of 54.0 ± 0.8 % of theoretical. Sections of the µCT samples for green samples for all binders are shown in Figure 6.11.

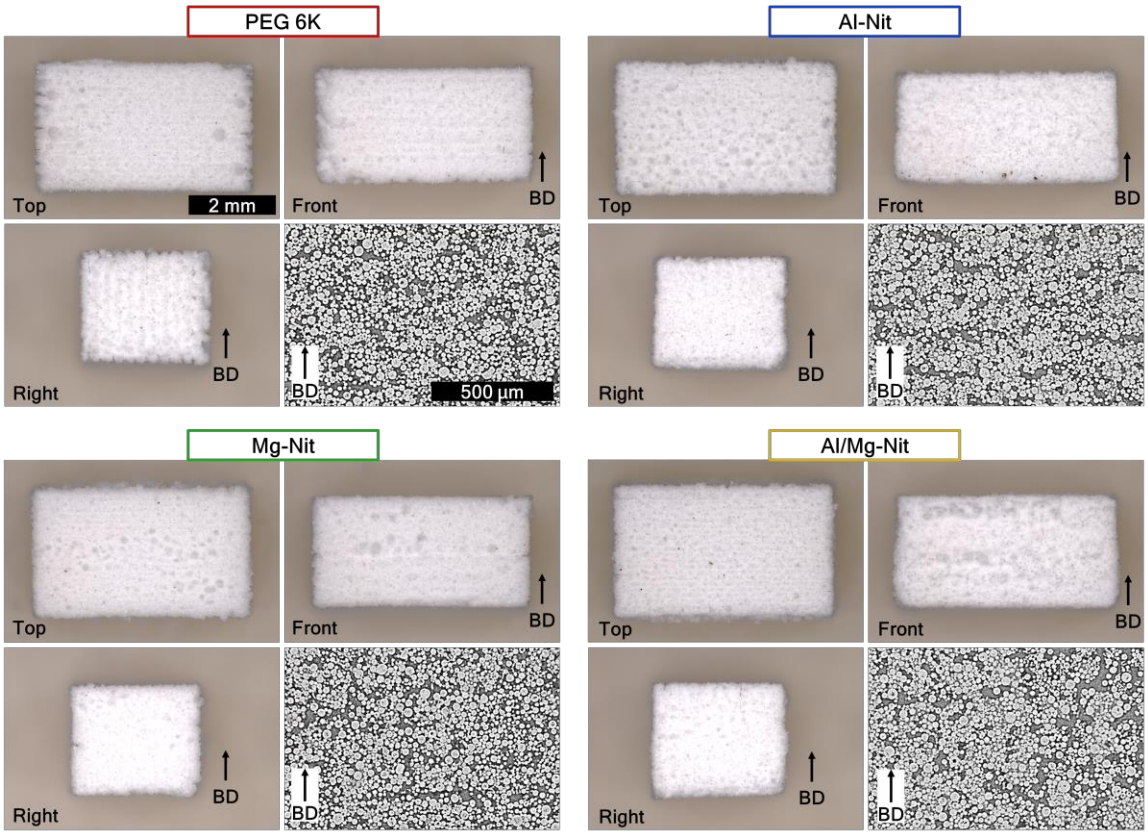

Figure 6.10: Exemplary images of as-printed (green) prism samples for polymer and reactive binders with sample tomogram from µCT characterization – BD indicates build direction.

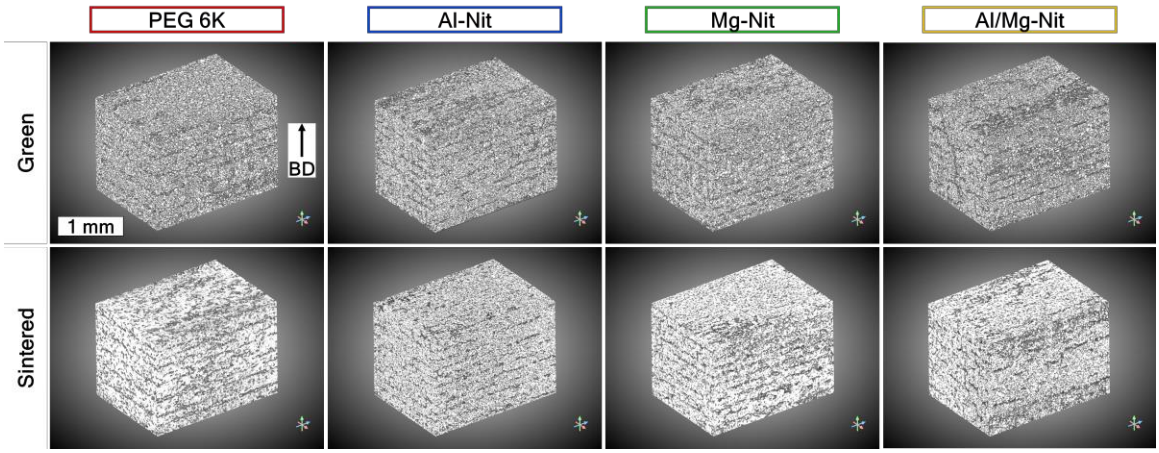

Figure 6.11: Sample sections of µCT samples for green and sintered samples for polymer and reactive binders.

Similarly, exemplary images of the printed prism samples in the sintered state are shown in Figure 6.12, along with a representative tomogram from µCT characterization. The PEG 6K samples had average dimensions of 4.60 ± 0.05 x 2.75 ± 0.03 x 2.37 ± 0.04 mm in the sintered state, with a geometric density of 70 ± 5% of theoretical and a sintered density measured by µCT of 72.2 ± 1.8% of theoretical. The Al-Nit samples had average dimensions of 4.78 ± 0.06 x 2.89 ± 0.05 x 2.48 ± 0.08 mm in the sintered state, with a geometric density of 67 ± 4% of theoretical and a sintered density measured by µCT of 66.0 ± 2.0% of theoretical. The Mg-Nit samples had average dimensions of 4.62 ± 0.03 x 2.71 ± 0.02 x 2.31 ± 0.04 mm in the sintered state, with a geometric density of 74 ± 3% of theoretical and a sintered density measured by µCT of 73.5 ± 1.0% of theoretical. The Al/Mg-Nit samples had average dimensions of 4.73 ± 0.10 x 2.83 ± 0.06 x 2.36 ± 0.04 mm in the sintered state, with a geometric density of 71 ± 5% of theoretical and a sintered density measured by µCT of 70.5 ± 1.3% of theoretical. Sections of the µCT samples for sintered samples for all binders are shown in Figure 6.11.

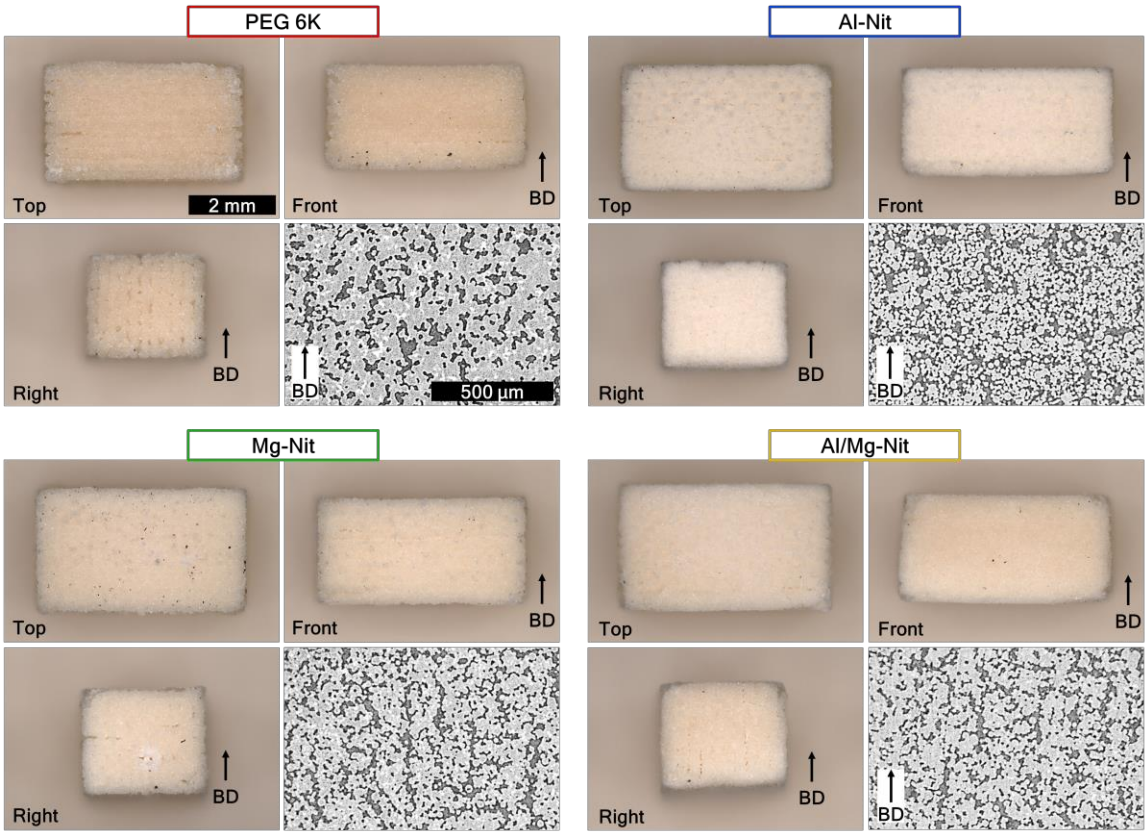

Figure 6.12: Exemplary images of sintered prism samples for polymer and reactive binders with sample tomogram from µCT characterization – BD indicates build direction.

The average geometric green and sintered density as percentages of theoretical for all samples, as well as the average linear and volumetric shrinkage percentages for all samples, is shown in Figure 6.13, with data presented as the average and standard deviation of the three samples for each binder. For the PEG binder, the density increased from 54% to 70% (+16% density) and the component shrank by 20.5 ± 2.6 % volumetric during sintering, Al-Nit achieved the lowest amount of densification (+13% density) and shrinkage (18.5 ± 1.9 % volumetric), which correlated with the limited densification that was seen in the SEM images. The mass added to the part through the decomposition of the aluminum nitrate binder to aluminum oxide accounts, on average, for 1.3% of the mass of the sintered sample (calculated using the estimated deposited binder solid mass, theoretical decomposition percentage and average mass of sintered samples), thus only a minimal fraction of the densification (+0.7% density) can be attributed to the additional mass

deposited by the reactive binder (calculated using estimated deposited binder solid mass and average volume of green part). The Al-Nit samples were hindered in densification due to the formation of the interparticle bridges of aluminum oxide (i.e., decomposed aluminum nitrate) that resulted in a longer distance for atom diffusion during sintering. However, the stability of the interparticle bridges resulted in Al-Nit having the lowest shrinkage of all the binders. The Mg-Nit binder samples achieved the greatest densification (+20% density) and shrinkage (25.3 ± 1.8 % volumetric) of all the binders. The mass added to the part through the decomposition of the magnesium nitrate binder to magnesium oxide accounts, on average, for 1.0% of the mass of the sintered sample, thus only a minimal fraction of the densification (+0.5% density) can be attributed to the additional mass deposited by the reactive binder. Thus, despite the formation of interparticle bridges of magnesium oxide (decomposed magnesium nitrate), densification was enhanced through the incorporation of the magnesium oxide. As is commonly done for ceramic processing, magnesium oxide prevents grain growth of the aluminum oxide and pins pores to the grain boundaries, thus enabling sintering with diffusion mechanisms that favor densification over grain growth [10,200]. Additionally, the Al/Mg-Nit binder also achieved greater densification (+17% density) and shrinkage (24.5 ± 1.8 % volumetric) than Al-Nit alone, suggesting that even the incorporation of small amounts of MgO (as is done in conventional ceramic powder processing [10,200]) can improve densification and overcome the deleterious effects of the aluminum oxide bridges. The mass added to the part through the decomposition of the aluminum/magnesium nitrate binder to aluminum/magnesium oxide accounts, on average, for 1.3% of the mass of the sintered sample, thus only a minimal fraction of the densification (+0.7% density change) can be attributed to the additional mass deposited by the reactive binder.

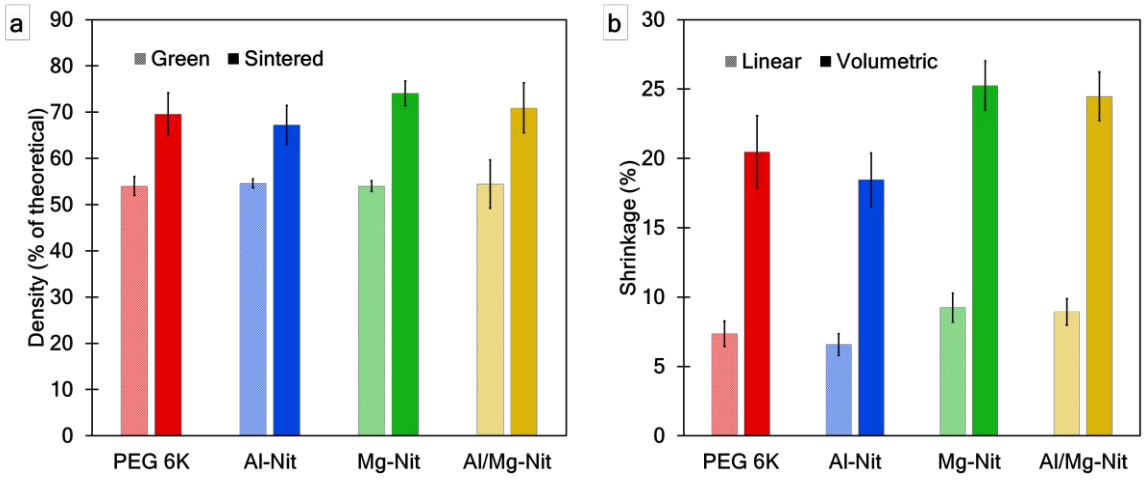

Figure 6.13: (a) Geometric green and sintered density values, and (b) average linear and volumetric shrinkage values for prism samples printed with polymer and reactive binders.

6.3.3 Binder strength evolution

To explore the evolution of binder strength with temperature, the deformation of T-shaped samples was monitored in unloaded and loaded conditions up to a temperature of 1300°C. In the unloaded condition, shown in Figure 6.14, showed that for certain geometric designs, all binders are capable of retaining shape without deformation. In this case, the binders in the solid state, the binders in the molten state, and the printed component after binder decomposition (i.e., without binder in the polymer case and with the oxide interparticle bridges in the reactive binder case) have sufficient strength for self-support without failure. For the nominal dimensions of 3 x 1 x 2mm for the cantilever and a green density of 55 % (see Table 6.5 for measured dimensions and density for T-shapes), the estimated shear stress at the cantilever root is 0.06 kPa. Thus, the strength of all binders in the solid, molten, and decomposed states exceeded 0.06 kPa in shear.

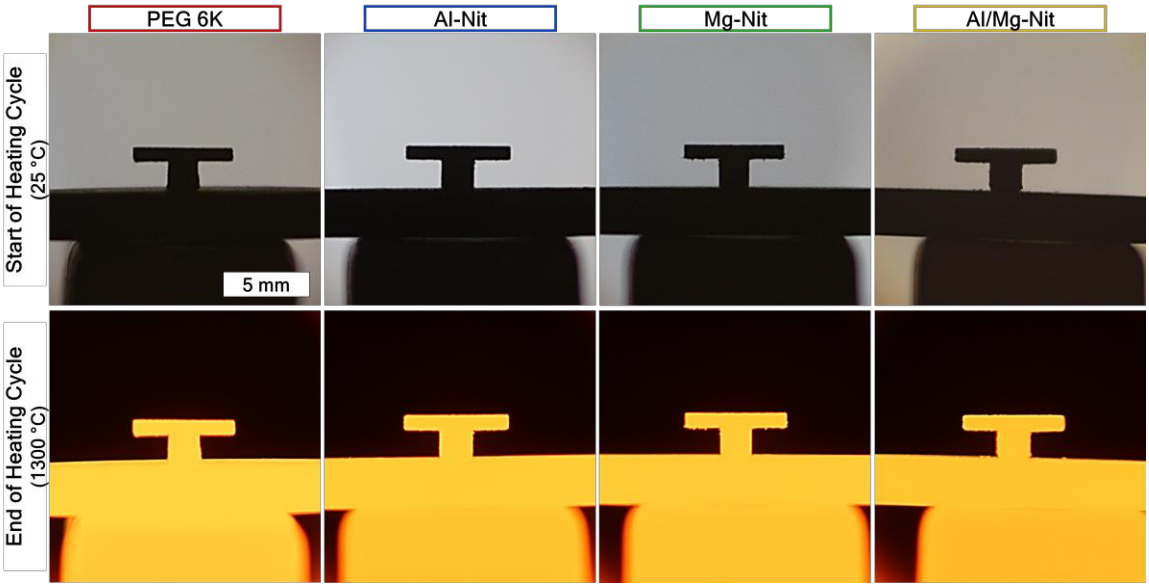

Figure 6.14: Imaging of T-shape samples (8.5 mm X 1 mm X 2 mm top and 2.5 mm X 2.5 mm X 2mm base) before and during heating to 1300 C° at 5 °C/min, showing that all binders enable processing of small, self-supported geometries.

Table 6.5: Summary of dimensions for t-shaped samples for dimensions specified in Figure 6.5.

Binder	**tl (µm)**	**th (µm)**	**bl (µm)**	**bh (µm)**	**w (µm)**	**Green Density (%)**
PEG 6K	8439 ± 36	1107 ± 23	2477 ± 19	2429 ± 18	2106 ± 22	55 ± 1
Al-Nit	8735 ± 38	1150 ± 31	2576 ± 36	2459 ± 102	2172 ± 11	55 ± 1
Mg-Nit	8525 ± 38	1121 ± 14	2551 ± 24	2403 ± 20	2048 ± 68	57 ± 1
Al/Mg-Nit	8638 ± 24	1141 ± 28	2583 ± 58	2477 ± 74	2099 ± 21	56 ± 1

When the load on the printed component was increased, by inverting the T-shape and placing an alumina disc on it (as shown in Figure 6.15), failure of the PEG 6K component and partial failure of the Mg-Nit component occurred during heating. Initial failure of the PEG binder was observed at 120 ± 7°C and complete loss of geometry (crushing) occurred at 417 ± 40°C. The sample was compressed to a pool of powder as showin in Figure 6.15. For the Al-Nit and Al/Mg-Nit binders, no compression nor warping was visible in the images, highlighting the utility of reactive binders for continued strength

during sintering. The Mg-Nit fractured at 145 ± 7°C, but did not result in complete loss of geometry as the PEG 6K sample did. The sample fractured due to shear of the base as a result of the weakened strength of the Mg-Nit binder in the molten state as compared to the Al-Nit binder which has fully decomposed to a solid oxide. A near 45° fracture line is visible in the sample after removal in Figure 6.15, suggesting a brittle fracture – this agrees prior work stating that low binder volume fractions result in brittle fracture of green components [182]. From the mass of the alumina disc (9.25g) , the nominal dimensions of the T-shape base, and a green density of 55 % (see Table 6.5 for measured dimensions and density for T-shapes), the compressive strength of the compact must exceed 18 kPa to prevent failure of the component. Thus all binders showed a compressive strength in excess of 18 kPa in the solid state, samples bound by molten PEG 6K exhibited a compressive strength less than 18 kPa (shear stress of 9 kPa exceeded), the unbound powder part showed a compressive strength much lower than 18 kPa (complete loss of shape after burn-off of PEG 6K binder), the Al-Nit and Al/Mg-Nit binder-bound samples showed compressive strength above 18 kPa in the molten and decomposed states, and samples bound by molten Mg-Nit exhibited a compressive strength lower than 18 kPa (shear stress of 9 kPa exceeded). As this shear stress is 100X greater than what was experienced by the unloaded T-shape, it is reasonable that the unloaded T-shape cantilever did not incur part failure.

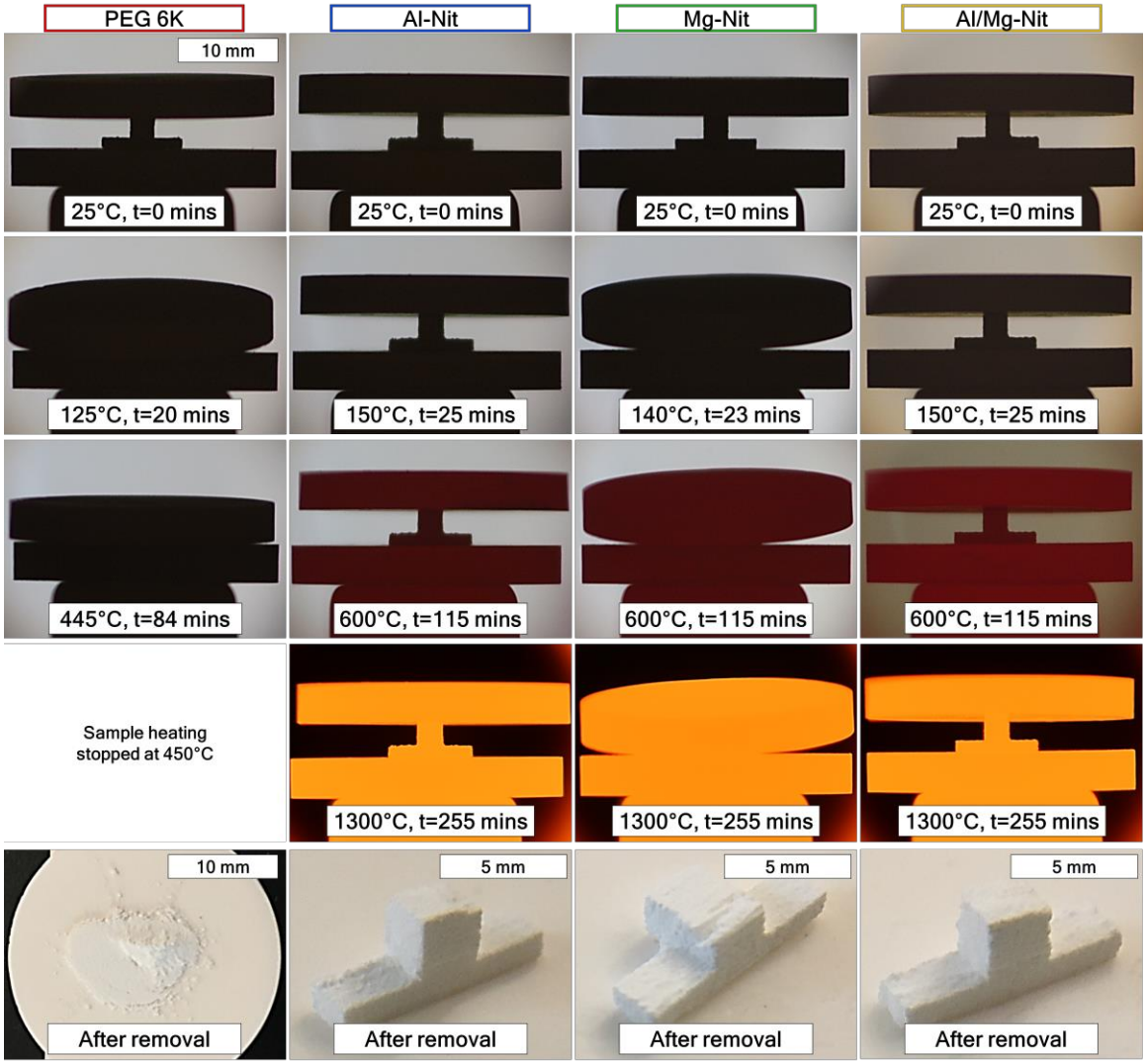

Figure 6.15: Evolution of binder strength with temperature for polymer and reactive binders in the loaded condition, highlighting the loss of strength for the polyethylene glycol (polymer) binder resulting in deformation and part failure and retained strength for metal salt binders after binder decomposition.

6.3.4 Warping

To explore the warping of components printed with different binders, the beam samples were monitored in a simply-supported condition up to 1300°C, shown in Figure 6.16.

Fracture of PEG sample beams due to strength loss during decomposition occurred at 223 ± 9°C. For the Al-Nit, a slight deformation occurred in the beam, with a maximum deflection of 0.4 ± 0.1 mm seen at 1300°C. Mg-Nit remains liquid to a much higher temperature than Al-Nit (450°C versus 160°C), and thus Mg-Nit exhibited significantly more deflection than Al-Nit, 1.3 ± 0.1 mm at 1300°C. The Al/Mg-Nit beams exhibited a deflection of 0.8 ± 0.1 mm at 1300°C – again, the introduction of magnesium nitrate with a higher decomposition temperature results in increased deformation as compared to the Al-Nit binder. Using the cantilever nominal dimensions and a green density of 55 % (see Table 6.6 for measured dimensions and density of beam samples), we estimate the shear stress on the cantilever to be 0.15 kPa, thus the strength of the binder in the solid state exceeds 0.15 kPa in shear, however the strength of the beam bound by molten PEG 6K binder is below 0.15 kPa in shear.

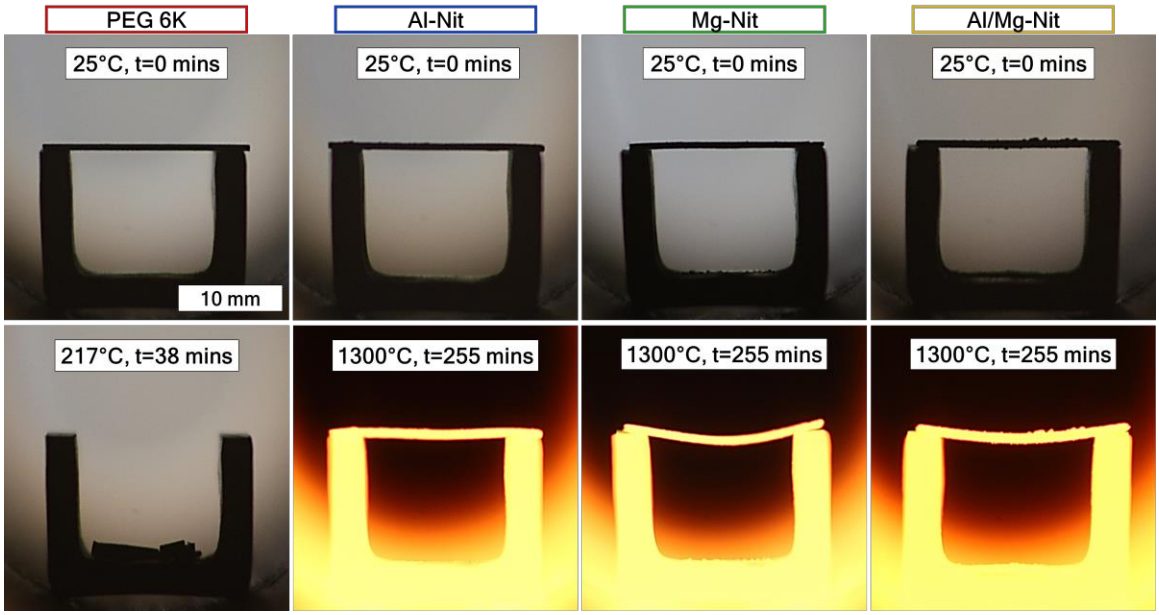

Figure 6.16: Part warping experiments using beam samples for polymer and reactive binders, highlighting loss of strength for polyethylene glycol (polymer) binder resulting in part loss and reduced deformation for reactive binders with warping dependence on reactive binder composition.

Table 6.6: Summary of dimensions for beam samples.

Binder	l (µm)	w (µm)	h (µm)	Green Density (%)
PEG 6K	20390 ± 67	2498 ± 28	628 ± 112	51 ± 9
Al-Nit	20250 ± 187	2555 ± 33	794 ± 37	53 ± 2
Mg-Nit	19631 ± 1459	2623 ± 157	770 ± 11	54 ± 3
Al/Mg-Nit	21648 ± 787	2666 ± 37	624 ± 124	54 ± 9

6.4 Conclusions

This work has presented the development and utilization of reactive binders deposited via BJAM to control the microstructure (i.e., porosity, binder bridge and interparticle geometry) and reduce geometric distortion of an aluminum oxide ceramic during sintering. The selection of reactive binder, and thus binder composition, influences the densification mechanics and part strength during sintering, with aluminum nitrate resulting in decreased densification and shrinkage compared to a polymer binder, and reactive binders that incorporate a sintering aid precursor of magnesium nitrate increasing densification and shrinkage. Additionally, the use of reactive metal salt binders resulted in increased part strength throughout the sintering process, with binders including aluminum nitrate capable of retaining the printed geometry during loaded sintering cycles while the polymer binder resulted in destruction of the part. Finally, the use of reactive metal salt binders resulted in improved geometric stability for unsupported beams, compared to the polymer binder. The densification for the experiments in this study was limited due to the use of relatively large initial particles (20 µm) of the starting ceramic material, yet still highlighted the potential benefits of utilizing reactive binders with sintering aid precursors. Future work will: explore the effect of reactive binders for parts printed with smaller particle size distributions to attempt to fabricate higher density components; perform mechanical characterization of printed components; study the evolution of material strength with temperature; investigate distortion and shrinkage, and uniformity thereof, for larger components; and study the effect of binder composition and loading on strength and distortion.

Chapter 7

Conclusion and Future Work

7.1 Summary of contributions

In summary, this thesis investigated the fundamentals of binder jet additive manufacturing utilizing custom-built equipment and developed novel binder compositions to assist in densification and dimensional control during post-processing.

In particular, the design, fabrication, and validation of a modular powder spreading testbed suited to study process fundamentals and novel adaptations of powder-based AM processes was presented. Testbed subsystems were validated using relevant measurement techniques and exemplary powder spreading experiments were performed to showcase full testbed functionality. The design, fabrication, and validation of a modular binder jetting testbed was presented. Testbed modules were validated using relevant measurement techniques and exemplary fluid jetting and binder jetting experiments were performed to showcase the system's functionality, with comparable performance to commercial testbeds (i.e., powder size on the order of 10 μm, layer height of 100 μm, inkjet droplet diameter on the order of 10 μm, printed primitive lines on the order of 100 μm and green density of 40-60%).

The development and characterization of custom polymer and reactive metal salt binders through a process that involved the exploration of binder ink rheology, binder-powder interactions, binder decomposition, and component green strength was presented. The influence of binder ink composition on the jetting and infiltration properties of each custom binder was explored. The reactive metal salt binders showcased comparable green strength to polymer binders in the as-deposited condition and continuous green strength at elevated temperatures, concurrent with the continued existence of material at the powder inter-particle necks, further suggesting the possible use of reactive binders for shrinkage and warping control of BJAM parts.

The investigation of powder spreading of ceramic powders utilizing the custom precision powder spreading testbed coupled with a non-contact, localized powder layer density measurement technique using x-ray imaging was performed. The effects of powder size, powder shape, traverse speed, roller rotation, roller surface texture and roughness, and powder dispensing mechanism were explored. Fine powders benefited from roller rotation with resultant higher layer density and uniformity, while the use of roller rotation reduced the powder layer density for coarse powders. For fine powders, lower traverse speeds resulted in higher powder layer density and uniformity. Powders with irregular shape resulted in lower powder bed densities than spherical powders due to increased interparticle friction and poorer particle packing. Surface roughness and texturing of roller did not improve layer density for fine powders. The surface geometry of the spreading implement greatly affected the spreading and powder layer density, with a roller geometry resulting in higher layer density for fine powders (with rotation) and coarse powders (without rotation) when compared to a rigid blade. Finally, the dispensing mechanism of fine powders also influenced the powder layer density – such that the use of a dispensing hopper ahead of a roller spreading implement resulted in higher layer density than a roller spreading implement with a piston-fed powder system. Tapped density presented an approximate upper limit to powder layer density for fine and coarse spherical powders.

The development and utilization of reactive binders deposited via BJAM to control the microstructure and reduce geometric distortion of an aluminum oxide ceramic during sintering were presented. The selection of reactive binder, and thus binder composition,

influenced the densification mechanics and part strength during sintering, with aluminum nitrate resulting in decreased densification and shrinkage compared to a polymer binder, and reactive binders that incorporate a sintering aid precursor of magnesium nitrate increasing densification and shrinkage. Additionally, the use of reactive metal salt binders resulted in increased part strength throughout the sintering process, with binders including aluminum nitrate capable of retaining the printed geometry during loaded sintering cycles while the polymer binder resulted in destruction of the part. Finally, the use of reactive metal salt binders resulted in improved geometric stability for unsupported beams over the polymer binder.

7.2 Future work

As always, there is further work to be done to realize the promise of AM for ceramics and other materials. This study focused solely on one ceramic material (i.e., aluminum oxide) and limited reactive metal salt compositions. The development and dissemination of custom equipment to explore the fundamentals of BJAM (i.e., powder spreading, binder development, inkjet deposition) enables the investigation of a broad variety of commonly utilized and novel powders and binders. Use of the powder spreading equipment to explore influence of finer powders, multi-modal distributions, and additional compaction schemes like vibration or roller compaction to further densify the bed is of interest. Additionally, the translation of the powder spreading characterization work to metal AM is underway and of great interest for powder-bed based AM methodologies. Further in-situ imaging of the powder spreading process could additionally assist in understanding interactions between powder and spreading implements, as well as provide data for calibration of powder spreading simulations. Finally, the use of the powder spreading testbed to develop flowabilty and spreadability metrics for powder from first principles is of great interest, particularly if simplified powder characterization experiments can be correlated with the metrics.

Additional development of custom binders, utilizing the described process could lead to further improvements in part dimensional stability and microstructural control. Also, the formation of composite materials, or encapsulated materials, is possible with the reactive binder jet AM approach. Additional characterization of decomposition kinetics will lead to a deeper understanding for the evolution of the binder material and thus its influence on strength and microstructural control. Additional use of the inkjet system and binder development process to fabricate inks for hybrid AM processes for microstructural control is already under way. Further work is required to fabricate larger BJAM samples for characterization of mechanical properties and correlation to sample microstructure. Additional sample fabrication could further enable a deeper understanding of the evolution of binder strength during sintering by coupling with in-situ mechanical testing. Coupling of reactive BJAM with the spreading of finer powders is of additional interest to further improve densification of components fabricated via BJAM.

7.3 Outlook

This thesis has demonstrated the following:

- Development of a precision, mechanized, motorized, multi-layer powder spreading testbed
- Development of a binder jet additive manufacturing testbed with full control over machine parameters
- Description of a development process for novel binder inks for use in BJAM
- Characterization of strength of reactive metal salt binders as equivalent or greater than polymer binders in the green state, with sustained strength after thermal treatment
- Influence of powder feedstock characteristics and machine spreading parameters on the formation of dense and homogenous powder layers

These achievements have enabled a deeper understanding of BJAM fundamentals and the fabrication of ceramic components with controlled microstructure through binder selection. Additionally, this work is anticipated to provide the AM community with the means of further accomplishing:

- Determination of optimal powder feedstock for fabrication of high-density layers
- Deposition of fine powders, with improved densification kinetics, through optimized deposition and spreading parameter selection
- Control of component microstructure, and thus macro-scale properties, through selection of reactive binder composition

As a whole, these contributions and anticipated future work will further enhance the fabrication of ceramics via AM. Optimization of powder spreading through feedstock and machine parameter selection and development of binders to tailor microstructural composition will combine to provide high-density, composition-controlled, high-quality fabrication of ceramics for incorporation into commercial applications.

Appendix A

Experimental data for powder spreading of ceramics

This appendix includes the data for the powder spreading experiments with individual and average data presented for each case of comparisons.

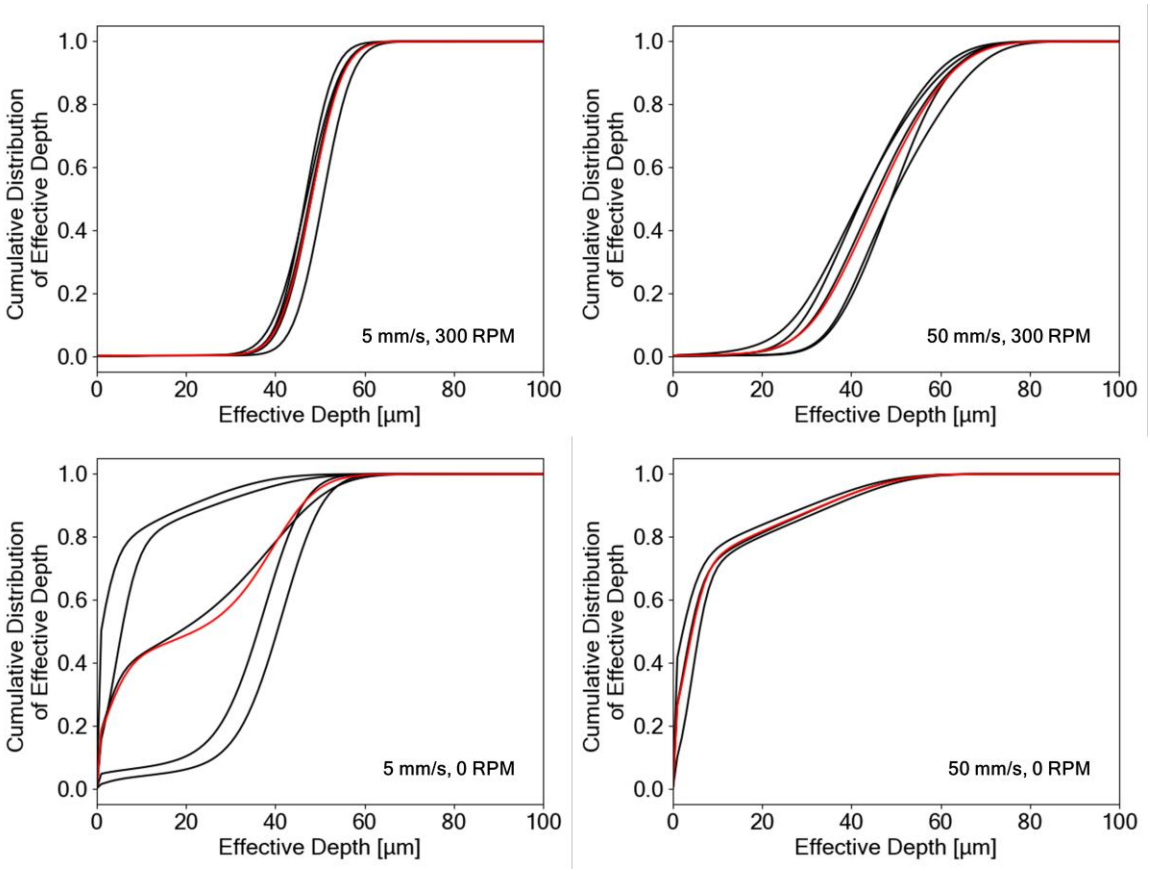

Figure A.1: Effective depth (powder layer density) measurement for 20 µm spherical aluminum oxide powder for different spreading speeds and roller rotation parameters, showing individual measurements (black) and average effective depth (red).

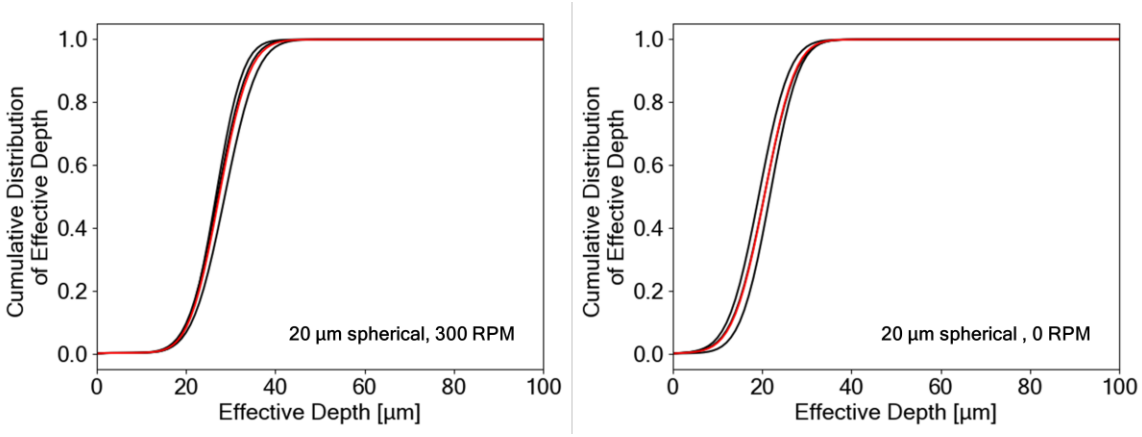

Figure A.2: Effective depth (powder layer density) measurement for 20 µm irregular aluminum oxide powder for 5 mm/s translational spreading speed and different roller rotation parameters, showing individual measurements (black) and average effective depth (red).

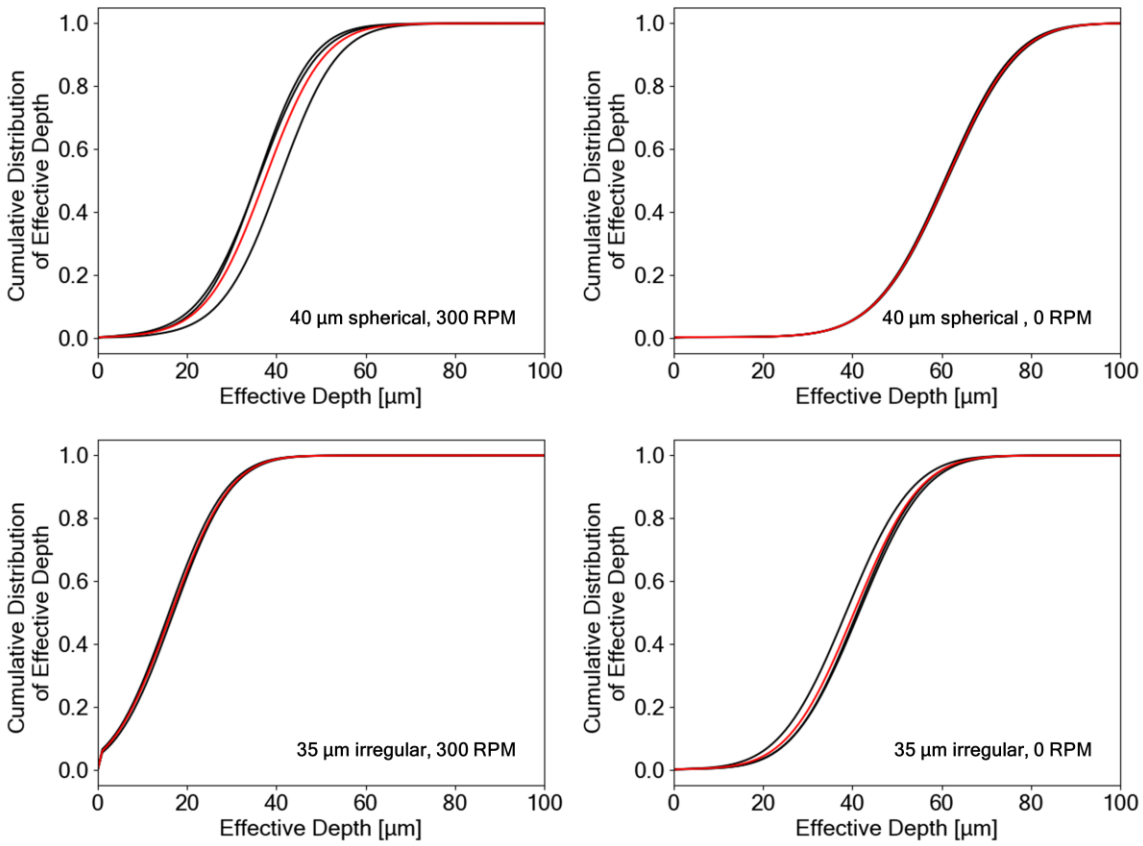

Figure A.3: Effective depth (powder layer density) measurement for 40 µm spherical and 35 µm irregular aluminum oxide powder for 5 mm/s translational spreading speed and different roller rotation parameters, showing individual measurements (black) and average effective depth (red).

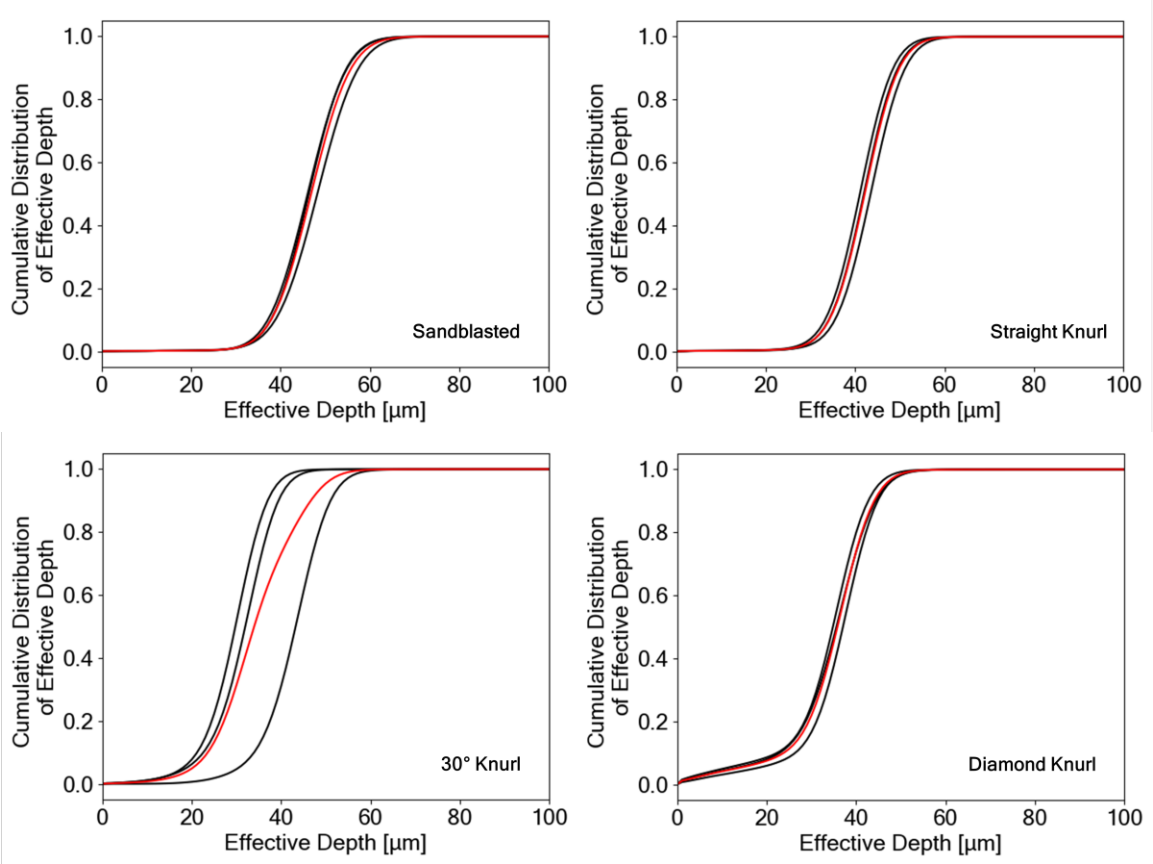

Figure A.4: Effective depth (powder layer density) measurement for 20 µm spherical aluminum oxide powder for 5 mm/s traverse speed, 300 RPM roller rotation parameters, and different roller surface textures, showing individual measurements (black) and average effective depth (red).

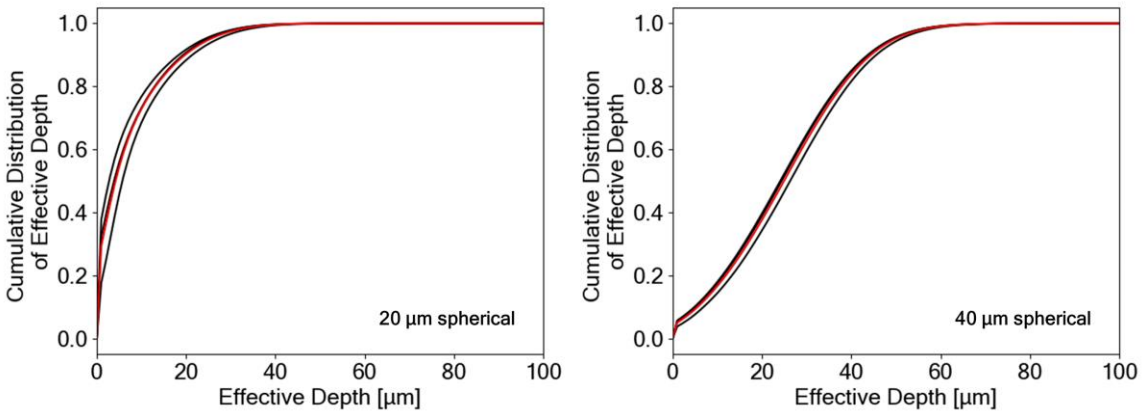

Figure A.5: Effective depth (powder layer density) measurement 20 µm spherical and 40 µm spherical aluminum oxide powder for 5 mm/s traverse speed, for blade recoater, showing individual measurements (black) and average effective depth (red).

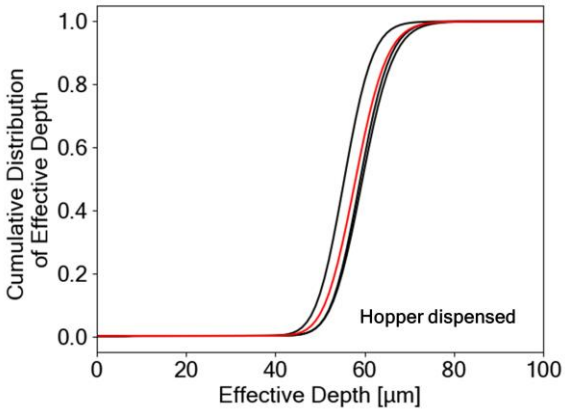

Figure A.6: Effective depth (powder layer density) measurement for 20 µm spherical aluminum oxide powder for 5 mm/s traverse spreading speed, 300 RPM roller rotation, with vibrating hopper dispensing, showing individual measurements (black) and average effective depth (red).

Appendix B

Surface profile characterization of powder spreading rollers

This appendix includes the additional characterization of the rollers used for powder spreading, with exemplary surface profiles measured by the confocal microscope.

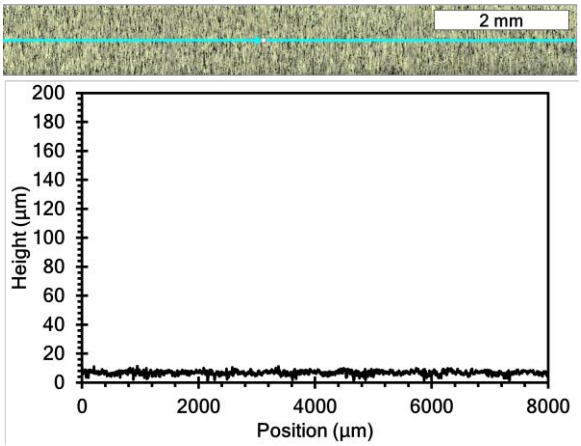

Figure B.1: Exemplary surface profile for smooth roller, with measurement line shown on microscope image of roller surface.

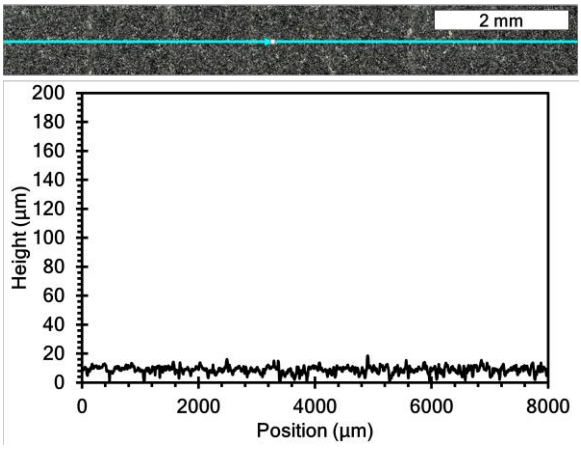

Figure B.2: Exemplary surface profile for sandblasted roller, with measurement line shown on microscope image of roller surface.

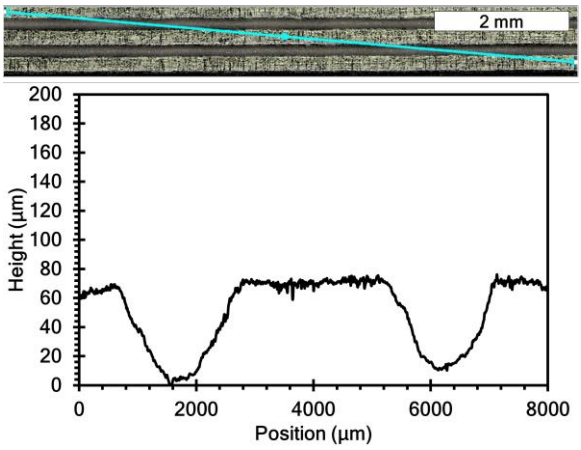

Figure B.3: Exemplary surface profile for sandblasted roller, with measurement line shown on microscope image of roller surface.

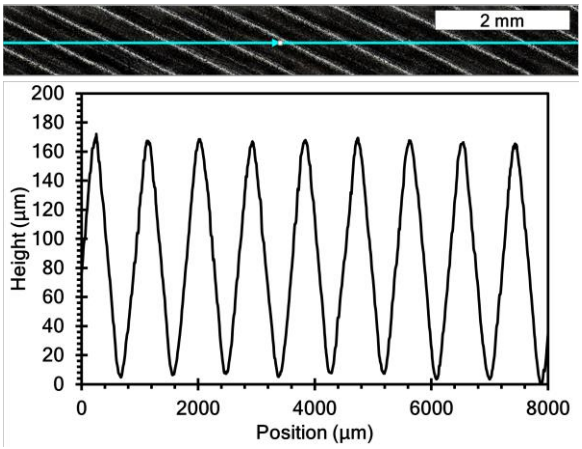

Figure B.4: Exemplary surface profile for sandblasted roller, with measurement line shown on microscope image of roller surface.

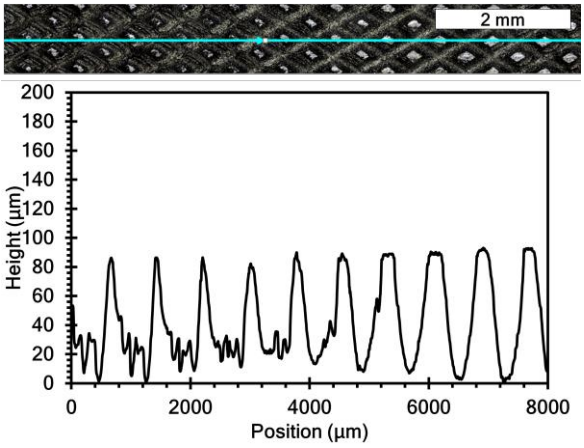

Figure B.5: Exemplary surface profile for sandblasted roller, with measurement line shown on microscope image of roller surface.

Bibliography

[1] I. Gibson, D. Rosen, B. Stucker, Additive Manufacturing Technologies: 3D Printing, Rapid Prototyping, and Direct Digital Manufacturing, 2nd ed., Springer-Verlag, New York, 2015. https://doi.org/10.1007/978-1-4939-2113-3.

[2] M. Ziaee, N.B. Crane, Binder jetting: A review of process, materials, and methods, Addit. Manuf. 28 (2019) 781–801. https://doi.org/10/gf6w3x.

[3] S. Mirzababaei, S. Pasebani, A Review on Binder Jet Additive Manufacturing of 316L Stainless Steel, J. Manuf. Mater. Process. 3 (2019) 82. https://doi.org/10/ghks76.

[4] A. Mostafaei, A.M. Elliott, J.E. Barnes, F. Li, W. Tan, C.L. Cramer, P. Nandwana, M. Chmielus, Binder jet 3D printing – Process parameters, materials, properties, and challenges, Prog. Mater. Sci. (2020) 100707. https://doi.org/10/ghjsr7.

[5] ExOne, ExOne Binder Jetting Video, n.d. https://www.youtube.com/watch?v=deA-7b3guT4&t=121s.

[6] R.M. German, Powder Metallurgy and Particulate Materials Processing: The Processes, Materials, Products, Properties and Applications, Metal Powder Industries Federation, 2005.

[7] R.M. German, A. Bose, Injection Molding of Metals and Ceramics, Metal Powder Industries Federation, 1997.

[8] M.N. Rahaman, Ceramic Processing, CRC Press, 2017.

[9] W.D. Kingery, H.K. Bowen, D.R. Uhlmann, Introduction to Ceramics, John Wiley & Sons, 1976.

[10] R.M. German, Sintering Theory and Practice, Wiley, 1996.

[11] W. Du, X. Ren, Z. Pei, C. Ma, Ceramic Binder Jetting Additive Manufacturing: A Literature Review on Density, J. Manuf. Sci. Eng. 142 (2020). https://doi.org/10/ggnhjz.

[12] X. Lv, F. Ye, L. Cheng, S. Fan, Y. Liu, Binder jetting of ceramics: Powders, binders, printing parameters, equipment, and post-treatment, Ceram. Int. 45 (2019) 12609–12624. https://doi.org/10/ggnfs5.

[13] J. Deckers, Additive Manufacturing of Ceramics: A Review, J. Ceram. Sci. Tech. (2014). https://doi.org/10/gfrkvb.

[14] J. Yoo, M.J. Cima, S. Khanuja, E.M. Sachs, Structural Ceramic Components by 3D Printing, Solid Free. Fabr. Symp. (1993) 11.

[15] Johnson Matthey, Leading the way in binder jet ceramic 3D printing | Johnson Matthey, (n.d.). https://matthey.com/en/inspiring-science/expert-insights/leading-the-way-in-binder-jet-ceramic-3d-printing (accessed June 10, 2021).

[16] D.W. Richerson, W.E. Lee, Modern Ceramic Engineering: Properties, Processing, and Use in Design, Fourth Edition, CRC Press, 2018.

[17] T. Ohji, M. Singh, Engineered Ceramics: Current Status and Future Prospects, John Wiley & Sons, 2015.

[18] W. Du, X. Ren, C. Ma, Z. Pei, Binder Jetting Additive Manufacturing of Ceramics: A Literature Review, in: American Society of Mechanical Engineers Digital Collection, 2018. https://doi.org/10/gkhrhf.

[19] W. Du, X. Ren, C. Ma, Z. Pei, Ceramic binder jetting additive manufacturing: Particle coating for increasing powder sinterability and part strength, Mater. Lett. 234 (2019) 327–330. https://doi.org/10.1016/j.matlet.2018.09.118.

[20] J. Moon, J.E. Grau, V. Knezevic, M.J. Cima, E.M. Sachs, Ink-Jet Printing of Binders for Ceramic Components, J. Am. Ceram. Soc. 85 (2002) 755–762. https://doi.org/10/cngrvn.

[21] L.A. Chavez, P. Ibave, B. Wilburn, D. Alexander, C. Stewart, R. Wicker, Y. Lin, The Influence of Printing Parameters, Post-Processing, and Testing Conditions on the Properties of Binder Jetting Additive Manufactured Functional Ceramics, Ceramics. 3 (2020) 65–77. https://doi.org/10/gkhx9c.

[22] L.O. Grant, M.B. Alameen, J.R. Carazzone, C.F.H. Iii, Z.C. Cordero, Mitigating Distortion During Sintering of Binder Jet Printed Ceramics, Solid Free. Fabr. Symp. (2018) 8.

[23] S.A.M. Tofail, E.P. Koumoulos, A. Bandyopadhyay, S. Bose, L. O'Donoghue, C. Charitidis, Additive manufacturing: scientific and technological challenges, market uptake and opportunities, Mater. Today. 21 (2018) 22–37. https://doi.org/10/gc6dhj.

[24] A. Allison, Additive Manufacturing: Strategic Research Agenda, AM Platform, 2014.

[25] A. Paolini, S. Kollmannsberger, E. Rank, Additive manufacturing in construction: A review on processes, applications, and digital planning methods, Addit. Manuf. 30 (2019) 100894. https://doi.org/10/gf927b.

[26] T. Wohlers, I. Campbell, O. Diegel, R. Huff, J. Kowen, Wohlers Report 2020: 3D Printing and Additive Manufacturing Global State of the Industry, Wohlers Associates, Inc, 2020.

[27] S.F.S. Shirazi, S. Gharehkhani, M. Mehrali, H. Yarmand, H.S.C. Metselaar, N.A. Kadri, N.A.A. Osman, A review on powder-based additive manufacturing for tissue engineering: selective laser sintering and inkjet 3D printing, Sci. Technol. Adv. Mater. 16 (2015) 033502. https://doi.org/10/gcpt74.

[28] F.H. Froes, R. Boyer, Additive Manufacturing for the Aerospace Industry, Elsevier, 2019.

[29] Z. Chen, Z. Li, J. Li, C. Liu, C. Lao, Y. Fu, C. Liu, Y. Li, P. Wang, Y. He, 3D printing of ceramics: A review, J. Eur. Ceram. Soc. 39 (2019) 661–687. https://doi.org/10/gf6fct.

[30] E. Herderick, Additive Manufacturing of Metals: A Review, Mater. Sci. Technol. (2011) 13.

[31] J.-P. Kruth, G. Levy, R. Schindel, T. Craeghs, E. Yasa, Consolidation of polymer powders by selective laser sintering, in: Proc. 3rd Int. Conf. Polym. Moulds Innov., 2008: pp. 15–30.

[32] S.C. Ligon, R. Liska, J. Stampfl, M. Gurr, R. Mülhaupt, Polymers for 3D Printing and Customized Additive Manufacturing, Chem. Rev. 117 (2017) 10212–10290. https://doi.org/10/gbwvfg.

[33] B. Nagarajan, Z. Hu, X. Song, W. Zhai, J. Wei, Development of Micro Selective Laser Melting: The State of the Art and Future Perspectives, Engineering. 5 (2019) 702–720. https://doi.org/10/gj5rrd.

[34] L.I. Escano, N.D. Parab, L. Xiong, Q. Guo, C. Zhao, K. Fezzaa, W. Everhart, T. Sun, L. Chen, Revealing particle-scale powder spreading dynamics in powder-bed-based additive manufacturing process by high-speed x-ray imaging, Sci. Rep. 8 (2018) 15079. https://doi.org/10/gfgfn9.

[35] H. Chen, Q. Wei, Y. Zhang, F. Chen, Y. Shi, W. Yan, Powder-spreading mechanisms in powder-bed-based additive manufacturing: Experiments and computational modeling, Acta Mater. 179 (2019) 158–171. https://doi.org/10/gkf89w.

[36] I. Gibson, D. Shi, Material properties and fabrication parameters in selective laser sintering process, Rapid Prototyp. J. 3 (1997) 129–136. https://doi.org/10/dh4bhj.

[37] S. Leuders, M. Thöne, A. Riemer, T. Niendorf, T. Tröster, H.A. Richard, H.J. Maier, On the mechanical behaviour of titanium alloy TiAl6V4 manufactured by selective laser melting: Fatigue resistance and crack growth performance, Int. J. Fatigue. 48 (2013) 300–307. https://doi.org/10/f4qdvp.

[38] A.D. Zwiren, T.F. Murphy, Comparison of Ss-316l Pm Material Processed Via Binder Jetting with Ss-316l Powder Processed by Pressing and Sintering, Int. J. Powder Metall. 54 (2018) 39–50.

[39] R.M. German, Particle Packing Characteristics, Metal Powder Industries Federation, 1989.

[40] R.M. German, Theory of thermal debinding, Int J Powder Met. 23 (1987) 237–245.

[41] T. Fan, Droplet-powder impact interaction in three dimensional printing, Thesis, Massachusetts Institute of Technology, 1996. https://dspace.mit.edu/handle/1721.1/10948 (accessed November 20, 2020).

[42] E. Sachs, M. Cima, J. Cornie, D. Brancazio, J. Bredt, A. Curodeau, T. Fan, S. Khanuja, A. Lauder, J. Lee, S. Michaels, Three-Dimensional Printing: The Physics and Implications of Additive Manufacturing, CIRP Ann. 42 (1993) 257–260. https://doi.org/10/fjxwwz.

[43] N.D. Parab, J.E. Barnes, C. Zhao, R.W. Cunningham, K. Fezzaa, A.D. Rollett, T. Sun, Real time observation of binder jetting printing process using high-speed X-ray imaging, Sci. Rep. 9 (2019) 2499. https://doi.org/10/gf7wpw.

[44] Y.S. Lee, W. Zhang, Mesoscopic Simulation of Heat Transfer and Fluid Flow in Laser Powder Bed Additive Manufacturing, Solid Free. Fabr. Symp. (2015).

[45] I.-H. Oh, N. Nomura, S. Hanada, Microstructures and Mechanical Properties of Porous Titanium Compacts Prepared by Powder Sintering, Mater. Trans. 43 (2002) 443–446. https://doi.org/10/b5jp42.

[46] M. Güden, E. Çelik, A. Hızal, M. Altındiş, S. Çetiner, Effects of compaction pressure and particle shape on the porosity and compression mechanical properties of sintered Ti6Al4V powder compacts for hard tissue implantation, J. Biomed. Mater. Res. B Appl. Biomater. 85B (2008) 547–555. https://doi.org/10/c8cjqc.

[47] J.M. Montes, F.G. Cuevas, J. Cintas, Porosity effect on the electrical conductivity of sintered powder compacts, Appl. Phys. A. 92 (2008) 375–380. https://doi.org/10/c6bdjd.

[48] R. Steinitz, Magnetic Properties of Iron Compacts in Relation to Sintering Temperature, J. Appl. Phys. 20 (1949) 712–714. https://doi.org/10/dkgs86.

[49] D.C. Jiles, C.V. Owen, W.A. Spitzig, Magnetic properties of porous iron compacts, J. Nondestruct. Eval. 6 (1987) 119–127. https://doi.org/10/cqvthz.

[50] K.H. Moyer, M.J. McDermott, M.J. Topolski, D.F. Kearney, Magnetic properties of iron alloys, Powder Technol. 30 (1981) 51–71. https://doi.org/10/fqwdgf.

[51] J. Francl, W.D. Kingery, Thermal Conductivity: IX, Experimental Investigation of Effect of Porosity on Thermal Conductivity, J. Am. Ceram. Soc. 37 (1954) 99–107. https://doi.org/10/fmqqnw.

[52] A.M. Elliott, P. Nandwana, D. Siddel, B.G. Compton, A Method for Measuring Powder Bed Density in Binder Jet Additive Manufacturing Process and the Powder Feedstock Characteristics Influencing the Powder Bed Density, Solid Free. Fabr. Symp. (2016) 7.

[53] I. Polozov, V. Sufiiarov, A. Shamshurin, Synthesis of titanium orthorhombic alloy using binder jetting additive manufacturing, Mater. Lett. 243 (2019) 88–91. https://doi.org/10.1016/J.MATLET.2019.02.027.

[54] M. Nastac, R. Lucas, A. Klein, Microstructure and Mechanical Properties Comparison of 316L Parts Produced by Different Additive Manufacturing Processes, Solid Free. Fabr. Symp. (2017) 10.

[55] E. Mendoza Jimenez, D. Ding, L. Su, A.R. Joshi, A. Singh, B. Reeja-Jayan, J. Beuth, Parametric analysis to quantify process input influence on the printed densities of binder jetted alumina ceramics, Addit. Manuf. 30 (2019) 100864. https://doi.org/10.1016/J.ADDMA.2019.100864.

[56] A. Mostafaei, P. Rodriguez De Vecchis, M.J. Buckenmeyer, S.R. Wasule, B.N. Brown, M. Chmielus, Microstructural evolution and resulting properties of differently sintered and heat-treated binder-jet 3D-printed Stellite 6, Mater. Sci. Eng. C. 102 (2019) 276–288. https://doi.org/10.1016/J.MSEC.2019.04.011.

[57] R.K. Enneti, K.C. Prough, Effect of binder saturation and powder layer thickness on the green strength of the binder jet 3D printing (BJ3DP) WC-12%Co powders, Int. J. Refract. Met. Hard Mater. 84 (2019) 104991. https://doi.org/10/ghks8x.

[58] C.L. Cramer, A.M. Elliott, J.O. Kiggans, B. Haberl, D.C. Anderson, Processing of complex-shaped collimators made via binder jet additive manufacturing of B4C and pressureless melt infiltration of Al, Mater. Des. 180 (2019) 107956. https://doi.org/10/ghks8z.

[59] M.P. Paranthaman, C.S. Shafer, A.M. Elliott, D.H. Siddel, M.A. McGuire, R.M. Springfield, J. Martin, R. Fredette, J. Ormerod, Binder Jetting: A Novel NdFeB Bonded Magnet Fabrication Process, JOM. 68 (2016) 1978–1982. https://doi.org/10/ghks87.

[60] A. Mostafaei, P. Rodriguez De Vecchis, I. Nettleship, M. Chmielus, Effect of powder size distribution on densification and microstructural evolution of binder-jet 3D-printed alloy 625, Mater. Des. 162 (2019) 375–383. https://doi.org/10/ggc6fg.

[61] K. Myers, A. Paterson, T. Iizuka, A. Klein, The Effect of Print Speed on Surface Roughness and Density Uniformity of Parts Produced Using Binder Jet 3D Printing, Solid Free. Fabr. Symp. (2019) 12.

[62] A. Budding, T.H.J. Vaneker, New Strategies for Powder Compaction in Powder-based Rapid Prototyping Techniques, Procedia CIRP. 6 (2013) 527–532. https://doi.org/10/gf7wqj.

[63] A. Zocca, C.M. Gomes, T. Mühler, J. Günster, Powder-Bed Stabilization for Powder-Based Additive Manufacturing, Adv. Mech. Eng. 6 (2014) 491581. https://doi.org/10/f57xhv.

[64] P.R. (Peter R. Baker, Three dimensional printing with fine metal powders, Thesis, Massachusetts Institute of Technology, 1997. https://dspace.mit.edu/handle/1721.1/46287 (accessed June 10, 2021).

[65] S.J. Gregorski, High green density metal parts by vibrational compaction of dry powder in three dimensional printing process, Thesis, Massachusetts Institute of Technology, 1996. https://dspace.mit.edu/handle/1721.1/8179 (accessed November 20, 2020).

[66] I. Yee, Powder Bed Surface Quality and Particle Size Distribution for Metal Additive Manufacturing and Comparison with Discrete Element Model, Masters Theses. (2018). https://doi.org/10/gkf89q.

[67] S. Cao, Y. Qiu, X.-F. Wei, H.-H. Zhang, Experimental and theoretical investigation on ultra-thin powder layering in three dimensional printing (3DP) by a novel double-smoothing mechanism, J. Mater. Process. Technol. 220 (2015) 231–242. https://doi.org/10/f66j8x.

[68] Z. Snow, R. Martukanitz, S. Joshi, On the development of powder spreadability metrics and feedstock requirements for powder bed fusion additive manufacturing, Addit. Manuf. 28 (2019) 78–86. https://doi.org/10/ghq4ss.

[69] H. Chen, Q. Wei, S. Wen, Z. Li, Y. Shi, Flow behavior of powder particles in layering process of selective laser melting: Numerical modeling and experimental verification based on discrete element method, Int. J. Mach. Tools Manuf. 123 (2017) 146–159. https://doi.org/10/gcjbq8.

[70] Y.M. Fouda, A.E. Bayly, A DEM study of powder spreading in additive layer manufacturing, Granul. Matter. 22 (2019) 10. https://doi.org/10/gg7r7f.

[71] P.S. Desai, C.F. Higgs, Spreading Process Maps for Powder-Bed Additive Manufacturing Derived from Physics Model-Based Machine Learning, Metals. 9 (2019) 1176. https://doi.org/10/gjnr54.

[72] Y. Bai, G. Wagner, C.B. Williams, Effect of Particle Size Distribution on Powder Packing and Sintering in Binder Jetting Additive Manufacturing of Metals, J. Manuf. Sci. Eng. 139 (2017). https://doi.org/10/gf7wp8.

[73] D.S. Uduwage, Binder Jet Additive Manufacturing of Stainless Steel-Hydroxyapatite Bio-composite, Grad. Theses Diss. Capstone Proj. (2015). https://cornerstone.lib.mnsu.edu/etds/432.

[74] M. Van den Eynde, L. Verbelen, P. Van Puyvelde, Assessing polymer powder flow for the application of laser sintering, Powder Technol. 286 (2015) 151–155. https://doi.org/10/f7xxwm.

[75] L. Cordova, T. Bor, M. de Smit, M. Campos, T. Tinga, Measuring the spreadability of pre-treated and moisturized powders for laser powder bed fusion, Addit. Manuf. 32 (2020) 101082. https://doi.org/10/gkhrzd.

[76] H. Chen, Y. Chen, Y. Liu, Q. Wei, Y. Shi, W. Yan, Packing quality of powder layer during counter-rolling-type powder spreading process in additive manufacturing, Int. J. Mach. Tools Manuf. 153 (2020) 103553. https://doi.org/10/gkf89v.

[77] U. Ali, Y. Mahmoodkhani, S. Imani Shahabad, R. Esmaeilizadeh, F. Liravi, E. Sheydaeian, K.Y. Huang, E. Marzbanrad, M. Vlasea, E. Toyserkani, On the measurement of relative powder-bed compaction density in powder-bed additive manufacturing processes, Mater. Des. 155 (2018) 495–501. https://doi.org/10/gkf89z.

[78] L. Tan Phuc, M. Seita, A high-resolution and large field-of-view scanner for in-line characterization of powder bed defects during additive manufacturing, Mater. Des. 164 (2019) 107562. https://doi.org/10/gg7r8p.

[79] I. Polozov, V. Sufiiarov, A. Shamshurin, Synthesis of titanium orthorhombic alloy using binder jetting additive manufacturing, Mater. Lett. 243 (2019) 88–91. https://doi.org/10/ggc6fb.

[80] Y. Bai, C.B. Williams, Binder jetting additive manufacturing with a particle-free metal ink as a binder precursor, Mater. Des. 147 (2018) 146–156. https://doi.org/10.1016/j.matdes.2018.03.027.

[81] M. Nasta, R. Lucas, A. Klein, Microstructure and Mechanical Properties Comparison of 316L Parts Produced by Different Additive Manufacturing Processes, Solids Free. Fabr. 2017. (2017).

[82] J. Liu, D.P. De Lo, Particle rearrangement during powder compaction, Metall. Mater. Trans. A. 32 (2001) 3117–3124. https://doi.org/10/bggzz8.

[83] H.F. Fischmeister, Powder Compaction: Fundamentals and Recent Developments, Proc. Inst. Mech. Eng. 196 (1982) 105–121. https://doi.org/10/dj35vw.

[84] I. Rishmawi, M. Salarian, M. Vlasea, Tailoring green and sintered density of pure iron parts using binder jetting additive manufacturing, Addit. Manuf. 24 (2018) 508–520. https://doi.org/10/ggsk9v.

[85] E.J.R. Parteli, T. Pöschel, Particle-based simulation of powder application in additive manufacturing, Powder Technol. 288 (2016) 96–102. https://doi.org/10/f77cc3.

[86] C. Meier, R. Weissbach, J. Weinberg, W.A. Wall, A.J. Hart, Critical influences of particle size and adhesion on the powder layer uniformity in metal additive manufacturing, J. Mater. Process. Technol. 266 (2019) 484–501. https://doi.org/10/ghktdt.

[87] M.J. Cima, E.M. Sachs, Three Dimensional Printing: Form, Materials, and Performance, Solid Free. Fabr. Symp. (1991) 187–194.

[88] E. Sachs, M. Cima, P. Williams, D. Brancazio, J. Cornie, Three dimensional printing: Rapid tooling and prototypes directly from a CAD model, J. Manuf. Sci. Eng. Trans. ASME. 114 (1992) 481–488. https://doi.org/10.1115/1.2900701.

[89] P. Nandwana, A.M. Elliott, D. Siddel, A. Merriman, W.H. Peter, S.S. Babu, Powder bed binder jet 3D printing of Inconel 718: Densification, microstructural evolution and challenges☆, Curr. Opin. Solid State Mater. Sci. 21 (2017) 207–218. https://doi.org/10/gc5r5n.

[90] M.T. Stawovy, K. Myers, S. Ohm, Binder jet printing of tungsten heavy alloy, Int. J. Refract. Met. Hard Mater. 83 (2019) 104981. https://doi.org/10/ghktg6.

[91] Y. Bai, C.B. Williams, An exploration of binder jetting of copper, Rapid Prototyp. J. 21 (2015) 177–185. https://doi.org/10/f68snm.

[92] T.A. Le Néel, P. Mognol, J.-Y. Hascoët, A review on additive manufacturing of sand molds by binder jetting and selective laser sintering, Rapid Prototyp. J. 24 (2018) 1325–1336. https://doi.org/10/gfktvg.

[93] M. Upadhyay, T. Sivarupan, M. El Mansori, 3D printing for rapid sand casting—A review, J. Manuf. Process. 29 (2017) 211–220. https://doi.org/10/gcgt44.

[94] E. Mendoza Jimenez, D. Ding, L. Su, A.R. Joshi, A. Singh, B. Reeja-Jayan, J. Beuth, Parametric analysis to quantify process input influence on the printed densities of binder jetted alumina ceramics, Addit. Manuf. 30 (2019) 100864. https://doi.org/10/ggnhpr.

[95] W. Du, M. Singh, D. Singh, Binder jetting additive manufacturing of silicon carbide ceramics: Development of bimodal powder feedstocks by modeling and

experimental methods, Ceram. Int. 46 (2020) 19701–19707. https://doi.org/10/ghktb6.

[96] M. Ziaee, E.M. Tridas, N.B. Crane, Binder-Jet Printing of Fine Stainless Steel Powder with Varied Final Density, JOM. 69 (2017) 592–596. https://doi.org/10/f9zc86.

[97] T. Colton, N.B. Crane, Influence of droplet velocity, spacing, and inter-arrival time on line formation and saturation in binder jet additive manufacturing, Addit. Manuf. (2020) 101711. https://doi.org/10/ghks9j.

[98] R.M. German, Sintering: From Empirical Observations to Scientific Principles, Butterworth-Heinemann, 2014.

[99] S.-J.J. Lee, Powder layer generation for three dimensional printing, Thesis, Massachusetts Institute of Technology, 1992. https://dspace.mit.edu/handle/1721.1/12452 (accessed December 29, 2020).

[100] S. Barui, H. Ding, Z. Wang, H. Zhao, S. Marathe, W. Mirihanage, B. Basu, B. Derby, Probing Ink–Powder Interactions during 3D Binder Jet Printing Using Time-Resolved X-ray Imaging, ACS Appl. Mater. Interfaces. 12 (2020) 34254–34264. https://doi.org/10/ghqqn2.

[101] Y. Bai, C. Wall, H. Pham, A. Esker, C.B. Williams, Characterizing Binder–Powder Interaction in Binder Jetting Additive Manufacturing Via Sessile Drop Goniometry, J. Manuf. Sci. Eng. 141 (2018). https://doi.org/10/gf7wpv.

[102] J.F. Bredt, Binder stability and powder/binder interaction in three dimensional printing, Thesis, Massachusetts Institute of Technology, 1995. https://dspace.mit.edu/handle/1721.1/10999 (accessed December 29, 2020).

[103] M. Esterman, Characterization of the powder/binder interaction in the three dimensional printing process, Thesis, Massachusetts Institute of Technology, 1990. https://dspace.mit.edu/handle/1721.1/13671 (accessed December 29, 2020).

[104] R.K. Holman, M.J. Cima, S.A. Uhland, E. Sachs, Spreading and Infiltration of Inkjet-Printed Polymer Solution Droplets on a Porous Substrate, J. Colloid Interface Sci. 249 (2002) 432–440. https://doi.org/10/btch83.

[105] B. Utela, D. Storti, R. Anderson, M. Ganter, A review of process development steps for new material systems in three dimensional printing (3DP), J. Manuf. Process. 10 (2008) 96–104. https://doi.org/10/fhcbqw.

[106] B.R. Utela, D. Storti, R.L. Anderson, M. Ganter, Development Process for Custom Three-Dimensional Printing (3DP) Material Systems, J. Manuf. Sci. Eng. 132 (2010). https://doi.org/10/cv4xhb.

[107] Y. Bai, C.B. Williams, Binderless Jetting: Additive Manufacturing of metal parts via jetting nanoparticles, Solid Free. Fabr. Symp. (2017) 12.

[108] R.K. Enneti, S.J. Park, R.M. German, S.V. Atre, Review: Thermal Debinding Process in Particulate Materials Processing, Mater. Manuf. Process. 27 (2012) 103–118. https://doi.org/10/drpr72.

[109] Y. Bai, C.B. Williams, Binder jetting additive manufacturing with a particle-free metal ink as a binder precursor, Mater. Des. 147 (2018) 146–156. https://doi.org/10/gdc3rb.

[110] Y. Bai, C.B. Williams, The effect of inkjetted nanoparticles on metal part properties in binder jetting additive manufacturing, Nanotechnology. 29 (2018) 395706. https://doi.org/10/ghks9f.

[111] A. Elliott, S. AlSalihi, A.L. Merriman, M.M. Basti, Infiltration of Nanoparticles into Porous Binder Jet Printed Parts, Am. J. Eng. Appl. Sci. 9 (2016). https://doi.org/10/ghks9g.

[112] P. Torabi, M. Petros, B. Khoshnevis, Selective Inhibition Sintering: The Process for Consumer Metal Additive Manufacturing, 3D Print. Addit. Manuf. 1 (2014) 152–155. https://doi.org/10/ghks9c.

[113] H.J. Yoo, Reactive binders for metal parts produced by Three Dimensional Printing, Thesis, Massachusetts Institute of Technology, 1997. https://dspace.mit.edu/handle/1721.1/32315 (accessed November 20, 2020).

[114] E.M. Sachs, C. Hadjiloucas, S. Allen, H.J. Yoo, Metal and ceramic containing parts produced from powder using binders derived from salt, US6508980B1, 2003. https://patents.google.com/patent/US6508980B1/en (accessed November 20, 2020).

[115] N.B. Crane, J. Wilkes, E. Sachs, S.M. Allen, Improving accuracy of powder-based SFF processes by metal deposition from a nanoparticle dispersion, Rapid Prototyp. J. 12 (2006) 266–274. https://doi.org/10/fmtmsh.

[116] M.L. Vlasea, B.M. Lane, F.F. Lopez, S. Mekhontsev, M.A. Donmez, Development of powder bed fusion additive manufacturing test bed for enhanced real time process control, Solid Free. Fabr. Symp. (2015) 527–539.

[117] P. Bidare, R.R.J. Maier, R.J. Beck, J.D. Shephard, A.J. Moore, An open-architecture metal powder bed fusion system for in-situ process measurements, Addit. Manuf. 16 (2017) 177–185. https://doi.org/10/ggbqkj.

[118] B. N. Turner, R. Strong, S. A. Gold, A review of melt extrusion additive manufacturing processes: I. Process design and modeling, Rapid Prototyp. J. 20 (2014) 192–204. https://doi.org/10/f6fhmc.

[119] B.N. Turner, S.A. Gold, A review of melt extrusion additive manufacturing processes: II. Materials, dimensional accuracy, and surface roughness, Rapid Prototyp. J. 21 (2015) 250–261. https://doi.org/10/f7czst.

[120] S. Vock, B. Klöden, A. Kirchner, T. Weißgärber, B. Kieback, Powders for powder bed fusion: a review, Prog. Addit. Manuf. 4 (2019) 383–397. https://doi.org/10/gg7r92.

[121] W.E. King, A.T. Anderson, R.M. Ferencz, N.E. Hodge, C. Kamath, S.A. Khairallah, A.M. Rubenchik, Laser powder bed fusion additive manufacturing of metals; physics, computational, and materials challenges, Appl. Phys. Rev. 2 (2015) 041304. https://doi.org/10/gf3jwx.

[122] C.Y. Yap, C.K. Chua, Z.L. Dong, Z.H. Liu, D.Q. Zhang, L.E. Loh, S.L. Sing, Review of selective laser melting: Materials and applications, Appl. Phys. Rev. 2 (2015) 041101. https://doi.org/10/gctr3t.

[123] D. Gilmer, L. Han, E. Hong, D. Siddel, A. Kisliuk, S. Cheng, D. Brunermer, A. Elliott, T. Saito, An in-situ crosslinking binder for binder jet additive manufacturing, Addit. Manuf. 35 (2020). https://doi.org/10/ghktcj.

[124] H. Zhao, C. Ye, S. Xiong, Z. Fan, L. Zhao, Fabricating an effective calcium zirconate layer over the calcia grains via binder-jet 3D-printing for improving the properties of calcia ceramic cores, Addit. Manuf. 32 (2020) 101025. https://doi.org/10/ghktcn.

[125] ExOne, Innovent+®, (n.d.). https://www.exone.com/en-US/3D-printing-systems/metal-3d-printers/Innovent (accessed November 20, 2020).

[126] B. Derby, Inkjet Printing of Functional and Structural Materials: Fluid Property Requirements, Feature Stability, and Resolution, Annu. Rev. Mater. Res. 40 (2010) 395–414. https://doi.org/10/dppfm2.

[127] S. Magdassi, The Chemistry Of Inkjet Inks, World Scientific, 2009.

[128] I.M. Hutchings, G.D. Martin, Inkjet Technology for Digital Fabrication, 1st ed., John Wiley & Sons, Ltd, 2013. https://doi.org/10.1002/9781118452943.

[129] D. Oropeza, R. Roberts, A.J. Hart, A modular testbed for mechanized spreading of powder layers for additive manufacturing, Rev. Sci. Instrum. 92 (2021) 015114. https://doi.org/10/ghszgr.

[130] R.M. German, A. Bose, Binder and Polymer Assisted Powder Processing, ASM International, 2020.

[131] I. Gibson, D. Rosen, B. Stucker, Additive manufacturing technologies: 3D printing, rapid prototyping, and direct digital manufacturing, second edition, 2015. https://doi.org/10.1007/978-1-4939-2113-3.

[132] E. Sachs, M. Cima, J. Cornie, Three-Dimensional Printing: Rapid Tooling and Prototypes Directly from a CAD Model, CIRP Ann. 39 (1990) 201–204. https://doi.org/10/dcqj3g.

[133] M. Ziaee, N.B. Crane, Binder jetting: A review of process, materials, and methods, Addit. Manuf. 28 (2019) 781–801. https://doi.org/10.1016/j.addma.2019.05.031.

[134] H. Miyanaji, M. Orth, J.M. Akbar, L. Yang, Process development for green part printing using binder jetting additive manufacturing, Front. Mech. Eng. 13 (2018) 504–512. https://doi.org/10/gjksxw.

[135] B.R. Utela, D. Storti, R.L. Anderson, M. Ganter, Development process for custom three-dimensional printing (3DP) material systems, J. Manuf. Sci. Eng. Trans. ASME. 132 (2010) 0110081–0110089. https://doi.org/10.1115/1.4000713.

[136] S.D. Hoath, Fundamentals of Inkjet Printing: The Science of Inkjet and Droplets, John Wiley & Sons, 2015.

[137] Y. Liu, B. Derby, Experimental study of the parameters for stable drop-on-demand inkjet performance, Phys. Fluids. 31 (2019) 032004. https://doi.org/10/gjmh2m.

[138] R. Masoodi, K.M. Pillai, eds., Wicking in Porous Materials: Traditional and Modern Modeling Approaches, 1st edition, CRC Press, Boca Raton, FL, 2012.

[139] E.W. Washburn, The Dynamics of Capillary Flow, Phys. Rev. 17 (1921) 273–283. https://doi.org/10/db48k7.

[140] M. Hilpert, A. Ben-David, Infiltration of liquid droplets into porous media: Effects of dynamic contact angle and contact angle hysteresis, Int. J. Multiph. Flow. 35 (2009) 205–218. https://doi.org/10/dbfkqd.

[141] The Critical Surface Tension of Wetting and the Role of Surfactants in Powder Wetting, in: Dispers. Powders Liq. Stab. Suspens., John Wiley & Sons, Ltd, n.d.: pp. 31–47. https://doi.org/10.1002/9783527656592.ch3.

[142] J.F. OLIVER, Wetting and Penetration of Paper Surfaces, in: Colloids Surf. Reprogr. Technol., AMERICAN CHEMICAL SOCIETY, 1982: pp. 435–453. https://doi.org/10.1021/bk-1982-0200.ch022.

[143] L. Galet, S. Patry, J. Dodds, Determination of the wettability of powders by the Washburn capillary rise method with bed preparation by a centrifugal packing technique, J. Colloid Interface Sci. 346 (2010) 470–475. https://doi.org/10/bwcnbn.

[144] A. Alghunaim, B. Zhang Newby, Influence of tube wettability on water contact angle of powders determined by capillary rise, Colloids Surf. Physicochem. Eng. Asp. 492 (2016) 79–87. https://doi.org/10/gjmh36.

[145] Z. Zhou, A. Lennon, F. Buchanan, H.O. McCarthy, N. Dunne, Binder jetting additive manufacturing of hydroxyapatite powders: Effects of adhesives on geometrical accuracy and green compressive strength, Addit. Manuf. 36 (2020) 101645. https://doi.org/10/gjmhvn.

[146] Y. Bai, C.B.B. Williams, Binderless Jetting: Additive Manufacturing of Metal Parts via Jetting Nanoparticles, Int. Solid Free. Fabr. Symp. (2017) 249–260.

[147] J.-W. Oh, S. Nahm, B. Kim, H. Choi, Anisotropy in Green Body Bending Strength due to Additive Direction in the Binder-Jetting Additive Manufacturing Process, Korean J. Met. Mater. 57 (2019) 227–235. https://doi.org/10/gjmhvt.

[148] Y. Zhou, Y. Tang, T. Hoff, M. Garon, F.Y. Zhao, The Verification of the Mechanical Properties of Binder Jetting Manufactured Parts by Instrumented Indentation Testing, Procedia Manuf. 1 (2015) 327–342. https://doi.org/10/gjmh2b.

[149] A. Zofka, D. Nener-Plante, Determination of Asphalt Binder Creep Compliance Using Depth-Sensing Indentation, Exp. Mech. 51 (2011) 1365–1377. https://doi.org/10/bfv73h.

[150] M.P. Mullarney, B.C. Hancock, Mechanical property anisotropy of pharmaceutical excipient compacts, Int. J. Pharm. 314 (2006) 9–14. https://doi.org/10/cn7ggx.

[151] R. Kuppuswamy, S.R. Anderson, L.L. Augsburger, S.W. Hoag, Estimation of capping incidence by indentation fracture tests, AAPS PharmSci. 3 (2001) 54. https://doi.org/10/bh7ch2.

[152] A. Elliott, S. Alsalihi, A.L. Merriman, M.M. Basti, Infiltration of nanoparticles into porous binder jet printed parts, Am. J. Eng. Appl. Sci. 9 (2016) 128–133. https://doi.org/10.3844/ajeassp.2016.128.133.

[153] A. Mostafaei, E.T. Hughes, C. Hilla, E.L. Stevens, M. Chmielus, Data on the densification during sintering of binder jet printed samples made from water- and gas-atomized alloy 625 powders, Data Brief. 10 (2017) 116–121. https://doi.org/10/gjksz5.

[154] S.M. Allen, E.M. Sachs, Three-dimensional printing of metal parts for tooling and other applications, Met. Mater. 6 (2000) 589–594. https://doi.org/10/fh8nv6.

[155] V.B. Fainerman, R. Miller, P. Joos, The measurement of dynamic surface tension by the maximum bubble pressure method, Colloid Polym. Sci. 272 (1994) 731–739. https://doi.org/10/dvm6n5.

[156] M.J. Qazi, S.J. Schlegel, E.H.G. Backus, M. Bonn, D. Bonn, N. Shahidzadeh, Dynamic Surface Tension of Surfactants in the Presence of High Salt Concentrations, Langmuir. 36 (2020) 7956–7964. https://doi.org/10/gjmq3r.

[157] Density and Viscosity of Concentrated Aqueous Solutions of Polyethylene Glycol | Journal of Chemical & Engineering Data, (n.d.). https://pubs.acs.org/doi/10.1021/je00015a050 (accessed April 1, 2021).

[158] S. Liu, D. Guo, G. Xie, Nanoscale lubricating film formation by linear polymer in aqueous solution, J. Appl. Phys. 112 (2012) 104309. https://doi.org/10/gjmrfx.

[159] D. Oropeza, R. Roberts, A.J. Hart, A modular testbed for mechanized spreading of powder layers for additive manufacturing, Rev. Sci. Instrum. (in press).

[160] C.V. Horie, Materials for Conservation, Second Edition: Organic consolidants, adhesives and coatings, n.d.

[161] Y.L. Wu, J. Hong, D. Peterson, J. Zhou, T.S. Cho, D.N. Ruzic, Deposition of aluminum oxide by evaporative coating at atmospheric pressure (ECAP), Surf. Coat. Technol. 237 (2013) 369–378. https://doi.org/10/f5rh33.

[162] I.F. Myronyuk, V.I. Mandzyuk, V.M. Sachko, V.M. Gun'ko, Structural and Morphological Features of Disperse Alumina Synthesized Using Aluminum Nitrate Nonahydrate, Nanoscale Res. Lett. 11 (2016) 153. https://doi.org/10/gjmts3.

[163] P. Gonzalez-Tello, F. Camacho, G. Blazquez, Density and Viscosity of Concentrated Aqueous Solutions of Polyethylene Glycol, J. Chem. Eng. Data. 39 (1994) 611–614. https://doi.org/10/fvnfxn.

[164] M. Ziaee, N.B. Crane, Binder jetting: A review of process, materials, and methods, Addit. Manuf. 28 (2019) 781–801. https://doi.org/10/gf6w3x.

[165] H.W. Mindt, M. Megahed, N.P. Lavery, M.A. Holmes, S.G.R. Brown, Powder Bed Layer Characteristics: The Overseen First-Order Process Input, Metall. Mater. Trans. A. 47 (2016) 3811–3822. https://doi.org/10/gkf89t.

[166] H. Miyanaji, K.M. Rahman, M. Da, C.B. Williams, Effect of fine powder particles on quality of binder jetting parts, Addit. Manuf. 36 (2020) 101587. https://doi.org/10/gkf89s.

[167] A.T. Sutton, C.S. Kriewall, M.C. Leu, J.W. Newkirk, POWDERS FOR ADDITIVE MANUFACTURING PROCESSES: CHARACTERIZATION TECHNIQUES AND EFFECTS ON PART PROPERTIES, Solid Free. Fabr. Symp. (2016).

[168] H.M. Beakawi Al-Hashemi, O.S. Baghabra Al-Amoudi, A review on the angle of repose of granular materials, Powder Technol. 330 (2018) 397–417. https://doi.org/10/gdfpjd.

[169] M. Simek, V. Grünwaldová, B. Kratochvíl, Comparison of Compression and Material Properties of Differently Shaped and Sized Paracetamols, Powder Part. 2017 (2016). https://doi.org/10/f9wjb5.

[170] T. Hao, Understanding empirical powder flowability criteria scaled by Hausner ratio or Carr index with the analogous viscosity concept, RSC Adv. 5 (2015) 57212–57215. https://doi.org/10/gkf89r.

[171] A. Mussatto, R. Groarke, A. O'Neill, M.A. Obeidi, Y. Delaure, D. Brabazon, Influences of powder morphology and spreading parameters on the powder bed topography uniformity in powder bed fusion metal additive manufacturing, Addit. Manuf. 38 (2021) 101807. https://doi.org/10/ghrq2x.

[172] T.-P. Le, X. Wang, K.P. Davidson, J.E. Fronda, M. Seita, Experimental analysis of powder layer quality as a function of feedstock and recoating strategies, Addit. Manuf. 39 (2021) 101890. https://doi.org/10/gh2m7q.

[173] M. Ahmed, M. Pasha, W. Nan, M. Ghadiri, A simple method for assessing powder spreadability for additive manufacturing, Powder Technol. 367 (2020) 671–679. https://doi.org/10/gkf894.

[174] M.Y. Shaheen, A.R. Thornton, S. Luding, T. Weinhart, The influence of material and process parameters on powder spreading in additive manufacturing, Powder Technol. 383 (2021) 564–583. https://doi.org/10/gh2qh7.

[175] L. Wang, A. Yu, E. Li, H. Shen, Z. Zhou, Effects of spreader geometry on powder spreading process in powder bed additive manufacturing, Powder Technol. 384 (2021) 211–222. https://doi.org/10/gkf892.

[176] S. Haeri, Y. Wang, O. Ghita, J. Sun, Discrete element simulation and experimental study of powder spreading process in additive manufacturing, Powder Technol. 306 (2017) 45–54. https://doi.org/10/f9hzff.

[177] W. Nan, M. Pasha, M. Ghadiri, Numerical simulation of particle flow and segregation during roller spreading process in additive manufacturing, Powder Technol. 364 (2020) 811–821. https://doi.org/10/gkf893.

[178] R.W. Penny, P.M. Praegla, M. Ochsenius, D. Oropeza, C. Meier, W.A. Wall, A.J. Hart, Spatial Mapping of Powder Layer Density for Metal Additive Manufacturing via X-ray Microscopy, ArXiv210313421 Phys. (2021). http://arxiv.org/abs/2103.13421 (accessed May 26, 2021).

[179] 2017 ASTM Standard B212-17, Standard Test Method for Apparent Density of Free-Flowing Metal Powders Using the Hall Flowmeter Funne, (n.d.).

[180] B. Utela, D. Storti, R. Anderson, M. Ganter, A review of process development steps for new material systems in three dimensional printing (3DP), J. Manuf. Process. 10 (2008) 96–104. https://doi.org/10.1016/j.jmapro.2009.03.002.

[181] J. Moon, J.E. Grau, V. Knezevic, M.J. Cima, E.M. Sachs, Ink-Jet Printing of Binders for Ceramic Components, J. Am. Ceram. Soc. 85 (2004) 755–762. https://doi.org/10.1111/j.1151-2916.2002.tb00168.x.

[182] S.J. Lombardo, R. Sachanandani, Models of the Strength of Green Ceramic Bodies as a Function of Binder Content and Temperature, in: Process. Prop. Adv. Ceram. Compos., John Wiley & Sons, Ltd, 2009: pp. 239–247. https://doi.org/10.1002/9780470522189.ch22.

[183] S.A. Uhland, R.K. Holman, S. Morissette, M.J. Cima, E.M. Sachs, Strength of Green Ceramics with Low Binder Content, J. Am. Ceram. Soc. 84 (2001) 2809–2818. https://doi.org/10/dm4bbd.

[184] L.O. Grant, M.B. Alameen, J.R. Carazzone, C.F. Higgs III, Z.C. Cordero, Mitigating Distortion During Sintering of Binder Jet Printed Ceramics, Solid Free. Fabr. Symp. (2018) 135–142.

[185] Powder Metallurgy, (2015). https://doi.org/10/gjmpzc.

[186] B. Mansfield, S. Torres, T. Yu, D. Wu, A Review on Additive Manufacturing of Ceramics, in: MSEC2019, Volume 1: Additive Manufacturing; Manufacturing Equipment and Systems; Bio and Sustainable Manufacturing, 2019. https://doi.org/10/gkgmgg.

[187] B. Khoshnevis, M. Yoozbashizadeh, Y. Chen, Metallic part fabrication using selective inhibition sintering (SIS), Rapid Prototyp. J. 18 (2012) 144–153. https://doi.org/10.1108/13552541211212122.

[188] S. et Al, H.J. Sachs, E.M., Hadjiloucas, C., Allen, S., Yoo, Metal and Ceramic Containing Parts Produced from Powder Using Binders Derived from Salt, 2003.

[189] Y. Bai, C.B. Williams, The effect of inkjetted nanoparticles on metal part properties in binder jetting additive manufacturing, Nanotechnology. 29 (2018). https://doi.org/10.1088/1361-6528/aad0bb.

[190] C. Hadjiloucas, Low shrinkage metal skeletons by three dimensional printing, Thesis, Massachusetts Institute of Technology, 1999. https://dspace.mit.edu/handle/1721.1/9415 (accessed March 31, 2021).

[191] N.B. Crane, Strengthening porous metal skeletons by metal deposition from a nanoparticle dispersion, Thesis, Massachusetts Institute of Technology, 2005. https://dspace.mit.edu/handle/1721.1/32385 (accessed March 31, 2021).

[192] P. Kunchala, K. Kappagantula, 3D printing high density ceramics using binder jetting with nanoparticle densifiers, Mater. Des. 155 (2018) 443–450. https://doi.org/10/ggnhnp.

[193] D. Godlinski, S. Morvan, Steel Parts with Tailored Material Gradients by 3D-Printing Using Nano-Particulate Ink, Mater. Sci. Forum. 492–493 (2005) 679–684. https://doi.org/10/dfjqfd.

[194] R. Techapiesancharoenkij, Bimetallic bars with local control of composition by three-dimensional printing, Thesis, Massachusetts Institute of Technology, 2004. https://dspace.mit.edu/handle/1721.1/16626 (accessed March 31, 2021).

[195] C. Falcony, M.A. Aguilar-Frutis, M. García-Hipólito, Spray pyrolysis technique; High-K dielectric films and luminescent materials: A review, Micromachines. 9 (2018) 1–33. https://doi.org/10.3390/mi9080414.

[196] D. Perednis, L.J. Gauckler, Thin film deposition using spray pyrolysis, J. Electroceramics. 14 (2005) 103–111. https://doi.org/10.1007/s10832-005-0870-x.

[197] P.S. Patil, Versatility of chemical spray pyrolysis technique, Mater. Chem. Phys. 59 (1999) 185–198. https://doi.org/10.1016/S0254-0584(99)00049-8.

[198] I.B. Cutler, C. Bradshaw, C.J. Christensen, E.P. Hyatt, Sintering of Alumina at Temperatures of 1400°C. and Below, J. Am. Ceram. Soc. 40 (1957) 134–139. https://doi.org/10/cnqgf6.

[199] C. Greskovich, J.A. Brewer, Solubility of Magnesia in Polycrystalline Alumina at High Temperatures, J. Am. Ceram. Soc. 84 (2001) 420–25. https://doi.org/10/c9b4st.

[200] M.F. Yan, Microstructural control in the processing of electronic ceramics, Mater. Sci. Eng. 48 (1981) 53–72. https://doi.org/10/frt9qx.

[201] J.G.J. Peelen, Alumina: Sintering and Optical Properties, J.G.J. Peelen, 1977.

[202] D. Oropeza, R. Roberts, A.J. Hart, A rapid development workflow for binder inks for additive manufacturing with application to polymer and reactive binder ink formulation, (submitted for review).

[203] D. Oropeza, A.J. Hart, A laboratory-scale binder jet additive manufacturing testbed for process exploration and material development, Int. J. Adv. Manuf. Technol. 114 (2021) 3459–3473. https://doi.org/10/gkhbcm.